

Variant selection in martensitic steels

Thèse N° 9635

Présentée le 12 juillet 2019

à la Faculté des sciences et techniques de l'ingénieur
Laboratoire de métallurgie thermomécanique - Chaire PX Group
Programme doctoral en science et génie des matériaux

pour l'obtention du grade de Docteur ès Sciences

par

Annick Pauline BAUR

Acceptée sur proposition du jury

Prof. A. Fontcuberta i Morral, présidente du jury
Prof. R. Logé, Dr. C. Cayron, directeurs de thèse
Dr X. Huang, rapporteur
Prof. S. Godet, rapporteur
Dr C. Leinenbach, rapporteur

2019

It is a capital mistake to theorize before you have all the evidence.

It biases the judgment.

— S. Holmes in *A study in scarlet* (A.C. Doyle, 1886)

Acknowledgements

My acknowledgements first go to Prof. Roland Logé and Dr. Cyril Cayron, my thesis director and co-director. I thank you Roland for your kind and caring supervision, where wise advices and attentive ears were always available. Thank you Cyril for teaching me material science far beyond the border of steel metallurgy and for encouraging and supporting me during these four years.

I am thankful also to all the members of my thesis jury: Dr. Xiaoxu Huang, Prof. Stéphane Godet, Dr. Christian Leinenbach and Prof. Anna Fontcuberta, for their time and their valuable comments.

I acknowledge also ArcelorMittal, who provided a large part of the material used in the experiments. I am particularly thankful to Kangying Zhu for her availability and kindness, and for the organisation of the *ArcelorMittal Thesis Day*. I would like to thank Arnaud Magrez and the staff of the *Crystal Growth Facility* at EPFL, for their kind help and support provided for my experiments.

This work also benefits from some fruitful exchanges with researchers worldwide, in particular Anton Muhlemann, Francesco della Porta, Matteo Villa and Francesco Maresca, as well as all the people who participated in the *ArcelorMittal Thesis Days*.

I would not have enjoyed my PhD studies as much as I did, if I was not so fortunate to having such friendly colleagues as mine! So, I would like to thank all LMTM lab members for being so kind and full of attentions. I am particularly thankful to my office mates, Margaux and Rita for bringing sunshine in our office, even during the greyish days of Neuchâtel's winters. A special thanks also to Priscille and Mathijs, who actively participated in my experiments, for their technical help, suggestions and ideas. I would also like to thank EPFL friends in Lausanne, in particular Predrag and Fabio, for making my journeys to Lausanne much more attractive than they would have been without them. From Lausanne, many thanks also to Stéf for sharing the PhD experience with me and for all the nice moments we spent together, here and there, for so many years.

Finally, I am profoundly thankful to my family, for their continued support, not only during this thesis work, but since the very beginning. Thanks also to Philo who was certainly not the person the most interested by my research work, but who contributed to it much more than what he would have expected. Thank you for simply making life brighter.

Neuchâtel, 24 June 2019

Abstract

The martensitic phase transformation in steel is one of the most famous solid state transformation because of its contribution in the development of the modern industry. This transformation from a face-centered cubic (FCC) high temperature phase, called the *austenite*, to a metastable body-centered cubic (BCC) low temperature phase, the *martensite*, is crucial in the steels metallurgy, as the strength of the material relies on it. Despite numerous studies, this transformation exhibits particular features that are still not fully understood. Among these, the *variant selection* phenomenon, observed when stress and/or strain is applied to the material during or prior to transformation, is of particular interest due to its implications in the industrial processing of steels.

Various criteria have been proposed in the literature to model variant selection, most of them being based on the work of the deformation associated with the transformation in the applied stress field. The deformation used in the computation of the work is generally determined by using the *Phenomenological Theory of the Martensite Crystallography* (PTMC). However, this theory considers different deformations to model the transformation, and there is currently a lack of consent on which of these different deformations is the most appropriate to account for the selection phenomenon.

In this thesis, we propose to use a novel mechanistic transformation model, called the *continuous distortion* model to study the selection phenomenon. This model describe the transformation of the FCC lattice to a BCC lattice by using an atomistic description of the lattice change.

The first part of this thesis is a study of the capabilities of the new model in accounting for crystallographic features of the transformation. Our study indicates that the crystallographic nature of the interfaces between the martensite and the austenite can be explained by combinations of different variants of the continuous model. It appears also that under the same assumptions, the mechanistic and the phenomenological model are equivalent.

In the second part of this thesis, the variant selection is studied experimentally. Different thermomechanical treatments are applied to various types of steels, and the produced microstructures are characterized by Electron BackScattered Diffraction (EBSD). The experimental results suggest that the deformation that needs to be consider in the computation of the work depends of the type of strain accommodation mechanism involved during the transformation. When the accommodation of the martensite product is achieved by dislocations, the deformation associated with individual variant should be considered in the computation of the work. On the contrary, when the accommodation is based on variants coupling, it is the

Abstract

combination of the deformations of the coupled variants that matters.

This thesis lays the foundations for a more unified vision of variant selection in martensitic steels, by considering a unique deformation model, and underlines the importance of the accommodation mechanisms in the selection phenomenon.

Key words: FCC-BCC martensitic phase transformation, variant selection, PTMC, continuous distortion model

Résumé

La transformation martensitique dans les aciers compte parmi les plus importantes transformations de phase à l'état solide, principalement en raison de sa contribution au développement de l'industrie moderne. En effet, cette transformation de l'austénite, une phase cubique à faces centrées (CFC), stable à haute température, en martensite, une phase cubique centrée (CC), métastable à basse température, est la clef des bonnes propriétés mécaniques des aciers. Cependant, en dépit des nombreuses études qui lui sont dédiées, cette transformation présente des caractéristiques qui échappent encore à une pleine compréhension. Parmi elles, la *sélection de variants*, observée lorsque des contraintes et/ou des déformations sont appliquées au matériau avant et durant la transformation de phase, revêt un intérêt particulier au vu de ses conséquences sur la production industrielle des aciers.

Différents critères de sélection de variants sont proposés dans la littérature, la plupart étant basés sur le travail de la déformation associée à la transformation dans le champ de contrainte appliqué. La déformation considérée dans l'évaluation du travail est généralement déterminée par le modèle classique de la transformation martensitique, appelé *Théorie Phénoménologique de la Cristallographie de la Martensite* (PTMC). Cependant, cette théorie utilise plusieurs déformations pour modéliser la transformation et il y a actuellement un manque de consensus concernant le choix de la déformation à considérer dans le calcul du travail.

Dans cette thèse, nous proposons d'étudier la sélection de variants en utilisant un nouveau modèle transformation, appelé *modèle continu de la distorsion*. Ce dernier décrit la transformation du réseau CFC en un réseau CC à l'échelle atomique et de manière continue, contrastant ainsi avec la nature phénoménologique du modèle classique.

La première partie de cette thèse propose une analyse des caractéristiques cristallographiques pouvant être expliquées par le nouveau modèle. Il a été mis en évidence que la nature cristallographique des interfaces entre la martensite et l'austénite peut être expliquée par la combinaison de différents variants du modèle continu. Il a également été montré que lorsque les mêmes hypothèses sont considérées, le modèle phénoménologique et le modèle continu sont équivalents. Dans la deuxième partie de la thèse, une étude expérimentale de la sélection de variants est proposée. Cette étude est effectuée en imposant des traitements thermomécaniques sur différents types d'aciers, puis en caractérisant les microstructures produites, à l'aide de diffraction d'électrons rétrodiffusés (EBSD). Ces expériences indiquent qu'un critère basé sur le travail de la déformation associée au modèle continu dans le champ de contrainte appliqué est approprié pour étudier la sélection de variants. Il apparaît aussi que la déformation pertinente pour calculer le travail dépend de la nature des mécanismes d'accommodation

Résumé

à l'oeuvre durant la transformation. Lorsque l'accommodation de la martensite est effectuée par plasticité, la déformation propre à chaque variant doit être considérée dans le calcul du travail. Au contraire, si l'accommodation se fait par association de variants, la déformation qui importe est la combinaison des déformations des différents variants considérés.

Ce travail pose les bases d'une vision plus unifiée de la sélection de variants dans les aciers martensitiques en utilisant un modèle unique et souligne l'importance des mécanismes d'accommodation dans le phénomène de sélection.

Mots clefs : transformation martensitique CFC-CC, sélection de variants, PTMC, modèle continu de la distorsion.

Contents

| | |
|--|-------------|
| Acknowledgements | i |
| Abstract (English/Français) | iii |
| List of figures | ix |
| List of tables | xiii |
| 1 Introduction | 1 |
| 2 State of the art | 11 |
| 3 Scope of the thesis | 23 |
| 4 Mathematical framework | 27 |
| 5 $\{225\}_\gamma$ habit planes in martensitic steels: from the PTMC to a continuous model | 39 |
| 6 Accommodation of the $\{225\}_\gamma$ habit plane by dislocations | 57 |
| 7 Intricate morphologies of laths and blocks in low-carbon martensitic steels | 65 |
| 7.1 Introduction | 66 |
| 7.2 Method | 71 |
| 7.3 Experiment | 73 |
| 7.4 Crystallographic interpretation and discussion | 81 |
| 7.5 Conclusion | 92 |
| 8 Variant selection in surface martensite | 99 |
| 9 On the chevron morphology of surface martensite | 113 |
| 10 Variant Selection in Fe-20Ni-1.8C under Bending | 129 |
| 11 Effect of tensile deformation on variant selection in $\{225\}_\gamma$ plate martensite and $\{557\}_\gamma$ lath martensite | 143 |
| 12 General discussion | 159 |

Contents

| | |
|--|------------|
| 13 Conclusions and perspectives | 169 |
| A Supplements to <i>Variant selection in surface martensite</i> | 173 |
| A.1 Characterization at lower magnification | 173 |
| A.2 Additional simulations | 174 |
| A.3 Isothermal surface martensite | 178 |
| A.4 Crystallography of the habit plane | 179 |
| A.5 The PTMC solutions | 180 |
| A.6 Quantitative analysis of the variant selection prediction | 183 |
| A.7 The PTMC solution with hard sphere ratio | 184 |
| A.8 Orientation relationships | 186 |
| B Supplements to <i>Intricate morphologies of laths and blocks in low-carbon martensitic steels</i> | 189 |
| C Supplements to <i>On the chevron morphology of surface martensite</i> | 199 |
| C.1 Additional maps | 199 |
| C.2 Crystallographic features | 202 |
| C.3 Variant selection predictions and predictions of the favoured austenite orientations based on the PTMC | 204 |
| D Variants table | 209 |
| D.1 Grouping of variants | 211 |
| Bibliography | 220 |
| Curriculum Vitae | 221 |

List of Figures

| | | |
|-----|---|----|
| 1.1 | Crystalline structure in steels | 2 |
| 1.2 | Kurdjumov-Sachs and Nishiyama-Wassermann variants | 3 |
| 1.3 | Continuous patterns in martensite pole figures | 3 |
| 1.4 | 24 Kurdjumov-Sachs variants | 4 |
| 1.5 | Surface relief and deviation of fiducial lines | 5 |
| 1.6 | Shape change associated with the transformation | 6 |
| 1.7 | Morphologies of ferrous martensite | 6 |
| 1.8 | Midrib and dislocations zone in martensite | 7 |
| 1.9 | Supercooling and superheating in martensitic transformations | 9 |
| 2.1 | Illustration of the Bain strain | 12 |
| 2.2 | Concepts behind the Phenomenological Theory of the Martensite Crystallography | 13 |
| 2.3 | Lattice invariant shear on a $\{225\}_{\gamma}$ habit plane | 14 |
| 2.4 | Microstructure associated with the Muhlemann and Koumatos' model | 16 |
| 2.5 | The continuous FCC-BCC transformation mechanism | 17 |
| 2.6 | Continuous transformation of a FCC unit cell | 18 |
| 2.7 | Schematic representation of a transformed austenite parent grain in lath marten- site in a low-carbon steel | 19 |
| 2.8 | Various types of couplings for different carbon steels | 19 |
| 2.9 | Variant selected in the model of Chiba | 21 |
| 4.1 | Condition of coherence at an interface between two transformed domains . . . | 34 |
| 4.2 | Maximization of the work of the transformation | 38 |
| 5.1 | Common $\{111\}$ planes and $\langle 110 \rangle$ directions of twin-related variants | 43 |
| 5.2 | Schematic representation of $(225)_{\gamma}$ thin plate of martensite. | 46 |
| 5.3 | $(225)_{\gamma}$ thin plate | 48 |
| 5.4 | Snapshots of the $(225)_{\gamma}$ thin plate formation | 49 |
| 5.5 | Comparison between the atomic displacements in the $(11\sqrt{6})_{\gamma}$ plane and in the $(111)_{\gamma}$ plane | 49 |
| 6.1 | Illustration of the deformation of a common lattice in the two crystals A and B. | 57 |
| 6.2 | Illustration of the dislocation array in the interface | 59 |

List of Figures

| | | |
|------|---|-----|
| 6.3 | Illustration of the atomic displacement associated with two twin-related variants (1 and 3) on a $(225)_\gamma$ plane | 60 |
| 7.1 | Schematic representation of the KS and NW variants. | 68 |
| 7.2 | Packet with the three blocks constituted by pairs of KS variants | 69 |
| 7.3 | Three hypotheses for the morphologies of the blocks | 69 |
| 7.4 | Simulated pole figures | 72 |
| 7.5 | TEM image and diffraction patterns of an assembly of martensite laths | 74 |
| 7.6 | TEM image and SAED patterns of a pair of intricate laths belonging to the same block | 75 |
| 7.7 | EBSD map of the as-quenched 1018 steel | 76 |
| 7.8 | Determination of the habit planes in the EBSD map | 78 |
| 7.9 | Regions A and B of the EBSD map of Fig. 7.7 | 79 |
| 7.10 | EBSD map acquired on the as-quenched 1018 steel with the orientation of a prior austenite grain close to a $\langle 111 \rangle_\gamma$ zone axis | 80 |
| 7.11 | Representation of the angular distortion part on the $(111)_\gamma$ plane | 85 |
| 7.12 | Rotation angle of the planes $(1, 1, l)_\gamma$ | 89 |
| 7.13 | Morphological/crystallographic model of the three blocks in a $(111)_\gamma \parallel (110)_\alpha$ packet | 90 |
| 8.1 | EBSD measurements of surface martensite | 104 |
| 8.2 | Prediction of variant selection for map 1 | 105 |
| 8.3 | Prediction of variant selection for map 2 | 106 |
| 8.4 | Twin-related variants combination for habit plane accommodation | 107 |
| 8.5 | Orientation relationships. | 109 |
| 9.1 | Optical micrograph of chevron martensite | 115 |
| 9.2 | EBSD map of chevron martensite | 116 |
| 9.3 | Crystallography and morphology of chevron martensite | 117 |
| 9.4 | Band contrast EBSD maps of the martensite and Histogram of the angle in degrees between the normal to the twinning plane and the normal to the free surface | 118 |
| 9.5 | Simulated pole figure of the chevron martensite | 121 |
| 9.6 | H_{zz} criterion for the martensite nucleation for a variant belonging to $(111)_\gamma \parallel (1\bar{1}0)_\alpha$ CPP packet | 122 |
| 9.7 | Map of H_{zz} and favoured austenite orientations | 124 |
| 10.1 | Four-point bending device | 132 |
| 10.2 | Bright-field optical micrograph of the sample in 4-point bending | 132 |
| 10.3 | EBSD map of a column of martensite | 133 |
| 10.4 | Histograms of the variants' occurrence considering the BCC and BCT | 134 |
| 10.5 | Trace analysis of the shape strain predicted by the Phenomenological Theory of Martensite Crystallography (PTMC) and variant selection prediction | 135 |

| | |
|---|-----|
| 10.6 Empirical criterion for variant selection | 136 |
| 10.7 Histograms of plate group occurrence considering a ranking based on the empirical criterion | 137 |
| 10.8 Variant selection in the single parent grain | 138 |
| 11.1 Representation of the thermomechanical treatments | 147 |
| 11.2 EBSD maps of the plate and lath martensite | 149 |
| 11.3 Histogramm of the variant occurrence with a ranking based on work of the shape strain | 151 |
| 11.4 Histogramm of the variant occurrence in the lath martensite with a ranking based on the work criterion | 152 |
| 11.5 EBSD map of lath martensite and CPP packet repartition | 153 |
| 11.6 Repartition of the 3 Nishijama-Wassermann variants inside the favoured CPP | 155 |
| 12.1 Effect of free surface | 163 |
| 12.2 EBSD map of surface martensite formed during bending | 164 |
| 12.3 TEM micrograph of $\{259\}_{\gamma}$ lenticular martensite | 165 |
| 12.4 Map of variant selection | 166 |
| 12.5 Morphologies related to the variant selection phenomenon | 167 |
| A.1 EBSD map of surface martensite at lower magnification (x65). | 173 |
| A.2 EBSD measurements of surface martensite and pole figures of the martensite | 174 |
| A.3 EBSD measurements of surface martensite and pole figures of the martensite | 175 |
| A.4 Prediction of variant selection for the map 1 | 176 |
| A.5 Prediction of variant selection for the map 2 | 177 |
| A.6 Bright field micrographs of surface martensite | 178 |
| A.7 Study of the habit plane of surface martensite | 179 |
| A.8 EBSD measurements of surface martensite | 180 |
| A.9 Chart of the PTMC solutions | 181 |
| A.10 Martensite pole figure of the two PTMC solutions | 181 |
| A.11 Prediction of variant selection for the map 1 | 182 |
| A.12 Prediction of variant selection for the map 2 | 182 |
| A.13 Superimposition of the experimental and predicted $\{100\}_{\alpha}$ pole figures | 183 |
| A.14 Superimposition of the experimental and predicted $\{110\}_{\alpha}$ pole figures | 183 |
| A.15 Simulations based on the IPS associated with hard-sphere ratio | 185 |
| A.16 Superimposition of the predicted and the measured $\{110\}_{\alpha}$ pole figure | 185 |
| A.17 Pole figures of the bulk martensite | 186 |
| A.18 Pole figures of the surface martensite | 186 |
| A.19 Orientation relationship at the grain boundaries | 187 |
| A.20 Orientation relationship in the plate | 188 |
| C.1 Band contrast EBSD map with annotation of the θ -angle | 199 |
| C.2 EBSD map of chevron martensite and associated pole figures of the martensite | 200 |

List of Figures

| | | |
|-----|---|-----|
| C.3 | EBSD map of chevron martensite and associated pole figures of the martensite | 201 |
| C.4 | Habit plane analysis | 202 |
| C.5 | Analysis of the orientation relationship | 203 |
| C.6 | Simulated pole figure of the chevron martensite | 205 |
| C.7 | Simulated pole figures of the chevron martensite | 205 |
| C.8 | Magnitude of H_{zz} as function of the θ angle in degrees between the normal to the twinning plane normal and the sample surface | 206 |
| | | |
| D.1 | Misorientation table between Kurdjumov-Sachs variants | 210 |
| D.2 | CPP group | 212 |
| D.3 | Bain group | 213 |
| D.4 | Plate group | 214 |

List of Tables

| | | |
|------|---|-----|
| 1.1 | Morphologies, habit plane and orientation relationship as function of the M_s | 8 |
| 5.1 | Crystallographic features of the FCC-BCC transformation of twin-related variants | 43 |
| 5.2 | Crystallographic features of the interface between twin-related variants | 45 |
| 7.1 | Chemical composition of the steels | 76 |
| 7.2 | Surface percentage of the different ORs | 77 |
| 7.3 | Angular compatibility between the laths and the surrounding blocks | 89 |
| 8.1 | Comparison of the quality for the predictions for the four different models. | 108 |
| 11.1 | Transformation temperatures and features of the heat treatments | 148 |
| 11.2 | Stress and strains associated with the treatments | 148 |
| 12.1 | Comparison between the PTMC and the continuous model in the $\{225\}_\gamma$ case | 160 |
| A.1 | Quality of the predictions with hard sphere lattice parameters | 184 |
| A.2 | Comparison of the quality for the predictions for the four different models. | 187 |
| D.1 | Variants grouping | 211 |

1 Introduction

This thesis deals with the martensitic transformation in steels. It focuses on the study of a transformation related phenomenon, the *variant selection*. In this introduction, generalities about the phase transformation are presented. In particular, the crystallography of the transformation is detailed.

Martensitic transformation in steels

The martensitic phase transformation in steels is of technological interest as the strength of steels essentially relies on it. This phase transformation is induced by a rapid quenching of a thermodynamically stable high temperature phase called the *austenite*. The product of this fast cooling is a metastable phase called the *martensite* in honor to the german metallographer Adolf Martens who developed metallographic techniques for characterizing iron-based alloys. This phase exhibits a fine microstructure and a significant amount of lattice defects, such as dislocations. The martensitic transformation in steels is defined as a *displacive* transformation, meaning that it is associated with a cooperative motion of atoms. Nishiyama (1901-1991), a pioneer in the study of the martensitic transformation in steels, uses a japanese word to describe it: *Shōgidaoshi*, translated by him "falling one after another in succession", like a domino [Nishiyama, 2012]. No diffusion occurs during the phase change, and the transformation can propagate at almost the velocity of sound. As a consequence of its displacive nature, the martensitic transformation is characterized by particular crystallographic and thermodynamics features, and proper morphologies.

Crystallography of the transformation

Nature of the lattice change

The martensitic transformation leads to a change in the crystalline structure. The crystalline structure of austenite is Face-Centered Cubic (FCC), and as the material is quenched below the transformation temperature, its structure changes to Body-Centered Cubic (BCC), Body-

Centered Tetragonal (BCT) or Hexagonal Close-Packed (HCP), depending on the alloys. The BCC/BCT martensite is formed in a large range of steels, whereas HCP is typically observed in high manganese steels. The BCC and BCT phases are generally called α or α' martensite. The HCP phase is named ϵ martensite. The austenite is noted γ . This thesis focuses on the FCC-BCC(T) transformation, and the ϵ martensite formation is not treated here. Schematic representations of the three different crystalline structures are presented in figure 1.1.

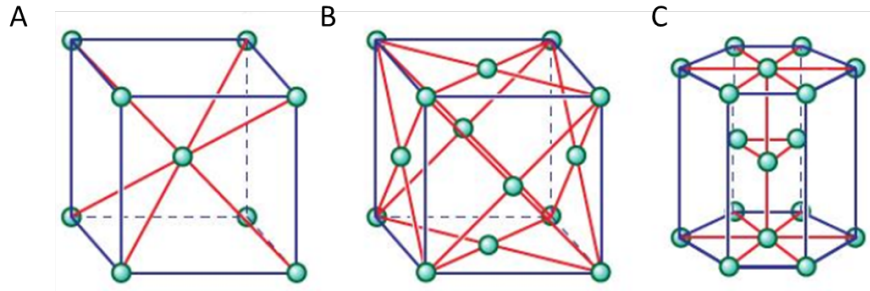


Figure 1.1: Crystalline structure commonly found in steels [Britannica, 2011]. **A:** BCC structure of the α martensite. **B:** FCC structure of the austenite. **C:** HCP structure of the ϵ martensite.

Orientation relationship and transformation variants

As a common feature to all displacive transformations, the daughter phase is not oriented randomly in respect to the parent lattice, it obeys some crystallographic rules which are called *orientation relationships*. These relationships are generally expressed in terms of parallelism between planes and directions of the parent and daughter phases. In martensitic steels, various orientation relationships are observed. The first measurement of orientation relationship in steel is due to Kurdjumov and Sachs in 1930 [Kurdjumov and Sachs, 1930], who studied the transformation in Fe-1.4%C. For that alloy, they reported that the close-packed planes as well as the close-packed directions of martensite and austenite are parallel: $(011)_{\alpha} \parallel (111)_{\gamma}$ and $[\bar{1}\bar{1}1]_{\alpha} \parallel [10\bar{1}]_{\gamma}$. The same parallelism between closed-packed planes was already reported in 1926 by Young in iron meteorites [Young, 1926]. In 1934, Nishiyama observed a slightly different orientation relationship when studying a Fe-30%Ni alloy [Nishiyama, 1934]. His measurement agrees with those of Wassermann in the same steel [Wassermann, 1933]. The reported orientation relationship is $(011)_{\alpha} \parallel (111)_{\gamma}$ and $[100]_{\alpha} \parallel [01\bar{1}]_{\gamma}$ now called the *Nishiyama-Wassermann* orientation relationship. Later, other orientation relationships were observed, by Greninger and Troiano in 1949 in Fe-22%Ni-0.8%C [Greninger and Troiano, 1949] and Pitsch in 1959, who studied thin foils of Fe-N [Pitsch, 1959]. The presence of an orientation relationship between parent and daughter crystal implies that each parent grain can transform in a fixed number of daughter crystal orientations. These are called the *orientation variants* or simply *variants* of the transformation. Depending on the nature of the orientation relationship, the number of orientation variants changes. For example, there are 24 Kurdjumov-Sachs variants and only 12 Nishiyama-Wassermann variants. The pole figures

in figure 1.2 show the variants associated with the Kurdjumov-Sachs orientation relationship in red and the Nishiyama-Wassermann orientation relationships in black.

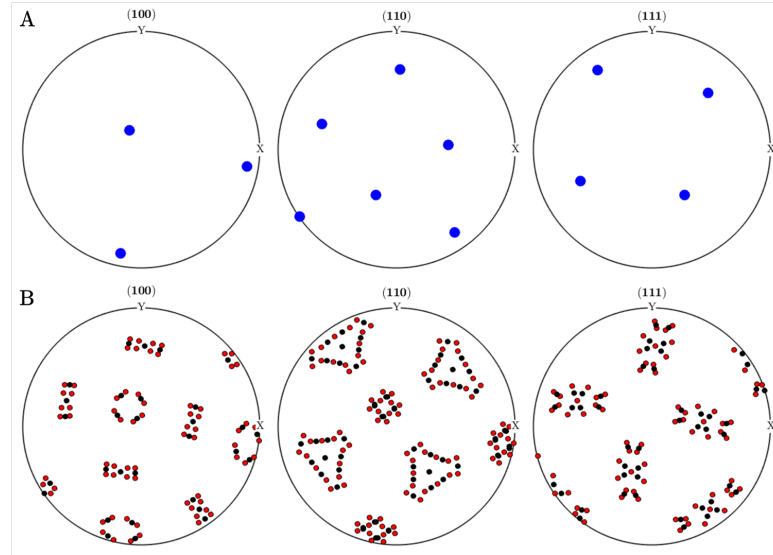


Figure 1.2: **A:** $\{100\}_\gamma$, $\{110\}_\gamma$ and $\{111\}_\gamma$ pole figures of a parent austenite grain. **B:** The 24 Kurdjumov-Sachs variants (in red) and 12 Nishiyama-Wassermann variants (in black) associated with the transformation of the parent grain in A. The variants are represented on the $\{100\}_\alpha$, $\{110\}_\alpha$ and $\{111\}_\alpha$ pole figures

Generally, it is acknowledged that the orientation relationship depends of the alloy composition and transformation temperature [Nishiyama, 2012]. However, recent EBSD studies performed by Cayron indicate that there exists a continuous orientation spread, characterized by continuous patterns in the pole figures, as shown in figure 1.3 [Cayron et al., 2010]. Cayron further shows that even in a single lath of low-carbon steel, the orientation relationship can vary between Pitsch, Kurdjumov-Sachs, Greninger-Troiano and Nishiyama-Wassermann [Cayron, 2014].

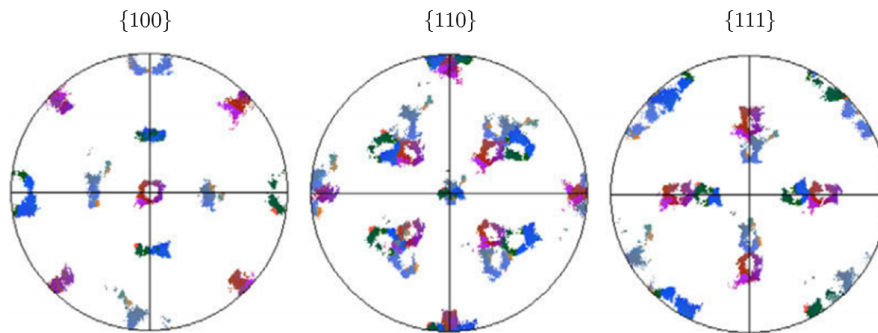


Figure 1.3: Experimental pole figures of martensite formed in an austenite grain ref. [Cayron et al., 2010]

The 24 Kurdjumov-Sachs variants. Among the different orientation relationships reported, the one of Kurdjumov-Sachs is of particular interest in this thesis, and as such the variants associated with this orientation relationship are detailed here. As mentioned above the Kurdjumov-Sachs orientation relationship has the specificity of keeping the respective close-packed planes and close-packed directions of the FCC and BCC lattices parallel. On the basis of such parallelism, groups of variants can be defined. The variants having their close-packed plane parallel to the same close-packed plane of the austenite are said to belong to the same *Close-Packed Plane* packet (CPP packet). The variants having their close-packed direction parallel to the same close-packed direction of the austenite belongs to the same *Close-Packed Direction* packet (CPD packet) [Cayron, 2014]. Figure 1.4 shows the 24 Kurdjumov-Sachs variants as squares on the four $\{111\}_\gamma$ close-packed planes of the austenite. Variants 1, 2, 3, 5, 6 and 8 thus belong to the same CPP packet¹. The edges of the triangles are the close-packed direction of the austenite. The variants are positioned on the edge that is parallel to their close-packed direction. Variants 1, 3, 4 and 9 belong to the same CPD direction. The pairs of variants that belong to the same CPP and CPD packets, for example variants 1 and 3, have a particular misorientation of 60° around $[111]_\alpha$ and they are said to be *twin-related* variants.

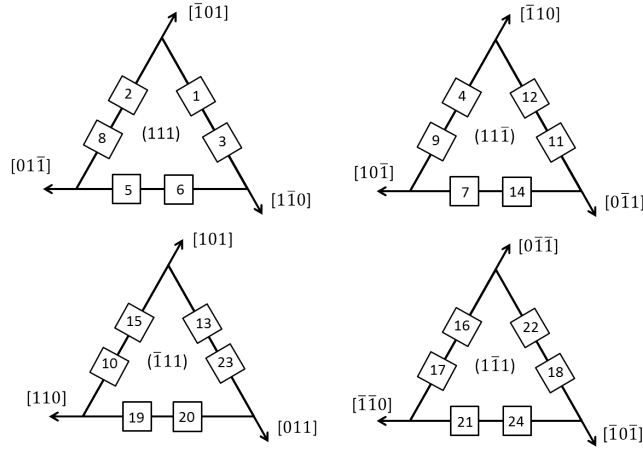


Figure 1.4: 24 Kurdjumov-Sachs variants represented on the $\{111\}_\gamma$ planes of the austenite.

Variant selection

All variants are supposed to form equiprobably when the transformation occurs. However, many researchers reported that some variants are formed preferentially, as a consequence of the application of an external stress [Higo et al., 1974, Gautier et al., 1989, Kundu and Bhadeshia, 2007, Abreu et al., 2009] or a prior deformation [Chiba et al., 2012, Miyamoto et al., 2012]. This phenomenon is called *variant selection*. In the two aforementioned cases, when stress or prior deformation is applied to the material, the variant selection is *global* and takes

¹We mention that the number given to the variants here is different from the numbering presented in Morito *et al.*'s work [Morito et al., 2003]. The present numbering is detailed in Appendix D.

place at the scale of the sample. Besides, *local* variant selection can also be observed. The concept of local variant selection describes the particular variants pairing or coupling that are often reported in steels [Bokros and Parker, 1963, Morito et al., 2003, Stormvinter et al., 2012]. Contrarily to the global variant selection, the local variant selection is operating at the grain scale. The variant selection phenomenon, at both local and global scale, is the topic of this thesis.

Shape change and surface relief

In the early days of the crystallographic study of the martensite transformation, the use of alloys with transformation temperature below room temperature was common, in order to simplify both the experimental method and the crystallographic analysis. Scheil is one of the initiators of such approach. He proposes to use Fe-28%Ni and Fe-29%Ni alloys, whose transformation temperature is around 0°C, to model the martensitic transformation in carbon steels [Scheil, 1932]. When pre-polished surfaces of such alloys are quenched below the transformation temperature, surface reliefs appear on the transformed zones. Similarly, existing scratch lines on the austenite are deviated where the martensite forms. Figure 1.5 illustrates the phenomenon. This observable shape change is considered as an essential feature of the

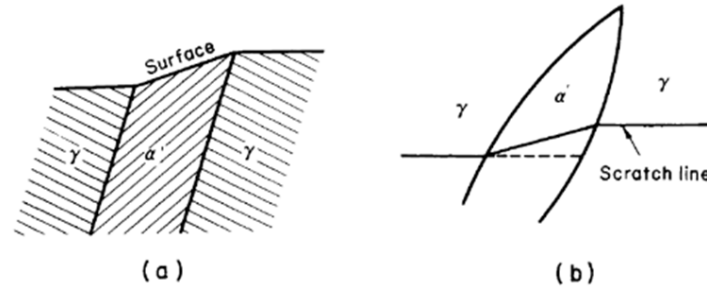


Figure 1.5: Illustration of the surface relief (a) and the deviation of fiducial lines (b) from ref. [Nishiyama, 2012]

martensitic transformation [Bowles and Barrett, 1952]. As such, it has been the object of detailed studies performed by Greninger and Troiano in Fe-22%Ni-0.8%C (1949) [Greninger and Troiano, 1949], and by Machlin and Cohen in Fe-30%Ni (1951) [Machlin and Cohen, 1951]. They both described the shape change as an homogeneous deformation in which a plane is kept invariant, this plane being the interface between the austenite and the martensite. This plane is called *habit plane* and is believed to be the plane where the transformation initiates. The crystallographic orientation of the habit plane is not random; there are about four different habit planes observed in martensitic steels $\{225\}_{\gamma}$, $\{259\}_{\gamma}$, $\{31015\}_{\gamma}$ and $\{557\}_{\gamma}$. The type of habit plane depends mainly on the martensitic start temperature, noted M_s . The alloys used by the two groups who first measured the shape change exhibit $\{259\}_{\gamma}$ habit plane. Both conclude that the shape change associated with the transformation is a combination of a shear s parallel to the habit plane and a dilatation δ normal to it, as illustrated in figure 1.6.

This type of deformation is named an *invariant plane strain* (IPS). The invariant plane strain

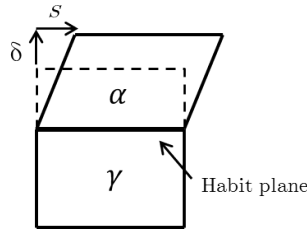


Figure 1.6: Schematic representation of the shape change associated with the martensitic transformation, with the combination of a shear s parallel to the habit plane and a dilatation δ normal to it.

is a key element in the majority of the future models of the transformation, in particular in the most famous one, the *Phenomenological Theory of the Martensite Crystallography* [Wechsler and Read, 1953, Bowles and Mackenzie, 1954a].

Morphology of the martensite

A wide range of martensite morphologies are observed in steels, and various studies have been carried out to understand the condition of formation of the different types of martensite morphologies [Jana and Wayman, 1970, Maki et al., 1973, Umemoto et al., 1983, Morito et al., 2003]. Generally the morphologies are classified in five different categories: *lath*, $\{225\}_{\gamma}$ -*plate*, *butterfly*, *lenticular* and *thin plate* [Maki, 2012]. Examples of these morphologies are presented in

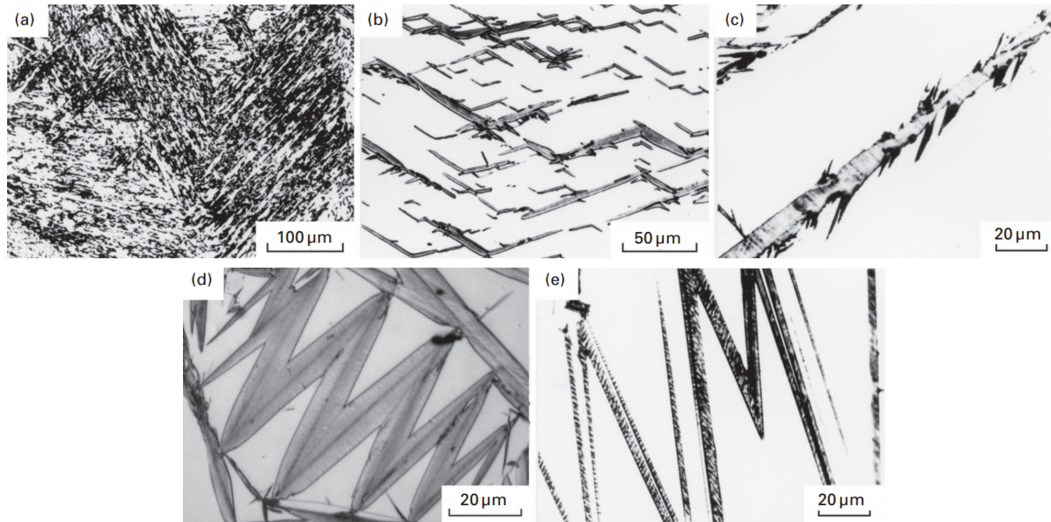


Figure 1.7: Optical micrograph of the different morphologies observed in ferrous martensite. **A:** lath in Fe-7%Ni-0.22%C. **B:** butterfly in Fe-20%Ni-0.73%C. **C:** $\{225\}_{\gamma}$ -plate in Fe-8%Cr-0.9%C. **D:** lenticular in Fe-29%Ni-0.26%C. **E:** thin plate in Fe-31%Ni-0.23%C. Micrographs taken from ref. [Maki, 2012]

figure 1.7 for different alloys. From figure 1.7, it can be noticed that changes of the morphology are observed according to the alloy composition. As an example, laths are formed in Fe-Ni-C alloy with 7% Ni and 0.22%C (figure 1.7A), whereas thin plates (figure 1.7E) are observed by increasing the Ni content to 31%. Along with the changes of morphologies, varies also the type of the habit plane and the orientation relationship. The details of the factors affecting the transition from one type of martensite to another are not yet fully understood [Maki, 2012]. However, the type of accommodation mechanism appears to be a crucial element. The prevalence of a particular accommodation mechanism essentially depends on the temperature at which the martensite starts to form. $\{557\}_\gamma$ lath martensite observed in low-carbon steel forms at relatively high temperature ($> 350^\circ\text{C}$). At such temperature, the motion of dislocations does not require a significant amount of energy, and the accommodation of lath martensite is essentially achieved through this mechanism. By increasing the carbon and the nickel content in the steel, the martensitic start temperature decreases. The accommodation mechanism thus progressively changes. In carbon steels containing between 0.55 and 1.4wt%C, $\{225\}_\gamma$ plates are formed at temperatures that range between 250°C and 100°C . These martensites exhibit a fine microstructure composed of $\{112\}_\alpha$ twins. Considering the Kurdjumov-Sachs orientation relationship observed with such alloys, $\{112\}_\alpha$ twins are in fact twin-related variants of the transformation. In $\{225\}_\gamma$ -plates, the twinned zone does not extend through the entire plate, and dislocations are generally observed inside $\{225\}_\gamma$ plates. Butterfly martensite produced at a slightly lower temperature (75°C) shares the same habit plane and accommodation process as $\{225\}_\gamma$ -plates [Sato and Zaefferer, 2009]. By further decreasing the M_s temperature below -30° , the habit plane moves toward $\{259\}_\gamma$. The martensite product is then lenticular. Its central part, called the *midrib*, appears unhomogenous and composed of twins. The nature of the twins is still unclear. $\{112\}_\alpha$ twins are often reported, but some researchers suggest the presence of additional $\{110\}_\alpha$ twins [Thomas, 1971]. Away from the midrib, toward the austenite/martensite interface, dislocations are observed. In alloys with even lower M_s , the sample needs to be quenched in liquid nitrogen to transform. The martensite products formed in such alloys are thin plates and have $\{31015\}_\gamma$ habit planes. The thin plates are composed exclusively of $\{112\}_\alpha$ twins. Figure 1.8 shows a schematic representation of the lenticular and thin plate martensite.

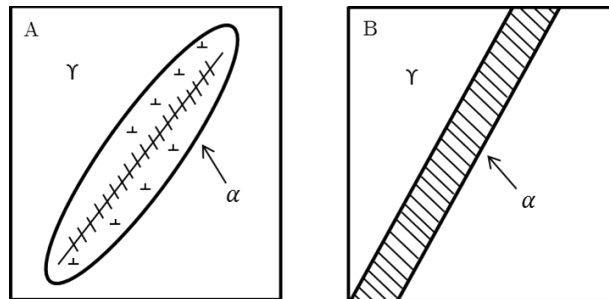


Figure 1.8: **A:** Illustration of a lenticular martensite with its twinned midrib and the dislocations zone. **B:** Illustration of a completely twinned thin plate of martensite

Chapter 1. Introduction

The main crystallographic features of the different types of martensite are summarized in table 1.1. The variations of the mean orientation relationship, the change of habit plane and the produced morphologies are presented as a function of the martensitic start temperature (M_s).

Table 1.1: Morphologies, habit plane and orientation relationship as function of the martensitic start temperature (M_s) from low M_s on the left to high M_s on the right. Table inspired from ref.[Sato and Zaefferer, 2009]. Abreviation of the different orientation relationships: Greninger-Troiano (GT), Nishiyama-Wassermann (NW) and Kurdjumov-Sachs (KS)

| | Low M_s | | | High M_s | |
|--------------------------|--------------------|--|--------------------|------------------------|------------------|
| Morphology | Thin plate | Lenticular | Butterfly | $\{225\}_\gamma$ plate | Lath |
| Habit Plane | $\{31015\}_\gamma$ | $\{259\}_\gamma$ or $\{31015\}_\gamma$ | $\{225\}_\gamma$ | $\{225\}_\gamma$ | $\{557\}_\gamma$ |
| Accommodation | Twins | Multiple twins+Dislocations | Twins+Dislocations | Twins+Dislocations | Dislocations |
| Orientation relationship | GT | GT/NW/KS | KS/NW | KS | KS |

Elements on the thermodynamics of the transformation

A major thermodynamical characteristic of the martensitic transformation is the supercooling necessary to start the transformation. Considering only the stability of the chemical bonds, the temperature of transition between the austenite and the martensite is the one that guarantees an equality between the free energy of the austenite F^γ and the free energy of the martensite F^α :

$$\Delta F^{\gamma \rightarrow \alpha} = F^\alpha - F^\gamma = 0 \quad (1.1)$$

In this notation, when the value of $\Delta F^{\gamma \rightarrow \alpha}$ becomes negative, the martensite is more stable than the austenite. The temperature at which $\Delta F^{\gamma \rightarrow \alpha} = 0$ is called T_0 . However, this temperature does not correspond to the measured transformation temperature M_s , which is significantly below T_0 . Similarly, the temperature at which the reverse transformation starts, A_s , is higher than the equilibrium temperature, $A_s > T_0$. Figure 1.9 illustrates that particularity. The condition $\Delta F^{\gamma \rightarrow \alpha} = 0$ is thus not sufficient to start the transformation, actually $|\Delta F^{\gamma \rightarrow \alpha}|$ has to be greater than some finite quantity [Kaufman and Cohen, 1958]:

$$|\Delta F^{\gamma \rightarrow \alpha}| > |\Delta F_{\text{mech}}| \quad (1.2)$$

The quantity ΔF^{mech} accounts for the non-chemical factors preventing the transformation, typically the interfacial energy and the strain energy. Indeed, the significant shape change associated with the transformation requires strain energy to be accommodated in the austenite matrix. In addition, the martensite products exhibit complex microstructures and hence a large number of interfaces are created during transformation.

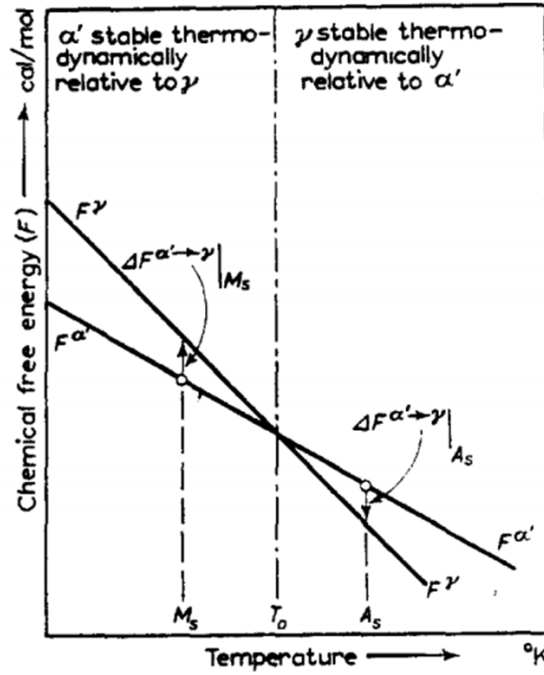


Figure 1.9: Illustration of the supercooling and the superheating observed in the martensitic transformation in iron-based alloys from [Kaufman and Cohen, 1958]. $\Delta F^{\alpha' \rightarrow \gamma}$ denotes the difference in free energy between the austenite and the martensite.

If the transformation is naturally hindered by the mechanical interaction between the martensite and the matrix, the M_s can be modified analogously by the application of external stress. Scheil (1932) observed the phenomenon [Scheil, 1932], and later Patel and Cohen quantified it [Patel and Cohen, 1953]. They showed that both an uniaxial compression and an uniaxial tension favour the transformation. On the contrary, the application of an hydrostatic pressure prevents it. In their experiments on Fe-20%Ni-0.5%C, they measured an increase of the M_s by 15°C and 10°C for an uniaxial tension and uniaxial compression respectively, and a decrease of 8.5°C with the application of an hydrostatic pressure. The changes in transformation temperature were measured for an applied stress of 103MPa.

In thermoelastic martensitic phase transformations occurring in shape memory alloys, the same type of phenomenon is observed. In these specific cases, the dependence of the transformation temperature with stress is classically studied by using the Clausius-Clapeyron equation [Otsuka and Wayman, 1999].

2 State of the art

In this chapter, the history of the modelling of the martensitic transformation is briefly presented. A particular attention is paid to the elements leading to the development of the most famous model of the transformation, the *Phenomenological Theory of the Martensite Crystallography*. Alternative mechanistic models are also presented.

A state of the art of the characterization and the modelling of the variant selection phenomenon is proposed. Both the local variant selection and the global variant selection are considered.

Modelling of the martensitic transformation

Early models and development of the PTMC

The history of the modelling of the martensitic transformation starts in the beginning of the 20th century with E.C. Bain, who proposed in 1924 a simple mechanism to change a FCC structure into BCC(T) [Bain and Dunkirk, 1924]. This process is illustrated in figure 2.1. Bain noted that an elongated BCT structure appears by combining two adjacent FCC cells. To convert it in a cubic (BCC) or slightly tetragonal (BCT) structure, the elongated BCT cell needs to be compressed in the vertical direction and stretched in the two other orthogonal directions. Such deformation is now called the *Bain strain*. The structural change associated with the martensitic transformation is successfully modelled by the Bain strain, but careful characterization of the orientation relationship performed slightly later (1930-1934) on various steels [Kurdjumov and Sachs, 1930] [Nishiyama, 1934] [Wassermann, 1933] concluded that Bain's model does not predict the correct orientation relationship. To our best knowledge the orientation relationship associated with the Bain strain has only been observed in an Fe-Pt alloy [Tadaki and Shimizu, 1970]. Conversely, the atomic correspondance, namely what becomes in the BCC lattice each direction of the FCC lattice, as defined in the Bain's model, is considered to be true in steels [Bowles and Wayman, 1972]. As a matter of fact, it has recently been proved that Bain's correspondance involves the minimum atomic motion [Koumatos and Muehlemann, 2016]. Considering figure 2.1, the Bain's correspondance implies that one of

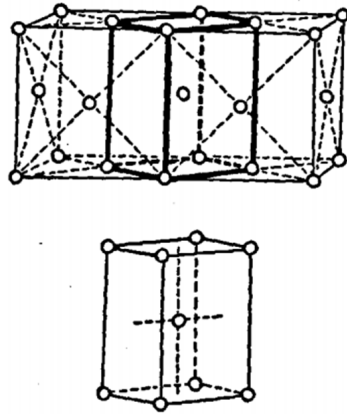


FIG. 3.—BODY-CENTERED TETRAGONAL LATTICE DELINEATED IN AUSTENITE (FACE-CENTERED CUBIC) STRUCTURE.

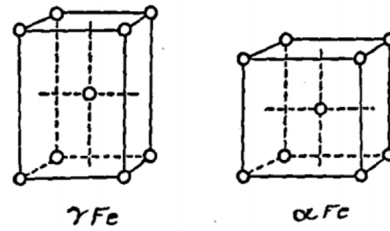


FIG. 4.—BODY-CENTERED TETRAGONAL LATTICE OF AUSTENITE AND BODY-CENTERED CUBIC LATTICE OF ALPHA IRON PRODUCED BY “UP-SETTING” THE FORMER; DRAWN TO SCALE FOR COMPARISON.

Figure 2.1: Illustration of the Bain strain taken from [Bain and Dunkirk, 1924]. On the left, the combination of the two adjacent FCC cells to create a BCT lattice. On the right, an illustration of the strain needed to achieved a cubic lattice.

the $\langle 100 \rangle_\gamma$ becomes a $\langle 100 \rangle_\alpha$ while the remaining two $\langle 100 \rangle_\gamma$ become two orthogonal $\langle 110 \rangle_\alpha$ directions. This early model profoundly affected how the transformation became envisioned, and the Bain correspondence is now assumed in the majority of the transformation models. A couple of years after Bain's proposal, both Nishiyama (1934) and Kurdjumov and Sachs (1930) proposed their own transformation models along with their measurements of the orientation relationship. The Kurdjumov-Sachs and the Nishiyama's models are quite similar, both based on the composition of two shears. However none of them is able to account for the habit plane and the surface relief associated with the transformation [Bowles and Barrett, 1952]. Later, in 1948, Jaswon and Wheeler proposed to study the transformation mechanism by using linear algebra, and they described the transformation as an homogenous deformation of the austenite lattice [Jaswon and Wheeler, 1948]. Their model allows to obtain the correct atomic structure and the Kurdjumov-Sachs orientation relationship. No plane is left invariant by the transformation, they suggested to relax the condition for the existence of a habit plane. They considered that the lack of rotation of a plane is a sufficient condition to allow the accommodation of the transformation on the habit plane. They showed that for their distortion, the $(225)_\gamma$ and the $(111)_\gamma$ are such planes. However, they were not able to explain why if both planes satisfy equally their criterion, only $\{225\}_\gamma$ are commonly observed in carbon steels, and not the $\{111\}_\gamma$. Their model was also criticized as it could not account for the surface relief and the observed shape change considered to be an invariant plane strain [Bowles and Barrett, 1952]. The same year Greninger and Troiano proposed a novel vision of the transformation by considering that two shears of different nature are involved in the transformation [Greninger and Troiano, 1949]. The first shear is associated with the shape change and acts homogeneously. The second one acts inhomogeneously in order to obtain the correct final BCC lattice. This second shear is considered as invisible for naked

eyes, and as such does not modify the observed shape change. The idea of such invisible shear will be used as a major ingredient in the *Phenomenological Theory of the Martensite Crystallography* (PTMC), which was born a couple of years later. The PTMC is the results of the works of two independent groups, Bowles and Mackenzie [Bowles and Mackenzie, 1954a] and Liebermann, Wechsler and Read [Wechsler and Read, 1953]. They expressed the transformation mechanism by using linear algebra. Both assume the Bain correspondence and use the concept of the second *invisible* shear proposed by Greninger and Troiano. They derived two different formulations that Christian showed to be equivalent [Christian, 1956]. In the Bowles and Mackenzie's version of the PTMC, the model stands in a single equation: $\mathbf{RB} = \mathbf{PQ}$. The left-hand side of the equation describes the lattice change by means of the Bain strain \mathbf{B} and a rotation \mathbf{R} allowing for a correct orientation relationship. The product \mathbf{RB} is called the *lattice strain*. The rotation \mathbf{R} is such that one line remains invariant during the transformation. Accordingly, this strain is called an *Invariant Line Strain* (ILS). On the right-hand side of the equation appears the matrix \mathbf{P} , called the *shape strain*. It describes the shape change as an *Invariant Plane Strain* (IPS), in agreement with the observed surface relief and shape change. The shape strain is multiplied by a matrix \mathbf{Q} , which is the inhomogeneous invisible shear introduced by Greninger and Troiano. Figure 2.2 illustrates the concepts behind the PTMC equation. On figure 2.2A, the austenite is partially deformed by an invariant plane

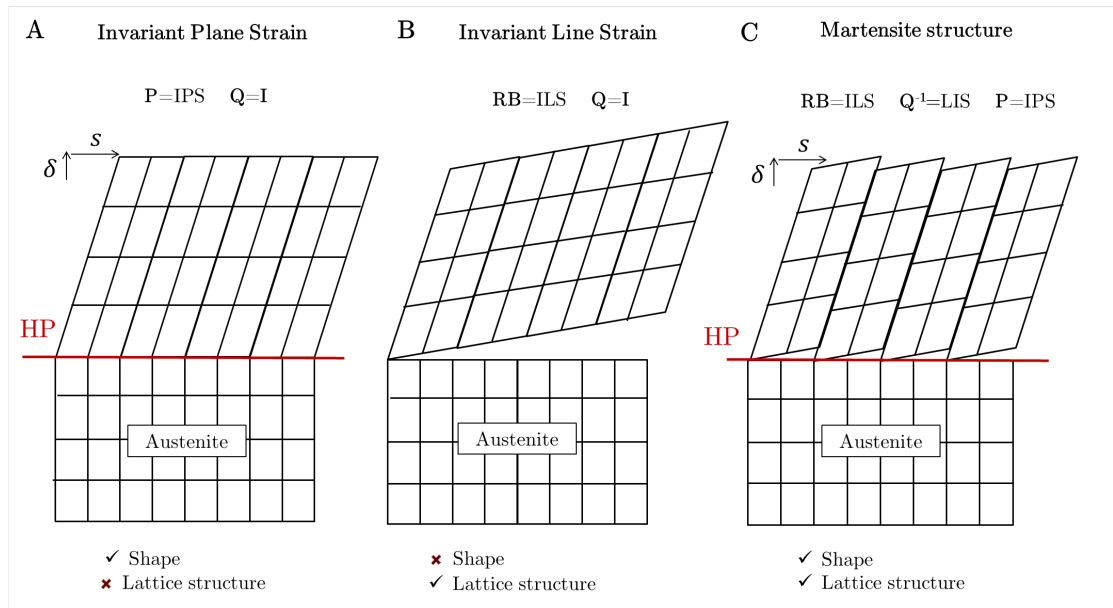


Figure 2.2: Illustration of the concepts behind the Phenomenological Theory of the Martensite Crystallography.

strain, where the invariant plane, the habit plane, is indicated in red. In that case, the austenite is only affected by the shape strain, $\mathbf{P} = \text{IPS}$ and $\mathbf{Q} = \mathbf{I}$. This situation is the one that is macroscopically observed and measured. However, such deformation does not lead to the correct BCC structure. The correct structure is obtained by deforming the austenite with an invariant line strain (ILS), like \mathbf{RB} . This deformation is illustrated on figure 2.2B. It gives the

correct lattice but the shape change does not correspond to the experimental observations. Actually, Greninger and Troiano pointed out - without formally demonstrating it- that it is not possible to change a structure from FCC to BCC by a deformation that is an invariant plane strain [Greninger and Troiano, 1949]. To tackle this issue, they introduced their second shear acting inhomogeneously, which is formalized in the PTMC by the matrix \mathbf{Q} . By combining the homogeneous shape change \mathbf{P} and the second shear \mathbf{Q} , as in figure 2.2C, the correct and well oriented BCC structure is obtained: $\mathbf{PQ} = \mathbf{RB}$. The inverse of \mathbf{Q} is named the *lattice invariant shear* (LIS), as it acts on \mathbf{RB} without changing the lattice, but allowing for the final shape change $\mathbf{P} = \mathbf{RBQ}^{-1}$. The lattice invariant shear proposed by Bowles and Mackenzie can be either twinning, similarly to the original Greninger and Troiano proposal, or slip. Figure 2.3 shows an illustration of these two types of lattice invariant shears when considering a $\{225\}_\gamma$ habit plane.

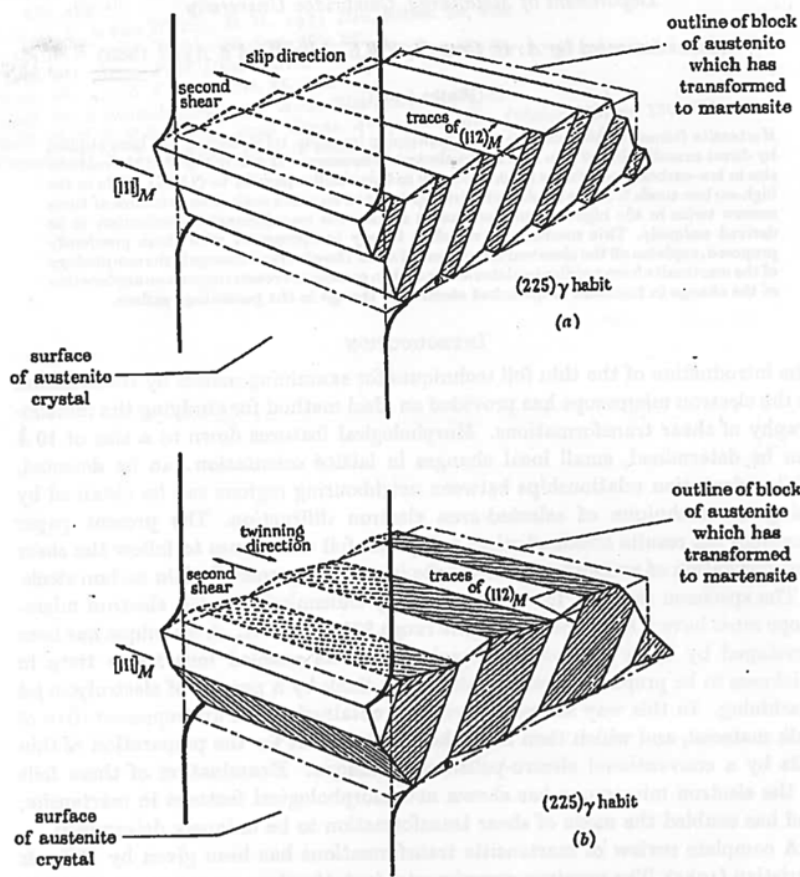


Figure 2.3: Illustration of the lattice invariant shear on a $\{225\}_\gamma$ habit plane [Kelly and Nutting, 1961]. **A:** by slip. **B:** by twinning.

The PTMC needs as input the lattice parameters of both the parent and the daughter phases. In addition, the nature of the lattice invariant shear \mathbf{Q} , defined by a shear plane and a shear direction, and the Bain correspondance have to be assumed. For the $\{225\}_\gamma$ and the $\{259\}_\gamma$

transformations that were well documented at the time of PTMC birth, a $\{112\}_\alpha < 111 \rangle_\alpha$ lattice invariant shear is considered. Based on these inputs, the shape strain and the orientation relationship can be determined. To account for the particular $\{225\}_\gamma$ habit plane case, an additional dilatation parameter, δ , is needed. This parameter multiplies the lattice strain \mathbf{RB} to keep the close-packed line of the austenite involved in the Kurdjumov-Sachs orientation relationship completely invariant: $\delta \mathbf{RB} = \mathbf{PQ}$. Because this dilatation was not measured experimentally, the use of such a parameter was not satisfactory. Therefore, a generalization of the PTMC was proposed independently by Acton and Bevis [Acton and Bevis, 1969], and by Ross and Crocker [Ross and Crocker, 1970] in 1969 and 1970 to account for the $\{225\}$ habit plane without using the dilatation parameter. They suggested to use two lattice invariant shears instead of a single one, and developed what is now called the *double shear theory*. However, this further complication of the original theory did not lead to significant improvements in the understanding of the transformation [Dunne and Wayman, 1971]. The double-shear formulation was nonetheless used later by Kelly, who claimed to account for both the $\{225\}_\gamma$ habit plane and the $\{557\}_\gamma$ habit plane [Kelly, 1992]. This latter habit plane has not been considered in the original PTMC, because such type of martensite was not accurately characterized at that time. Indeed, $\{557\}_\gamma$ martensite appears essentially in fully transformed material, which renders difficult the evaluation of the shape strain and the characterization of the habit plane.

Today, PTMC is the classical approach to study the crystallography of martensitic steels. To help in the long computations associated with the theory, a freeware has been developed recently [Gu et al., 2016].

Modern PTMC

The PTMC described above is presented in its Bowles and Mackenzie version [Bowles and Mackenzie, 1954a]. As already mentioned, another group, Liebermann, Wechsler and Read worked at the same time on the same topic and developed a different, but equivalent, expression of the PTMC [Wechsler and Read, 1953]. Contrarily to Bowles and Mackenzie who used matrix multiplications, they propose to model the martensite crystallography by linear combination of distortion matrices. The distortion matrices that are combined are lattice strains of type \mathbf{RB} . They are combined in pairs such that the resulting average distortion of each pair is exactly an invariant plane strain. Following the same approach of variants combination, Ball and James developed in the late eighties what is sometimes called the *modern* PTMC [Ball and James, 1987]. Their approach has then been democratized to non-mathematicians by Bhattacharya [Bhattacharya, 2003]. This modern PTMC is essentially based on the mathematical description of the interfaces between the phases (austenite-martensite) and between the martensite variants. It differs from the original PTMC theory by being explicitly based on free energy minimization [Ball and James, 1987]. Thanks to their generalization of the PTMC approach, they extended the theory to a wide range of transformations. Particularly, it achieved some success in modelling shape memory alloys [Chluba et al., 2015]. As a consequence, this theory is much more commonly used in that type of material than is steels. To our best

knowledge, Muehlemann and Koumatos are the only ones to propose an analysis of the steel crystallography by means of this modern PTMC [Muehlemann and Koumatos, 2015]. They proposed a model accounting for $\{557\}_\gamma$ habit planes. Similarly to the classical PTMC, their model is a double shear model. It is described as a *twins within twins* model as illustrated in figure 2.4.

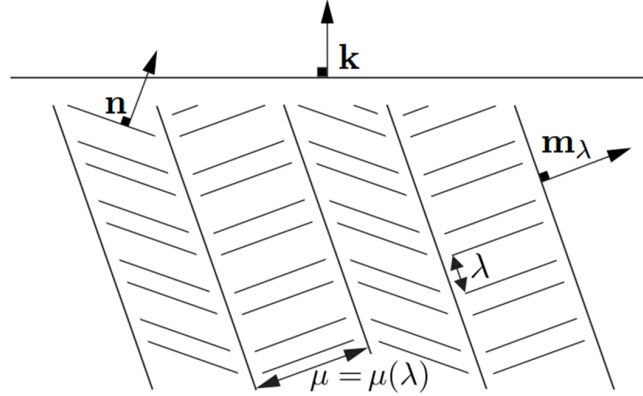


Figure 2.4: Illustration of the microstructure associated with the Muhlemann and Koumatos *twins within twins* model for the $\{557\}_\gamma$ habit plane martensite. k is the normal to the habit plane. Taken from ref. [Muehlemann and Koumatos, 2015]

However, contrarily to Kelly who used a trial-and-error method to find an appropriate set of shear systems [Kelly, 1992], Muhlemann and Koumatos' work allows to find the pair of shears, starting only from the lattice parameters and knowing the final habit plane orientation. On the mathematical stand point, the proposed *twins within twins* model is flawless, but the type of microstructure associated with it (see figure 2.4) does not correspond to the experimental observations of $\{557\}_\gamma$ low-carbon steels. Actually, the microstructure proposed is much closer to what is observed in shape memory alloys.

Alternative mechanistic models

In both its modern and classical versions, the main limitation of the PTMC is in its name. It is *phenomenological*. This particularity is underlined by Bowles and Mackenzie when presenting their model. The lack of consideration of the atomic trajectory disappointed several researchers [Bogers and Burgers, 1964] [Cayron, 2015]. They therefore proposed their own models based on atomic descriptions. In 1964, Bogers and Burgers used hard spheres to model the motion of atoms and proposed a succession of two shears to transform the FCC lattice into a BCC lattice [Bogers and Burgers, 1964]. However, their mechanism cannot explain the observed habit plane and shape change. Later from 2010 to 2015, Cayron proposed different models, based on the same hard sphere description of the atoms [Cayron et al., 2010, Cayron, 2013, Cayron, 2015]. His latest model allows to continuously evolve from an

FCC lattice to a BCC lattice, both lattices being in Kurdjumov-Sachs orientation relationship. The transformation mechanism does not keep any plane invariant, but both the $(111)_\gamma$ and the $(225)_\gamma$ are untilted by transformation. He discovered afterwards that his mechanism was a continuous version of the Jaswon and Wheeler's model [Jaswon and Wheeler, 1948]. The transformation is described by a single matrix $\mathbf{F}(x = \cos(\beta))$, called distortion matrix. The distortion matrix allows, for each increment of the angular parameter x , to compute the intermediate distorted FCC lattices:

$$\mathbf{F}(x) = \begin{bmatrix} 1 - x + \frac{1}{3}\sqrt{\frac{1-x}{1+x}}(\sqrt{6x} + \sqrt{3x}) & \frac{\sqrt{x}}{3}(-3\sqrt{x} + \sqrt{\frac{1-x}{1+x}}(\sqrt{6} + \sqrt{3x})) & \frac{1}{\sqrt{3}}(\sqrt{\frac{1-x}{1+x}}(\sqrt{2x} + x) - \sqrt{1-x^2}) \\ x - 1 + \frac{1}{3}\sqrt{\frac{1-x}{1+x}}(\sqrt{6x} + \sqrt{3x}) & \frac{\sqrt{x}}{3}(3\sqrt{x} + (\sqrt{\frac{1-x}{1+x}})(\sqrt{6} + \sqrt{3x})) & \frac{1}{\sqrt{3}}(\sqrt{\frac{1-x}{1+x}}(\sqrt{2x} + x) - \sqrt{1-x^2}) \\ \sqrt{\frac{x}{3}}\sqrt{\frac{1-x}{1+x}}(\sqrt{2} - 2\sqrt{x}) & \sqrt{\frac{x}{3}}\sqrt{\frac{1-x}{1+x}}(\sqrt{2} - 2\sqrt{x}) & \frac{1}{\sqrt{3}}(\sqrt{\frac{1-x}{1+x}}(\sqrt{2x} - 2x) + 2\sqrt{1-x^2}) \end{bmatrix} \quad (2.1)$$

The transformation begins at $x = \frac{1}{2}$, where $\mathbf{F}(\frac{1}{2}) = \mathbf{I}$, implying that there is no deformation of the austenite. It finishes at $x = \frac{1}{3}$, where the deformed austenite corresponds to the martensite structure. A schematic representation of the transformation mechanism is proposed in figure 2.5. The transformation can be essentially seen as an opening of the β angle in the FCC close-packed plane. The β angle changes from 60° to 70.5° as the lattice transforms from a FCC structure to a BCC one. From this particularity, such transformation is called an *angular distortion* [Cayron, 2016]. This distortion is equivalent to the invariant line strain of the PTMC, where the invariant line in that case is the close-packed direction of the two phases (the line QP on figure 2.5). As a matter of fact, the distortion \mathbf{F} can be decomposed into the product of a rotation and the Bain strain by using a polar decomposition $\mathbf{F} = \mathbf{R}\mathbf{B}$. As compared with the

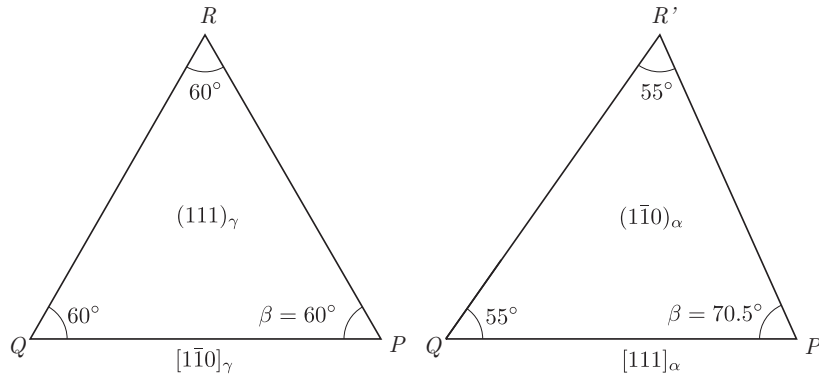


Figure 2.5: Schematic representation of the continuous FCC-BCC transformation mechanism from Cayron. Inspired from figure 10 in ref. [Cayron, 2015]. On the left, the initial FCC structure is represented by its $(111)_\gamma$ plane which transforms (on the right) in a $(1\bar{1}0)_\alpha$ plane, while keeping the $[1\bar{1}0]_\gamma$ parallel to the $[111]_\alpha$.

PTMC, this model offers a satisfyingly simple description of transformation as it deals only with a single matrix. In addition, as a major advantage, it provides a complete description of the atomic path, allowing to see the transformation as a continuous process, as presented in

figure 2.6. However, like the Jaswon and Wheeler model, it is not able to account for a shape change being an invariant plane strain.

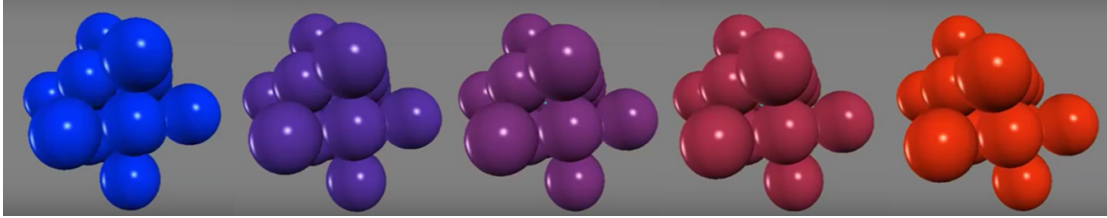


Figure 2.6: Illustration of the continuous transformation of a FCC unit cell (blue) to a BCC unit cell (red) according to the Cayron's continuous model associated with the Kurdjumov-Sachs orientation relationship. Full film available on the LMTM website (www.lmtm.epfl.ch).

Characterization and modelling of the variant selection

Local variant selection

References to local variant selection are present in both versions of the PTMC, where variants pairing are considered to accommodate the transformation on the habit plane. In the Bowles and Mackenzie model for the $(225)_\gamma$ martensite habit plane, the authors explicitly noted that the invariant lattice shear is equal to "half the twinning shear", such that the "variants are related in pairs" [Bowles and Mackenzie, 1954b]. A few years later, variants pairing in lenticular martensite is also reported [Bokros and Parker, 1963]. Bokros and Parker studied the transformation in Fe-30Ni single crystals and observed that the transformation occurs in a burst, by group of four variants "that catalyze the transformation on one another". This group is called *plate group*. In that case the variants pairing is not due to the accommodation of the habit plane, but is the result of an autocatalytic process. Lath martensite produced in low-carbon steels also exhibits particular variant pairing, as reported by Morito *et al.* [Morito et al., 2003]. Their study suggests that $\{557\}_\gamma$ habit plane martensite tends to form *packets* of variants belonging to the same close-packed plane group. Within such packet, the low-misoriented variants are paired to create *blocks*. An illustration of this variants pairing architecture is presented in figure 2.7. Morito *et al.* used the $\{557\}_\gamma$ double shear theory proposed by Kelly to explain the observed pairings. The analysis was not completely satisfactory, in particular the coupling of low-misoriented variants remains unclear [Morito et al., 2003].

A general study on variant pairing in carbon steel has been conducted by Stormvinter *et al.* in 2012 by using EBSD measurements [Stormvinter et al., 2012]. This study evidences the effect of carbon content on variant coupling and shows results in excellent agreement with the previous studies. At low carbon content, the variants pairing occurs, forming blocks and the assembly of blocks creating packets, as described by Morito, then by increasing slightly the amount of carbon (Fe-0.75C) the martensite tends to pair by twin-related variants, and with higher carbon content, the variants pairing is based on plate groups. An illustration of

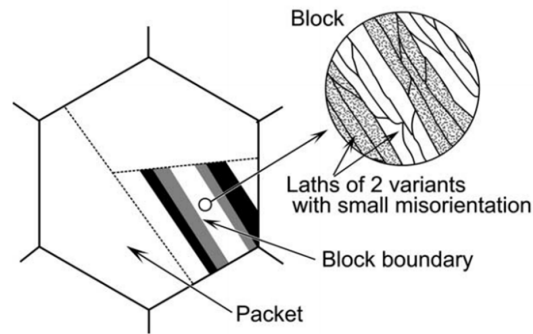


Figure 2.7: Schematic representation of a transformed austenite parent grain in lath martensite in a low-carbon steel. Details of the variant pairing in blocks and packets. Illustration from ref. [Morito et al., 2003]

these different pairings is presented in figure 2.8. The local variant selection appears to be a well-documented and precisely characterized phenomenon, but it remains rather poorly understood. Apart from the Bokros and Parker's model for the plate group formation based on shape strain interactions, there is a lack of convincing links between the transformation mechanism and the different type of variants pairing.

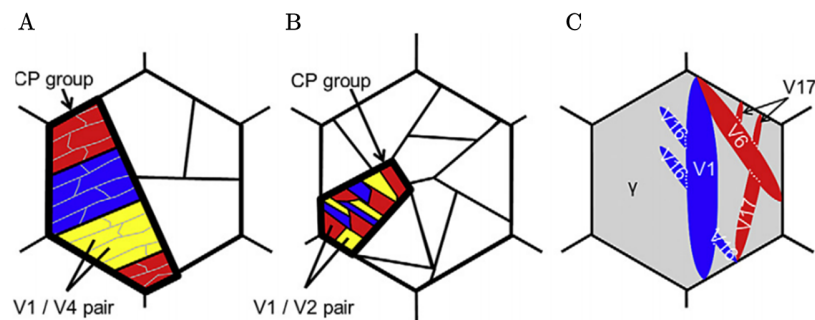


Figure 2.8: Illustration of the various types of coupling for different carbon steels. **A:** Low-carbon steel (0-0.3C). **B:** 0.75C steel. **C:** 1.8C carbon steel. From ref. [Stormvinter et al., 2012]

Global variant selection

Effect of applied stress

Erich Scheil is one of the first researchers who investigates the effect of stress on the martensite formation in 1932 [Scheil, 1932]. His experiments indicate that applied tensile stress assists the transformation and increases the martensitic start temperature. Later, in 1953, Patel and Cohen proposed a criterion for quantifying the effect [Patel and Cohen, 1953]. This criterion is based on the interaction energy U between the shape strain associated with the

transformation and the applied stress. In the original version, this criterion is computed by decomposing the stress in a shear component τ parallel to the habit plane and a normal component σ perpendicular to the habit plane. The interaction is expressed as the sum of the product of the normal component σ with the dilatation δ associated with the transformation and the product of the resolved shear τ with the transformation shear s :

$$U = \tau s + \sigma \delta \quad (2.2)$$

The interaction energy of Patel and Cohen can also be seen as the work W of the transformation strain in the applied stress field. This computation can be generalized for any transformation strain \mathbf{F} and applied stress tensor $\mathbf{\Sigma}$ by using the inner product of the two matrices:

$$W = (\mathbf{F} - \mathbf{I}) : \mathbf{\Sigma} = \text{tr}((\mathbf{F} - \mathbf{I})\mathbf{\Sigma}^T) \quad (2.3)$$

where \mathbf{I} is the identity matrix. Once accepted as an appropriate way of quantifying the effect of stress on the transformation, the Patel and Cohen criterion has then been naturally used to study variant selection [Higo et al., 1974, Gautier et al., 1989]. Bhadeshia and co-workers in particular, by publishing an important number of papers on that topic, made that criterion the classical way to study variant selection in martensite [Kundu and Bhadeshia, 2007, Abreu et al., 2009]. Eventually, they claimed that computing such criterion with the shape strain associated with the transformation is the only proper way to study the variant selection phenomenon [Bhadeshia et al., 2008]. In the majority of the variant selection studies, the shape strain is determined by the PTMC predictions.

Past and more recent experiments however suggest that the Patel and Cohen criterion is not always appropriate. Kato and Mori in 1976 [Kato and Mori, 1976] and later Mishiro in 2013 [Mishiro et al., 2013] clearly noted that the work of the shape strain predicted by the PTMC does not govern the variant selection. According to their results the work of the lattice strain \mathbf{RB} or simply the Bain strain \mathbf{B} better accounts for the selection. Similar results were also reported by Jesser and Olsen in their study on the effect of stress on the martensitic transformation in thin iron films [Olsen and Jesser, 1971].

Effect of prior austenite deformation

Because of its major implication in the industrial process of steels, the effect of the prior plastic deformation of the austenite on the variant selection has been the topic of numerous studies. Kundu *et al.* proposed to model the variant selection using the same type of approach as the one used for the variant selection due to an applied stress [Kundu, 2009]. They computed the Patel and Cohen criterion considering the residual stresses as the applied stress. Chiba *et al.* performed experiments to study the effect of ausforming on the formation of lenticular martensite. They observed a significant variant selection which could not be explained by the Patel and Cohen criterion [Chiba et al., 2012]. They concluded that the selection was related to the elongated morphology of the prior austenite grain. As a result of the ausforming process the grain have an elongated shape and the variants that have their habit plane oriented parallel

to the elongated direction are more prone to form as they cause less disturbance to the grain boundary. Figure 2.9 gives a schematic illustration of the selection process.

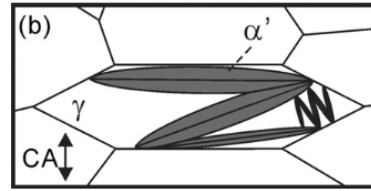


Figure 2.9: Illustration of the variant selected in the model of Chiba *et al.*. Illustration from ref. [Chiba et al., 2012]

Miyamoto *et al.* also relate the variant selection caused by ausforming to the deformed microstructure of the austenite [Miyamoto et al., 2012]. As a result of the ausforming process, microbands of dense dislocation walls are formed in the austenite. The microbands appear on the primary and the secondary slip systems. The variant selection analysis indicates that the variants that were preferentially formed were those whose habit plane was relatively parallel to these two systems, hence parallel to the microbands of the prior austenite grain. Slip system activity on the austenite is also mentioned by other authors as an influencing factor for variant selection, even if not explicitly associated to microstructural features. In the successive models of Jonas and coworkers, each variant is associated with a given slip system, and the activity of the system determines the variant selection [Butrón-Guillén et al., 1997, Sum and Jonas, 1999]. In these models, additional selection rules are also applied. As an example, the work of the Bain strain in the residual stress field is considered. This work has to be positive to allow the growth of the variants. More recently, Tomida proposed a very comprehensive study of variant selection in textured steels [Tomida, 2018]. He compared the different models available in the literature and concluded that the models are "incapable of quantitatively or even qualitatively predicting the transformation textures of α' in hot-rolled steels" [Tomida, 2018]. As a consequence, he proposes a variant selection mechanism based on the consideration of the elastic anisotropy of austenite matrix, which favours the variant exhibiting a low elastic energy and satisfying the so-called *double Kurdjumov-Sachs relation*. This relation, presented by the same author in a previous paper [Tomida et al., 2013], considers that martensite variants tend to form in Kurdjumov-Sachs, or close Kurdjumov-Sachs orientation relationship with the parent grain, but also with the neighboring parent grains.

If a common consent exists in the modelling of the variant selection caused by applied stress by using a criterion based on the work of the transformation strain in the applied stress field - even though the choice of the transformation strain is a topic of debate -, it seems that there is no such agreement for the modelling of the effect of prior deformation on variant selection. Additionally, it appears that there is no unified vision of the variant selection caused by applied stress and by prior deformation.

3 Scope of the thesis

Objectives

The state of the art on the variant selection models presented in the previous chapter indicates that there is no unique model accounting for all the reported cases of variant selection. The Patel and Cohen criterion [Patel and Cohen, 1953] computed on the basis of PTMC predictions, even though considered as the classical model, happens to fail in predicting the phenomenon. Other models are proposed, but they lack generality or physical basis. In addition, the PTMC which is the pillar of the majority of the variant selection models is *phenomenological* and as such it could be a reason for preventing a comprehensive understanding of the phenomenon. The objective of the thesis is to investigate variant selection for various types of martensite in order to evidence the rules that govern the phenomenon and attempt to offering a more unified vision of it.

Methods

The variant selection is studied in different types of martensite: surface martensite, $\{225\}_\gamma$ plate, $\{557\}_\gamma$ lath martensite and $\{259\}_\gamma$ lenticular martensite. The variant selection is induced either by an external applied stress or by a prior deformation and it is characterized by using EBSD measurements. Two transformations models are considered in this work. The PTMC model as it is undoubtedly the most commonly accepted model of the transformation, and the continuous FCC-BCC model proposed by Cayron [Cayron, 2015].

Outline

This thesis is written under the form of a compilation of articles. Several of these articles are already published and others have been submitted to journals. Unpublished works are also presented in article form. To each article corresponds a chapter. In addition, a brief presentation of the mathematics used in this thesis is proposed. The overview of the different chapters composing this thesis is presented here.

- Chapter 4 offers an overview of the mathematical framework used in this thesis. Mathematical definitions of the different crystallographic features associated with the martensitic transformation are proposed.
- Chapters 5, 6 and 7 focus on the study of the habit plane accommodation in martensitic steels. Chapters 5 and 7 explain the habit plane accommodation by local variant selection. Chapter 5 demonstrates that the equibalanced combination of twin-related variants of the FCC-BCC continuous distortion keeps the $\{225\}_{\gamma}$ globally invariant. It further shows that for that particular habit plane the PTMC model and the continuous model are equivalent. In chapter 7, a careful characterization of the crystallography of the $\{557\}_{\gamma}$ lath martensite is presented. A model based on the coupling of low-misoriented variants forming bifoliated blocs is proposed. This morphology allows a good accommodation of the lath on a $\{557\}_{\gamma}$, as the deformation associated with it offers a good angular compatibility with the surrounding blocs forming a packet. In Chapter 6, an alternative way of accommodating the continuous FCC-BCC distortion on a $\{225\}_{\gamma}$ without considering twin-related variants coupling is proposed. Using the Frank-Bilby equation, we show that a set of screw dislocations allows for the accommodation of the habit plane.
- Chapters 8 and 9 present the study of variant selection in surface martensite. In chapter 8, a criterion to model the observed variant selection is proposed. On this basis, different transformation models are compared. In chapter 9, the particular chevron morphology observed on the surface martensite produced on annealed samples is studied. We show that the symmetry of the morphology is related to the variant selection phenomenon.
- Chapter 10 offers a study of the effect of 4-point bending on the variant selection in $\{259\}_{\gamma}$ lenticular martensite formed in a Fe-Ni-C alloy. A significant variant selection is observed which cannot be accounted by the classical PTMC model. An empirical crystallographic rule is proposed to model the selection.
- Chapter 11 proposes an investigation of the effect of tensile deformation on variant selection in low and high carbon steels. The selection is studied by computing the work of the deformation associated with the transformation in the applied stress field. It appears that the deformation that needs to be considered essentially depends on the strain accommodation process. Actually, our study suggests that the deformation

which matters is the result of appropriate combinations of lattice distortions of different variants.

- Chapter 12 consists in a general discussion on the different aspects studied in this thesis. The first part of this discussion is dedicated to the comparison of the different crystallographic models used in this thesis, and the second part proposes a global view of our results on variant selection in different martensitic steels.
- Chapter 13 concludes this thesis work and presents a few perspectives on the variant selection topic.

The supplementary materials accompanying the different publications are available in the Appendices A-C of the thesis.

4 Mathematical framework

Conventions and notations

The mathematical notations and conventions used in this thesis are presented below. The vectors are column vectors and are written in small bold letters. The matrices are written in bold capital letters. A vector \boldsymbol{v} is transformed by a matrix \boldsymbol{M} as follows:

$$\boldsymbol{v}' = \boldsymbol{M}\boldsymbol{v} \quad (4.1)$$

The study of phase transformations implies the use of different bases. When the basis in which the elements are expressed is not clear, a subscript is added on the vector or on the matrix. A vector \boldsymbol{v} and a matrix \boldsymbol{M} expressed in a basis \mathcal{B}_1 are written $\boldsymbol{v}_{|\mathcal{B}_1}$ and $\boldsymbol{M}_{|\mathcal{B}_1}$, respectively. The identity matrix is noted \boldsymbol{I} .

Bases

For an appropriate description of phase transformations, one should consider at least as many bases as the number of different crystals involved in the transformation. In the FCC-BCC transformation associated with the Kurdjumov-Sachs OR, there are 24 distinct α crystals. Therefore at least 25 basis are needed: one for the parent γ phase and 24 for the α phase. The parent basis \mathcal{B}^γ is the orthonormal crystallographic basis formed by the vectors $[100]_\gamma$, $[010]_\gamma$ and $[001]_\gamma$. There are in addition 24 orthonormal daughter bases \mathcal{B}^{α_i} , respectively formed by the $[100]_{\alpha_i}$, $[010]_{\alpha_i}$ and $[001]_{\alpha_i}$.

Change of basis and coordinates transformation matrices

The coordinate-transformation matrix between two bases \mathcal{B}_1 and \mathcal{B}_2 is noted $\boldsymbol{T} = [\mathcal{B}_1 \rightarrow \mathcal{B}_2]$ and is defined such that its columns are the vectors of the basis $\mathcal{B}_2 = \{\boldsymbol{u}; \boldsymbol{v}; \boldsymbol{w}\}$ expressed in

the basis \mathcal{B}_1 :

$$\mathbf{u}_{/\mathcal{B}_1} = \begin{pmatrix} a \\ b \\ c \end{pmatrix} \quad \mathbf{v}_{/\mathcal{B}_1} = \begin{pmatrix} d \\ e \\ f \end{pmatrix} \quad \mathbf{w}_{/\mathcal{B}_1} = \begin{pmatrix} g \\ h \\ i \end{pmatrix} \quad (4.2)$$

One has,

$$\mathbf{T} = [\mathcal{B}_1 \rightarrow \mathcal{B}_2] = \begin{bmatrix} a & d & g \\ b & e & h \\ c & f & i \end{bmatrix} \quad ; \quad [\mathcal{B}_2 \rightarrow \mathcal{B}_1] = [\mathcal{B}_1 \rightarrow \mathcal{B}_2]^{-1} \quad (4.3)$$

The vector \mathbf{v} and the matrix \mathbf{M} expressed in \mathcal{B}_1 , noted $\mathbf{v}_{/\mathcal{B}_1}$ and $\mathbf{M}_{/\mathcal{B}_1}$ are, then, respectively expressed in \mathcal{B}_2 as follows:

$$\mathbf{v}_{/\mathcal{B}_2} = [\mathcal{B}_2 \rightarrow \mathcal{B}_1] \mathbf{v}_{/\mathcal{B}_1} = \mathbf{T}^{-1} \mathbf{v}_{/\mathcal{B}_1} \quad (4.4)$$

$$\mathbf{M}_{/\mathcal{B}_2} = [\mathcal{B}_2 \rightarrow \mathcal{B}_1] \mathbf{M}_{/\mathcal{B}_1} [\mathcal{B}_1 \rightarrow \mathcal{B}_2] = \mathbf{T}^{-1} \mathbf{M}_{/\mathcal{B}_1} \mathbf{T} \quad (4.5)$$

It should be mentioned that coordinates transformation matrices are describing *passive* transformations: A vector is not moved by the coordinates transformations matrix \mathbf{T} , it is simply expressed in a different basis from the initial one. Let's consider a vector $\mathbf{v}_{/\mathcal{B}_1}$ expressed originally in the basis \mathcal{B}_1 . This vector can be expressed in any other basis \mathcal{B}_2 by using the coordinates transformation matrix $\mathbf{T}^{-1} = [\mathcal{B}_2 \rightarrow \mathcal{B}_1]$ as presented in equation 4.4. During this operation, the vector \mathbf{v} remains unchanged such that $\mathbf{v}_{/\mathcal{B}_1}$ and $\mathbf{v}_{/\mathcal{B}_2}$ are the same vectors, but they are simply expressed in different bases. A passive matrix cannot completely describe a phase transformation, *active* matrices that are actually distorting the vectors are needed. **Distortion matrices** which are presented in detail below are such matrices.

Transformation-related matrices

Distortion matrices

The distortion matrix \mathbf{F} is the primary measure of the transformation. It describes the mechanism of the transformation from a parent phase γ to a daughter phases α . The distortion is defined such that any crystallographic direction $\mathbf{u}_{/\mathcal{B}^\gamma} = (u_x, u_y, u_z)$ of the parent phase is transformed in $\mathbf{u}'_{/\mathcal{B}^\gamma} = (u'_x, u'_y, u'_z)$ according to the following equation:

$$\mathbf{u}' = \mathbf{F} \mathbf{u} \quad (4.6)$$

The distortion \mathbf{F} is generally called *deformation gradient* in classical metallurgical books. This matrix is defined in the parent phase basis \mathcal{B}^γ .

Distortion \mathbf{F} can describe a complete transformation, or it can describe partial transformation if one uses a continuous description of the transformation. In that latter case, the distortion matrix varies as function of a leading parameter β , $\mathbf{F} = \mathbf{F}(\beta)$. This leading parameter is bounded by two extremal values β_i and β_f . When the parameter equals β_i , the austenite remains untransformed, and $\mathbf{F}(\beta_i) = \mathbf{I}$. The transformation is complete when the parameter reaches the value β_f . The matrix describing the complete transformation is thus $\mathbf{F}(\beta_f)$. In between, there exists an infinity of matrices, each of them describing a step in the transformation mechanism.

The distortion \mathbf{F} allows to compute the image of directions upon transformation. Beside the transformation of directions, it can also be interesting to see how planes are transformed. To measure this transformation one uses the matrix \mathbf{F}^* which is the distortion matrix \mathbf{F} expressed in the reciprocal lattice. \mathbf{F}^* transforms plane of normal \mathbf{n} in planes of normal $\mathbf{m} = \mathbf{F}^* \mathbf{n}$. \mathbf{F}^* and \mathbf{F} are linked by the following relationship¹:

$$\mathbf{F}^* = \mathbf{F}^{-T} \quad (4.7)$$

The matrix \mathbf{F}^* is defined in the same basis as the one of \mathbf{F} , namely \mathcal{B}^γ .

In continuum mechanics, one generally takes the hypothesis that the reverse transformation is given by the inverse of the deformation gradient \mathbf{F}^{-1} . However, it is worth noting that with distortion matrices, as defined here, the reverse transformation is not simply the inverse of the transformation \mathbf{F}^{-1} . The reason for that is related to the way the distortion matrices are defined. Indeed, a distortion matrix acts on the parent crystal and deforms it. The original parent basis becomes distorted, but it is still not the crystallographic basis of the daughter product. The inverse of the distortion matrix \mathbf{F}^{-1} therefore transforms the aforementioned distorted basis in the parent basis, which is not the same as transforming the daughter basis in a distorted basis that represents the parent basis, as would be the distortion matrix of the reverse transformation.

Parent-daughter coordinates transformation matrix

The distortion \mathbf{F} describes how the directions of the parent lattice change during the transformation but gives no information on the crystallography of the daughter phase. To know the coordinates of the daughter phase expressed in the parent phase basis, or *vice versa*, one uses coordinates transformation matrices \mathbf{T} as presented in section 4.

Superscripts are generally used to indicate the basis considered. $\mathbf{T}^{\gamma \rightarrow \alpha} = [\mathcal{B}^\gamma \rightarrow \mathcal{B}^\alpha]$ and its inverse $(\mathbf{T}^{\gamma \rightarrow \alpha})^{-1} = [\mathcal{B}^\alpha \rightarrow \mathcal{B}^\gamma] = \mathbf{T}^{\alpha \rightarrow \gamma}$ allow to pass from the coordinate system of the daughter phase (α) to the parent phase (γ), or *vice versa*, respectively.

¹An elegant demonstration of this relationship can be found in Ref. [Bowles and Mackenzie, 1954a]: Any direction \mathbf{x} is transformed by \mathbf{F} , such that $\mathbf{y} = \mathbf{F}\mathbf{x}$. We remind here that the vectors \mathbf{x} and \mathbf{y} are column vectors. If \mathbf{x} belongs to a plane of normal \mathbf{n} , we have $\mathbf{n}^T \mathbf{x} = 0$. Similarly, \mathbf{y} belongs to a transformed plane of normal \mathbf{m} , such that $\mathbf{m}^T \mathbf{y} = 0$. We can write: $\mathbf{m}^T \mathbf{y} = \mathbf{n}^T \mathbf{x}$. By replacing \mathbf{y} we obtain, $\mathbf{m}^T \mathbf{F}\mathbf{x} = \mathbf{n}^T \mathbf{x}$. This is true for any \mathbf{x} . We can thus rewrite: $\mathbf{m}^T = \mathbf{n}^T \mathbf{F}^{-1} \rightarrow \mathbf{m} = \mathbf{F}^{-T} \mathbf{n}$. \square

Correspondence matrix

The correspondence matrix \mathbf{C} is used to know what becomes each direction of the parent phase in the daughter phase. Similarly to the coordinates transformation matrix \mathbf{T} , the correspondence matrix is noted with appropriate superscript. $\mathbf{C}^{\alpha \rightarrow \gamma}$ gives, for each parent crystal direction what it becomes in the daughter phase. Correspondence matrices always exhibit rational numbers.

The three transformation-related matrices presented above, the **distortion matrix** \mathbf{F} , the **coordinates transformation matrix** \mathbf{T} and the **correspondence matrix** \mathbf{C} , satisfy the following equality:

$$\mathbf{C}^{\alpha \rightarrow \gamma} = \mathbf{T}^{\alpha \rightarrow \gamma} \mathbf{F} \quad (4.8)$$

Variants of the transformation

To be rigorous when describing phase transformations, it is important to distinguish the *distortion variants*, the *orientation variants* and the *correspondence variants*. The first are related to the orientation of the daughter crystals and the second refers to the mechanism of transformation that creates the daughter crystals. The correspondence variants are based on the correspondence matrix. Contrarily to the distortion and the orientation variants they are not explicitly described here, as they are not directly used in this thesis. The mathematical definitions for the different variants of the transformation proposed below are due to Cayron [Cayron, 2006, Cayron, 2018].

Distortion variants

The distortion variant describes the way in which the parent lattice needs to be distorted to produce the daughter phase. Distortion variants are defined by their proper distortion matrix \mathbf{F}^{α_i} .

$$\mathbf{F}^{\alpha_i} = \mathbf{g}_i \mathbf{F}^{\alpha_1} (\mathbf{g}_i)^{-1} \quad (4.9)$$

Here, the distortion associated with the martensite crystal α_1 is arbitrarily considered as reference. The \mathbf{g}_i are symmetry of the point group of austenite \mathbb{G}^γ . We mention here that even if noted with a small letter, the \mathbf{g}_i are 3x3 matrices. As each \mathbf{g}_i does not necessarily create a new distortion, there might be less distortion variants than symmetries in the point group. The subgroup

$$\mathbb{H}_F^\gamma = \{\mathbf{g}_i \in \mathbb{G}^\gamma, \mathbf{g}_i \mathbf{F}^{\alpha_1} (\mathbf{g}_i)^{-1} = \mathbf{F}^{\alpha_1}\} \quad (4.10)$$

contains the symmetry elements that leave the distortion \mathbf{F}^{α_1} invariant. The number of different distortions, namely the number of distortion variants is given by:

$$N_F^\alpha = \frac{\mathbb{G}^\gamma}{\mathbb{H}_F^\gamma} \quad (4.11)$$

Orientation variants

The orientation variant tells how the daughter crystal α_i is oriented with respect to its parent phase, but it does not tell anything about the transformation mechanism. Orientation variants are defined by their proper coordinates transformation matrix $\mathbf{T}^{\gamma \rightarrow \alpha_i}$ and thus only depend on the orientation relationship:

$$\mathbf{T}^{\gamma \rightarrow \alpha_i} = \mathbf{g}_i \mathbf{T}^{\gamma \rightarrow \alpha_1} \quad (4.12)$$

The \mathbf{g}_i are not directly those of the point group of austenite \mathbb{G}^γ , but depend on both the point group of the austenite \mathbb{G}^γ and the point group of the martensite \mathbb{G}^α . In particular, the symmetries common to both point groups have to be determined. To do so it is necessary to express the symmetries of the martensite in the basis of the austenite. The intersection group \mathbb{H}_T^γ is thus defined as:

$$\mathbb{H}_T^\gamma = \mathbb{G}^\gamma \cap \mathbf{T}^{\gamma \rightarrow \alpha_1} \mathbb{G}^\alpha (\mathbf{T}^{\gamma \rightarrow \alpha_1})^{-1} \quad (4.13)$$

The \mathbf{g}_i that create new orientation variants have to be chosen in the cosets $\mathbf{g}_i \mathbb{H}_T^\gamma$ that partitioned \mathbb{G}^γ . All symmetries within the same coset lead to the same orientation. The number of distinct orientation variants is given by:

$$N_T^\alpha = \frac{\mathbb{G}^\gamma}{\mathbb{H}_T^\gamma} \quad (4.14)$$

It is worth mentioning that different distortion variants could lead to the same orientation variant, this is typically the case in the FCC-HCP system, where three different distortions of the FCC lattice give the same final HCP lattice orientation. In the FCC-BCC transformation studied in this thesis, there is the same number of orientation and distortion variants, independently of the orientation relationship considered.

Measure of the deformation

In this work, the measure of the deformation associated with the phase transformation is based on the measure of the displacements of each material point from its undeformed, initial position \mathbf{x} to its transformed position \mathbf{x}' . These displacements are computed by using the *displacement gradient* \mathbf{H} [Curnier, 2005]. The matrix \mathbf{H} is simply defined as follows:

$$\mathbf{x}' - \mathbf{x} = \mathbf{F}\mathbf{x} - \mathbf{x} = (\mathbf{F} - \mathbf{I})\mathbf{x} \rightarrow \mathbf{H} = \mathbf{F} - \mathbf{I} \quad (4.15)$$

Considering the displacement $\mathbf{u} = \mathbf{x}' - \mathbf{x}$, the matrix \mathbf{H} can also be seen as $\mathbf{H} = \nabla \mathbf{u}$.

Features of the transformation

Volume change of the transformation

The volume change accompanying the phase transformation can be directly computed from the distortion matrix \mathbf{F} . The ratio between an original volume element V_γ and the resulting transformed volume element V_α is given by:

$$V_\alpha = \det(\mathbf{F})V_\gamma \quad (4.16)$$

Invariant directions

Two conditions are needed for a direction to be invariant: first, it has to be undistorted, meaning that the transformed direction and the parent direction are collinear, and second the length of any vector along this direction should not change upon transformation. It is in the properties of the transformation matrix \mathbf{F} that such features have to be found. The first condition implies that the candidates \mathbf{v} for the invariant direction have to satisfy the following equality:

$$\mathbf{F}\mathbf{v} = \lambda \mathbf{v} \quad (4.17)$$

This is an eigenvalue problem where the eigenvalues express the change of length of the eigenvector \mathbf{v} during transformation. If an eigenvector is associated with an eigenvalue λ equal to 1, it means that the second condition is satisfied and the direction is invariant. If λ is different from 1 the direction remains unrotated upon transformation, but is not fully invariant as the direction is stretched of the value λ . The existence of an invariant line is a crucial point in the PTMC theory, and the purpose of the rotation \mathbf{R} that multiplies the Bain strain \mathbf{B} is to guarantee that the lattice strain $\mathbf{R}\mathbf{B}$ keeps a line invariant. This invariant line is a necessary condition to achieve a macroscopic shape deformation that has an invariant plane. Generally in the PTMC, unless the orientation relationship is exactly Kurdjumov-Sachs and the lattice parameters are in hard-sphere ratio, the invariant line is not crystallographic. In that case, the invariant line is the close-packed direction of the austenite involved in the

orientation relationship $[1\bar{1}0]_\gamma \parallel [111]_\alpha$. The continuous FCC-BCC distortion model assumes a Kurdjumov-Sachs orientation relationship and lattice parameters in hard-sphere ratio; in that case also the invariant line is $[1\bar{1}0]_\gamma \parallel [111]_\alpha$.

Untilted planes as potential habit planes

A plane is said *untilted* when the normal to the plane remains unrotated upon transformation. An invariant plane is necessarily untilted, however an untilted plane is not necessarily invariant. For example, an in-plane distortion will left the normal unrotated, and thus the plane untilted, but the plane cannot be considered as invariant because of the in-plane distortion. In our vision as well as in Jaswon and Wheeler's one [Jaswon and Wheeler, 1948], investigating untilted planes is a good way of studying the habit plane phenomenon in martensitic steels. In the PTMC, the habit plane must be completely invariant, and being *only* untilted is not considered as a sufficient condition.

Looking for untilted planes of any transformation is similar to searching invariant directions. The directions are transformed by the distortion \mathbf{F} expressed in the direct lattice. Similarly, the planes are transformed by the matrix \mathbf{F}^* , which is the matrix of distortion \mathbf{F} expressed in the reciprocal lattice. For the untilted planes, the following eigenvalue problem to be solved is:

$$\mathbf{F}^* \mathbf{n} = \lambda \mathbf{n} \quad (4.18)$$

It is important to note here that, contrarily to the invariant direction calculation, an eigenvalue of 1 does not imply that the plane is invariant. Actually, the eigenvalues of \mathbf{F}^* give an indication on the change of spacing between the atomic planes during transformation. The study of the distortion matrix in the reciprocal lattice is not sufficient to find the invariant planes of the transformation.

Coherent interface

Martensite-martensite interface

Some conditions on the distortion matrices are needed to allow for the existence of a coherent interface between two daughter crystals upon transformation. These conditions are illustrated in figure 4.1. Let us consider a parent crystal Ω that will transform into two distinct domains Ω'_1 and Ω'_2 by two different distortions \mathbf{F}_1 and \mathbf{F}_2 , respectively. The plane \mathcal{S}_γ is the plane in the parent phase that corresponds to the interface \mathcal{S}_α , between the domains Ω'_1 and Ω'_2 after transformation. To ensure a coherent interface \mathcal{S}_α , all the vectors \mathbf{x} belonging to the interface \mathcal{S}_γ have to be transformed the same way by the respective distortion matrices \mathbf{F}_1 and \mathbf{F}_2 . We thus need $\mathbf{F}_1 \mathbf{x} = \mathbf{F}_2 \mathbf{x}, \forall \mathbf{x} \in \mathcal{S}_\gamma$. Mathematically it consists in finding $\ker(\mathbf{F}_1 - \mathbf{F}_2)$. To guarantee a coherent interface, exactly two non-collinear vectors \mathbf{x}_1 and \mathbf{x}_2 have to belong the kernel. This condition is equivalent to the so-called *kinematic compatibility* [Bhattacharya, 2003],

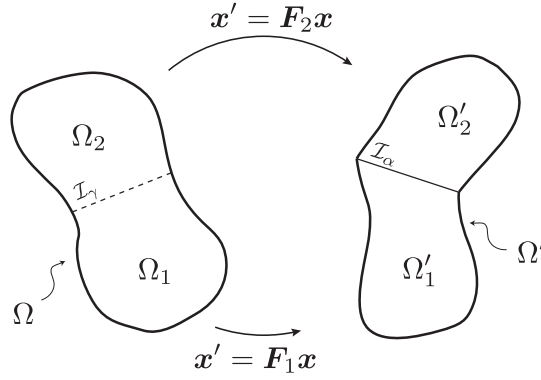


Figure 4.1: Condition of coherence at an interface between two transformed domains

also called the *Hadamard jump* condition [Ball and James, 1987].

Additionally, it can be shown that if two distortion variants are such that there exists two non-collinear vectors \mathbf{x}_1 and \mathbf{x}_2 in the kernel, any linear combination of the two distortions preserves the volume change of the transformation:

$$\det(\lambda \mathbf{F}_1 + (1 - \lambda) \mathbf{F}_2) = \det \mathbf{F}_1 = \det \mathbf{F}_2 \quad (4.19)$$

Proof: This proof is not novel, as its constitutive elements can be found in the litterature, for exemple in the work of Muhlemann and Koumatos [Muehlemann and Koumatos, 2015]. However, we could not find the proof in its complete form, namely starting from a condition on the dimension of the kernel, as defined above, and concluding with the formal volume preservation, as stated in equation 4.19. We therefore propose to present it here.

The condition for a coherent interface between two distortion variants \mathbf{F}_1 and \mathbf{F}_2 as defined above specifies that it should exist two non-collinear vectors in $\ker(\mathbf{F}_1 - \mathbf{F}_2)$:

$$\dim(\ker(\mathbf{F}_1 - \mathbf{F}_2)) = 2 \quad (4.20)$$

We have also that $\mathbf{F}_1 - \mathbf{F}_2$ is a linear map in a three dimensional space. The *rank theorem* thus states:

$$\text{rank}(\mathbf{F}_1 - \mathbf{F}_2) + \dim(\ker(\mathbf{F}_1 - \mathbf{F}_2)) = 3 \quad (4.21)$$

It implies that the rank of $\mathbf{F}_1 - \mathbf{F}_2$ is equal to one. The matrices \mathbf{F}_1 and \mathbf{F}_2 are said to be *rank-one connected*. Expressed in such terms, the criterion for a coherent interface is known as the *Hadamard jump* condition [Ball and James, 1987]. A rank-one matrix can be written as an outer product of two vectors, such that:

$$\mathbf{F}_1 - \mathbf{F}_2 = \mathbf{a} \mathbf{n}^T \quad (4.22)$$

where \mathbf{a} and \mathbf{n} are two column vectors.

As a consequence, we can write:

$$\mathbf{F}_1 - \mathbf{F}_2 = \mathbf{a}\mathbf{n}^T \rightarrow \mathbf{F}_1 = \mathbf{F}_2 + \mathbf{a}\mathbf{n}^T \quad (4.23)$$

By the factorisation of \mathbf{F}_2 , the sum is transformed in a multiplication:

$$\mathbf{F}_1 = \mathbf{F}_2(\mathbf{I} + \mathbf{F}_2^{-1}\mathbf{a}\mathbf{n}^T) \quad (4.24)$$

The volume change associated with different elements in equation 4.24 can be computed. The determinant of the product of two matrices is the product of the determinant of each matrix separately. So, we have:

$$\det(\mathbf{F}_1) = \det(\mathbf{F}_2(\mathbf{I} + \mathbf{F}_2^{-1}\mathbf{a}\mathbf{n}^T)) = \det(\mathbf{F}_2) \cdot \det(\mathbf{I} + \mathbf{F}_2^{-1}\mathbf{a}\mathbf{n}^T) \quad (4.25)$$

As $\det(\mathbf{F}_1) = \det(\mathbf{F}_2)$,

$$\det(\mathbf{I} + \mathbf{F}_2^{-1}\mathbf{a}\mathbf{n}^T) = 1 \quad (4.26)$$

The *matrix determinant lemma* states that $\det(\mathbf{I} + \mathbf{b}\mathbf{m}^T) = 1 + \mathbf{b}^T\mathbf{m}$ for any column vectors \mathbf{b} and \mathbf{m} . This lemma being applied to equation 4.26, we have,

$$\det(\mathbf{I} + \mathbf{F}_2^{-1}\mathbf{a}\mathbf{n}^T) = 1 + (\mathbf{F}_2^{-1}\mathbf{a})^T\mathbf{n} = 1 \quad (4.27)$$

As a consequence $(\mathbf{F}_2^{-1}\mathbf{a})^T\mathbf{n} = 0$. Geometrically, it means that the vectors $\mathbf{F}_2^{-1}\mathbf{a}$ and \mathbf{n} are orthogonal. From equation 4.24, the linear combination of \mathbf{F}_1 and \mathbf{F}_2 can be written as follows:

$$\lambda\mathbf{F}_1 + (1 - \lambda)\mathbf{F}_2 = \lambda\mathbf{F}_2(\mathbf{I} + \mathbf{F}_2^{-1}\mathbf{a}\mathbf{n}^T) + (1 - \lambda)\mathbf{F}_2 = \mathbf{F}_2(\mathbf{I} + \lambda\mathbf{F}_2^{-1}\mathbf{a}\mathbf{n}^T) \quad (4.28)$$

The determinant can then be computed:

$$\det(\lambda\mathbf{F}_1 + (1 - \lambda)\mathbf{F}_2) = \det(\mathbf{F}_2) \cdot \det(\mathbf{I} + \lambda\mathbf{F}_2^{-1}\mathbf{a}\mathbf{n}^T) \quad (4.29)$$

As seen before, $\mathbf{F}_2^{-1}\mathbf{a}$ and \mathbf{n} are orthogonal. Multiplying the vector $\mathbf{F}_2^{-1}\mathbf{a}$ by λ will not change its direction, and thus $\lambda(\mathbf{F}_2^{-1}\mathbf{a})^T\mathbf{n} = 0$. Therefore,

$$\det(\lambda\mathbf{F}_1 + (1 - \lambda)\mathbf{F}_2) = \det(\mathbf{F}_2) \quad \square \quad (4.30)$$

The volume change is thus preserved for any linear combination of \mathbf{F}_1 and \mathbf{F}_2 . It is important to note here that not all pairs of variant satisfy the Hadamard jump condition. Therefore, one should be careful when combining variants and verify that the average transformation leads to the same volume change as each individual variant. As an additional comment, it is worth noting that the equation 4.28 evidences the equivalence between the Bowles and Mackenzie version of the PTMC based on matrix multiplication [Bowles and Mackenzie, 1954a] and the

Lieberman, Wechsler and Read version based on linear combination of lattice strain variants [Wechsler and Read, 1953]. Indeed, Liebermann Wechsler and Read consider distortions \mathbf{F} that are lattice strains which can be decompose into an \mathbf{RB} product. Additionally, $\lambda \mathbf{F}_2^{-1} \mathbf{a}$ and \mathbf{n} being orthogonal, the matrix $\mathbf{I} + \lambda \mathbf{F}_2^{-1} \mathbf{a} \mathbf{n}^T$ is nothing else than a shear parallel to a plane of normal \mathbf{n} . Actually, it is exactly the lattice invariant shear \mathbf{Q}^{-1} of Bowles and Mackenzie.

Habit plane as a coherent interface

When discussing the coherent interface as described above, the interface considered is a martensite-martensite interface. However, another important interface to study is the habit plane, the martensite-austenite interface. In our approach and as described in the previous section an *untitled* plane is a sufficient criterion for the existence of habit planes in steels. However, from a PTMC stand point it is not enough and the shape deformation must admit a completely invariant plane. In the Liebermann, Wechsler and Read PTMC, an invariant plane strain is obtained by combining two variants, called *twins* in the original paper. The distortions of the twins \mathbf{F}_1 and \mathbf{F}_2 satisfy the Hadamard jump condition. They show that it is possible to combine the two distortions such that the average deformation is exactly an invariant plane strain: $\lambda \mathbf{F}_1 + (1 - \lambda) \mathbf{F}_2 = \mathbf{IPS}$. Liebermann, Wechsler and Read further showed that for steels the volume fraction λ allowing an invariant plane can take two different values λ and $1 - \lambda$. These values depend on the lattice parameter of the two phases and the tetragonality of the martensite [Wechsler and Read, 1953]. In the Bowles and Mackenzie version, the habit plane is made invariant by the action of the lattice invariant shear and the two different volume fraction of twins are deduced from the shear amplitude.

Supercompatibility and cofactor condition. Ball and James proposed a criterion for a *supercompatibility* of the austenite-twinned martensite interface [Ball and James, 1987]. This criterion is called the *cofactor condition*. It can be seen as an extension of the invariant plane strain criterion stated by Liebermann, Wechsler and Read. Satisfying the cofactor condition implies that an IPS is obtained by *any* ratio λ of the distortions \mathbf{F}_1 and \mathbf{F}_2 . The mathematical details linked to the exact expression of the cofactor condition will not be presented here as it is beyond the scope of this mathematical introduction. We thus redirect the interested reader to the work of Chen *et al.* [Chen et al., 2013]. We nonetheless mention that up to date there is no known material satisfying this condition, even though particular shape memory alloys are "close" to it [Chluba et al., 2015]. Following the success of the application of the cofactor condition to real materials, della Porta *et al.* proposed a mathematical measure to evaluate "how closely a material satisfies the cofactor condition" allowing thus to compare different materials [Della Porta, 2019].

Effect of applied stress on variant selection

A classical way of quantifying the effect of applied stress on variant selection consists in computing the Patel and Cohen criterion [Patel and Cohen, 1953], or its generalization as presented in the state of the art on variant selection in chapter 2, equation 2.3. Here we would like to briefly explain why such a criterion is applicable for the study of variant selection, by using thermodynamic calculations. We will also propose an illustration of this criterion through a simple mechanical model.

At a given pressure p and temperature T , the variation of the Gibbs free energy is given by: $dG = dU + pdV - TdS$, where the variation in internal energy dU is equal to the sum of the work δW and heat δQ exchanged by the system. The variation in Gibbs free energy can be expressed for each variant α_i of the transformation: $dG^{\alpha_i} = dU^{\alpha_i} + pdV^{\alpha_i} - TdS^{\alpha_i}$. A thermodynamic system always tends to minimize its Gibbs free energy, such that among all the variants, the variant α_j having $dG^{\alpha_j} < dG^{\alpha_i}$, $i \neq j$, is the most favoured. The contributions of pdV and TdS do not vary as function of the variant formed. Indeed, the change of volume as well as the change in entropy are the same for all variants. As a consequence, the only contribution which can modify the value of the dG^{α_i} is the variation of the internal energy $dU^{\alpha_i} = \delta W^{\alpha_i} + \delta Q^{\alpha_i}$. The term δQ^{α_i} corresponds to the heat exchanged by the system. The heat exchanged is the same for all variants. On the contrary, the value of the work δW^{α_i} can vary as a function of the variant formed. It is typically the case when an external force is applied to the system. To explain the variation of work from one variant to another caused by the application of the force, we propose to split the term of work as follows:

$$\delta W = -\delta W_{\text{interface}} - \delta W_{\text{def}} - \delta W_{\sigma} \quad (4.31)$$

All the contributions have a negative sign as they represent the work performed by the system and not the work received by the system. The term $\delta W_{\text{interface}}$ is the interfacial energy associated with the transformation. This quantity is a function of the geometry of the martensite nuclei considered and the specific interfacial free energy. For a given nucleus dimension, this quantity is the same for all variants. The contribution δW_{def} defines the work performed by the nuclei of martensite in order to deform the surrounding austenite. For symmetry reasons, this quantity is identical for all variants. The last part of the total work δW is the contribution δW_{σ} associated with the applied force. This quantity describes the work of the deformation associated with the transformation in the applied stress field. It is precisely this contribution that changes as a function of the variant, and causes variant selection. The work of each variant $\delta W_{\sigma}^{\alpha_i}$ can be expressed in terms of the displacement gradient \mathbf{H}^{α_i} associated with each variant and the applied stress field tensor $\boldsymbol{\Sigma}$, as follows:

$$\delta W_{\sigma}^{\alpha_i} = \boldsymbol{\Sigma} : \mathbf{H}^{\alpha_i} \quad (4.32)$$

The value $\delta W_{\sigma}^{\alpha_i}$ thus directly depends on the variant considered. As stated before, the energetically most favoured variant is the one that has $dG^{\alpha_j} < dG^{\alpha_i}$, which is equivalent as searching $-\delta W_{\sigma}^{\alpha_j} < -\delta W_{\sigma}^{\alpha_i}$, as all the other contributions to the Gibbs free energy are identical for all

variants. The variant selection is thus based on the maximization of the work $\delta W_{\sigma}^{\alpha_i}$, as it is commonly considered in the literature, for instance in the Patel and Cohen criterion [Patel and Cohen, 1953].

An illustration of this criterion is proposed in figure 4.2, by using a simple mechanical model. On figure 4.2A we represented a square of austenite (in blue) loaded in compression by the

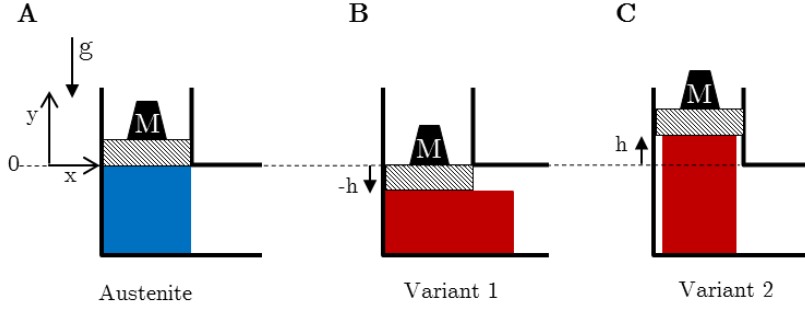


Figure 4.2: **A:** Initial configuration. An austenite square (in blue) is submitted to an applied force represented by the mass M . **B:** Transformed configuration where the austenite square has transformed in the rectangular variant 1 (in red). **C:** Transformed configuration where the austenite square has transformed in the rectangular variant 2 (in red).

mass M , placed on its top. The mass is submitted to the gravity g . We consider that the system is at the temperature of transformation M_s and that a mechanical instability can trigger the phase transformation. The transformation considered in this example is a 2d Bain transformation leading to two rectangular variants illustrated in red in figure 4.2B and 4.2C. The deformation of variant 1 is a compression along the y -direction and an elongation along the x -direction. Conversely, the deformation associated with variant 2 is an elongation along the y -direction and a compression along the x -direction. Here, the variant selection can be seen as a minimization of the potential energy E_p associated with the mass M in each configuration. Considering an initial configuration with a potential energy $E_p^0 = 0$, we have $E_p^{\alpha_1} = -Mgh$ for variant 1, and for variant 2, we have $E_p^{\alpha_2} = Mgh$. The variation of the potential energy being equal to the work of the external conservative forces: $\delta W = -dE_p$. We thus have $\delta W^{\alpha_1} = Mgh$ and $\delta W^{\alpha_2} = -Mgh$, such that the variant exhibiting the highest work is associated with the lower energy configuration. In this simple example, variant 1 is more favoured than variant 2.

5 $\{225\}_\gamma$ habit planes in martensitic steels: from the PTMC to a continuous model

Authors: A.P. Baur, C. Cayron and R.E. Logé, Laboratory of thermomechanical metallurgy-PX group Chair, Institute of materials, Ecole Polytechnique Fédérale de Lausanne, 2002 Neuchâtel, Switzerland.

Cited as: A.P. Baur et al., $\{225\}_\gamma$ habit plane in martensitic steels: from the PTMC to a continuous model, *Scientific Reports*, volume 7, Article number: 40938 (2017).

Authors contributions: Conceptualization, A.P.B., C.C. and R.E.L.; methodology, A.P.B. and C.C.; software, A.P.B.; validation, A.P.B. and C.C.; formal analysis, A.P.B. and C.C.; investigation, A.P.B.; resources, A.P.B.; data curation, A.P.B.; writing—original draft preparation, A.P.B., C.C. and R.E.L.; writing—review and editing, A.P.B., C.C. and R.E.L.; visualization, A.P.B.; supervision, C.C. and R.E.L.; project administration, C.C.; funding acquisition, C.C. and R.E.L.

Abstract

Fine twinned microstructures with $\{225\}_\gamma$ habit planes are commonly observed in martensitic steels. The present study shows that an equilibrated combination of twin-related variants associated with the Kurdjumov-Sachs orientation relationship is equivalent to the Bowles and Mackenzie's version of the PTMC for this specific $\{225\}_\gamma$ case. The distortion associated with the Kurdjumov-Sachs orientation relationship results from a continuous modeling of the FCC-BCC transformation. Thus, for the first time, an atomic path can be associated with the PTMC.

Introduction

Martensitic transformation in steels has been widely studied for the last century and remains a major field of research. This solid-phase transformation exhibits some particular crystallographic features such as the presence of habit planes between austenite (γ) and martensite (α), established orientation relationships between the two phases and a specific shape change. Based on these characteristics, various models have been developed in order to describe and understand the transformation. In the mid 50's, two independent groups, Bowles and Mackenzie [1], and Weschler, Liebermann and Read [2] developed a similar approach to explain the main features of the transformation. These two equivalent models gave rise to one of the most famous theory of phase transformation: the *Phenomenological Theory of Martensitic Crystallography* (PTMC).

Among all the observed habit planes of martensite, the $\{225\}_\gamma$ family is one of the most studied, because of the difficulties to be explained by the PTMC. The $\{225\}_\gamma$ habit planes are visible in different martensite morphologies, such as thin plate martensite and butterfly martensite. Martensite morphologies with $\{225\}_\gamma$ habit planes have a common characteristic: an internal inhomogeneous structure showing a high density of twins.

The first model that offers an explanation for $\{225\}_\gamma$ habit planes is due to Jaswon and Wheeler in 1948 [3]. They proposed a transformation mechanism where such a family of plane remains untilted during the transformation, but not fully invariant. Based on the same atomic correspondence between martensite and austenite, the Bowles and Mackenzie's version of the PTMC is the first model that can account for the invariant $\{225\}_\gamma$ habit planes. They were however criticized because an additional dilatation parameter was needed in the model. Many experiments have been performed in order to observe and measure this dilatation. They all concluded that this parameter do not differ substantially from unity [4] [5] [6]. The Bowles and Mackenzie's explanation for these habit planes was abandoned and almost forgotten.

Several other models have then been developed avoiding the use of the dilatation parameter [7] [8] [9] [10]. The current one, called the *double shear theory*, was proposed independently by Acton and Bevis (1969) [9] and Ross and Crocker (1970) [10]. In this theory, a second *lattice invariant shear*, crystallographically independent from the first one, is added to the original PTMC theory. However, as wisely observed by Dunne and Wayman [11]: "It appears that the refined and indeed elegant generalization of the original theory, wherein a single shear is replaced by two, leads to improved but not completely satisfactory prediction for the $\{225\}_\gamma$

case. It is further disappointing that the generalization, compared to the original theory, imparts a complexity which provides no selection rules for the initial choice of shear elements. The present theoretical situation is thus one of *modus vivendi*."

Starting from *a priori* completely different hypothesis than those of PTMC, Cayron recently proposed a continuous model for the FCC-BCC transformation [12]. To derive the atomic path, he assumed that the atoms behave as hard spheres and the final orientation relationship is exactly Kurdjumov-Sachs. It turns out that he in fact rediscovered the Jaswon and Wheeler distortion and proposes a continuous atomic path for it.

By investigating the properties of the distortion, the present paper shows that an appropriate combination of twin-related variants of this model is exactly equivalent to the Bowles and Mackenzie modeling of the $\{225\}_\gamma$. It solves therefore, for this particular case, the question of the atomic path that could not be given by the PTMC. The crystallographic features of the $\{225\}_\gamma$ plate martensite, like the shape strain and the twinning system, are directly derived from the distortion using simple linear algebra concepts and are in total agreement with the Bowles and Mackenzie analysis.

Furthermore, an answer is proposed to an old open question raised by Jaswon and Wheeler in the conclusion of their article, namely, "the reason for the choice of $\{225\}_\gamma$ habit in preference to an octahedral habit, since both have been shown to satisfy the condition of undergoing no directional change." [3].

Results

Distortion associated with the Kurdjumov-Sachs orientation relationship

Experimental observations show that the orientation relationship between austenite and martensite is often found to be the Kurdjumov-Sachs relationship [13]:

$$(111)_\gamma \parallel (1\bar{1}0)_\alpha \quad ; \quad [1\bar{1}0]_\gamma \parallel [111]_\alpha \quad (5.1)$$

Considering atoms as hard spheres, the FCC-BCC martensitic transformation according to this particular orientation relationship can then be described by the total distortion matrix [12] :

$$\mathbf{D} = \begin{bmatrix} \frac{\sqrt{6}}{18} + 1 & \frac{\sqrt{6}}{18} & -\frac{\sqrt{6}}{6} + \frac{1}{3} \\ \frac{\sqrt{6}}{18} - \frac{1}{3} & \frac{\sqrt{6}}{18} + \frac{2}{3} & -\frac{\sqrt{6}}{6} + \frac{1}{3} \\ -\frac{\sqrt{6}}{9} + \frac{1}{3} & -\frac{\sqrt{6}}{9} + \frac{1}{3} & \frac{\sqrt{6}}{3} + \frac{1}{3} \end{bmatrix} \quad (5.2)$$

This matrix expressed according to the orientation relationship (5.1) is equivalent to the matrix \mathbf{D}_0^{KS} calculated in equation 32 of reference [12] that was associated with the following equivalent orientation relationship: $(\bar{1}11)_\gamma \parallel (\bar{1}10)_\alpha$ and $[110]_\gamma \parallel [111]_\alpha$. This matrix expresses the total distortion, from the initial to the final state. The continuous analytical expression

Chapter 5. $\{225\}_\gamma$ habit planes in martensitic steels: from the PTMC to a continuous model

associated with this distortion is given in reference [12].

The FCC-BCC distortion \mathbf{D} of equation (5.2) is not an invariant plane strain, but an invariant line strain, as only the $[\bar{1}10]_\gamma$ direction is undistorted during the transformation. By computing the distortion matrix in the reciprocal lattice $\mathbf{D}^* = \mathbf{D}^{-T}$ and extracting its eigenvectors, one can show that there are two planes which are not tilted by the distortion: $(111)_\gamma$ and $(11\sqrt{6})_\gamma = (0.35, 0.35, 0.86)_\gamma$. The $(111)_\gamma$ plane is explicitly imposed to be untilted by the Kurdjumov-Sachs orientation relationship (5.1). On the contrary, the second plane $(11\sqrt{6})_\gamma$ is not explicitly described by the Kurdjumov-Sachs orientation relationship and is of interest as it is oriented at 0.5° from the well-known $(225)_\gamma$ habit planes.

Variants of the distortion associated with the Kurdjumov-Sachs orientation relationship

Due to the orientation relationship and the crystalline symmetries, there exist 24 variants of Kurdjumov-Sachs. The distortion matrix \mathbf{D}^{α_i} relative to each variant α_i is thus found using the symmetry properties of the FCC-BCC transformation [14] [15]. In the present paper, we arbitrarily consider that the distortion matrix \mathbf{D} presented in equation (5.2) is the distortion matrix relative to the first variant $\mathbf{D} = \mathbf{D}^{\alpha_1}$. The absolute basis \mathcal{B}_0^γ for expressing the transformation matrix is therefore equal to the basis relative to the first variant $\mathcal{B}_0^\gamma = \mathcal{B}_1^\gamma$. By convention, if the basis in which the vectors and matrix are expressed is different from the absolute basis \mathcal{B}_0^γ . This basis appears explicitly in the notation as a right-down index. For example, a matrix \mathbf{M} expressed in the α_i crystal is written $\mathbf{M}_{/\mathcal{B}_0^{\alpha_i}}$. When the basis is the absolute one \mathcal{B}_0^γ , the basis is not specified in the index.

The transformation matrix relative to all the 24 variants in the absolute basis \mathcal{B}_0^γ can be computed by using an appropriate change of basis:

$$\mathbf{D}^{\alpha_i} = [\mathcal{B}_0^\gamma \rightarrow \mathcal{B}_i^\gamma] \mathbf{D}_{/\mathcal{B}_i^{\alpha_i}}^{\alpha_i} [\mathcal{B}_i^\gamma \rightarrow \mathcal{B}_0^\gamma] = \mathbf{g}_i^\gamma \mathbf{D}_{/\mathcal{B}_i^{\alpha_i}}^{\alpha_i} (\mathbf{g}_i^\gamma)^{-1} \quad i = 1, 2 \dots 24 \quad (5.3)$$

with $\mathbf{g}_i^\gamma = [\mathcal{B}_0^\gamma \rightarrow \mathcal{B}_i^\gamma]$ a symmetry matrix of austenite.

For each variant α_i , one arbitrarily chooses one \mathbf{g}_i^γ in its coset $\mathbf{g}_i^\gamma \mathbf{K}^\gamma$, where $\mathbf{K}^\gamma = \mathbf{G}^\gamma \cap \mathbf{D}^{\gamma \rightarrow \alpha} \mathbf{G}^\gamma (\mathbf{D}^{\gamma \rightarrow \alpha})^{-1}$ and \mathbf{G}^γ is the point group of the austenite [15]. It is worth mentioning that in the particular case of FCC-BCC transformation, there is no distinction between orientational and distortional variants.

Among these 24 variants, there are 12 different pairs of twin-related variants. The twin-related variants of each pair have the particularity of sharing the same $\{111\}_\gamma$ plane and the same $\langle 110 \rangle_\gamma$ direction. This feature is illustrated in figure 5.1 for each particular $\{111\}_\gamma$ plane. 3D representation of the crystallographic arrangements of the twin-related variants can be found in the supplementary material 3 of reference [16].

In addition, it can be noted that the transformation matrix corresponding to each variant of

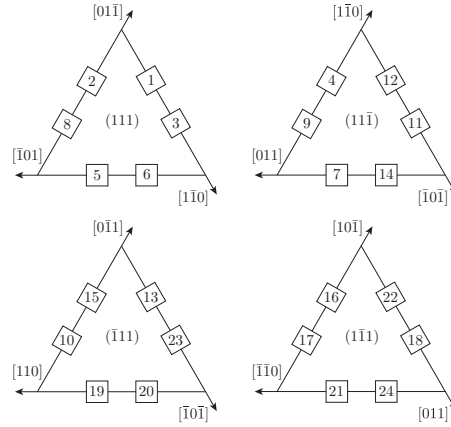


Figure 5.1: Common $\{111\}$ planes and $\langle 110 \rangle$ directions of twin-related variants

these pairs leaves the same plane $\{11\sqrt{6}\}_\gamma$ untitled. Table 5.1 summarizes the crystallographic nature of the pairs, indicating which planes are untitled and which direction is undistorted during the transformation. This table can also be read to identify the proper orientation relationship for each variant, this orientation relationship being defined by the invariant direction and the untitled plane of type $\{111\}_\gamma$. The twin-related variants of each pair can be

Table 5.1: Crystallographic features of the FCC-BCC transformation of twin-related variants

| Variants | α_1 | α_2 | α_4 | α_5 | α_7 | α_{10} | α_{11} | α_{13} | α_{16} | α_{18} | α_{19} | α_{21} |
|---------------------|---------------------------|---------------------------|---|---------------------------------|---------------------------------------|---|---------------------------------------|---------------------------------------|---|---------------------------------------|---------------------------------------|---------------------------------------|
| | α_3 | α_8 | α_9 | α_6 | α_{14} | α_{15} | α_{12} | α_{23} | α_{17} | α_{22} | α_{20} | α_{24} |
| Pairs | p_1 | p_2 | p_3 | p_4 | p_5 | p_6 | p_7 | p_8 | p_9 | p_{10} | p_{11} | p_{12} |
| Invariant direction | $[1\bar{1}0]$ | $[01\bar{1}]$ | $[\bar{1}10]$ | $[\bar{1}01]$ | $[011]$ | $[01\bar{1}]$ | $[101]$ | $[101]$ | $[\bar{1}01]$ | $[011]$ | $[110]$ | $[110]$ |
| Untilted planes | (111) $(11\sqrt{6})$ | (111) $(\sqrt{6}11)$ | $(11\bar{1})$ $(\bar{1}\bar{1}\sqrt{6})$ | (111) $(1\sqrt{6}\bar{1})$ | $(11\bar{1})$ $(\sqrt{6}\bar{1}1)$ | $(\bar{1}11)$ $(\sqrt{6}\bar{1}\bar{1})$ | $(11\bar{1})$ $(1\sqrt{6}\bar{1})$ | $(\bar{1}11)$ $(\bar{1}\sqrt{6}1)$ | $(\bar{1}1\bar{1})$ $(\bar{1}\sqrt{6}\bar{1})$ | $(1\bar{1}1)$ $(\sqrt{6}\bar{1}1)$ | $(\bar{1}11)$ $(\bar{1}1\sqrt{6})$ | $(1\bar{1}1)$ $(1\bar{1}\sqrt{6})$ |

expressed in the same *semi-eigenbasis* $\mathcal{B}_{p_j}^\gamma$ for $j = 1, \dots, 12$ defined by the common $\langle 110 \rangle_\gamma$ invariant line, the normal to the common $\{11\sqrt{6}\}_\gamma$ untitled plane and the cross product of these two vectors.

The terminology of *semi-eigenbasis* is used here in opposition to the classical eigenbasis. Indeed as the distortion associated with the Kurdjumov-Sachs orientation relationship has only one invariant line, it is not diagonalizable, and thus cannot be expressed in an eigenbasis [12]. In the rest of the paper, the mathematical development will be performed explicitly only for the pair p_1 of variants α_1 and α_3 , but the same calculation is applicable to all pairs p_j . The transformation matrices of the twin-related variants α_1 and α_3 expressed in their common semi-eigenbasis are then:

$$\mathbf{D}_{/\mathcal{B}_{p_1}^\gamma}^{\alpha_1} = \begin{bmatrix} 1 & \frac{\sqrt{3}}{6} & -\frac{1}{6} \\ 0 & 1 & -\frac{\sqrt{3}}{9} \\ 0 & 0 & \frac{4}{3}\sqrt{\frac{2}{3}} \end{bmatrix} \quad \mathbf{D}_{/\mathcal{B}_{p_1}^\gamma}^{\alpha_3} = \begin{bmatrix} 1 & -\frac{\sqrt{3}}{6} & \frac{1}{6} \\ 0 & 1 & -\frac{\sqrt{3}}{9} \\ 0 & 0 & \frac{4}{3}\sqrt{\frac{2}{3}} \end{bmatrix} \quad (5.4)$$

Chapter 5. $\{225\}_\gamma$ habit planes in martensitic steels: from the PTMC to a continuous model

If expressed in their appropriate semi-eigenbasis $\mathcal{B}_{p_j}^\gamma$, the distortion matrices of each of the twin-related variants of every pairs p_j are equal to the ones presented in equation (5.4).

The Kurdjumov-Sachs invariant plane strain

By inspection, it exists only one possibility to achieve an invariant plane strain (IPS) from a linear combination of these two matrices, and it is a mixture with 1:1 volume ratio of each of the twin-related variants,

$$\mathbf{D}_{/\mathcal{B}_{p_1}^\gamma}^{IPS} = \frac{1}{2} \mathbf{D}_{/\mathcal{B}_{p_1}^\gamma}^{\alpha_1} + \frac{1}{2} \mathbf{D}_{/\mathcal{B}_{p_1}^\gamma}^{\alpha_3} = \begin{bmatrix} 1 & 0 & 0 \\ 0 & 1 & -\frac{\sqrt{3}}{9} \\ 0 & 0 & \frac{4}{3}\sqrt{\frac{2}{3}} \end{bmatrix} = \begin{bmatrix} 1 & 0 & 0 \\ 0 & 1 & -s \\ 0 & 0 & 1 + \delta \end{bmatrix} \quad (5.5)$$

This matrix shows that a fine combination of alternating twin-related variants can produce a shape strain which is an IPS, having the $\{11\sqrt{6}\}_\gamma$ as invariant plane. The invariant plane of the average distortion \mathbf{D}^{IPS} is disoriented by 0.5° from the $\{225\}_\gamma$. The magnitude of the shape shear is $s = \frac{\sqrt{3}}{9} \approx 0.19$ and the dilatation normal to the habit plane is $\delta = \frac{4}{3}\sqrt{\frac{2}{3}} - 1 \approx 0.089 = +8.9\%$. It should be noted that for twin-related variants pairs, a linear combination satisfy the volume conservation: $\det|\mathbf{D}^{\alpha_1}| = \det|\mathbf{D}^{\alpha_3}| = \det|\mathbf{D}^{IPS}|$.

Interface between the twin-related variants

To complete the crystallographic study of the $\{225\}_\gamma$ habit planes one needs to verify the geometrical compatibility of the transformation at the interface between the two twin-related variants. In other words, it is necessary that the interface plane between each twin-related variants is transformed in the same way by both variant. Mathematically, it consists in searching two non-collinear vectors $\mathbf{v} \in \{\mathbf{v}_I, \mathbf{v}_{II}\}$ such that for each of them [17] [18], $\mathbf{D}^{\alpha_1} \mathbf{v} = \mathbf{D}^{\alpha_3} \mathbf{v}$. This condition is equivalent to calculating the Kernel of $\mathbf{A}^{p_1} = \mathbf{D}^{\alpha_1} - \mathbf{D}^{\alpha_3}$:

$$(\mathbf{D}^{\alpha_1} - \mathbf{D}^{\alpha_3}) \mathbf{v} = \mathbf{A}^{p_1} \mathbf{v} = 0 \quad \Leftrightarrow \quad \mathbf{v} \in \text{Ker}(\mathbf{A}^{p_1}) \quad (5.6)$$

The computation shows that two non-collinear vectors $\mathbf{v}_I^{p_1}$ and $\mathbf{v}_{II}^{p_1}$ belong to the Kernel. Together they define the interface plane between the two twin-related variants. The normal \mathbf{n}^{p_1} to this interface plane is simply found by calculating a cross-product, $\mathbf{n}^{p_1} = \mathbf{v}_I^{p_1} \times \mathbf{v}_{II}^{p_1}$. Such Kernel can be computed for each pair p_j of twin-related variants.

It is usual to express the interface between the two variants in their own basis $\mathcal{B}_0^{\alpha_i}$. The distortion of the planes, expressed in the α_i basis $\mathcal{B}_0^{\alpha_i}$, is given by the correspondence matrix for each $i = 1, 2, \dots, 24$ in the reciprocal lattice $(\mathbf{C}^{\alpha_i \rightarrow \gamma})^*$. The interface plane between the twin-

related variant is then:

$$\mathbf{n}_{/\mathcal{B}_0^{\alpha_i}}^{p_j} = (\mathbf{C}^{\alpha_i \rightarrow \gamma})^* \mathbf{n}^{p_j} \quad j = 1, 2 \dots 12 \quad i = 1, 2 \dots 24 \quad (5.7)$$

The results of the predicted interface between two twin-related variants are reported in table 5.2 for each pair p_j of twins. Six different interfaces belonging to the $\{110\}_\gamma$ planes family have been found. According to equation (5.7), they correspond to $\{112\}_\alpha$.

Table 5.2: Crystallographic features of the interface between twin-related variants

| Variants | α_1 | α_2 | α_4 | α_5 | α_7 | α_{10} | α_{11} | α_{13} | α_{16} | α_{18} | α_{19} | α_{21} |
|-----------------|-------------------------------|-----------------------|-----------------------|-----------------------|-----------------------|-----------------------|-----------------------|-----------------------|-----------------------|-----------------------|-----------------------|-----------------------|
| | α_3 | α_8 | α_9 | α_6 | α_{14} | α_{15} | α_{12} | α_{23} | α_{17} | α_{22} | α_{20} | α_{24} |
| Pairs | p_1 | p_2 | p_3 | p_4 | p_5 | p_6 | p_7 | p_8 | p_9 | p_{10} | p_{11} | p_{12} |
| Interface plane | in \mathcal{B}_0^γ | ($\bar{1}\bar{1}0$) | ($0\bar{1}\bar{1}$) | ($\bar{1}\bar{1}0$) | (101) | ($0\bar{1}1$) | ($0\bar{1}\bar{1}$) | ($10\bar{1}$) | ($10\bar{1}$) | (101) | ($0\bar{1}1$) | ($\bar{1}10$) |
| | in $\mathcal{B}_0^{\alpha_i}$ | ($\bar{1}\bar{2}1$) | ($\bar{1}\bar{2}1$) | ($\bar{1}\bar{2}1$) | ($\bar{1}\bar{2}1$) | ($\bar{1}\bar{2}1$) | ($\bar{1}\bar{2}1$) | ($\bar{1}\bar{2}1$) | ($\bar{1}\bar{2}1$) | ($\bar{1}\bar{2}1$) | ($\bar{1}\bar{2}1$) | ($\bar{1}\bar{2}1$) |

Equivalence with Bowles & Mackenzie model

In the Bowles and Mackenzie's paper *The crystallography of martensite transformations III* [1], the shape deformation associated with their prediction is expressed in the basis \mathcal{B}_0^γ as follows,

$$\mathbf{P} = \mathbf{I} + m \mathbf{d} \mathbf{p}' \quad (5.8)$$

where $\mathbf{d} = -\frac{1}{2\sqrt{3}}[1, 1, -2]$ and $\mathbf{p}' = (1, 1, \sqrt{6})$ and $m = \frac{2}{3}(\sqrt{3} - \sqrt{2})$.

This transformation matrix can be expressed in its proper *semi-eigenbasis* in the same manner that has been used previously for the twin-related variant. It takes a form that is exactly the same as the Kurdjumov-Sachs invariant plane strain \mathbf{D}^{IPS} produced by the composition of twin-related variants.

$$\mathbf{P} = \begin{bmatrix} 1 & 0 & 0 \\ 0 & 1 & -\frac{\sqrt{3}}{9} \\ 0 & 0 & \frac{4}{3}\sqrt{\frac{2}{3}} \end{bmatrix} = \mathbf{D}^{IPS} \quad (5.9)$$

Consequently, the Bowles and Mackenzie's version of the PTMC allows the prediction of the same $\{11\sqrt{6}\}_\gamma$ planes as the ones that are shown to stay invariant by an appropriate combination of twin-related variants.

Discussion

It has been shown that an heterogeneous structure of infinitely small twin-related variants in equal proportion leaves a plane completely invariant. This plane is a $\{11\sqrt{6}\}_\gamma$ plane disoriented from the well-known $\{225\}_\gamma$ plane by only 0.5° . The macroscopic shape deformation resulting from such a combination of variants, each of these variants undergoing an invariant line strain, is exactly an invariant plane strain.

Figure 5.2 schematically represents a $(225)_\gamma$ thin plate of martensite according to the present results.

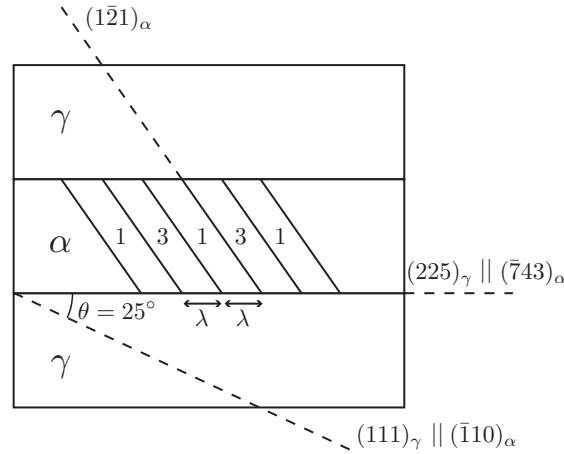


Figure 5.2: Schematic representation of $(225)_\gamma$ thin plate of martensite. Cross-sectional view normal to $[1\bar{1}0]_\gamma \parallel [111]_\alpha$.

The thin plate martensite showing a high density of alternate twin-related variants α_1 and α_3 is represented surrounded by the austenitic matrix. The crystallographic orientations of the γ and α phases are defined thanks to the dashed lines representing particular planes. The trace of the $(225)_\gamma$ predicted habit plane is also shown. This plane corresponds to the $(\bar{7}43)_\alpha$ in the martensite phase. In the present study, all twelve habit planes predicted by the Kurdjumov-Sachs invariant plane strain \mathbf{D}^{IPS} are the $\{225\}_\gamma$ planes at 25° from the $\{111\}_\gamma$ planes involved in the Kurdjumov-Sachs relationship. This particular feature is in full agreement with the experimental studies of Shimizu, Oka and Wayman on Fe-Cr-C alloy [19]. Each pair p_j of twin-related variants is then associated unequivocally with one of these twelve $\{225\}_\gamma$ habit planes. The proportion λ of each of the twin-related variants α_1 and α_3 that is needed to produce the invariant plane strain is unique and the ratio is found to be 1:1. This result corresponds to the value experimentally deduced by Kelly and Nutting [20] when they studied the martensitic transformation in carbon steels. It is also the same proportion that is considered in the Bowles and Mackenzie's model for this specific habit plane.

The present study also shows that the interface plane between two Kurdjumov-Sachs twin-related variants is unique, as there are exactly two non-collinear vectors in the Kernel computed in equation (5.6). The results suggest that the martensite twins are not created from mechanical twinning, but are due to a particular association of variants, these variants being

twin-related. We conclude that a local variant selection occurs to accommodate the phase transformation on the habit plane. Away from the habit plane, however, the transformation might need additional mechanisms, like plasticity by dislocations gliding to accommodate the shape strain related to the transformation. Such additional mechanisms can be observed in $\{225\}_\gamma$ habit planes martensitic steels [21].

The shape strain \mathbf{D}^{IPS} associated with an equilibrated combination of twin-related variants can be clearly identified in equation (5.5). This shape strain is exactly the same as the one predicted by the PTMC and computed in equation (5.9). The calculated shear is 0.19 and the dilatation normal to the habit plane is +8.9%. The shear strain is in good agreement with the magnitude experimentally measured in ferrous martensite which varies between 0.18 [22] and 0.22 [23]. However, the dilatation normal to the habit plane is overestimated. Indeed, the dilatation reported in the literature is about +3% [23]. This discrepancy was expected because the atoms were assumed to be hard spheres of constant radius, whereas a slight decrease of the atomic size (few %) is observed during the transformation. This atomic size change is not captured by our model such that we overestimated the volume change associated with the FCC-BCC transformation, and hence the dilatation normal to the habit plane as well.

The hard-sphere assumption is done in both the Bowles and Mackenzie's PTMC model for the $\{225\}_\gamma$ case and our model. Indeed, for this specific habit plane, the PTMC requires the dilatation parameter to be different from 1, such that the $[1\bar{1}0]_\gamma$ and the $[111]_\alpha$ atomic rows match. As commented by Bowles, this dilatation is exactly equivalent to an hard sphere modeling of the atoms ([1], part III). In both models, the matching of the $[1\bar{1}0]_\gamma$ and the $[111]_\alpha$, and the exact Kurdjumov-Sachs orientation relationship are required to let the $(225)_\gamma$ completely invariant. To compensate the natural decrease of the atom size and the consequent atomic mismatch along the $[1\bar{1}0]_\gamma \parallel [111]_\alpha$ closed-pack direction, accommodation mechanisms by dislocations in the austenite need to be considered. Back in the 70's, for example, Bowles envisaged multiple $\{111\}_\gamma$ slip systems to preserve an invariant habit plane [24]. More recently, Stanford and Dunne used similar arguments to explain the austenite/ ϵ -martensite interface in Fe-Mn-Si alloys [25]. The Bowles and Mackenzie's dilatation parameter was controversial and so is also the hard sphere modeling of the atoms. However, this approach has the advantage of allowing the description of the atomic trajectories. In this respect, using the hard-sphere model may allow more significant insights into the effective transformation mechanism than the consideration of artificial double shear systems, mentioned in the introduction.

It is remarkable that both the atomistic and the phenomenological modeling lead to the same results. In fact, even though these approaches are *a priori* based on opposite starting hypothesis, they share one common assumption: the atomic correspondence between the austenite and the martensite. The Bowles and Mackenzie model is historically based on the observation of the macroscopic shape strain associated with the transformation. An initial guess on the lattice invariant shear is required and the orientation relationship can then be derived. It only deals with the initial and the final states, but allows to cover a broad range of transformation, morphologies and habit planes. On the contrary, in the model proposed by Cayron, one assumes the final orientation relationship and imposes a steric condition on the atomic trajectories, by the mean of the hard sphere assumption. A precise atomic path

Chapter 5. $\{225\}_\gamma$ habit planes in martensitic steels: from the PTMC to a continuous model

can thus be defined for the transformation. The shape strain and the twinning system are then directly derived from the model with simple calculations. The predicted twinning system corresponds exactly to the lattice invariant shear assumed in the PTMC and experimentally observed [19], which confirms the equivalence of the two models in the $\{225\}_\gamma$ case.

In their original papers, Bowles and Mackenzie emphasize the phenomenological nature of their theory. As reformulated by Dunne [24], they stressed that the theory provides "a framework that any proposed transformation mechanism must satisfy". The distortion associated with Kurdjumov-Sachs orientation relationship is shown to fit perfectly in this framework, for this particular $\{225\}_\gamma$ case. Our model is thus a step toward a complete mechanistic representation of the transformation. In this regard, it might be noted that the mathematical approach used in this paper has also been successfully applied for $\{557\}_\gamma$ habit planes in dislocated martensite [26].

The present study explains the invariant nature of the $\{225\}_\gamma$ habit planes thanks to fundamental, but rather abstract, linear algebra concepts. So, in order to visualize the crystallography of $\{225\}_\gamma$ thin plates, some computer simulations have been performed at the atomic scale. These simulations consist in computing the two final twin-related BCC lattices within their parent austenitic matrix. The computation of the transformation is based on the matrices \mathbf{D}^{α_1} and \mathbf{D}^{α_3} from equation (5.3). Only the iron atoms are considered and illustrated in figure 5.3. Figure 5.3(a), analogous to the schematic figure 5.2, shows the accurate atomic positions. It illustrates clearly the Kurdjumov-Sachs orientation relationship, $[1\bar{1}0]_\gamma$ being parallel to $[111]_\alpha$ direction, and $(111)_\gamma$ plane parallel to $(1\bar{1}0)_\alpha$. All the crystallographic features presented schematically in figure 5.2 are also illustrated here. Figure 5.3(b) shows a tridimensional view of the simulated $\{225\}_\gamma$ plate. The proposed modeling of the $\{225\}_\gamma$ habit plane martensite is

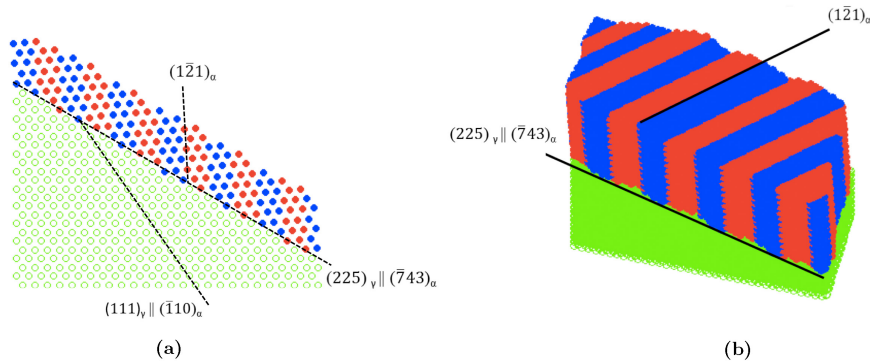


Figure 5.3: Illustrations of the $(225)_\gamma$ thin plate: **(a)** projection along $[1\bar{1}0]_\gamma \parallel [111]_\alpha$ and **(b)** 3D view. Green dots: iron atoms in austenite. Blue and red dots: iron atoms in martensitic twin-related variants α_1 and α_3 .

based on an atomic description of the FCC-BCC phase transformation [12]. A movie of the simulated $\{225\}_\gamma$ thin plate of martensite was computed. It is available in the supplementary material. Snapshots of this film are presented in figure 5.4.

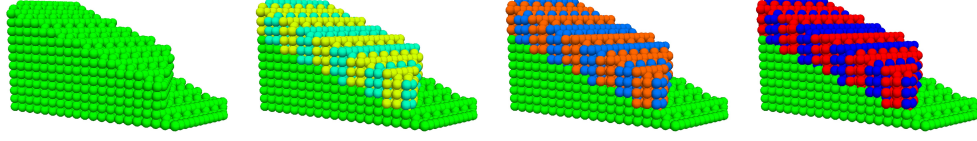


Figure 5.4: Snapshots of the $(225)_\gamma$ thin plate formation. Green dots: iron atoms in austenite. Blue and red dots: iron atoms in martensitic twin-related variants α_1 and α_3 .

As previously mentioned, the distortion associated with the Kurdjumov-Sachs orientation relationship leaves two families of plane untilted, $\{111\}_\gamma$ and $\{11\sqrt{6}\}_\gamma$. However, it is usually the second family of planes which is experimentally observed. As mentioned in the introduction and already questioned by Jaswon and Wheeler [3], a major question is then to understand why. The present approach proposes a clear answer, illustrated in figure 5.5. In the distortion,

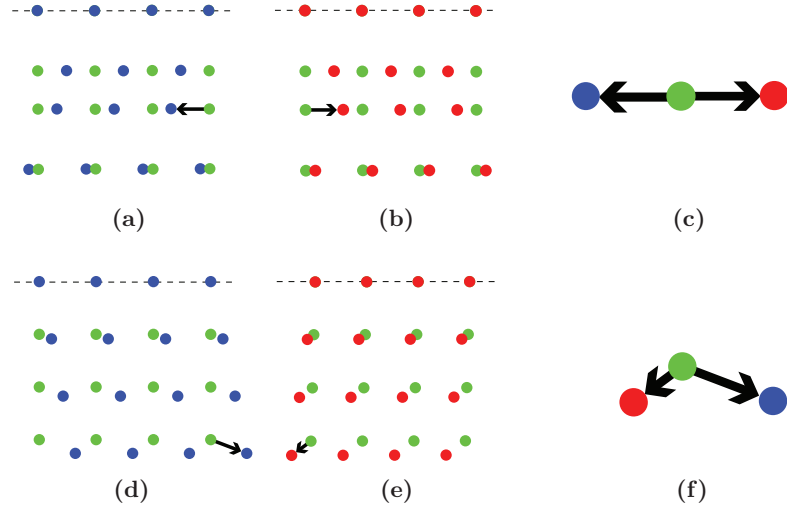


Figure 5.5: Comparison between the atomic displacements in the $(11\sqrt{6})_\gamma$ plane **(a)**, **(b)** and **(c)** and in the $(111)_\gamma$ plane **(d)**, **(e)** and **(f)**. Green dots: iron atoms in austenite. Blue and red dots: iron atoms in martensitic twin-related variants α_1 and α_3 .

each of the untilted planes is deformed within the plane, as the spacing between the atoms in this plane changes during the transformation [12]. The matrices computed in equation (5.4) show that for the $(225)_\gamma$ habit plane the atoms are displaced in opposite directions for each twin of a given pair of twin-related variants such that the average displacement on this plane is zero. This average cancellation is illustrated in figures 5.5(a) and 5.5(b). They show the atomic positions in a $(11\sqrt{6})_\gamma$ habit plane for both variants α_1 and α_3 . The $(11\sqrt{6})_\gamma$ plane being irrational, it cannot form a 2D crystallographic lattice. Therefore, in the simulations, this plane is defined by all the atomic positions \mathbf{u} such that: $[11\sqrt{6}] \cdot \mathbf{u} = 0 \pm tol$, where tol is a tolerance factor equal to 0.05. Black arrows are sketched on figure in order to better visualize the atomic displacements. The invariant $[1\bar{1}0]_\gamma$ direction, where the atoms positions in austenite and in martensite match is noted on the picture with a dashed horizontal line. To

Chapter 5. $\{225\}_\gamma$ habit planes in martensitic steels: from the PTMC to a continuous model

be compared with figures 5.5(a) and 5.5(b), figures 5.5(d) and 5.5(e) show the atomic positions after transformation for each of the twin-related variants α_1 and α_3 in the $(111)_\gamma$ plane. Figures 5.5(c) and 5.5(f) offer detailed views of the displacements for each variant in the $(225)_\gamma$ plane and in the $(111)_\gamma$ plane. Figure 5.5(c) illustrates the average cancellation of the displacements. On the contrary, as showed in figure 5.5(f), in the $(111)_\gamma$ plane, there is a displacement on the vertical axis that goes in the same direction for both variants. Indeed, the red and blue dots both shift in a direction $[01\bar{1}]_\gamma$ relatively to the initial FCC lattice in the same manner. Such a displacement cannot be cancelled by any combination of these two variants. This result can also be proved mathematically by applying an analogous approach for $(111)_\gamma$ as the one we used to show the invariant nature of $(225)_\gamma$ planes. We notice that all the volume change intrinsic to the FCC-BCC transformation occurs by the distortion of the $(111)_\gamma$ plane. Therefore $\{111\}_\gamma$ planes cannot be invariant during the transformation.

In conclusion, this study shows that a fine alternate structure of Kurdjumov-Sachs twin-related variants in equal proportion creates a macroscopic invariant plane strain having $(11\sqrt{6})_\gamma$ as invariant plane, lying at 0.5° from the observed $(225)_\gamma$ plane. The shape strain resulting from this combination of twin-related variants consists in a shear of magnitude 0.19 parallel to the habit plane and a dilatation normal to the habit plane of +8.9%. This shape strain corresponds exactly to the result of the Bowles and Mackenzie's version of the PTMC. For this special $(225)_\gamma$ case, the two models are shown to be equivalent. We also demonstrated that because of the geometrical compatibility at the interface, Kurdjumov-Sachs twin-related variants share an interface plane of type $\{112\}_\alpha$, which corresponds to the twinning system that is assumed in the PTMC.

In this specific case, a continuous atomic displacement can be associated with the original Bowles and Mackenzie's model, offering, for the first time, a mechanistic dimension to a theory which up to now was phenomenological.

Methods

Mathematical notations and conventions

The mathematical notations and conventions used in the present paper are briefly presented here. The vectors are column vectors and are written in small bold letters. The matrices are written in bold capital letters. A vector \boldsymbol{v} is transformed by a matrix \boldsymbol{M} as follows:

$$\boldsymbol{v}' = \boldsymbol{M}\boldsymbol{v} \quad (5.10)$$

The coordinate-transformation matrix between two basis \mathcal{B}_1 and \mathcal{B}_2 is noted $\mathbf{T} = [\mathcal{B}_1 \rightarrow \mathcal{B}_2]$ and is defined such that its columns are the vectors of the basis \mathcal{B}_2 expressed in the basis \mathcal{B}_1 :

$$\mathbf{a}_{/\mathcal{B}_1}^{\mathcal{B}_2} = \begin{pmatrix} a \\ b \\ c \end{pmatrix} \quad \mathbf{b}_{/\mathcal{B}_1}^{\mathcal{B}_2} = \begin{pmatrix} d \\ e \\ f \end{pmatrix} \quad \mathbf{c}_{/\mathcal{B}_1}^{\mathcal{B}_2} = \begin{pmatrix} g \\ h \\ i \end{pmatrix} \quad (5.11)$$

One has,

$$\mathbf{T} = [\mathcal{B}_1 \rightarrow \mathcal{B}_2] = \begin{bmatrix} a & d & g \\ b & e & h \\ c & f & i \end{bmatrix} \quad ; \quad [\mathcal{B}_2 \rightarrow \mathcal{B}_1] = [\mathcal{B}_1 \rightarrow \mathcal{B}_2]^{-1} \quad (5.12)$$

The vector \mathbf{v} and the matrix \mathbf{M} expressed in \mathcal{B}_1 , noted $\mathbf{v}_{/\mathcal{B}_1}$ and $\mathbf{M}_{/\mathcal{B}_1}$ are, then, respectively expressed in \mathcal{B}_2 by:

$$\mathbf{v}_{/\mathcal{B}_2} = [\mathcal{B}_2 \rightarrow \mathcal{B}_1] \mathbf{v}_{/\mathcal{B}_1} = \mathbf{T}^{-1} \mathbf{v}_{/\mathcal{B}_1} \quad (5.13)$$

$$\mathbf{M}_{/\mathcal{B}_2} = [\mathcal{B}_2 \rightarrow \mathcal{B}_1] \mathbf{M}_{/\mathcal{B}_1} [\mathcal{B}_1 \rightarrow \mathcal{B}_2] = \mathbf{T}^{-1} \mathbf{M}_{/\mathcal{B}_1} \mathbf{T} \quad (5.14)$$

Semi-eigenbasis of twin-related variants

The distortion matrices of variants α_1 and α_3 forming the first pair p_1 are expressed in their common semi-eigenbasis, using the following coordinates-transformation matrix:

$$[\mathcal{B}_0^\gamma \rightarrow \mathcal{B}_{p_1}^\gamma] = \frac{1}{2} \begin{bmatrix} \sqrt{2} & -\frac{\sqrt{6}}{2} & \frac{\sqrt{2}}{2} \\ -\sqrt{2} & -\frac{\sqrt{6}}{2} & \frac{\sqrt{2}}{2} \\ 0 & 1 & \sqrt{3} \end{bmatrix} \quad [\mathcal{B}_{p_1}^\gamma \rightarrow \mathcal{B}_0^\gamma] = [\mathcal{B}_0^\gamma \rightarrow \mathcal{B}_{p_1}^\gamma]^{-1} \quad (5.15)$$

The distortion matrices \mathbf{D}^{α_1} and \mathbf{D}^{α_3} of each twin-related variant α_1 and α_3 can then be expressed in the common semi-eigenbasis.

$$\mathbf{D}_{/\mathcal{B}_{p_1}}^{\alpha_1} = [\mathcal{B}_{p_1}^\gamma \rightarrow \mathcal{B}_0^\gamma] \mathbf{D}^{\alpha_1} [\mathcal{B}_0^\gamma \rightarrow \mathcal{B}_{p_1}^\gamma] \quad (5.16)$$

$$\mathbf{D}_{/\mathcal{B}_{p_1}^\gamma}^{\alpha_3} = [\mathcal{B}_{p_1}^\gamma \rightarrow \mathcal{B}_0^\gamma] \mathbf{D}^{\alpha_3} [\mathcal{B}_0^\gamma \rightarrow \mathcal{B}_{p_1}^\gamma] \quad (5.17)$$

Computation of the correspondence matrix

The matrix that transforms the coordinates of each crystal α_i into the coordinates of the crystal γ is $\mathbf{T}^{\gamma \rightarrow \alpha_i}$ [14]:

$$\mathbf{T}^{\gamma \rightarrow \alpha_i} = \mathbf{g}_i^\gamma \mathbf{T}^{\gamma \rightarrow \alpha_1} \quad i = 1, 2, \dots, 24 \quad (5.18)$$

where $\mathbf{T}^{\gamma \rightarrow \alpha_1} = [\mathcal{B}_0^\gamma \rightarrow \mathcal{B}_0^{\alpha_1}]$. \mathcal{B}_0^γ and $\mathcal{B}_0^{\alpha_1}$ are formed by the usual crystallographic vectors of the Bravais lattice of the γ and α_1 crystals, respectively.

The correspondence matrix $\mathbf{C}^{\alpha_i \rightarrow \gamma}$ allows the computation of the image by the distortion \mathbf{D}^{α_i} of any vector in the γ crystal expressed in the basis $\mathcal{B}_0^{\alpha_i}$ of the product crystal α_i .

Indeed, the image of any vector $\mathbf{u}_{/\mathcal{B}_0^\gamma}$ by the distortion is given by:

$$\mathbf{u}'_{/\mathcal{B}_0^\gamma} = \mathbf{D}^{\alpha_i} \mathbf{u}_{/\mathcal{B}_0^\gamma} \quad i = 1, \dots, 24 \quad (5.19)$$

To express the transformed vector $\mathbf{u}'_{/\mathcal{B}_0^\gamma}$ in the $\mathcal{B}_0^{\alpha_i}$ basis one needs the transformation matrix presented in equation (5.18):

$$\mathbf{u}'_{/\mathcal{B}_0^{\alpha_i}} = [\mathcal{B}_0^{\alpha_i} \rightarrow \mathcal{B}_0^\gamma] \mathbf{u}'_{/\mathcal{B}_0^\gamma} = (\mathbf{T}^{\gamma \rightarrow \alpha_i})^{-1} \mathbf{u}'_{/\mathcal{B}_0^\gamma} = (\mathbf{g}_i^\gamma \mathbf{T}^{\gamma \rightarrow \alpha_1})^{-1} [(\mathbf{g}_i^\gamma) \mathbf{D}(\mathbf{g}_i^\gamma)^{-1}] \mathbf{u}_{/\mathcal{B}_0^\gamma} \quad i = 1, \dots, 24 \quad (5.20)$$

where $(\mathbf{g}_i^\gamma) \mathbf{D}(\mathbf{g}_i^\gamma)^{-1}$ is the distortion matrix of variant α_i expressed in the absolute basis \mathcal{B}_0^γ , as computed in equation (5.3).

Based on equation (5.20), the correspondence matrix is then:

$$\mathbf{C}^{\alpha_i \rightarrow \gamma} = (\mathbf{g}_i^\gamma \mathbf{T}^{\gamma \rightarrow \alpha_1})^{-1} (\mathbf{g}_i^\gamma) \mathbf{D}(\mathbf{g}_i^\gamma)^{-1} = (\mathbf{T}^{\gamma \rightarrow \alpha_1})^{-1} \mathbf{D}(\mathbf{g}_i^\gamma)^{-1} \quad i = 1, 2, \dots, 24 \quad (5.21)$$

Considering the distortion associated with the Kurdjumov-Sachs orientation relationship presented in relation (5.1) and the present coordinate-transformation matrix, the correspondence

matrix $\mathbf{C}^{\alpha_1 \rightarrow \gamma}$ is:

$$\mathbf{C}^{\alpha_1 \rightarrow \gamma} = \begin{bmatrix} 1 & 0 & 1 \\ 0 & -1 & 0 \\ 1 & 0 & -1 \end{bmatrix} \quad (5.22)$$

And the correspondence matrix in the reciprocal lattice is then:

$$(\mathbf{C}^{\alpha_i \rightarrow \gamma})^* = (\mathbf{C}^{\alpha_i \rightarrow \gamma})^{-T} \quad i = 1, 2, \dots, 24 \quad (5.23)$$

Acknowledgment

This work has been supported by the Swiss National Science Foundation (200021_159955), which is therefore gratefully acknowledged. The authors would also like to thank PX Group for its financial support to the laboratory.

Additional information

The authors declare no competing financial interests.

Bibliography

- [1] Bowles, J.S., Mackenzie, J.K. The crystallography of martensite transformations I, II and III. *Acta Metal*, **2**, 129-137, (1954).
- [2] Weschler, M.S., Liebermann, D.S., Read, T.A. On the theory of the formation of martensite. *Trans. AIME*, **197**, 1503-1515, (1953).
- [3] Jaswon, M.A., Wheeler, J.A. Atomic displacements in austenite-martensite transformation. *Acta Cryst*, **1**, 216-224, (1948).
- [4] Krauklis, P., Bowles, J.S. Direct measurement of length changes in (225) martensite habit plane. *Acta Metal*, **17**, 997-1004, (1969).
- [5] Dunne, D.P. Bowles, J.S., Measurement of the shape strain in the (225) and (259) martensitic transformation, *Acta Metal*, **17**, 201, (1969)
- [6] Jana, S., Wayman, C.M. Crystallography of the $\{225\}_F$ martensite transformation in an Fe-Mn-Cr-C alloy, *Met. Trans*, **1**, 2815-2823, (1970).
- [7] Otte H.M. On the imperfection in martensite and their relation to the formation of martensite. *Trans. AIME*, **218**, 342-351, (1960).
- [8] Weschler, M.S. , Read, T.A., Liebermann, D.S. The crystallography of the austenite-martensite transformation. The (111) shear solutions. *Trans. AIME*, **218**, 202-207, (1960).
- [9] Acton, A.F., Bevis, M. A generalised martensite crystallography theory. *Mater. Sci. Eng.*, **5**, 19-29, (1969).
- [10] Ross, N.D.H., Crocker, A.G. A generalised theory of martensite crystallography and its application to transformations in steels. *Acta Metal*, **18**, 405-418, (1970).
- [11] Dunne, D.P., Wayman, C.M. An assessment of the double shear theory as applied to ferrous martensitic transformation. *Acta Metal*, **19**, 425-438, (1971).
- [12] Cayron, C. Continuous atomic displacements and lattice distortion during fcc-bcc martensitic transformation. *Acta Mater*, **69**, 189-202, (2015).
- [13] Kurdjumov, G., Sachs, G. Über den Mechanismus der Stahl härtung. *Z. Phys*, **74**, 325-343, (1930).

Bibliography

- [14] Cayron, C. Groupoid of orientational variants. *Acta Cryst*, **A62**, 21-40, (2006).
- [15] Cayron, C. Angular distortion of phase transition in the FCC-BCC-HCP system, *Acta Mater.*, **111**, 417-441, (2016).
- [16] Cayron, C. One-step model of the face-centred-cubic to body-centred-cubic martensitic transformation. *Acta Cryst.* **A69**, 498-509, (2013).
- [17] Bhattacharya, K. In *Microstructure of martensite: why it forms and how it gives rise to the shape-memory effect*. 27-28 (Oxford University Press, 2003).
- [18] Janovec, V., Přivratská, J. Domain structures. International Tables for Crystallography. D:3:3.4:449-505, (2006) .
- [19] Shimizu, K., Oka, M., Wayman, C.M. The association of martensite platelets with austenite stacking faults in an Fe-8Cr-1C alloy. *Acta Metal*, **18**, 1005-1011, (1970).
- [20] Kelly, P.M., Nutting, J. The martensite transformation in carbon steels. *Proc. Royal Society*, **259**, 45-58, (1960).
- [21] Sandvik, B.P.J., Wayman, C.M. The substructure of $(252)_f$ martensite formed in an Fe-8Cr-1C alloy. *Metallurgical transactions A*, **14A**, 2455-2468, (1983).
- [22] Wayman, C.M. Shear Transformation and Microstructure. *Metallography*, **8**, 105-130, (1975).
- [23] Bhadeshia, H.K.D.H., Honeycombe, R.W.K. In *Steels: Microstructure and Properties (third edition)*, 99 (2006), doi:10.1016/B978-075068084-4/50002-9.
- [24] Dunne, D.P., An historical account of the development of the Bowles-Mackenzie theory of the crystallography of martensite transformation, In: *International conference on martensitic transformation-2008 (eds Olson, G.B., Liebermann, D.S. and Saxena, A.)*, The minerals, metals and material society, 47-53, (2009).
- [25] Stanford, N.E., Dunne, D.P. Effect of Si on the reversibility of stress-induced martensite in Fe-Mn-Si shape memory alloys, *Acta Mater*, **58**, 6752-6762, (2010).
- [26] Cayron, C., Baur, A.P., Logé R.L. Crystallography of low-alloy martensitic steels: $\{557\}_\gamma$ habit planes of the blocks and self-accommodation in the packets, arXiv:1606.04257, (2016) .

Authors contributions

The work has been initiated by C.C. A.B. wrote the manuscript text and prepared the video and the figures. C.C. and R.L. supervised the work. All authors reviewed the manuscript.

6 Accommodation of the $\{225\}_\gamma$ habit plane by dislocations

The strain accommodation mechanism of the habit plane is an important feature of the martensitic transformation. In our previous work (chapter 5), we showed that the combination in equal proportion of twin-related variants of the distortion associated with the Kurdjumov-Sachs orientation relationship leaves the $\{225\}_\gamma$ habit plane globally invariant [1]. However, the accommodation mechanisms of a single variant of martensite on this particular plane has not been studied yet. Here, we propose to analyse this aspect of the transformation using the Frank-Bilby equation [2] [3]. Such analysis focuses only on the dislocations involved in the accommodation of the habit plane, and gives no information on the accommodation of a full martensite product.

Generalities on the Frank-Bilby equation

Let us consider an interface between two different lattices A and B. Each of the two lattices can be computed as the product of the distortion of a common reference lattice, through the transformation matrices F_A and F_B , respectively as illustrated in figure 6.1. The Frank-Bilby

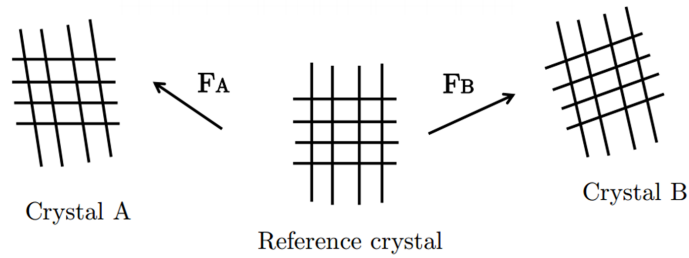


Figure 6.1: Illustration of the deformation of a common lattice in the two crystals A and B.

equation allows the computation of the net Burgers vector \mathbf{b}_T that is needed to guarantee the geometrical compatibility on the interface between the two lattices A and B [2] [3]:

$$\mathbf{b}_T = [F_A^{-1} - F_B^{-1}] \cdot \mathbf{p} \quad (6.1)$$

where \mathbf{p} is a probe vector lying in the interface and \mathbf{b}_T describes net Burgers vector that crosses the probe vector \mathbf{p} . \mathbf{b}_T is a continuous representation of the dislocations needed to accommodate the distortion. In a real crystal, dislocations are discrete linear defects defined by their line and their Burgers vector \mathbf{b} . To have a proper definition of the misfit dislocations near the interface, the net Burgers vector \mathbf{b}_T needs to be decomposed in different sets of discrete dislocations. Posing n_i as the number of dislocations in each set i crossing the probe vector \mathbf{p} , we can write:

$$\mathbf{b}_T = \sum_i n_i \mathbf{b}_i \quad (6.2)$$

In the context of phase transformations, it is suitable to consider the parent lattice as reference lattice [2]. Equation (6.1) can thus be rewritten in the following manner:

$$\mathbf{b}_T = [\mathbf{I} - \mathbf{F}^{-1}] \cdot \mathbf{p} \quad (6.3)$$

where \mathbf{F} is the distortion of the initial parent lattice to the transformed lattice.

Study of the $\{225\}_\gamma$ habit plane

For this study, we arbitrarily choose to consider the interface between variant α_1 and the austenite γ . This interface is the $(225)_\gamma$ and the invariant line associated with variant α_1 is $[1\bar{1}0]_\gamma \parallel [111]_\alpha$.

By using the continuous distortion \mathbf{F} [4] to model the complete transformation, the Frank-Bilby equation on the $(225)_\gamma$ habit plane gives:

$$\mathbf{b}_T = [\mathbf{I} - (\mathbf{F}_1)^{-1}] \cdot \mathbf{p}_\perp = \frac{1}{2\sqrt{6}} \|\mathbf{p}_\perp\| \cdot [1\bar{1}0]_\gamma = \lambda \cdot [1\bar{1}0]_\gamma \quad (6.4)$$

for a vector \mathbf{p}_\perp oriented along the $[225]_\gamma \times [1\bar{1}0]_\gamma$ direction.

It can be shown that this result is true for any vector \mathbf{p} in the interface. The vectors belonging to the interface can be expressed by a linear combination of a vector \mathbf{p}_\parallel along $[1\bar{1}0]_\gamma$ and the vector \mathbf{p}_\perp along $[225]_\gamma \times [1\bar{1}0]_\gamma$: $\mathbf{p} = a\mathbf{p}_\parallel + b\mathbf{p}_\perp$. By replacing \mathbf{p}_\perp in the Frank-Bilby equation (6.4) by \mathbf{p} , we have:

$$\mathbf{b}_T = [\mathbf{I} - (\mathbf{F}_1)^{-1}] \cdot \mathbf{p} = a[\mathbf{I} - (\mathbf{F}_1)^{-1}] \cdot \mathbf{p}_\parallel + b[\mathbf{I} - (\mathbf{F}_1)^{-1}] \cdot \mathbf{p}_\perp = b\lambda[1\bar{1}0]_\gamma \quad (6.5)$$

As \mathbf{p}_\parallel is the invariant line of the transformation, its contribution to the net Burgers vector \mathbf{b}_T is zero, such that for any vector in the interface, the net Burgers vector \mathbf{b}_T is always oriented along the $[1\bar{1}0]_\gamma \parallel [111]_\alpha$.

The value of λ depends on the norm of the probe vector \mathbf{p} , as it represents the number of dislocation lines that are crossing \mathbf{p} . It can be noted from the result of equation (6.4) that the direction of the net Burgers vector \mathbf{b}_T is crystallographic, such that it is possible to decompose it into a single set of discrete dislocations.

Hence, equation (6.2) can be written as follows:

$$\mathbf{b}_T = n\mathbf{b} = n \cdot \frac{1}{2}[\bar{1}\bar{1}0]_\gamma \quad (6.6)$$

The Frank-Bilby equation allows the computation of the net Burger's vector associated with a given interface, but it gives *a priori* no information on the dislocation line. However, in our particular case assuming that the net Burger vector is decomposed in a single set of dislocation, as in equation 6.6, the dislocation line can simply be guessed from the Frank-Bilby equation itself. As already mentioned, the magnitude of $\|\mathbf{b}_T\|$ offers an indication of the number of dislocation lines that are crossed by the probe vector \mathbf{p} . In addition, for a single set of dislocations, all dislocation lines are parallel. Therefore, a probe vector parallel to the dislocation line crosses no dislocation line. Looking for the dislocation line is thus equivalent to searching probe vectors that give $\mathbf{b}_T = 0$ or, in other words, to compute the kernel of the linear map given in the Frank-Bilby equation: $\ker(\mathbf{I} - (\mathbf{F}_1)^{-1})$. There is only one vector in this kernel and it is the invariant line $[\bar{1}\bar{1}0]_\gamma \parallel [111]_\alpha = \mathbf{p}_\parallel$. An illustration of the latter explanation is proposed in figure 6.2. The single array of dislocations is represented with the red lines in a $\{225\}_\gamma$ interface delimited by the black rectangle. The dislocation line is noted ξ . It can be seen that the only way to choose a probe vector that crosses no dislocation consists in choosing a probe vector along the dislocation line ξ . In such situation, as the probe vector does not cross any dislocations $\mathbf{b}_T = 0$. It is only the case for $\mathbf{p} = \mathbf{p}_\parallel$. From this result, we can now deduce

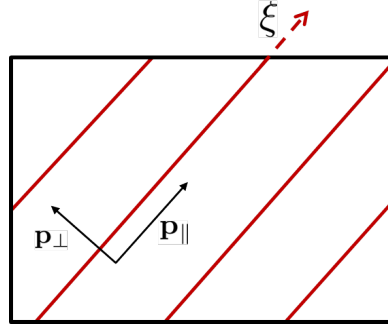


Figure 6.2: Illustration of the dislocation array (in red) in the interface. The dislocation line is noted ξ . \mathbf{p}_\parallel and \mathbf{p}_\perp are two possible probe vectors in the interface.

that the net Burgers vector \mathbf{b}_T associated with the $\{225\}_\gamma$ habit plane consists of an array of screw dislocations of type $\frac{1}{2}[\bar{1}\bar{1}0]_\gamma = \frac{1}{2}[111]_\alpha$. This conclusion is in agreement with one of the most detailed analysis of the microstructure of $\{225\}_\gamma$ martensite proposed by Sandwick and Wayman in 1983 [5]. Their analysis concerns the Fe-8Cr-1C alloy. They concluded that the $\{252\}_\gamma$ martensite/austenite interface of an *untwinned* martensite product contains an array of parallel screw dislocations of type $\frac{a_\gamma}{2}[\bar{1}01] = \frac{a_\alpha}{2}[\bar{1}\bar{1}1]$. In the crystallographic convention they choose for their study, the Kurdjumov-Sachs orientation relationship is $(111)_\gamma \parallel (011)_\alpha$ and $[\bar{1}01]_\gamma \parallel [\bar{1}\bar{1}1]_\alpha$. The observed screw dislocations are thus lying parallel to the invariant line.

According to equation (6.2), we have $n \cdot \frac{1}{2}[\bar{1}\bar{1}0] = \lambda[\bar{1}\bar{1}0]$ and thus we can deduce the number of

screw dislocations that are cut by the probe vector is $n = 2\lambda$. Considering the lattice parameter of austenite to be approximately 3.6 \AA , we can then compute the average distance d between two screw dislocations. Over its length, the probe vector $\|\mathbf{p}\|$ crosses 2λ dislocation lines. A rough estimate of the average distance between two dislocations can thus be computed by dividing the length of the probe vector by the number of crossed dislocations: $d = \frac{a_\gamma \|\mathbf{p}\|}{2\lambda} = 8.8 \text{ \AA}$. The computed distance appears very small as it is less than 4 times the inter-atomic spacing. The huge density of dislocations resulting from the computation could be possibly explained by the fact that the present calculation does not account for any elastic deformation of the lattice, and the misfit is only accommodated by dislocations. As a comparison, in the study of Sandwick and Wayman, a measure of the mean distance separating the observed dislocations has been performed and it is concluded that this spacing was about 13 \AA [5].

The detailed study of the interface has been performed for variant α_1 , however the same can be done for each variant. The associated dislocations needed to accommodate the interface are screw dislocations oriented along the invariant $\langle 110 \rangle_\gamma \parallel \langle 111 \rangle_\alpha$. In a previous work [1], we showed that $\{225\}_\gamma$ habit planes are kept globally invariant by an equibalanced combination of twin-related variants. We use here the term *globally invariant* as the distortion associated with a single variant does not itself lead to an invariant habit plane, but the atomic displacements caused are such that they are exactly compensated by its twin-related variant, leaving the $\{225\}_\gamma$ globally invariant. It is thus worth paying a more careful attention to the exact type of dislocations that are associated with the distortion \mathbf{F}_3^{KS} which is twin-related to \mathbf{F}_1^{KS} . In this case, we find $\mathbf{b}_{T_3} = \lambda[\bar{1}10]_\gamma$, thus $\mathbf{b}_{T_1} = -\mathbf{b}_{T_3}$. This equality is true for each pair of twin-related variants. The dislocations that are associated with one variant on $\{225\}_\gamma$ are thus compensated by the dislocations associated with its twin-related variant. Figure 6.3 taken from the chapter on the accommodation of the $\{225\}_\gamma$ habit plane by twin-related variants pairing (chapter 5) allows to better visualize this compensation. The dislocation perspective proposed in the Frank-Bilby analysis is another way of considering the global invariance of the habit plane thanks to twin-related variants accommodation.

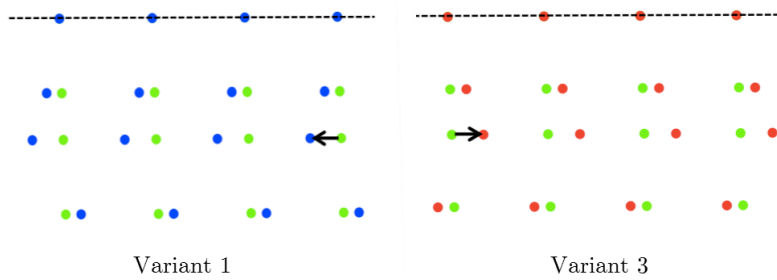


Figure 6.3: Illustration of the atomic displacement associated with two twin-related variants (1 and 3) on a $\{225\}_\gamma$ plane. The initial austenite position are marked in green, and the transformed position are marked in blue and red for variant 1 and 3, respectively. The dashed line indicates the invariant line, *i.e.* the dislocation line of the proposed solution for an accommodation based on dislocations.

In conclusion, the misfit dislocations that can possibly accommodate the continuous Kurdjumov-Sachs distortion on a $(225)_\gamma$ habit plane are determined using the Frank-Bilby equation. The study proposes a solution of the strain accommodation of the $(225)_\gamma$ interface based on a single set of screw dislocations $\frac{a_\gamma}{2} [1\bar{1}0] = \frac{a_\alpha}{2} [111]$. This dislocation structure is in good agreement with the experimental data. As a final remark, it is worth mentioning that the dislocation structure calculated here is in adequation with the dislocation structure proposed by Frank in its model [6], and it is also the same as the one computed by the molecular dynamics model of Maresca *et al.* for the $\{225\}_\gamma$ habit plane [7].

Bibliography

- [1] A.P. Baur, C. Cayron, R.E. Logé, $\{225\}_\gamma$ habit plane in martensitic steels: from the PTMC to a continuous model, *Sci. Rep.*, **1**, (2017), DOI: 10.1038/srep40938
- [2] R. Bullough, B.A. Bilby, Continuous distribution of dislocations: Surface dislocations and the crystallography of martensitic transformation, *Proceedings of the Physical Society*, **69**, 12, (1956), (1276-1286).
- [3] J.W. Christian, Crystallography of martensitic transformation *in* The theory of transformations in metals and alloys, 3rd edition, *Pergamon Press*, (2012).
- [4] C. Cayron, Continuous atomic displacements and lattice distortion during fcc-bcc martensitic transformation, *Acta Mater.*, **69**, (2015), 189-202.
- [5] B.P.J. Sandwick, C.M. Wayman, The substructure of $(252)_f$ martensite formed in an Fe-8Cr-1C alloy, *Met. Trans. A*, **14A**, (1983), 2455-2458.
- [6] E.C. Frank, Martensite, *Acta Metallurgica*, **1**, (1953).
- [7] F. Maresca, W.A. Curtin, The austenite/lath martensite interface in steels: Structure, athermal motion, and in-situ transformation strain revealed by simulation and theory *Acta Materialia*, **134**, 2017, (302-323).

7 Intricate morphologies of laths and blocks in low-carbon martensitic steels

Authors: C. Cayron, A.P. Baur and R.E. Logé, Laboratory of Thermomechanical Metallurgy-PX group Chair, Institute of materials, Ecole Polytechnique Fédérale de Lausanne, 2002 Neuchâtel, Switzerland.

Cited as: *Cayron et al., Intricate morphologies of laths and blocks in low-carbon martensitic steels, Materials and Design 154, (2018), 81–95.*

Authors contributions: Conceptualization, C.C., A.P.B. and R.E.L.; methodology, C.C., A.P.B.; software, C.C.; validation, C.C.; formal analysis, C.C.; investigation, C.C.; resources, C.C.; data curation, C.C.; writing—original draft preparation, C.C.; writing—review and editing, C.C., A.P.B. and R.E.L.; visualization, C.C. ; supervision, C.C.; project administration, C.C.; funding acquisition, C.C. and R.E.L.

Abstract

Low-carbon martensitic steels are made of intricate assemblies of martensitic laths: the twenty-four lath variants are grouped into packets on the four $\{111\}_{fcc}$ planes, and each packet is composed of three blocks of pairs of low-misoriented variants. The orientation relationship between the laths and their parent austenitic grains ranges from Kurdjumov-Sachs toward Nishiyama-Wassermann. The paper presents electron microscopy investigations that confirm that the habit planes of the laths are the $\{557\}$ planes that contain the common fcc-bcc dense directions. The morphology of many blocks appears as a bifoliate structure made of the habit planes of the two low-misoriented lath variants they contain. A theoretical model is proposed to discuss the results. The average of the two Kurdjumov-Sachs distortions associated with the variants in a block is a Nishiyama-Wassermann distortion. The $\{557\}$ lath plane of each of the two variants in a block is untilted by the Nishiyama-Wassermann distortion of one of the two neighboring blocks in the packet. Complete self-accommodation is also obtained in individual packets. These results could explain simultaneously the $\{557\}$ lath planes and the lath/block intricacy in the packets.

7.1 Introduction

7.1.1 Morphologies of the laths and blocks

Low-carbon steels and iron nickel alloys containing less than 28wt-%Ni exhibit after quenching microstructures constituted of body centered cubic (bcc, α) lath martensite. An extensive review of their microstructures and properties was recently published by Krauss [1]. The mean orientation relationship (OR) of martensite with its parent face centered cubic (fcc, γ) austenite is close to Nishiyama-Wasserman (NW) [2, 1, 3], or in-between NW and Kurdjumov-Sachs (KS) [4], i.e. close to Kelly [5] or Greninger-Troiano (GT) [6]. The study of martensitic laths by optical microscopy is difficult because of their fine and highly intricate structures, and because in most of the low-carbon steels the martensitic transformation is complete and there is no retained austenite. Despite these difficulties, Marder and Krauss [7] elegantly took advantage that the long straight lines visible in metallography are twin boundaries of prior parent austenitic grains to calculate their orientations and statistically determine the habit planes of martensite in the austenite reference frame; and they found that they are close to $\{557\}_{\gamma}$. Then, transmission electron microscopy (TEM) allowed them and other researchers to observe martensite at higher scales [8]-[13] revealing complex structures. Hoekstra [9] used the same method as Marder and Krauss to determine the orientation of the prior austenitic grains, but in addition to the optical microscopy images, he could succeed in preparing some TEM lamellae of the same features, which allowed him to determine the indices of the habit planes in the martensite reference frame. It was concluded that the habit planes are close to $\{569\}_{\gamma} \parallel \{2710\}_{\alpha}$. Sandvik and Wayman [10] noticed that some laths exhibit an exact KS OR, but only locally, and in general the OR deviates from KS toward NW [10]. We recall here that the KS OR is a double parallelism rule: one for the close-packed planes (CPP) $\{111\}_{\gamma} \parallel \{110\}_{\alpha}$,

and one for the close-packed directions (CPD) $\langle 110 \rangle_\gamma \parallel \langle 111 \rangle_\alpha$. Sandvik and Wayman also confirmed that the habit planes are the $\{557\}_\gamma$ planes that are 9.4° far from the common CPP. They could not experimentally determine whether or not the habit plane contains the common CPD, but they inferred it from Hoekstra's study [10], and they concluded that the habit planes are $\{557\}_\gamma \parallel \{145\}_\gamma$. Over the last two decades, the coupling of TEM with Electron Back Scatter Diffraction (EBSD) has allowed the get a better idea of the structure of martensite at different scales [12, 13]. It is now established that the laths are grouped into four packets on the $\{111\}_\gamma \parallel \{110\}_\alpha$ CPPs. These packets are sometimes called morphological packets [14], or CPP packets [15]. Although the KS OR is only local, it was admitted for sake of simplicity that the twenty-four lath variants can be indexed as KS variants. Morito et al. [12, 13] showed that each packet contains six KS variants grouped by pairs of low-misoriented variants, called "blocks". The two KS variants in a block are linked by a rotation of 10.5° around the normal to the $(111)_\gamma \parallel (110)_\gamma$ plane [15]. An example of pair of KS variants forming a block is $(\alpha_1^{KS}, \alpha_6^{KS})$ marked by the blue ellipse in Fig. 7.1a. Examples of other pairs are $(\alpha_2^{KS}, \alpha_3^{KS})$, $(\alpha_5^{KS}, \alpha_8^{KS})$, $(\alpha_7^{KS}, \alpha_9^{KS})$, $(\alpha_4^{KS}, \alpha_{12}^{KS})$, $(\alpha_{11}^{KS}, \alpha_{14}^{KS})$. It was also confirmed that the habit planes of the laths are the $\{557\}_\gamma$ planes that contain the dense direction $[\bar{1}10]_\gamma \parallel [1\bar{1}1]_\alpha$, and they are more precisely $(557)_\gamma \parallel (561)_\alpha$ [13]. In the present paper, the variants will be also indexed as KS variants, and the KS OR chosen for variant α_1 is $(111)_\gamma \parallel (110)_\alpha \& [\bar{1}10]_\gamma = [1\bar{1}1]_\alpha$ as shown in Fig. 7.1a. The six variants in the crystallographic packet $(111)_\gamma \parallel (110)_\alpha$ are represented in Fig. 7.2. Please note that the indices of the variants used in this work are different from those chosen by Morito et al. [12, 13] because the variants are not calculated in the same way (we used an algebraic coset decomposition detailed in Ref. [16]); the variants $(\alpha_1^{KS}, \alpha_6^{KS})$ were noted $(\alpha_1^{KS}, \alpha_4^{KS})$ by Morito et al. Also notice that the blocks are written in the figure as NW variants, for example the block (α_1, α_6) is noted α_1^{NW} (Fig. 7.1b and Fig. 7.2); this will be justified in the next sections. As Marder and Krauss [7] used optical microscopy, it is probable that they observed the blocks and not the laths. So, one can infer that that the blocks, as the laths, are made of $\{557\}_\gamma$ planes. However, a logical problem seems to emerge when one wants to define a habit plane to the blocks. For example, if the block α_1^{NW} formed by the variants α_1 and α_6 is considered; the two variants share the common $(111)_\gamma \parallel (110)_\alpha$ CPP plane but do not share a CPD. The CPD for α_1 is indeed $[1\bar{1}0]_\gamma \parallel [1\bar{1}1]_{\alpha_1}$, and that of α_6 is $[0\bar{1}1]_\gamma \parallel [1\bar{1}1]_{\alpha_6}$, as represented by the bold black lines in Fig. 7.1b. This means that the habit plane of the laths α_1 is $(557)_\gamma$ and that of the laths α_6 is $(755)_\gamma$. Therefore, one can wonder: could a habit plane be attributed to the block α_1^{NW} , and if the answer is positive what would it be, $(557)_\gamma$ or $(755)_\gamma$? One could imagine a symmetric configuration in which the habit plane of the block could be the $\{575\}_\gamma$ plane that does not contain any of dense directions of the two KS variants, as illustrated in Fig. 7.3a. This hypothesis would imply that the habit plane of a block is none the habit plane of the two variants it contains. Krauss proposed another hypothesis in which the habit plane of one of the two variants dominates the block morphology [17], i.e. the habit plane of the block is either $(557)_\gamma$ or $(755)_\gamma$. As there are two possibilities for each of the three blocks in a packet, eight configurations are possible; one is illustrated in Fig. 7.3b. However, the TEM images in Ref. [8, 13] show that the variants are in equal proportions. In addition, if one of the two variants were really dominant in its block, it should be highly elongated along

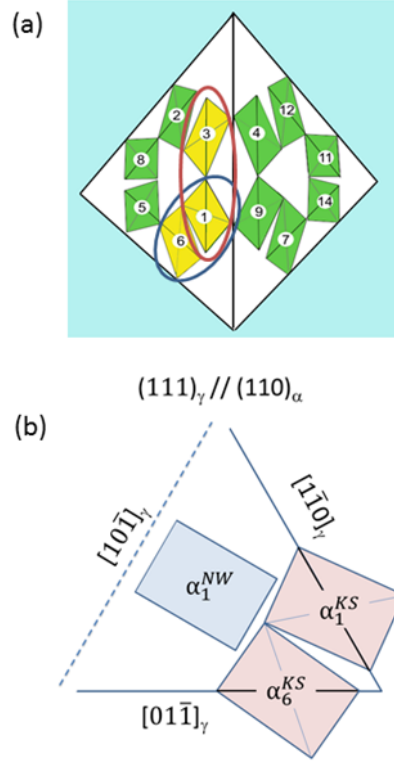


Figure 7.1: Schematic representation of the KS and NW variants. (a) 3D view with the $\{111\}_\gamma$ faces forming a regular pyramid, and the $\{110\}_\gamma \parallel \{111\}_\gamma$ planes of the 24 KS variants represented by the rectangles. The KS OR imposes that for each variant a close-packed $\langle 111 \rangle_\alpha$ direction is parallel to a $\langle 110 \rangle_\gamma$ direction, i.e. a diagonal of the rectangle is parallel to an edge of pyramid. The packets are formed by the 6 variants lying on the same $\{111\}_\gamma$ face. The special twin-related pairs and the blocky pairs are colored in yellow, and marked by the red and blue ellipses, respectively. (b) Planar view of the packet $(111)_\gamma \parallel (110)_\alpha$ plane showing one block constituted of the KS variants α_1^{KS} and α_6^{KS} , with the average block orientation noted by α_1^{NW} .

its CPD because this direction would be also contained in the habit plane of the block, whereas the second variant should be very short; which was not observed. A third hypothesis can be made: the morphology of the blocks is not a mere plate, but is a complex bifoliate structure made of the two $\{575\}_\gamma$ planes of the two lath variants constituting the blocks, as illustrated in Fig. 7.3c. The three hypotheses can be distinguished by observing the morphologies of the blocks and laths and by indexing the habit planes simultaneously in the austenite and martensite reference frames. Let us consider the three planes $\{557\}_\gamma$ that are at 9.4° far from the common CPP $(111)_\gamma \parallel (110)_\alpha$ of the packet. By using the Bain correspondence related to the variant α_1^{KS} , it can be shown that $(557)_\gamma$ and $(755)_\gamma$ correspond to $\{156\}_{\alpha_1}$ planes, while $(575)_\gamma$ corresponds to a $\{570\}_{\alpha_1}$ plane. Only the first plane, i.e. the $(557)_\gamma$ plane, contains the unrotated CPD $[\bar{1}10]_\gamma = [1\bar{1}1]_{\alpha_1}$. The $(755)_\gamma$ plane is also transformed into a $\{156\}_{\alpha_1}$ plane, but the KS distortion induces a rotation of the second CPD $[01\bar{1}]_\gamma$ and a slight rotation of the plane.

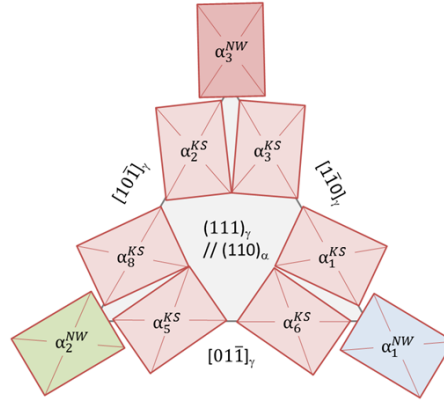


Figure 7.2: Schematic view of a packet with the three blocks constituted by pairs of KS variants. The rectangles are the $(110)_\alpha$ planes of the KS variants that are parallel to the $(111)_\gamma$ plane. The average orientation of a block is noted by the average orientation between the two KS variants (it will be shown that it is a NW OR). The blocks α_1^{NW} , α_2^{NW} , α_3^{NW} are constituted of the pairs α_1^{KS} - α_6^{KS} , α_5^{KS} - α_8^{KS} , α_2^{KS} - α_3^{KS} , respectively.

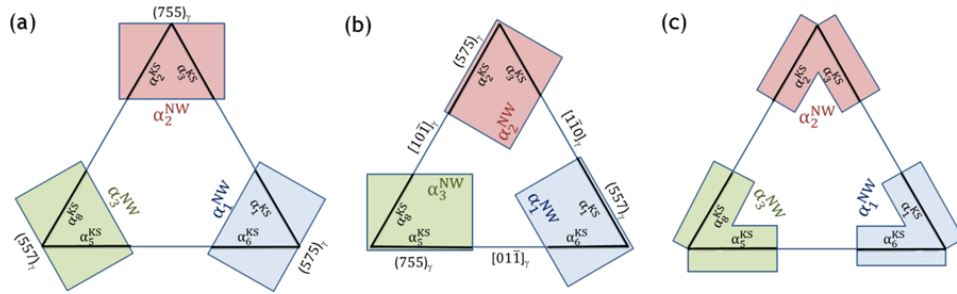


Figure 7.3: Three hypotheses for the morphologies of the blocks. (a) The habit plane of the block is the one of the three $\{557\}_\gamma$ planes that is at 9.4° from the $(111)_\gamma$ plane but is none of the habit planes of two variants; for the block α_1^{NW} it would be the plane $(557)_\gamma \parallel \{750\}_{\alpha_1} \parallel \{750\}_{\alpha_6}$. (b) The habit plane of a block is the $\{557\}_\gamma$ habit plane of one of the two lath variants constituting the block; for the block α_1^{NW} , it can be for example the plane $(557)_\gamma \parallel \{156\}_{\alpha_1}$. (c) The blocks are not plates but have a complex bifoliate morphology made of the two $\{557\}_\gamma$ habit planes of the lath variants.

Consequently, in case (a) the habit plane of the block α_1^{NW} would be $(557)_\gamma \parallel \{750\}_{\alpha_1} \parallel \{750\}_{\alpha_6}$; in case (b) it would be the $\{557\}_\gamma$ habit plane of one of the two lath variants constituting the block, for example the plane $(557)_\gamma \parallel \{156\}_{\alpha_1}$; in case (c) the block would be made of the two $\{557\}_\gamma$ habit planes of the lath variants $(557)_\gamma \parallel \{156\}_{\alpha_1} + (755)_\gamma \parallel \{156\}_{\alpha_6}$. The EBSD and TEM experimental work that will be presented in the first part of the paper aims at getting a better idea of the structure of the blocks and laths and at determining which of the hypothesis (a), (b) or (c) is correct.

7.1.2 Theoretical models for the $\{557\}_\gamma$ habit planes

From a theoretical point of view, the complexity of lath martensite remains in great part unsolved. The phenomenological theory of martensitic crystallography (PTMC) has failed to explain the $\{557\}$ habit planes, at least in its early versions of 1953-54 [18, 19], and it was nearly forty years later, in 1992, that Kelly [20] used the double-shear version of the PTMC initially developed by Ross and Crocker [21] in order to make the theory more compatible with the experimental results. He used “floating” lattice invariant shear (LIS) systems with, for first LIS, shears of type $(hhl)[1\bar{1}0]_\gamma$ where the $(hhl)_\gamma$ planes varied from $(00\bar{1})_\gamma$ to $(110)_\gamma$, and for second LIS, shears on planes between $(311)_\gamma$ and $(3\bar{1}\bar{1})_\gamma$. He noticed that lath martensite with a habit plane close to $\{557\}_\gamma$ can be formed with at least 35 different combinations of LIS. Kelly’s double shear version of PTMC was used by Lambert-Perlade et al. [1] and Morito et al. [13] to discuss their EBSD results. They respectively chose $(\bar{2}31)[11\bar{1}]_\alpha$ & $(211)[1\bar{1}\bar{1}]_\alpha$ and $(112)[1\bar{1}\bar{1}]_\alpha$ & $(110)[1\bar{1}\bar{1}]_\alpha$, as double LIS systems. More recently, Iwashita et al. [22] used a PTMC version developed by Khachaturyan [23] with $(\bar{1}01)[101]_\gamma$ & $(101)[\bar{1}01]_\gamma$ double-slip, and they adjusted the magnitude of shear on both planes to obtain results close to the experiments, i.e. an habit plane close to $\{557\}_\gamma$ and an orientation relationship close to KS. Later, Qi, Khachaturyan and Morris [24] followed a similar approach and explored all the combinations related to simple and double slips with the variants chosen among the twenty-four KS variants and slips chosen among seventy-two systems. They tested more than 23’000 possibilities and concluded that the choice that gives a solution close to the experimental results is the composite case of two KS variants sharing the same Bain axis, and more precisely the variants forming a block. A recent model also based on double shears but without free parameters except the choices of the shears was recently proposed by Koumastos and Muehleman [25]. Kelly [20] states that the “double shear version of the phenomenological theory [...] explains ALL the known crystallographic characteristics of lath martensite” (sic); however, to our point of view, the trial-and-error method and the high degree of freedom given to the LIS significantly reduce the “predictive” or “explicative” character of these PTMC approaches. Any theory should be evaluated by the outputs/inputs ratio. Another point should be mentioned. From the calculated amplitude of the LIS, Kelly predicted that the dislocation spacing should be close to 4 nm, and concluded that this value was in excellent agreement with the experimental TEM observations of dislocations at austenite/martensite interfaces made by Sandvik and Wayman [11], but doubts exist on the real nature of the TEM contrasts observed at the interfaces ¹.

¹An important issue can be raised here. The closely spaced parallel black lines shown in Ref. [11] were assumed to be interfacial dislocations, and the possibility that they could be Moiré fringes was quickly discarded by Sandvik and Wayman. However, the nearly perfect regularity of the fringes is puzzling, even for dislocation arrays; and if they were dislocations, they would be too close to be resolved by TEM because their deformation fields would overlap. Consequently, legitimate doubts can be raised on the interpretation of the lines. Thölen [26] showed by TEM simulations that dislocations and Moiré fringes are indistinguishable when their spacing is less than one extinction distance (typically 20-50 nm), which is clearly the case for the lines observed in Ref. [11]. The risk of confusion was also raised by Waitz and Karnthaler [27], and some authors show that similar regularly and closely spaced lines visible in TEM at the interfaces are actually Moiré fringes [28, 29]. Moreover, even if one accepts that such lines are interfacial dislocations, then one should at least admit that they are not specific of displacive phase transformations because they are observed at the interfaces of massive phase transformation products [29], and at low-angle boundaries and special boundaries of stainless steels and aluminum alloys [30, 31, 32]. The

For the last years, we have developed an alternative model to PTMC [33]-[36]. The analytical forms of the atomic displacements and lattice distortion were determined by considering the iron atoms as hard-spheres of constant size, and the OR was the unique input [35, 36]. The $\{225\}_\gamma$ habit plane simply emerged as an eigenvalue of the reciprocal distortion matrix, i.e. as an untilted plane [35, 37], and this plane could be rendered fully invariant by combining the two twin-related KS variants in a packet sharing a common CPD $[\bar{1}10]_\gamma \parallel [1\bar{1}1]_\alpha$ [38] (marked by the red ellipse in Fig. 7.1a). In the theoretical part of the paper, it will be shown that the average distortion of the two KS variants in a block, i.e. the mean distortion of a block, is a NW distortion, and one of the three $\{557\}_\gamma$ planes close to the CPP is untilted by this distortion. This plane does not contain the common CPD of any of the two KS variants. In the example of the block α_1^{NW} , the plane untilted by the NW distortion will be shown to be the $(575)_\gamma$ plane. This plane will be shown to be an interface of good compatibility for one of the two laths in each of the two other blocks in the packet. A qualitative representation of the morphology and crystallography of the lath/block structure in a packet will be proposed.

7.2 Method

The steels investigated in this work are a 1018 steel, a 8Cr-1W (Eurofer) steel and a 9Cr-1Mo (EM10) steel chosen for their low carbon contents ($< 0.2\%$). Their compositions are given in Table 1. The steels were cut, sealed in a quartz tube under vacuum, heat treated at 1000°C for one hour, and water quenched. For the three steels under study, the only phase that could be identified is the bcc phase; there was no retained austenite.

Some TEM lamellae were prepared in the as-quenched 1018 steel by mechanical grinding and polishing down to 100 microns, punching disks at a diameter of 3 mm, and electropolishing with a Tenupol (Struers) machine with the electrolyte A2 at -15°C . The TEM lamellae were observed on an OSIRIS (FEI) TEM microscope working at 200 kV. The samples were positioned in a screw-tightened sample holder in order to maintain them firmly in position and impede that they get stuck on the magnetic lens. The TEM images and the selected area diffraction (SAED) patterns were acquired on Gatan Orius 4k x 2.6k CCD camera. The 90° rotation angle between the diffraction and image modes at medium and high magnifications were corrected by rotating the SAEDs. We have spent time on the microscope to find three or four different variants of neighborhood martensite in diffraction conditions in order to be able to calculate the orientation of their prior austenitic grains. The zone axes of the experimental SAEDs of the martensitic laths were manually indexed, and the zone axis of austenite was calculated by using the software GenOVa (Generation of orientational variants). GenOVa was also used to simulate the theoretical SAED patterns of the variants and compare them with the experiments [39]. A new functionality was also created; it plots the traces of the habit planes expected from the simulated SAEDs in the experimental TEM images. A snapshot of this option is reported in Supplementary Material S1 (appendix B).

validation of the double-shear PTMC for low carbon alloys by using TEM features that could be Moiré artifacts can be questioned.

All the steels in Table 1 have been studied by EBSD. The samples were polished down to 1 micron and electropolished at room temperature at 20 V with the electrolyte A2 of Struers. The EBSD maps were acquired with a XLF30 (FEI) scanning electron microscope (SEM) equipped with a Nordlys 2 camera and Aztec (Oxford Instruments) software. The acceleration voltage was 20 kV, the magnifications were chosen quite low (x500, x650 and x1200), and the step sizes were 0.1 or 0.3 μm . The indexation rates of the EBSD maps acquired in the present work were between 65% and 75%, and all the maps have been dilated in order to remove the unindexed pixels and put in contact the neighboring grains. These rates are quite low, but they are usual for as-quenched steels because of the high densities of dislocations and subgrain boundaries. The software ARPGE (Automatic Reconstruction of Parent Grains) was used to automatically reconstruct the prior parent grains and determine their orientations [40]. An angular tolerance of 5° was chosen to identify the daughter bcc grains; the GT OR was used for the reconstruction, with tolerance angles starting at 3° (“nucleation” step) and increasing up to 15° (“growth” step). After reconstruction, the orientations of the parent grains were used to automatically index the bcc grains as if they were KS variants and identify the crystallographic CPP packets. The validity of the reconstruction was checked by plotting the pole figures (PF) of the daughter bcc grains for some prior austenitic grains. These pole figures usually exhibit special continuous features, such as circles and small two-fold bow ties in the $\langle 100 \rangle_\alpha$ PFs, three-fold stars and four-fold crosses in the $\langle 110 \rangle_\alpha$ PFs, and large two-fold bow ties in the $\langle 111 \rangle_\gamma$ PFs. Examples of such features are given in Ref. [33, 34]. The $\langle 100 \rangle_\gamma$ reconstructed directions should appear in the centers of the $\langle 100 \rangle_\alpha$ circles, the $\langle 111 \rangle_\gamma$ directions should be in the centers of the $\langle 110 \rangle_\alpha$ three-fold stars, and the $\langle 110 \rangle_\gamma$ directions in the middles of the $\langle 111 \rangle_\alpha$ bow ties. The angular resolution of the reconstruction method is in the range of 2 to 5° depending on the quality of the EBSD maps, the internal misorientations of the austenitic grains before transformation, and the presence of twins in the prior grains [40]. A simulation that illustrates the correspondence between the $\langle 111 \rangle_\gamma$ and $\langle 110 \rangle_\alpha$ directions is given Fig. 7.4. The continuous PF features are a sign of the continuity between the Pitsch,

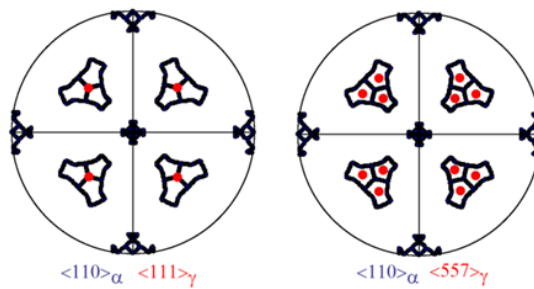


Figure 7.4: Simulated pole figures of the three-fold stars made by the directions $\langle 110 \rangle_\alpha$ of the 24 variants with OR spreading from KS to NW (see Ref. [33] for details), with (a) the $\langle 111 \rangle_\gamma$ parent directions, and (b) the $\langle 557 \rangle_\gamma$ parent directions.

KS and NW ORs that come from internal gradients; and, to our point of view, they should be considered as a plastic trace of fcc-bcc distortion mechanism [33, 34, 35]. Note that these gradients make very difficult the distinction between the low-misorientation operators O_3

(10.5° around $\langle 111 \rangle_\alpha$) and O_5 (10.5° around $\langle 110 \rangle_\alpha$) that link the variants $\alpha_1^{KS} - \alpha_4^{KS}$ and $\alpha_1^{KS} - \alpha_6^{KS}$, respectively (Fig. 7.1). A special module has been developed in the software ARPGE to draw the traces of some expected habit planes. This new functionality allows plotting the traces of the equivalent planes $\{hkl\}_\gamma$ for all the parent grains, and the traces of the planes $(hkl)_\alpha$ that are parallel to a fcc plane of type $\{hkl\}_\gamma$ (within a certain tolerance angle) in each bcc grain. An example is given in Supplementary Material S2 for the case of an iron-nickel meteorite (appendix B); it shows that the traces of the bcc $\{110\}_\alpha$ planes of kamacite that are parallel to a $\{111\}_\gamma$ plane of fcc taenite are in good agreement with the morphology of the kamacite plates, as expected for octahedrites. In the paper, this functionality will be used to check which of the hypotheses (a), (b) or (c) in Fig. 7.3 is experimentally observed.

7.3 Experiment

7.3.1 TEM observations

According to Morito et al. [12, 13], the habit planes of the laths are those that contain the dense direction without rotation of the CPD, i.e. $(557)_\gamma \parallel \{156\}_\alpha$. The TEM observations presented in this section are in full agreement with Morito's result. An example is given in Fig. 7.5 with the as-quenched 1018 steel. In the observed area, four different SAED patterns of laths noted K, L, M and N could be found and indexed in the same tilt conditions (Fig. 7.5b), i.e. without tilting the TEM lamella. The orientation of their parent austenitic grain could be unambiguously determined, and then the SAED patterns could be perfectly simulated (Fig. 7.5c). They are associated with the variants $\alpha_{12}^{KS}, \alpha_{14}^{KS}, \alpha_{15}^{KS}$ and α_{24}^{KS} , respectively. The operators (misorientations between the variants) related to the variants $\alpha_{12}^{KS}, \alpha_{14}^{KS}, \alpha_{15}^{KS}$ and α_{24}^{KS} can be found in the Supplementary Material 3 of Ref. [34]. The zone axes of the SAEDs were identified to $[1\bar{1}3]_{\alpha_{12}}, [1\bar{1}0]_{\alpha_{14}}, [\bar{5}13]_{\alpha_{15}}$ and $[\bar{1}31]_{\alpha_{24}}$, respectively. The zone axis of the austenitic grain is $[112]_\gamma$. The laths K and L belong to the same packet and are closely interlaced, but note that they do not form a block because the angle between the zone axes is too high. The laths M and N belong to two other distinct packets. The traces of the habit planes of the four laths were simulated with GenOVa by testing two possibilities:

$$(a) \{557\}_\gamma \parallel \{057\}_\alpha \quad \text{or} \quad (b) \{557\}_\gamma \parallel \{156\}_\alpha \quad (7.1)$$

within a tolerance of 3° for both conditions. Please note that condition (a) corresponds to the hypothesis (a) of Fig. 7.3, and condition (b) would agree with hypothesis (b) or (c) of Fig. 7.3. For each of the two conditions, two planes are generally found, but only the one in best agreement with the morphology will be shown. This best fit is obtained with the condition (b), as shown in Fig. 7.5d. The habit planes of the laths K, L, M and N are $(57\bar{5})_\gamma \parallel (561)_{\alpha_{12}}, (75\bar{5})_\gamma \parallel (561)_{\alpha_{14}}, (\bar{7}55)_\gamma \parallel (561)_{\alpha_{15}}, (5\bar{5}7)_\gamma \parallel (561)_{\alpha_{24}}$, respectively. These results agree with Morito's observations; the habit planes of the laths are the $\{557\}_\gamma$ planes that are at 9.4° far from the common CPP, and they contain the common CPD by the KS OR. Another area close to that of Fig. 7.5 and observed with the same sample tilt angles is shown in Fig. 7.6. The two

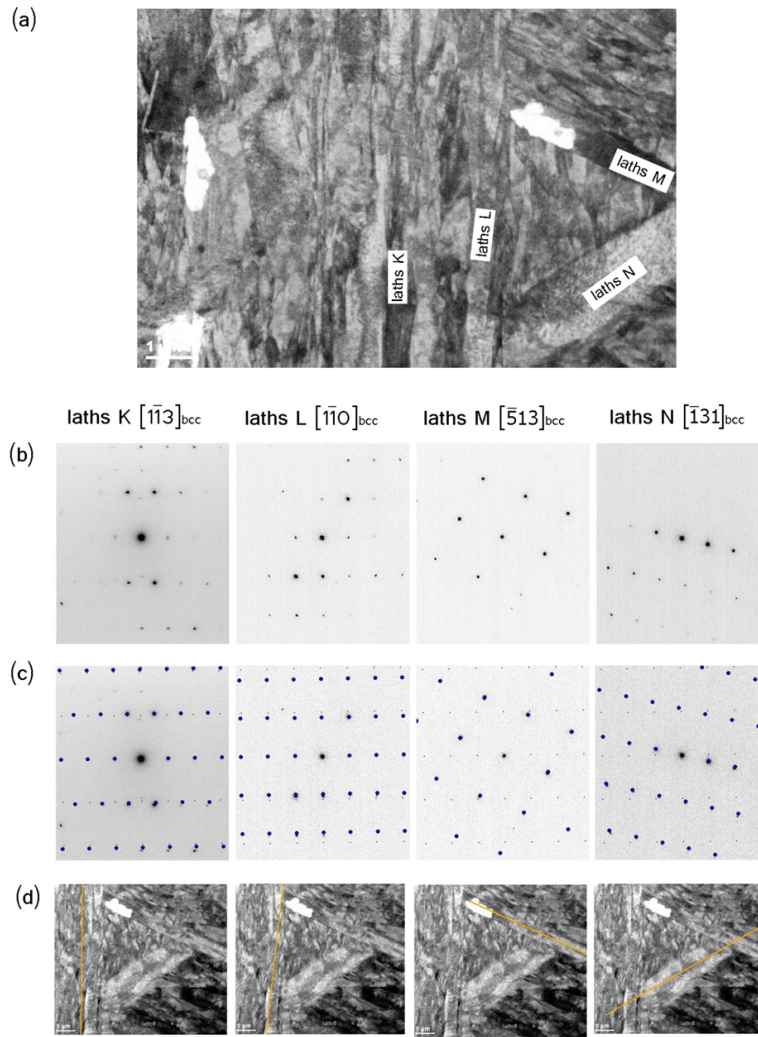


Figure 7.5: TEM image and diffraction patterns of an assembly of martensite laths in the as-quenched 1018 steel. (a) Bright field image showing the laths noted K, L, M, N. (b) Experimental SAEDs obtained with an identical sample tilt for the four laths. (c) Simulated SAEDs overlapped on the experimental SAEDs. (d) Simulated traces of the habit plane $(557)_{\gamma} \parallel \{156\}_{\alpha}$ expected from the orientations of the laths (yellow lines). Note that the small grey dots in the SAEDs in the line (c) are those simulated for the $[112]_{\gamma}$ zone axis of the prior parent austenitic crystal; they do not appear in the experimental SAEDs of line (b) because there is no retained austenite.

martensitic variants, noted E and F, constitute a block. Note that the SAED of laths E in Fig. 7.6b is the same as that of lath N in Fig. 7.5b, and their habit planes are parallel. The main difference between them is that the lath N is large and isolated whereas the laths E are finer and interlaced with the other laths F of the block. It is concluded that the laths E and F are variants of the same parent austenitic grain oriented along the zone axis $[112]_{\gamma}$ as for the laths K, L, M and N,. The SAED of laths F is slightly misorientated from that of laths E, as shown by its weaker intensities. Here again, it could be checked that the habit plane of the laths agrees

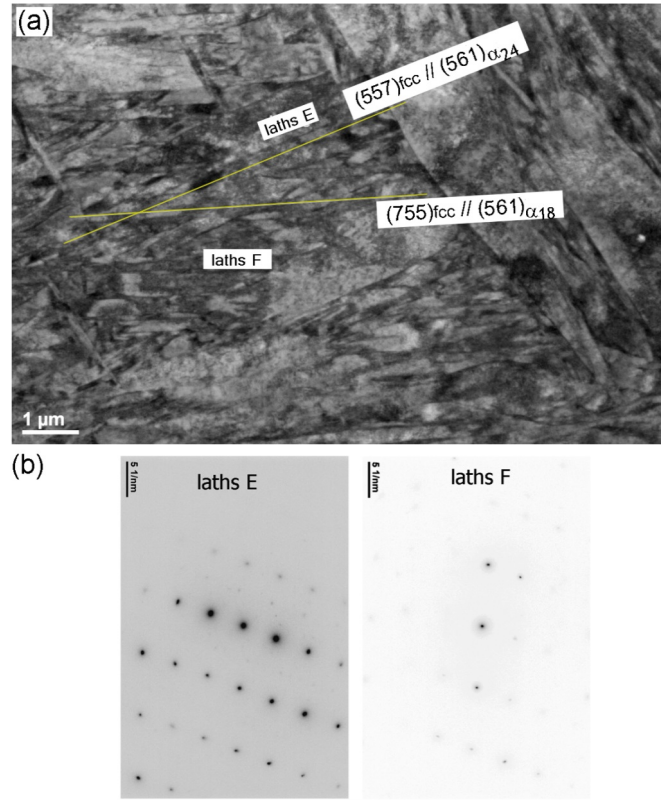


Figure 7.6: TEM image and SAED patterns of a pair of intricate laths belonging to the same block in the as-quenched 1018 steel. The SAEDs were acquired in the same sample tilt condition and in a zone close to that of Fig. 5. (a) Bright field image showing the laths noted E and F, with in yellow the traces of the habit planes $(557)_\gamma \parallel \{156\}_\alpha$ simulated from the SAEDs. (b) Experimental SAEDs that were used to plot the expected traces.

with Morito's observations: the habit plane of the laths E is $(5\bar{5}7)_\gamma \parallel (561)_{\alpha_{24}}$, and that of laths F is $(7\bar{5}5)_\gamma \parallel (561)_{\alpha_{18}}$.

7.3.2 EBSD observations

The TEM results confirm that the habit planes of the laths are the planes $(557)_\gamma \parallel \{156\}_\alpha$. The question about the morphology of the blocks introduced in section 1.1 remains however unanswered for the moment because of the limited field of view of the TEM observations. The technique EBSD is more appropriate to study the blocks and the packets because of its larger fields of view. In order to compare the three hypotheses schematized in Fig. 7.3, four EBSD maps were acquired at low magnifications on each of the low-carbon steels reported in Table 1.

The EBSD data were treated with ARPGE. The prior austenitic grains were reconstructed, and their orientations calculated. In each parent grain, the martensitic grains were indexed as KS

Table 7.1: Chemical composition of the three low-carbon steels used in the study

| wt-% | Cr | Mo | W | C | N | V | Ni | Si | Mn | Ta |
|---------|-----|-----|------|-------|------|------|------|------|-----|-----|
| 1018 | - | - | - | 0.18 | - | - | - | - | 0.8 | - |
| Eurofer | 9.0 | - | 1.04 | 0.109 | 0.02 | 0.18 | 0.07 | 0.04 | 0.5 | 0.1 |
| EM10 | 8.8 | 1.1 | - | 0.096 | 0.02 | 0.03 | 0.18 | 0.37 | 0.5 | - |

variants, and their habit planes have been studied by testing the possibilities (a) and (b) of equation 7.1 within a tolerance of 3° for both conditions. The two cases were evaluated by comparing the traces of the predicted habit planes with the morphologies of the bcc grains visible in the EBSD maps. All the maps were treated automatically with the same parameters. An example of analysis is given for the as-quenched 1018 steel in Fig. 7.7. First, the initial

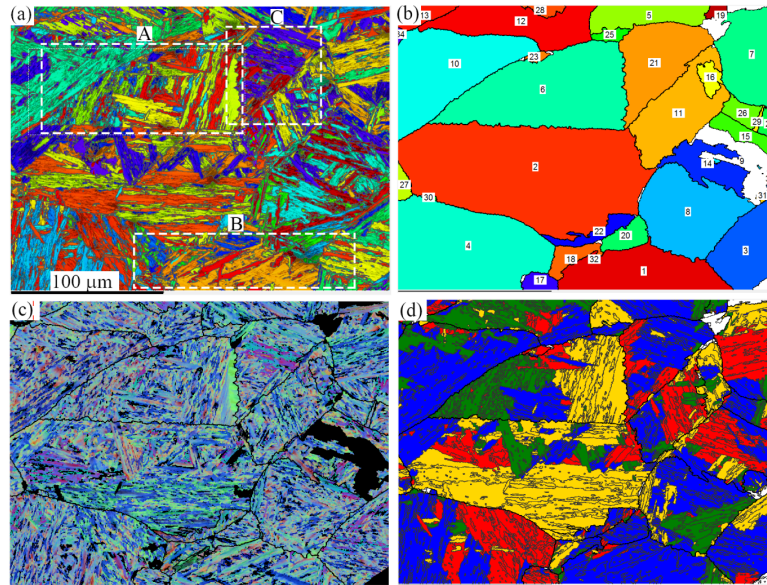


Figure 7.7: EBSD map of the as-quenched 1018 steel. (a) Daughter bcc grains, (b) reconstructed austenitic grains, (c) orientation gradients in the bcc grains in RGB colors (Red = Pitsch, Green = KS, Blue = NW), (d) CPP packets in each prior austenitic grains represented with four colors.

EBSD map of the martensitic grains (Fig. 7.7a) is used to reconstruct the prior fcc austenitic grains (Fig. 7.7b), then the bcc martensitic grains are indexed as KS variants, and their internal misorientations ranging from KS to NW are colored in Fig. 7.7c with a RGB code (Red = Pitsch, Green = KS and Blue = NW) as described in Ref. [15]. This method also allows the quantification of the ratios of the Pitsch, KS, NW and GT ORs. The results for all the steels are presented in Table 2; they are very close, which confirms that a majority of pixels in the blocks have ORs close GT/NW.

The histograms of disorientations are reported in Supplementary Material S3 (appendix B). By plotting the rotation axes related to the misorientation angle, one can notice that the 60°

Table 7.2: Surface percentage of the different orientation relationships (ORs) determined from the analysis of the EBSD maps. An error bar of 15% of these numbers is roughly estimated from the different measurements.

| OR | Pitsch | KS | NW | GT |
|---------|--------|-----|-----|-----|
| 1018 | 3% | 22% | 44% | 31% |
| Eurofer | 7% | 25% | 34% | 34% |
| EM10 | 8% | 29% | 30% | 33% |

misorientations are split into two groups: $(60^\circ, <110>_\alpha)$ and $(60^\circ, u)$ with the axis u being at 3° from the $<111>_\alpha$ axis. This distribution of operator axes was satisfactorily simulated with GenOVa with the GT OR (not detailed here). In each prior austenitic grain, the four CPP packets are identified and arbitrarily colored in blue, yellow, red and green (Fig. 7.7d). The quality of the parent grain reconstruction is checked by plotting in stereographic pole figures the experimental orientations of the martensitic grains with the calculated orientations of the austenitic grains they are inherited from, and then by checking that they correspond to the theoretical pole figures, such as those presented in Fig. 7.4. The traces of the planes according to the condition (a) or (b) were also automatically plotted in all the bcc grains of the map; the results are shown in Fig. 7.8a and Fig. 7.8b, respectively. Whatever the condition (a) or (b), in general two possible habit planes are found within a tolerance angle of 3° , as already noticed for the TEM analyses. One can acknowledge that for condition (b), one of the two traces generally fits very well with the long direction of the blocks. A good fit is more frequently observed with the condition (b) than with condition (a), it is obtained roughly at 70% in condition (b) and only at 20% in condition (a). The EBSD maps acquired in the other as-quenched steels lead to same results. They represent more than fifty prior austenitic grains and approximatively three hundreds blocks. Two of these maps are reported in Supplementary Material S4 (appendix B). We conclude that condition (b) is statistically more relevant than condition (a); i.e. the habit plane of a block generally follows the same condition as that of one of the two lath variants from which it is constituted, i.e. $\{557\}_\gamma \parallel \{156\}_\alpha$ with α being one of the two KS variants of the block. In a second stage, we put our attention on the 30% of blocks of bad fits, and more particularly on those located in the zones A and B marked by the dashed rectangles in Fig. 7.7a and corresponding to the prior parent grains PG6 and PG21, respectively. It was found that all the blocks analyzed in these two zones have for habit plane(s) some of the twelve $\{557\}_\gamma$ planes (Fig. 7.9a,b), but not necessarily following the condition (a) or (b). This was checked by plotting all the twelve $\{557\}_\gamma$ planes in the prior austenitic grains, and by manually translating those parallel to the long directions of the block. The fit was always very good, within a tolerance better than 5° . We conclude that the habit planes of the block exhibit $\{557\}_\gamma$ interfaces, even when the condition (b), i.e. $\{557\}_\gamma \parallel \{156\}_\alpha$ is not fulfilled. The zone C is the unique exception among all the EBSD maps acquired in this study; none of the twelve $\{557\}_\gamma$ traces fit with the elongated directions of the blocks. We plotted the traces of other families of habit planes usually reported in literature, and found that among them a good agreement was obtained with the $\{225\}_\gamma$ planes.

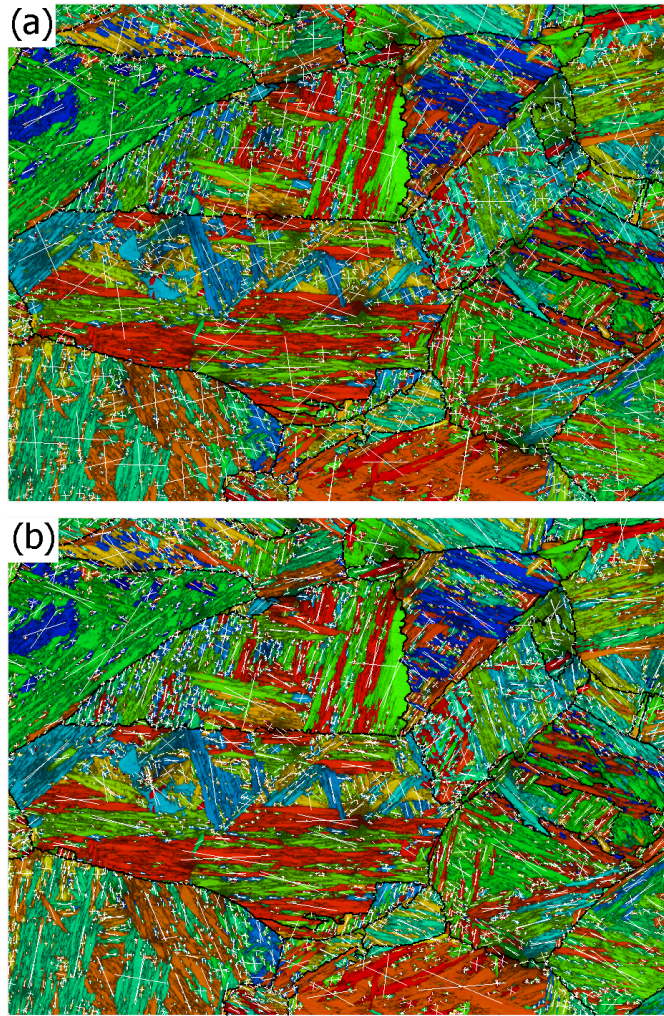


Figure 7.8: Determination of the habit planes in the EBSD map of Fig. 7.7 by automatically plotting for all the bcc grains (a) the traces of the planes $\{057\}_\alpha \parallel \{557\}_\gamma$, and (b) the traces of the planes $\{156\}_\alpha \parallel \{557\}_\gamma$. The agreement between the traces and the morphology is perfect for none of the two cases, but more often better in the case (b).

From these EBSD analyses, it is concluded that the majority of blocks have a $\{557\}_\gamma$ habit plane that is the same as one of its two lath variants. Therefore, case (a) of Fig. 7.3 is excluded, and cases (b) or (c) remain possible. Due to the sectioning effect at the surface and the fact the two $\{557\}_\gamma$ habit planes in case (c) have a low misorientation (16°), cases (b) and (c) are difficult to distinguish from each other. Thus, to get a better idea of the block morphology, we focused our attention on the blocks located in the parent grains orientated close to a direction $\langle 111 \rangle_\gamma$ because in such an orientation one the four packets is parallel to the surface, and the habit planes of the laths in this packet are nearly viewed flat. Such a parent grain was identified for example at the bottom of the zone B of the EBSD map of Fig. 7.7a. The two laths in orange in Fig. 7.9b form a block, their habit planes were indexed as $(755)_\gamma$ and $(575)_\gamma$ and they obey the condition $\{557\}_\gamma \parallel \{156\}_\alpha$. This configuration fit well with a bifoliate morphology schematized

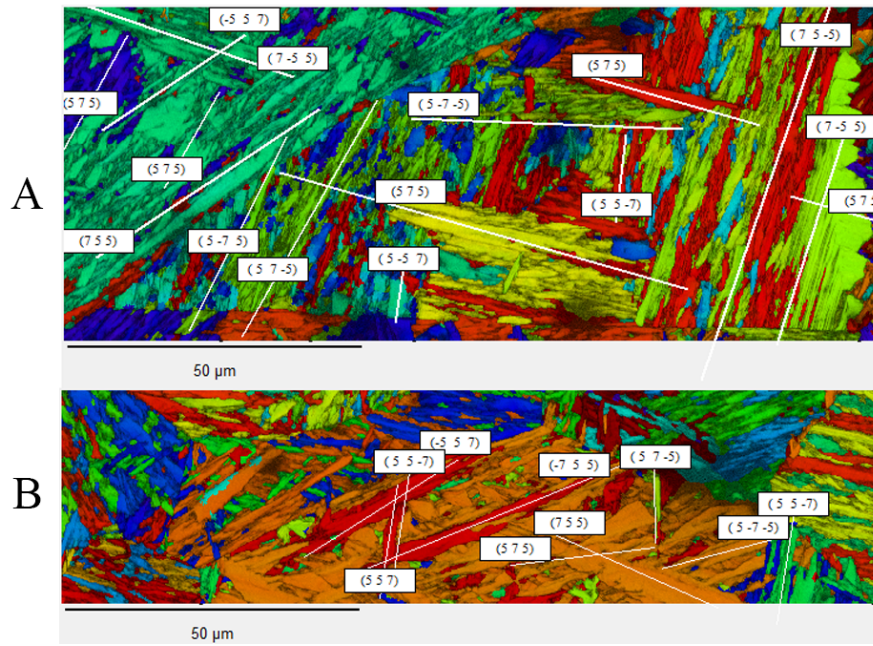


Figure 7.9: Regions A and B of the EBSD map of Fig. 7.7 (corresponding to PG6 and PG1, respectively). Traces of the $\{557\}_\gamma$ planes that fit with the morphology of the blocks even if none of the conditions $\{057\}_\alpha \parallel \{557\}_\gamma$ or $\{156\}_\alpha \parallel \{557\}_\gamma$ is fulfilled

in Fig. 7.3c. Another prior austenitic grain orientated close a direction $\langle 111 \rangle_\gamma$ direction was identified in the center of the EBSD of Fig. 7.10. The blocks at the corners of the map form a triangle because they belong to three sectioned packets, but the brown and blue blocks in the center of the map and marked by the white arrows are viewed as plates because they belong to the fourth packet that is nearly flat-on. The brown block appear as made of two plates, one is on the $(\bar{5}57)_\gamma$ plane and is flat, and the another one is on the $(55\bar{7})_\gamma$ plane and is sectioned. Therefore, the brown grain is also bifoliate, but the crystallography is different from the case (c). The lath on $(55\bar{7})_\gamma$ plane belong to another block and another packet than the lath on the $(\bar{5}57)_\gamma$ plane; the two laths are connected to by the low-misorientation operator O_3 (10.5° around $\langle 111 \rangle_\alpha$, see [34] for details), as variant α_1 and α_4 in Fig. 7.1a, and not by the operator O_5 . These results confirms that the blocks are bifoliate, but sometimes the two plates of foliation are not close to the same $\{111\}_\gamma$ plane. These last cases may correspond to the 30% of the “bad” fits observed previously. The TEM and EBSD experiments confirm earlier studies on lath martensite in low-carbon steels. The laths are grouped by packets, the packets are divided into three blocks, and each block is constituted by a pair of low-misoriented KS variants. The analysis of the TEM results show that the habit planes of the laths are $(557)_\gamma \parallel \{156\}_\alpha$ and they contain the common CPD. The KS OR permitted to satisfactorily simulate the diffraction patterns of the laths in different blocks. The EBSD data show that the bcc grains exhibit gradients of orientations from Pitsch, KS and NW, with an average OR close to GT. The blocks have a plate morphology with a habit plane that is most of the time $(575)_\gamma \parallel \{156\}_\alpha$, which agrees with the hypotheses (b) and (c) of Fig. 7.3. By looking in the EBSD maps at the parent

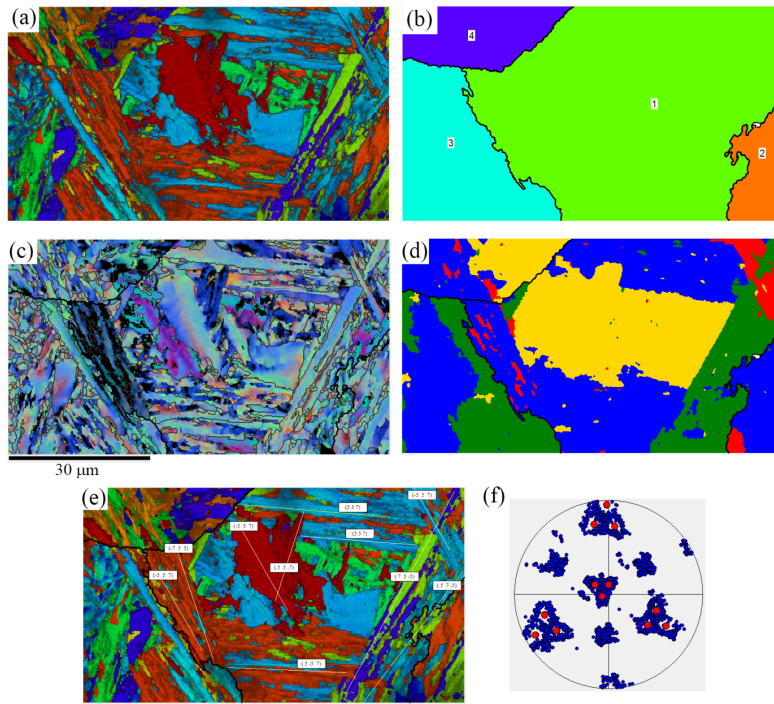


Figure 7.10: An EBSD map acquired on the as-quenched 1018 steel with the orientation of a prior austenite grain close to a $\langle 111 \rangle_\gamma$ zone axis. (a) Initial map of the bcc martensite, (b) prior austenitic grains reconstructed by ARPGE, (c) gradients of ORs in the martensitic grains colored in RGB (Red = Pitsch, Green = KS, Blue = NW), (d) CPP packets in the parent austenitic grains, (e) $\{557\}_\gamma$ traces manually positioned along the blocks where the fit is acceptable, (f) pole figure of the reconstructed parent grain PG1 with the $\langle 110 \rangle_\alpha$ directions of bcc martensitic they contain and the calculated $\langle 557 \rangle_\gamma$ directions. The orientation of the parent grain PG1 is close to a $\langle 557 \rangle_\gamma$ direction, which explains why some blocks (in brown and blue, marked by the white arrows) are seen flat-on. The brown block is composed of two plates, one flat-on (white arrow) and the other inclined or edge-on (black arrow).

grains that are orientated in a direction close to $\langle 111 \rangle_\gamma$, many blocks appear with a complex bifoliate structure made of plates lying on two different 557_γ planes; for some of them the $\{557\}_\gamma$ planes are close to the same $\{111\}_\gamma$ plane, which agrees with the hypothesis (c) of Fig. 7.3, and for others the planes are close to two distinct $\{111\}_\gamma$ planes, which is a case than was not expected from literature. In the rest of paper, we will try to explain why the local KS OR observed at the lath scale deviates toward NW at the block scale, and we will propose a qualitative explanation of the $(575)_\gamma$ habit planes and the complex bifoliate morphology of the blocks.

7.4 Crystallographic interpretation and discussion

Before discussing the experimental results, we would like to quickly explain our general approach of martensitic transformations. After having explored different alternative models for fcc-bcc martensitic transformation, such as the double-step model [33] and the one-step model based on Pitsch OR [34], we have orientated our researches for the last years toward a one-step model based on the KS OR [35]. The two-step model is probably relevant to steels in which the intermediate hcp phase exists, as it is the case in FeCrNi and FeMn steels [41]; and the one-step Pitsch model [34] is probably relevant for nitrogen iron alloys in which Pitsch OR is observed [42]; but we came to seriously consider that for a vast majority of steels, the one-step distortion that leads to the KS OR is the “natural”, “spontaneous” distortion and that the other orientations (Pitsch, NW, GT) result from this KS distortion due to the back-stresses induced in the surrounding matrix [35]. Thus, we consider that KS is the natural distortion in the low-carbon steels, and that the tendency toward the NW OR results from the coupling of the two-low misoriented variants in the blocks. We will show that it is possible to explain why the average OR tends to NW at the block scale, even if KS exists locally at the lath scale. We will also show that the $\{557\}_\gamma$ planes have some specific properties relatively to the NW OR that could explain their formation.

7.4.1 Reminder on the calculation of orientation and distortion variants

Before entering the discussion, some notations and formulae must be recalled. We note the reference basis of the γ phase $\mathbf{B}_0^\gamma = (\mathbf{a}_0^\gamma, \mathbf{b}_0^\gamma, \mathbf{c}_0^\gamma)$ with $\mathbf{a}_0^\gamma = [100]_\gamma$, $\mathbf{b}_0^\gamma = [010]_\gamma$, $\mathbf{c}_0^\gamma = [001]_\gamma$. The *distortion* matrix is formed by the coordinates of the transformed vectors $(\mathbf{a}_0^\gamma)', (\mathbf{b}_0^\gamma)', (\mathbf{c}_0^\gamma)'$ expressed in the reference basis \mathbf{B}_0^γ , written by

$$\mathbf{D}^{\gamma \rightarrow \alpha} = [\mathbf{B}_0^\gamma \rightarrow \mathbf{B}^{\gamma'}] \quad (7.2)$$

This matrix can be calculated by finding a primitive basis of the parent phase and by following how this basis is distorted during the transformation [35]. The distortion matrix gives in columns the images of the directions. The images of the planes are given by the reciprocal matrix

$$(\mathbf{D}^{\gamma \rightarrow \alpha})^* = (\mathbf{D}^{\gamma \rightarrow \alpha})^{-T} \quad (7.3)$$

where “-T” means “inverse of the transpose”.

We also note $\mathbf{T}^{\gamma \rightarrow \alpha}$ the matrix of coordinate transformation, which gives the coordinates of the vectors of the reference basis \mathbf{B}_0^α of the α crystal in the reference basis \mathbf{B}_0^γ of the γ crystal:

$$\mathbf{T}^{\gamma \rightarrow \alpha} = [\mathbf{B}_0^\gamma \rightarrow \mathbf{B}_\alpha] \quad (7.4)$$

$\mathbf{T}^{\gamma \rightarrow \alpha}$ only depends on the orientation relationship.

A distinction should be made between the orientational variants and the distortional (shape)

variants. The orientational variants only depend on the orientation relationship and not on the mechanism. They can be mathematically defined from the subgroup \mathbb{H}^γ of the crystallographic symmetries that are common to the parent and daughter crystals. This subgroup is given by the orientation matrix $\mathbf{T}^{\gamma \rightarrow \alpha}$ and by the point groups of parent and daughter phases, \mathbb{G}^γ and \mathbb{G}^α :

$$\mathbb{H}^\gamma = \mathbb{G}^\gamma \cap \mathbf{T}^{\gamma \rightarrow \alpha} \mathbb{G}^\alpha (\mathbf{T}^{\gamma \rightarrow \alpha})^{-1} \quad (7.5)$$

The orientational variants are the cosets $\alpha_i = g_i^\gamma \mathbb{H}^\gamma$ and their orientation matrices are $\mathbf{T}^{\gamma \rightarrow \alpha_i} = g_i^\gamma \mathbf{T}^{\gamma \rightarrow \alpha}$ with $g_i \in \alpha_i$. The number of orientational variants is $N_\alpha = \frac{|\mathbb{G}^\gamma|}{|\mathbb{H}^\gamma|}$. Details are given in Ref.[16].

The distortional shape variants depend on the mechanism, and more specifically on the distortion matrix. They can be defined similarly as for the orientational variants but by replacing the orientation matrix $\mathbf{T}^{\gamma \rightarrow \alpha_i}$ by the distortion matrix $\mathbf{D}^{\gamma \rightarrow \alpha}$. The subgroup \mathbb{K}^γ of shape symmetries that are common to both parent and daughter crystals is

$$\mathbb{K}^\gamma = \mathbb{G}^\gamma \cap \mathbf{D}^{\gamma \rightarrow \alpha} \mathbb{G}^\gamma (\mathbf{D}^{\gamma \rightarrow \alpha})^{-1} \quad (7.6)$$

The distortional variants are the cosets $d_i = g_i^\gamma \mathbb{K}^\gamma$ and their distortion matrices are $\mathbf{D}^{\gamma \rightarrow \alpha_i} = g_i^\gamma \mathbf{D}^{\gamma \rightarrow \alpha} (g_i^\gamma)^{-1}$ with $g_i^\gamma \in d_i$. The number of distortional variants is $M^\alpha = \frac{|\mathbb{G}^\gamma|}{|\mathbb{K}^\gamma|}$. Details are given in Ref.[36].

The distortion matrices associated with the KS OR and with the NW OR will be noted \mathbf{D}^{KS} and \mathbf{D}^{NW} , and simply called here “KS distortion matrix” and “NW distortion matrix”, respectively. However, it is important to keep in mind that these two matrices are not those proposed by Kurdjumov and Sachs [4] and by Nishiyama and Wassermann [2, 3] in their seminal papers, for which the lattice deformation results from a simple shear combined with an expansion and a contraction along some crystallographic directions. Please also note that the distortion matrix $\mathbf{D}^{\gamma \rightarrow \gamma}$ was noted $\mathbf{D}_0^{\gamma \rightarrow \alpha}$ in ref. [35], the index “0” meaning the reference basis \mathbf{B}_0^γ . In the present work, the index i is attributed to the index of the distortional variant, i.e. it is the matrix of the distortional variant i obtained with the KS OR, and noted for sake of simplicity $\mathbf{D}^{\gamma \rightarrow \alpha_i} = \mathbf{D}_i^{KS}$. By default, the identity matrix is g_1^γ , and the distortion matrix obtained with g_1^γ (or any matrix in \mathbb{K}^γ) is noted \mathbf{D}_1^{KS} .

7.4.2 Calculations of the KS and NW distortion matrices

The KS OR that we used in our previous works [35] was $(\bar{1}11)_\gamma \parallel (\bar{1}10)_\alpha$ & $[110]_\gamma = [111]_\alpha$. This choice was made to avoid the negative signs on the invariant line $[110]_\gamma = [111]_\alpha$. Another equivalent choice is often made: $(111)_\gamma \parallel (110)_\alpha$ & $[\bar{1}10]_\gamma = [\bar{1}11]_\gamma$. In order to facilitate the comparison with literature, this OR was chosen for the variant α_1 (Fig. 7.1). The fcc-bcc distortion matrices can be calculated from \mathbf{D}^{KS} given in Ref. [35] by using the symmetry

matrix

$$g = \begin{bmatrix} 0 & -1 & 0 \\ 1 & 0 & 0 \\ 0 & 0 & 1 \end{bmatrix} \quad (7.7)$$

and by applying the coordinate transformation $(g_i)^{-1} \mathbf{D} g_i$. Thus, the KS distortion matrix associated with variant α_1 is

$$\mathbf{D}_1^{KS} = \begin{bmatrix} 1 + \frac{\sqrt{6}}{18} & \frac{\sqrt{6}}{18} & \frac{1}{3} - \frac{\sqrt{6}}{6} \\ -\frac{1}{3} + \frac{\sqrt{6}}{18} & \frac{2}{3} + \frac{\sqrt{6}}{18} & \frac{1}{3} - \frac{\sqrt{6}}{6} \\ \frac{1}{3} - \frac{\sqrt{6}}{9} & \frac{1}{3} - \frac{\sqrt{6}}{9} & \frac{1}{3} - \frac{\sqrt{6}}{3} \end{bmatrix} \quad (7.8)$$

The calculations prove that the intersection groups \mathbb{H}^γ and \mathbb{K}^γ are equal, both being constituted of the identity and inversion elements. Therefore, the orientational and distortional variants are equivalent, and there is a one-to-one equivalence between the distortion matrix \mathbf{D}_i^{KS} and the orientational variant α_i^{KS} . Among the twenty-four KS distortion matrices, two are of particular interest relatively to \mathbf{D}_1^{KS} ; they are \mathbf{D}_3^{KS} and \mathbf{D}_6^{KS} . The matrix \mathbf{D}_3^{KS} gives the variant α_3^{KS} linked to α_1^{KS} by the operator O_1 [15] (they are twin-related), and their association makes fully invariant the $\{225\}_\gamma$ plane [38]. The matrix \mathbf{D}_6^{KS} gives the variant α_6^{KS} that shares the same $(111)_\gamma \parallel (110)_\alpha$ plane as α_1^{KS} , α_3^{KS} and α_6^{KS} . As already mentioned in introduction and illustrated in Fig. 7.1b, the variants α_1^{KS} and α_6^{KS} are linked by a rotation of 10.5° around the $[111]_\gamma \parallel [110]_\alpha$ axis, i.e. by the operator O_5 [15]. The distortion matrix \mathbf{D}_6^{KS} associated with

the variant α_6^{KS} is deduced from \mathbf{D}_1^{KS} by using the symmetry matrix $g_6^\gamma = \begin{bmatrix} 0 & 0 & 1 \\ 0 & 1 & 0 \\ 1 & 0 & 0 \end{bmatrix}$

$$\mathbf{D}_6^{KS} = g_6^\gamma \mathbf{D}_1^{KS} (g_6^\gamma)^{-1} = \begin{bmatrix} \frac{1}{3} + \frac{\sqrt{6}}{3} & \frac{1}{3} - \frac{\sqrt{6}}{9} & \frac{1}{3} - \frac{\sqrt{6}}{9} \\ \frac{1}{3} - \frac{\sqrt{6}}{6} & \frac{2}{3} + \frac{\sqrt{6}}{18} & -\frac{1}{3} + \frac{\sqrt{6}}{18} \\ \frac{1}{3} - \frac{\sqrt{6}}{6} & \frac{\sqrt{6}}{18} & 1 + \frac{\sqrt{6}}{18} \end{bmatrix} \quad (7.9)$$

It can be checked that \mathbf{D}_1^{KS} and \mathbf{D}_6^{KS} leave invariant the directions $[1\bar{1}0]_\gamma$ and $[01\bar{1}]_\gamma$, respectively. It will be shown in the next section that the average of \mathbf{D}_1^{KS} and \mathbf{D}_6^{KS} is a distortion that leaves unrotated the third CPD in the $(111)_\gamma$ plane, i.e. the $[10\bar{1}]_\gamma$ direction, and that this matrix is exactly equal to that of the distortion related to the NW OR. For this reason, the block formed by the pair of variants α_1^{KS} and α_6^{KS} is noted α_1^{NW} .

For the moment, one needs to calculate the NW distortion matrix by a method that is not based

on averaging. We use the fact that the NW variant α_1^{NW} with the orientation $(111)_\gamma \parallel (110)_\alpha$ and $[10\bar{1}]_\gamma \parallel [001]_\alpha$ is located at 5.26° between the two variants α_1^{KS} and α_6^{KS} , as illustrated in Fig. 7.1b. The rotation matrix that re-orientes α_1^{KS} toward α_1^{NW} is the rotation \mathbf{R} of 5.2° around $[111]_\gamma$, and the one that re-orientes α_6^{KS} toward α_1^{NW} is the rotation \mathbf{R}^{-1} of -5.26° around $[111]_\gamma$, with:

$$\mathbf{R} = \begin{bmatrix} \frac{1}{9}(3+3\sqrt{2}+\sqrt{3}) & \frac{1}{9}(3-2\sqrt{3}) & \frac{1}{9}(3-3\sqrt{2}+\sqrt{3}) \\ \frac{1}{9}(3-3\sqrt{2}+\sqrt{3}) & \frac{1}{9}(3+3\sqrt{2}+\sqrt{3}) & \frac{1}{9}(3-2\sqrt{3}) \\ \frac{1}{9}(3-2\sqrt{3}) & \frac{1}{9}(3-3\sqrt{2}+\sqrt{3}) & \frac{1}{9}(3+3\sqrt{2}+\sqrt{3}) \end{bmatrix} \quad (7.10)$$

The distortion matrix associated with the variant α_1^{NW} is thus

$$\mathbf{D}_1^{NW} = \mathbf{R}\mathbf{D}_1^{KS} = \mathbf{R}^{-1}\mathbf{D}_6^{KS} = \begin{bmatrix} \frac{1}{6}(2+\sqrt{2}+2\sqrt{3}) & \frac{1}{6}(2-\sqrt{2}) & \frac{1}{6}(2+\sqrt{2}-2\sqrt{3}) \\ \frac{1}{3}(1-\sqrt{2}) & \frac{1}{3}(1+\sqrt{2}) & \frac{1}{3}(1-\sqrt{2}) \\ \frac{1}{6}(2+\sqrt{2}-2\sqrt{3}) & \frac{1}{6}(2-\sqrt{2}) & \frac{1}{6}(2+\sqrt{2}+2\sqrt{3}) \end{bmatrix} \quad (7.11)$$

It can be checked that this matrix leaves the $[10\bar{1}]_\gamma$ direction unrotated; this direction is just elongated by a ratio $\frac{2\sqrt{3}}{3} \approx 1.155$. Further calculations (not detailed here) prove that there are as many NW orientational variants as distortional ones. Therefore, there is again a one-to-one correspondence between the orientational and the distortional variants for the NW OR. The polar decomposition of \mathbf{D}_1^{NW} will be used in the next section. It is written

$$\mathbf{D}_1^{NW} = \mathbf{R}_1^{NW}\mathbf{B}_y = \begin{bmatrix} \frac{1}{12}(6+2\sqrt{3}+\sqrt{6}) & \frac{-1+\sqrt{2}}{2\sqrt{3}} & \frac{1}{12}(-6+2\sqrt{3}+\sqrt{6}) \\ \frac{1}{6}(\sqrt{3}-\sqrt{6}) & \frac{1}{\sqrt{3}}+\frac{1}{\sqrt{6}} & \frac{1}{6}(\sqrt{3}-\sqrt{6}) \\ \frac{1}{12}(-6+2\sqrt{3}+\sqrt{6}) & \frac{-1+\sqrt{2}}{2\sqrt{3}} & \frac{1}{12}(6+2\sqrt{3}+\sqrt{6}) \end{bmatrix} \begin{bmatrix} \frac{2}{\sqrt{3}} & 0 & 0 \\ 0 & \sqrt{\frac{2}{3}} & 0 \\ 0 & 0 & \frac{2}{\sqrt{3}} \end{bmatrix} \quad (7.12)$$

The rotation \mathbf{R}_1^{NW} is of angle $\text{ArcCos}(\frac{1}{3} + \frac{1}{\sqrt{6}})$ and of axis $[\bar{1}01]_\gamma$, and \mathbf{B}_y is the classical Bain distortion matrix with the contraction axis oriented along the $[010]_\gamma$ direction.

7.4.3 The NW distortion matrix as the average of two KS distortion matrices

By considering how the vectors are transformed by \mathbf{D}_1^{KS} and \mathbf{D}_6^{KS} , as illustrated in Fig. 7.11, one gets the feeling that the averaging of the two KS distortion matrices should lead to the NW distortion matrix \mathbf{D}_1^{NW} . This could explain why the ORs found experimentally at low scales and medium resolutions in the EBSD maps tends to NW, whereas those found locally at higher scales and better resolutions by TEM diffraction are closer to KS. Can this average relation be rigorously proved? The more general question is: how to average two distortion matrices \mathbf{D}_1 and \mathbf{D}_2 ? The classical averaging formula used in the PTMC [19, 23, 43] is arithmetic; it consists in linearly adding the distortion matrices with a weight factor (here $\frac{1}{2}$) such that the resulting

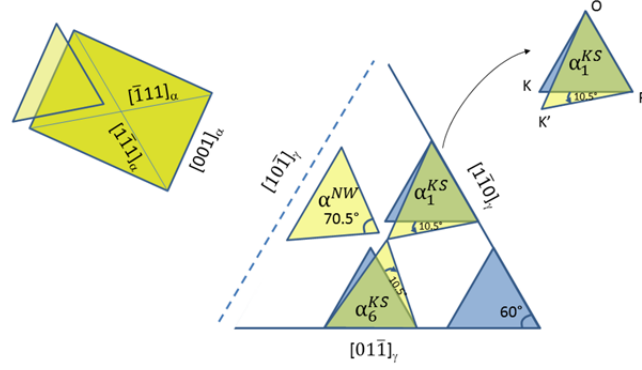


Figure 7.11: Representation of the angular distortion part on the $(111)_\gamma$ plane of the KS distortion associated with the two KS variants α_1^{KS} and α_6^{KS} . Instead of using rectangles, the variants are represented by triangles formed by the dense directions $\langle 111 \rangle_\gamma$. The $(111)_\gamma \rightarrow (110)_\alpha$ fcc-bcc transformation occurs by opening by 10.5° the angle between the $\langle 111 \rangle_\alpha$ directions. In the KS OR, only one direction is rotated while the other remains parallel to a dense direction of austenite.

distortion matrix is

$$L = \frac{1}{2}D_1 + \frac{1}{2}D_2 \quad (7.13)$$

By considering the numerical values (chopped at 10^{-4}) of the matrices given in equations 7.8 and 7.9, and in equation 7.11, it appears that L is not exactly equal to D_1^{NW} :

$$L \approx \begin{bmatrix} 1.14296 & 0.0986253 & -0.0068736 \\ -0.136083 & 0.802749 & -0.136083 \\ -0.0068736 & 0.0986253 & 1.14296 \end{bmatrix} \quad D_1^{NW} \approx \begin{bmatrix} 1.14639 & 0.0976311 & -0.0083147 \\ -0.138071 & 0.8047378 & -0.138071 \\ -0.0083147 & 0.0976311 & 1.14639 \end{bmatrix} \quad (7.14)$$

Why does the arithmetic average formula 7.13 work only approximately (at $5 \cdot 10^{-3}$) but not exactly? The fundamental reason is that formula 7.13 does not always respect the invariance of the determinant. The determinant of a distortion matrix gives the ratio of the atomic volume of the daughter phase divided by the atomic volume of the parent phase, i.e. the density of the parent phase divided by the density of the daughter phase. For fcc-bcc transformations this ratio is $\frac{4}{3}\sqrt{\frac{2}{3}} \approx 1.08866$ in a hard-sphere model. Combining two distortion matrices should not modify this ratio because it is a volume property. However, the determinant is not a linear function of matrices. Thus, formula 7.13 can only be applied if it conserves the volume. This condition is obeyed when the kinematic compatibility between the two variants is verified, i.e. when the interface between them is distorted similarly by the individual distortion of each variant [43]. This is not the case here. Does an averaging formula different from that of equation 7.13 and leading exactly to the NW distortion matrix exist? The answer is positive.

The idea lies in the fact that both α_1^{KS} and α_6^{KS} are two variants slightly misoriented; they belong to the same Bain packet; their $\langle 100 \rangle$ directions form the same $\langle 100 \rangle$ Bain circle in the pole figure; they have the same Bain matrix in their polar decomposition. Both distortion matrices \mathbf{D}_1^{KS} and \mathbf{D}_6^{KS} can be decomposed as a product of a rotation and the Bain matrix \mathbf{B}_y :

$$\mathbf{D}_1^{NW} = \mathbf{R}_1^{KS} \mathbf{B}_y = \begin{bmatrix} \frac{1}{12}(\sqrt{2} + 6\sqrt{3}) & \frac{1}{6} & -\frac{-2+\sqrt{6}}{4\sqrt{3}} \\ \frac{-6+\sqrt{6}}{12\sqrt{3}} & \frac{1}{6} + \sqrt{\frac{2}{3}} & -\frac{-2+\sqrt{6}}{4\sqrt{3}} \\ \frac{1}{6}\sqrt{5-2\sqrt{6}} & -\frac{1}{3} + \frac{1}{\sqrt{6}} & \sqrt{\frac{7}{12} + \frac{1}{\sqrt{6}}} \end{bmatrix} \begin{bmatrix} \frac{2}{\sqrt{3}} & 0 & 0 \\ 0 & \sqrt{\frac{2}{3}} & 0 \\ 0 & 0 & \frac{2}{\sqrt{3}} \end{bmatrix} \quad (7.15)$$

$$\mathbf{D}_6^{NW} = \mathbf{R}_6^{KS} \mathbf{B}_y = \begin{bmatrix} \sqrt{\frac{7}{12} + \frac{1}{\sqrt{6}}} & -\frac{1}{3} + \frac{1}{\sqrt{6}} & \frac{1}{6}\sqrt{5-2\sqrt{6}} \\ -\frac{-2+\sqrt{6}}{4\sqrt{3}} & \frac{1}{6} + \sqrt{\frac{2}{3}} & \frac{-6+\sqrt{6}}{12\sqrt{3}} \\ -\frac{-2+\sqrt{6}}{4\sqrt{3}} & \frac{1}{6} & \frac{1}{12}(\sqrt{2} + 6\sqrt{3}) \end{bmatrix} \begin{bmatrix} \frac{2}{\sqrt{3}} & 0 & 0 \\ 0 & \sqrt{\frac{2}{3}} & 0 \\ 0 & 0 & \frac{2}{\sqrt{3}} \end{bmatrix} \quad (7.16)$$

The rotations \mathbf{R}_1^{KS} and \mathbf{R}_6^{KS} are of angle $\text{ArcCos}(-\frac{5}{12} + \frac{7}{12\sqrt{2}} + \frac{1}{\sqrt{3}} + \frac{1}{\sqrt{6}})$, and their rotation axes are $[1 - \sqrt{2}, 7 - 5\sqrt{2} - 4\sqrt{3} + 3\sqrt{6}, 1]$ and $[1, 7 - 5\sqrt{2} - 4\sqrt{3} + 3\sqrt{6}, 1 - \sqrt{2}]$, respectively. The distortion matrices can be averaged while maintaining the determinant invariant; this is done by averaging the rotation matrices \mathbf{R}_1^{KS} and \mathbf{R}_6^{KS} , and then by multiplying the mean rotation by the Bain matrix \mathbf{B}_y . The question is now: how to average two rotation matrices? This question is not simple and has been the subject of a broad literature well beyond materials science. There are many formulae that can be applied depending on the chosen metrics (geodesic, quaternion, chordal etc.) [44, 45]. The average of two rotations should give a rotation. Besides, we search a formula in which the two rotation matrices can be interchanged. Such a remarkable formula exists; it was proposed by Moahker in 2002 [46]: the geometric mean of two rotations \mathbf{R}_1 and \mathbf{R}_2 is

$$\langle \mathbf{R}_1, \mathbf{R}_2 \rangle = \mathbf{R}_1 (\mathbf{R}_1^T \mathbf{R}_2)^{\frac{1}{2}} = \mathbf{R}_2 (\mathbf{R}_2^T \mathbf{R}_1)^{\frac{1}{2}} = \langle \mathbf{R}_2, \mathbf{R}_1 \rangle \quad (7.17)$$

This formula is of prime importance, although not yet well known in crystallography and metallurgy. If two distortion matrices \mathbf{D}_1 and \mathbf{D}_2 are based on the same symmetric matrix \mathbf{B} , i.e. $\mathbf{D}_1 = \mathbf{R}_1 \mathbf{B}$ and $\mathbf{D}_2 = \mathbf{R}_2 \mathbf{B}$, their mean is thus given by

$$\langle \mathbf{D}_1, \mathbf{D}_2 \rangle = \langle \mathbf{R}_1, \mathbf{R}_2 \rangle \mathbf{B} \quad (7.18)$$

Applied to the KS rotations \mathbf{R}_1^{KS} and \mathbf{R}_6^{KS} , it gives

$$\langle \mathbf{R}_1^{KS}, \mathbf{R}_6^{KS} \rangle = \begin{bmatrix} \frac{1}{12}(6 + 2\sqrt{3} + \sqrt{6}) & \frac{-1+\sqrt{2}}{2\sqrt{3}} & \frac{1}{12}(-6 + 2\sqrt{3} + \sqrt{6}) \\ \frac{1}{6}(\sqrt{3} - \sqrt{6}) & \frac{1}{\sqrt{3}} + \frac{1}{\sqrt{6}} & \frac{1}{6}(\sqrt{3} - \sqrt{6}) \\ \frac{1}{12}(-6 + 2\sqrt{3} + \sqrt{6}) & \frac{-1+\sqrt{2}}{2\sqrt{3}} & \frac{1}{12}(6 + 2\sqrt{3} + \sqrt{6}) \end{bmatrix} \quad (7.19)$$

The matrix is exactly the rotation obtained by the polar decomposition of \mathbf{D}_1^{NW} in equation 7.12. The matrix \mathbf{B} is \mathbf{B}_γ of equations 7.12, 7.15 and 7.16. Thus, we get exactly the equation that was expected:

$$\langle \mathbf{D}_1^{KS}, \mathbf{D}_6^{KS} \rangle = \mathbf{D}_1^{NW} \quad (7.20)$$

The calculations prove that geometric average of the distortion matrices related to the KS variants in a block is equal to a NW distortion matrix. This theoretical result is in good agreement with the fact that locally the OR of a lath can be close to KS, and more globally, at the block scale, it tends to be closer to NW.

7.4.4 The $\{557\}_\gamma$ plane emerging from the NW distortion

We have considered many hypotheses to explain the $(575)_\gamma$ habit planes; some were based on variant coupling, others implied adding small obliquity corrections etc., but the only one that we consider valuable because of its simplicity and the absence of extra parameters is the one that is now presented. The average distortion matrix related to the two KS variants in a block is a NW distortion matrix. Can the observed $\{557\}_\gamma$ habit planes be explained by this NW distortion matrix, for example by using the “untilted-plane” criterion already applied for the $\{225\}_\gamma$ habit planes in the high-carbon steels [35, 37]? If the hypothesis is correct, the habit plane of a block should be untilted by the NW distortion, i.e. it should be equal to one of the eigenvectors of the NW distortion matrix expressed in the reciprocal space:

$$(\mathbf{D}_1^{NW})^* = (\mathbf{D}_1^{NW})^{-T} = \begin{bmatrix} \frac{1}{8}(2 + \sqrt{2} + 2\sqrt{3}) & \frac{1}{4}(2 - 2\sqrt{2}) & \frac{1}{8}(2 + \sqrt{2} - 2\sqrt{3}) \\ \frac{1}{4}(1 - \sqrt{2}) & \frac{1}{2} + \frac{1}{\sqrt{2}} & \frac{1}{4}(1 - \sqrt{2}) \\ \frac{1}{8}(2 + \sqrt{2} + 2\sqrt{3}) & \frac{1}{4}(2 - \sqrt{2}) & \frac{1}{8}(2 + \sqrt{2} + 2\sqrt{3}) \end{bmatrix} \quad (7.21)$$

This matrix has for eigenvalues $\frac{3}{2\sqrt{2}} \approx 1.0607$, 1 and $\frac{\sqrt{3}}{2} \approx 0.8660$, and for respective eigenvectors the planes $(1, \sqrt{2}, 1)_\gamma$, $(1, 1, 1)_\gamma$ and $(\bar{1}, 0, 1)_\gamma$. The plane $(1, \sqrt{2}, 1)_\gamma$ is at 0.3° far from the $(575)_\gamma$ plane, and will be simply noted $(575)_\gamma$. The planes equivalent to $(575)_\gamma$ for the distortions of the two other blocks, \mathbf{D}_2^{NW} and \mathbf{D}_3^{NW} , are the $(557)_\gamma$ and $(755)_\gamma$, respectively. We have concluded in Ref. [35] that $(111)_\gamma$ cannot be a habit plane for martensite because it is the plane in which the fcc-bcc volume change is “localized”, i.e. the $(111)_\gamma$ plane is untilted but highly distorted because of the rotation of some of the directions it contains. Indeed, in the ideal case of hard-sphere model, the fcc-bcc volume change uniquely comes from the increase of angle between two $\langle 110 \rangle_\gamma$ CPDs in the CPP (Fig. 7.1c) from 60° to 70.5° while the lengths of the two directions remain constant; the surface increases by $\frac{4}{3}\sqrt{\frac{2}{3}} \approx 1.088$, which is exactly the fcc-bcc volume change expected with a hard-sphere model. To our knowledge, the only case of $\{111\}_\gamma$ habit planes concerns the “octahedrite” meteorites (see Supplementary Material S1 (appendix B), but it is probable that the very low cooling rates of these objects (few degrees per thousand years) allowed diffusive accommodation mechanisms, such as dislocation climbing, that usually are not activated during rapid cooling.

The two remaining candidates are the $(575)_\gamma$ and $(\bar{1}01)_\gamma$ planes. The $(575)_\gamma$ plane is obviously a good candidate to interpret the $\{575\}_\gamma$ habit planes; however, this plane is $(575)_\gamma \parallel \{057\}_\alpha$, which corresponds to case (a) of Fig. 7.3; i.e. it does not contain the $[\bar{1}10]_\gamma$ CPD of the variants α_1^{KS} . This case was experimentally investigated and eventually excluded in the previous section. Despite this apparent discrepancy with the experiments, we consider that the fact that the plane untilted by the NW distortion matrix is a $\{557\}_\gamma$ plane (up to 0.3°) is not coincidence. In order to conciliate the calculations with the observations, an interpretation is proposed in the following section.

7.4.5 The $\{557\}_\gamma$ habit planes and the intricacy of the blocks

The TEM observations have showed that the habit planes of the laths are most often $(575)_\gamma \parallel \{156\}_\alpha$. The EBSD maps exhibit blocks that have often a bifoliate morphology made of two plates lying on distinct $\{557\}_\gamma$ planes. One foil is made of the $\{557\}_\gamma \parallel \{156\}_{\alpha_1}$ habit plane of one lath variant, and the other foil is made of the $\{557\}_\gamma \parallel \{156\}_{\alpha_6}$ habit plane of second lath variant of the block, as shown in Fig. 7.3c. It was also observed that some blocks are constituted of $\{557\}_\gamma$ planes that do not belong to the same packet, as in Fig. 7.10a. This additional complexity could probably be explained by a second coupling between the low-misoriented variants linked by the operator O_3 (10.5° around $\langle 111 \rangle_\alpha$), but in order to remain as simple as possible, it will be assumed in the rest of the paper that a block is a structure only made of the two $\{557\}_\gamma \parallel \{156\}_\alpha$ planes that are the habit planes of the two KS variants it contains, i.e. those linked by the operator O_5 (10.5° around $\langle 110 \rangle_\gamma$).

Can the $\{557\}_\gamma$ habit plane be theoretically explained despite the fact that the $\{557\}_\gamma$ habit planes calculated from equation 7.21 do not contain the invariant dense direction whereas the experiments show they do? We make the hypothesis that the individual laths are created by the fcc-bcc transformation with the KS distortion given in Ref. [35], for example by equations 7.8 and 7.9 for the variants α_1^{KS} and α_6^{KS} , respectively, and that the habit plane of a lath should contain the common CPD, for example $[\bar{1}10]_\gamma = [1\bar{1}1]_{\alpha_1}$ for variant α_1^{KS} . This last condition means that the habit plane of the lath α_1^{KS} is a plane of type $(hkl)_\gamma \parallel (h'k'l')_\alpha$ such $h = k$ and $h' - k' + l' = 0$. Among all the possible planes of type $(hhl)_\gamma$ with $h \neq l$, the plane $(557)_\gamma$ is special because (i) it is only slightly tilted by 0.5° by the distortion matrix D_1^{KS} [35], and (ii) it is not tilted at all by the average distortion D_2^{NW} of the adjacent block α_2^{NW} , as illustrated in Fig. 7.12. With the same argument, the plane $(755)_\gamma$ is special for the lath variant α_6^{KS} because it is slightly tilted by 0.5° by the distortion D_6^{KS} and is not tilted at all by the average distortion of the adjacent block D_3^{NW} . In other words, the planes $(557)_\gamma$ and $(755)_\gamma$ of the laths α_1^{KS} and α_6^{KS} in the block α_1^{NW} are special because they are only slightly tilted by their own distortion field, and not tilted at all by the average distortion of the neighboring blocks α_2^{NW} and α_3^{NW} , respectively. It is thus probable that the two habit planes constituting the bifoliate structure of a NW block are the planes $\{557\}_\gamma$ as illustrated in Fig. 7.3c because these planes show a good angular compatibility with the neighboring blocks in the packet. The pairs of habit planes constituting the bifoliated blocks α_1^{NW} , α_2^{NW} , and α_3^{NW} are $(557)_\gamma + (755)_\gamma$, $(755)_\gamma + (575)_\gamma$ and $(575)_\gamma + (557)_\gamma$, respectively. They are given in the lines of Table 7.3.

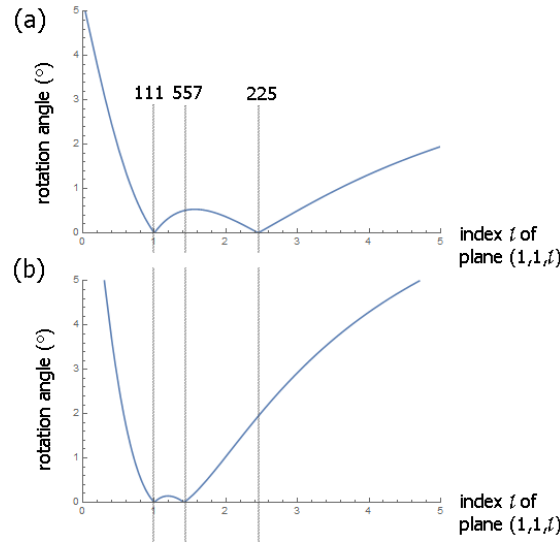


Figure 7.12: Rotation angle of the planes $(1, 1, l)_\gamma$ is l a real number, by (a) the distortion matrix \mathbf{D}_1^{KS} of the lath α_1^{KS} , and by (b) the distortion matrix \mathbf{D}_2^{NW} of the block α_2^{NW} . The special values $l = 1, 7/5$ and $5/2$ marked by the vertical lines correspond to the planes $(111)_\gamma$, $(557)_\gamma$ and $(225)_\gamma$.

Table 7.3: Table of good angular compatibility between the laths α_i^{KS} and the surrounding blocks α_j^{NW} . The first grey line indicates the three NW blocks α_j^{NW} belonging to the packet $(111)_\gamma \parallel (110)_\alpha$ with their untilted plane $\{557\}_\gamma$, i.e. the eigenvector of the distortion matrix $(\mathbf{D}_j^{NW})^*$. In the first grey column are reported the three blocks α_i^{NW} with their pair of KS lath variants. A cross is marked at position (i, j) when the untilted plane $\{557\}_\gamma$ of the block α_j^{NW} contains the common dense direction $\langle 110 \rangle_\gamma \parallel \langle 111 \rangle_\alpha$ of the lath α_i^{KS} ; it is the habit plane of the lath. The bifoliate structure of the blocks appears in the table by the two crosses in the lines of the blocks. The two crosses aligned in the same column correspond to KS lath variants that belong to two different blocks but share the same $\{557\}_\gamma$ habit plane.

| | Block α_1^{NW} (575) $_\gamma$ | Block α_2^{NW} (557) $_\gamma$ | Block α_3^{NW} (755) $_\gamma$ |
|---------------------------------------|--|--|--|
| Block α_2^{NW} α_1^{KS} | | x | |
| α_6^{KS} | | | x |
| Block α_2^{NW} α_5^{KS} | | | x |
| α_8^{KS} | x | | |
| Block α_3^{NW} α_2^{KS} | x | | |
| α_3^{KS} | | x | |

The planes $(755)_\gamma$, $(575)_\gamma$ and $(557)_\gamma$ are the block interfaces $\alpha_1^{NW}/\alpha_2^{NW}$, $\alpha_2^{NW}/\alpha_3^{NW}$, and $\alpha_3^{NW}/\alpha_1^{NW}$, respectively; they are also the habit planes of the KS laths $\alpha_6^{KS} \parallel \alpha_5^{KS}$, $\alpha_8^{KS} \parallel \alpha_2^{KS}$, and $\alpha_3^{KS} \parallel \alpha_1^{KS}$, respectively. They are given in the columns of Table 3. This complex intricate configuration is schematized in Fig. 7.13. This interpretation of the $\{557\}_\gamma$ habit planes

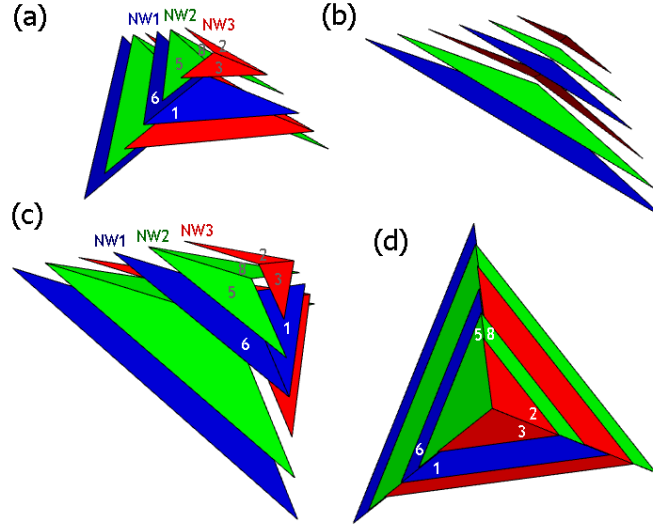


Figure 7.13: Morphological/crystallographic model of the three blocks in a $(111)_\gamma \parallel (110)_\alpha$ packet. The blocks α_1^{NW} , α_2^{NW} and α_3^{NW} are colored in blue, green and red, respectively. A block is a composite structure made of two $\{557\}_\gamma$ planes, which are the $(557)_\gamma \parallel \{156\}_\alpha$ habit planes of the two KS laths it contains. The three $\{557\}_\gamma$ planes located at 9.4° far from the $(111)_\gamma$ plane are represented by the triangles. The number in the triangles represents the index i of the lath α_i^{KS} .

proposed is different from those previously reported in literature that usually assume that the $\{557\}_\gamma$ habit planes of martensite in low-carbon steels come from the internal structure of the laths that contain sets of regularly spaced dislocations. Here, we infer that the $\{557\}_\gamma$ habit planes are the result of a good angular compatibility between the laths and the surrounding blocks.

7.4.6 Transformation temperature, plastic accommodation and variant pairing

In high-carbon steels, the KS distortion has for irrational untilted plane $(11\sqrt{6})_\gamma \approx (225)_\gamma$ plane [35], and a combination of two twin-related KS variants makes this $(225)_\gamma$ plane fully invariant [38]. In the case of low-carbon steels, we have shown that the average of the KS distortions associated with the two low-misoriented variants in a block is a NW distortion, and the irrational plane untilted by this distortion is $(1\sqrt{21}) \approx (575)_\gamma$. However, contrarily to the $(225)_\gamma$ planes, this plane is not rendered fully invariant by variant pairing. This difference between the high and low carbon contents may probably be understood by considering the transition temperature M_s . In high-carbon steels, the low M_s impedes dislocation plasticity

around the martensite products, which favors self-accommodation by association of variants. In low carbon steels, the higher Ms allows for the plasticity required to absorb the important incompatibilities associated with the fact that the $\{557\}_\gamma$ habit plane is not fully invariant. The accommodation may be obtained by stacking dislocations inside the surrounding fcc matrix, as suggested in Fig. 7.9 of Ref. [35], or inside the bcc crystal during its formation, as imagined in Fig. 7.2 of Ref. [47]. Whatever the microstructural details, we think that the important transformation plasticity in the low-carbon steels takes the form of the continuum misorientations between the Pitsch, KS and NW ORs [15, 33, 34]. Mesoscopically, two rotational gaps generated by the fcc-bcc distortion, one of 5.26° around the CPD and one of 5.26° around the CPD should be accommodated, which can be realized with two wedge disclinations [48, 49]. These disclinations are supposed to be at the origin of continuous rotations A and B observed in the pole figures [33]. The accommodation by a different type of variant-pairing implying less dislocation plasticity in the high-carbon steels is in agreement with a lower spreading of the ORs [50, 51].

7.4.7 Self-accommodation in individual packets

We would like to finish the discussion by considering other self-accommodation effects. The case of association of two blocks (four KS variants) has been investigated, but no special interesting result could be extracted. More interesting is the association of the three blocks forming a packet. This configuration is sufficient to accommodate the strains at the maximum, leaving only the hydrostatic part due to the volume change. Let us consider the pairs $\alpha_1^{KS} - \alpha_6^{KS}$, $\alpha_5^{KS} - \alpha_8^{KS}$ and $\alpha_2^{KS} - \alpha_3^{KS}$ forming the blocks α_1^{NW} , α_2^{NW} and α_3^{NW} , respectively, as indicated in Fig. 7.2. It is reasonable to assume that the average of the six KS distortions is equivalent to the average of the three NW distortions. We also assume that the average of the product is the product of averages, i.e.

$$\langle \mathbf{D}_1^{NW}, \mathbf{D}_2^{NW}, \mathbf{D}_3^{NW} \rangle = \langle \mathbf{R}_1^{NW}, \mathbf{R}_2^{NW}, \mathbf{R}_3^{NW} \rangle \langle \mathbf{B}_1, \mathbf{B}_2, \mathbf{B}_3 \rangle \quad (7.22)$$

Averaging three rotations linked by a three-fold symmetry $g_{2\pi/3}$ is a special case of the example 2 treated by Moakher [46] in which the rotation axes are coplanar. In such a case, the rotation angle of the mean rotation is zero; thus, $\langle \mathbf{R}_1^{NW}, \mathbf{R}_2^{NW}, \mathbf{R}_3^{NW} \rangle = \text{Identity}$. In addition, since the matrices \mathbf{B}_x , \mathbf{B}_y and \mathbf{B}_z are diagonal in the same basis, their geometric average is simply

$$\langle \mathbf{B}_1, \mathbf{B}_2, \mathbf{B}_3 \rangle = (\mathbf{B}_1, \mathbf{B}_2, \mathbf{B}_3)^{\frac{1}{3}} = \begin{bmatrix} \frac{2^{\frac{5}{6}}}{\sqrt{3}} & 0 & 0 \\ 0 & \frac{2^{\frac{5}{6}}}{\sqrt{3}} & 0 \\ 0 & 0 & \frac{2^{\frac{5}{6}}}{\sqrt{3}} \end{bmatrix} \quad (7.23)$$

Consequently, the average of the six KS variants in a packet, or equivalently the average of their three mean NW distortion matrices, is an isotropic matrix equal to $\frac{2^{\frac{5}{6}}}{\sqrt{3}}$ times the identity matrix.

It is the best distortion that can be obtained by accommodation; its determinant $\frac{4\sqrt{2}}{3} \approx 1.088$

gives the volume change from fcc to bcc expected from a hard-sphere model. If the real change of atomic size during the transformation is taken into account, the multiplicative coefficient is lower, close to 1.016. Anyway, this change does not modify the calculations and conclusion: in the limit of the hypotheses made on the geometric averaging formulae, the martensitic transformation is self-accommodated with the six KS variants of an individual packet; the formation of any of the four packets is sufficient to obtain self-accommodation; there is no need to form the 24 variants.

7.5 Conclusion

The low-carbon steels are constituted of a highly intricate microstructure of lath martensite. In each prior austenitic grains, martensite is structured into four crystallographic packets constituted of three blocks made of pairs of low-misoriented KS variants. The fact that the orientation relationship within the prior parent austenitic grains is not strict but follows gradients from KS toward NW is not well explained in literature, so as the fact that the habit planes deviate from the common $\{111\}_\gamma$ plane to be actually close to $\{557\}_\gamma$. The present experimental and theoretical work proposes some elements of responses that are different from those classically used in literature.

Three low-carbon steels were studied by TEM and EBSD with the help of dedicated software. It was checked by carefully indexing the TEM diffraction patterns obtained on laths belonging to the same prior austenitic grains that their habit planes are $(557)_\gamma \parallel \{156\}_\alpha$. The EBSD maps confirm that the orientation gradients inside the blocks range from KS toward NW. Most of the blocks appear as plates on $\{557\}_\gamma$ planes or as bifoliate structures made of the two $(557)_\gamma$ habit planes of the two lath variants.

Crystallographic arguments were used to interpret these results. The average distortion associated with the two low-misoriented KS variants constituting a block is a NW distortion. The average formula used for the calculation is geometric; it allows respecting the expected volume change even if the kinematical condition of compatibility is not fulfilled. One of three $\{557\}_\gamma$ planes close to the common plane $\{111\}_\gamma \parallel \{110\}_\alpha$ is absolutely untilted by the NW distortion. Consequently, the $\{557\}_\gamma$ habit planes of the two laths forming a bifoliate block are special because each of them contains a common dense direction, is only slightly tilted by its own distortion field, and is not tilted at all by the NW distortion of one of the neighboring block in the packet. In addition, the calculations show that the martensitic transformation can be completely self-accommodated in individual packets by the co-formation of the six KS variants, the resulting mean distortion being only the hydrostatic matrix due to the fcc-bcc volume change. It is thus proposed that the $\{557\}_\gamma$ habit planes and the bifoliate morphology of martensite in the low carbon steels are the result of a good angular compatibility between the laths and the surrounding blocks in the packets. The blocks are in contact two-by-two by the $\{557\}_\gamma$ habit planes of the laths they contain, which produces a highly intricate microstructure.

Acknowledgements

We acknowledge the Swiss National Science Foundation for his support (grant n°200021-159955). PX Group is thanked for its financial support to the laboratory. We are also very grateful to our colleagues Dr Yann de Carlan at CEA-Saclay and Dr Ian Zuazo at ArcelorMittal who provided us some of the steels used in this study.

Note 1 The values of the mean displacement per atom calculated in section 7.3. of Ref.[35] were based on a classical unit cell formed by the atoms with positioned in $[0,0,0]$, $[1,0,0]$, $[0,1,0]$, $[0,0,1]$, $[1,1,0]$, $[1,0,1]$, $[0,1,1]$, $[1,1,1]$, $[1/2,1/2,0]$, $[1/2,0,1/2]$, $[0,1/2,1/2]$, $[1/2,1/2,1]$, $[1/2,1,1/2]$, $[1,1/2,1/2]$. The corner atoms (eight atoms) count for $1/8$, and the atoms in the centers of the faces (six atoms) for $\frac{1}{2}$; the unit cell contains 4 atoms. The average displacement is calculated by summing the pondered displacements of the 14 atoms and dividing the result by 4. The mean displacement was calculated with the Bain, Pitsch and KS distortion matrices. Unfortunately, we realized during the preparation of present paper, that the result obtained in Ref.[35] depends on the choice of the reference frame. This is because the origin $[0,0,0]$ of the basis is a corner of the unit cell whereas it should be its center. The results obtained with a cell centered in $[0,0,0]$, i.e. by translating the vectors by $[1/2,1/2,1/2]$ now give mean displacements that do not depend on the choice of the reference frame. The mean displacements recalculated with the centered unit cell are 0.347 \AA for Bain, 0.461 \AA for KS and 0.429 \AA for Pitsch. Therefore, we were wrong when we said that the displacements associated with the Pitsch and KS distortion were lower than for Bain distortion. The rest of the paper [35] is not affected by this error, and the conclusion that the distortion associated with the KS OR is a good candidate to be the natural distortion and could explain the $\{225\}_\gamma$ habit planes in the high carbon steels still holds, as confirmed in Ref. [38].

Note 2 We take the opportunity of the paper to correct a typo error in the indices of the phases that appeared in equation (5) of Ref. [36] during the edition process. The orientation relationships should be read:

- KS: $[110]_\gamma = [111]_\alpha$ and $(\bar{1}11)_\gamma \parallel (\bar{1}10)_\alpha$
- Burgers: $[111]_\gamma = [100]_\epsilon$ and $(\bar{1}10)_\gamma \parallel (001)_\epsilon$
- SN: $[110]_\gamma = [100]_\epsilon$ and $(\bar{1}11)_\gamma \parallel (001)_\epsilon$

Note 3 This work is in the continuity of our efforts [33, 34, 35, 38] to develop an alternative to the phenomenological theory. It is in agreement with our initial hypothesis that only one matrix, the angular distortion matrix associated with the KS OR, is sufficient to explain important feature of martensite, such as gradients of orientation relationships, the $\{225\}_\gamma$ habit planes in high-carbon steels [35, 38], and now the intricate lath/block morphologies on $\{557\}_\gamma$

Chapter 7. Intricate morphologies of laths and blocks in low-carbon martensitic steels

habit planes in low-carbon steels. Although the irrational character of these habit planes was sensed for a long time, it is only now that irrational values are proposed. According to our model, the $\{225\}_{\gamma}$ and $\{557\}_{\gamma}$ habit planes are in fact $\{11\sqrt{6}\}_{\gamma}$ and $\{11\sqrt{2}\}_{\gamma}$ planes, respectively. Our research continues on the $\{259\}_{\gamma}$ habit planes of martensite in Fe-Ni-C steels.

Bibliography

- [1] G. Krauss, Tempering of Lath Martensite in Low and Medium Carbon Steels: Assessment and Challenges, *Steel Res.* 88 (2017) 1700038.
- [2] Z. Nishiyama, X-ray Investigation on the Mechanism of the Transformation from Face-Centered Cubic Lattice to Body-Cubic Lattice, *Sci. Rep. Tohoku Imp. Univ.* 23 (1934) 637-644.
- [3] G. Wassermann, Einfluss der alpha-gamma-Umwandlung eines irreversiblen Nickelstahls auf Kristallorientierung und Zugfestigkeit, *Archiv Eisenhüttenwesen* 6 (1933) 347–351.
- [4] G. Kurdjumov, G. Sachs, Über den Mechanismus der Stahlhärtung, *Z. Phys.* 64 (1930) 325-343.
- [5] P.M. Kelly, A. Jostsons, R.G. Blake, The orientation relationship between lath martensite and austenite in low carbon, low alloy steels, *Acta Metall. Mater.* 38 (1990) 1075-1081.
- [6] A.B. Greninger, A. R. Troiano, The Mechanism of Martensite Formation, *Metals Trans.* 185 (1949) 590-598.
- [7] A. R. Marder, G. Krauss, The Formation of Low-Carbon Martensite in Fe-C Alloys, *Trans. ASM* 62 (1969) 957-964.
- [8] C.A. Apple, R.N. Caron, G. Krauss, Packet Microstructure in Fe-0.2 pct C Martensite, *Metall. Trans.* 5 (1974) 593-599.
- [9] S. Hoekstra, A check of the IPS theory with the aid of an accurate determination of habit planes and orientation relationships in bainitic steels, *Acta Metall.* 28 (1980) 507-517.
- [10] B.P.J. Sandvik, C.M. Wayman, Characteristics of lath martensite: Part I. Crystallographic and substructural features, *Metall. Trans. A14* (1983) 809-822.
- [11] B.P.J. Sandvik, C.M. Wayman, Characteristics of lath martensite: Part II. The Martensite-Austenite Interface, *Metall. Trans. A14* (1983) 823-834.
- [12] S. Morito, H. Tanaka, R. Konishi, T. Furuhashi, T. Maki, The morphology and crystallography of lath martensite in Fe-C alloys, *Acta Mater.* 51 (2003) 1789-1799.

Bibliography

- [13] S. Morito, X. Huang, T. Furuhashi, T. Maki, N. Hansen, The morphology and crystallography of lath martensite in alloy steels, *Acta Mater.* 54 (2006) 5323-5331.
- [14] A. Lambert-Perlade, A.F. Gourgues, A. Pineau, Austenite to bainite phase transformation in the heat-affected zone of a high strength low alloy steel, *Acta Mater.* 52 (2004) 2337-2348.
- [15] C. Cayron, EBSD imaging of orientation relationships and variant groupings in different martensitic alloys and Widmanstätten iron meteorites, *Mater. Charact.* 94 (2014) 93-110.
- [16] C. Cayron, Groupoid of orientational variants, *Acta Cryst.* A62 (2006) 21-40.
- [17] G. Krauss, *Steels, Processing, Structure, and Performance*, 2d edition, ASM International, ISBN 10:1-62708-083-X, 2015, pp 85-97.
- [18] J.S. Bowles, J.K. Mackenzie, The crystallography of martensite transformations III: Face-centred to body-centred tetragonal transformations, *Acta Metall.* 2 (1954) 224-234.
- [19] M.S. Wechsler, D.S. Lieberman, T.A. Read, On the theory of the formation of martensite, *J. Metals* 197 (1953) 1503-1515.
- [20] P.M. Kelly, Crystallography of lath martensite in steels, *Mater. Trans. JIM* 33 (1992) 235-242.
- [21] N.H.D. Ross, A.G. Crocker, A generalised theory of martensite crystallography and its application to transformations in steels, *Acta Metall.* 18 (1970) 405-418.
- [22] K. Iwashita, Y. Murata, Y. Tsukada, K. Koyama, Formation mechanism of the hierarchic structure in the lath martensite phase in steels, *Phil. Mag.* 91 (2011) 4495-4513.
- [23] A. G. Khachaturyan, *Theory of Structural Transformations in Solids*, Wiley, New York, 1983.
- [24] L. Qi, A.G. Khachaturyan, J.W. Morris Jr, The microstructure of dislocated martensitic steel: Theory, *Acta Mater.* 76 (2014) 23-39.
- [25] K. Koumatos, A. Muehleman, A Parameter Free Double Shear Theory for Lath Martensite. <https://arxiv.org/pdf/1802.01196.pdf> (2018).
- [26] A.R. Thölén, On the ambiguity between moiré fringes and the electron diffraction contrast from closely spaced dislocations, *phys. stat. sol. (a)* 2 (1970) 537-550.
- [27] T. Waitz, H.P. Karnthaler, Analysis of HRTEM Contrasts of Overlapping Structures at Transformation Interfaces *phys. stat. sol. (a)* 166 (1998) 107-114.
- [28] J. Hamelink, The dislocation structure of twist boundaries and the influence of impurities, Ph.D. thesis, University of Delft (1987).

-
- [29] J.F. Nie, B.C. Muddle, Orientation and Structure of Planar Facets on the Massive Phase γ_{m} in a Near-TiAl Alloy, *Metall. Mater. Trans.* 33A (2002) 2381-2389.
- [30] D. Smith, Microscopy of Static and Dynamic Properties of Interfaces, *J. Phys.* 36 C4 (1975) 1-15.
- [31] D.J. Dingley, R.C. Pond, On the interaction of crystal dislocations with grain boundaries, *Acta Metall.* 27 (1979) 667-682.
- [32] C.T. Forwood, L.M. Clarebrough, *Electron Microscopy of Interfaces in Metals and Alloys*, Adam Hilger, Bristol, UK, IOP Publishing Ltd 1991.
- [33] C. Cayron, F. Barcelo, Y. de Carlan, The mechanisms of the fcc-bcc martensitic transformation revealed by pole figures, *Acta Mater.* 58 (2010) 1395-1402.
- [34] C. Cayron, One-step model of the face-centred-cubic to body-centred-cubic martensitic transformation, *Acta Cryst.* A69 (2013) 498-509.
- [35] C. Cayron, Continuous atomic displacements and lattice distortion during fcc-bcc martensitic transformation, *Acta Mater.* 96 (2015) 189-202.
- [36] C. Cayron, Angular distortive matrices of phase transitions in the fcc-bcc-hcp system, *Acta Mater.* 111 (2016) 417-441.
- [37] M.A. Jaswon, J.A. Wheeler, Atomic displacements in austenite-martensite transformation, *Acta Cryst.* 1 (1948) 216-224.
- [38] A. Baur, C. Cayron, R. Logé, $\{225\}_{\gamma}$ habit planes in martensitic steels: from the PTMC to a continuous model, *Sci. Reports* 7 (2017) DOI: 10.1038/srep40938.
- [39] C. Cayron, GenOVa: A computer program to generate orientational variants, *J. Appl. Cryst.* 40 (2007) 1179-1182.
- [40] C. Cayron, ARPGE: a computer program to automatically reconstruct the parent grains from electron backscatter diffraction data, *J. Appl. Cryst.* 40 (2007) 1183-1188.
- [41] C.C. Kinney, I. Yi, K.R. Pytlewski, A.G. Khachaturyan, N.J. Kim, J.W. Morris Jr. The microstructure of as-quenched 12Mn steel, *Acta Mater.* 125 (2017) 442-454.
- [42] W. Pitsch, The martensite transformation in thin foils of iron-nitrogen alloys, *Philos. Mag.* 4 (1959) 577-584.
- [43] K. Bhattacharya, *Microstructure of martensite*, Oxford, Oxford University Press, 2003.
- [44] R. Hartley, J. Trumpf, Y. Dai, H. Li, Rotation Averaging, *Int. J. Comput. Vis.* (2012) DOI 10.1007/s11263-012-0601-0
- [45] A. Morawiec, *Orientations and rotations: Computations in crystallographic textures*. Springer, Berlin, 2004.

Bibliography

- [46] M. Moakher, Means and averaging in the group of rotations, *SIAM Journal on Matrix Analysis and Applications* 24 (2002) 1–16.
- [47] C. Cayron, F. Barcelo, Y. de Carlan, Reply to “Comments on “The mechanism of the fcc-bcc martensitic transformation revealed by pole figures””, *Scripta Mater.* 64 (2011) 103-106.
- [48] A.E. Romanov, A.L. Kolesnikova, Application of dislocation concept to solid structures, *Prog. Mater. Sci.* 54 (2009) 740-769.
- [49] P. Müllner, A.H. King, Deformation of hierarchically twinned martensite, *Acta Mater.* 58 (2010) 5242-5261.
- [50] A.R. Chintha, V. Sharma, S. Kundu, Analysis of martensite pole figure from crystallographic view point, *Metall. Mater. Trans.* 44A (2013) 4861–4865.
- [51] A. Stormvinter, A. Borgenstam, G. Miyamoto, T. Furuhashi, H. Kristoffersen, *Proceedings of the Int. Conf. on Solid-Solid Phase Transformations in Inorganic Materials 2015*, pp. 539-545.

8 Variant selection in surface martensite

Authors: A.P. Baur, C. Cayron and R.E. Logé, Laboratory of Thermomechanical Metallurgy-PX group Chair, Institute of materials, Ecole Polytechnique Fédérale de Lausanne, 2002 Neuchâtel, Switzerland.

Cited as: Baur et al., Variant selection in surface martensite, *J. Appl. Crystallogr.* 2017 Dec 1; 50(Pt 6): 1646–1652.

Authors contributions: Conceptualization, A.P.B., C.C. and R.E.L.; methodology, A.P.B. and C.C.; software, A.P.B.; validation, A.P.B. and C.C.; formal analysis, A.P.B. and C.C.; investigation, A.P.B.; resources, A.P.B. and C.C.; data curation, A.P.B.; writing—original draft preparation, A.P.B., C.C. and R.E.L.; writing—review and editing, A.P.B., C.C. and R.E.L.; visualization, A.P.B.; supervision, C.C. and R.E.L.; project administration, C.C.; funding acquisition, C.C. and R.E.L.

Abstract

A significant variant selection is reported in isothermal martensite formed on the surface of a Fe-30%Ni sample. The selection phenomenon is modelled using different descriptions of the martensitic phase transformation. In particular, matrices based on the Phenomenological Theory of the Martensitic Crystallography, the Jaswon & Wheeler distortion and the continuous FCC-BCC distortion are compared. All descriptions allow good predictions of the variant selection. However, the Jaswon & Wheeler distortion and the continuous distortion better accounts for other features of surface martensite, such as the $\{225\}_\gamma$ habit plane and the accommodation mechanism by twin-related variants pairing.

Introduction

Variant selection in martensitic steels is a well documented phenomenon because of its implications on the industrial process of steel. It is reported when stress is applied to the material either before (Wittridge & Jonas, 2000) (Miyamoto *et al.*, 2012) or during transformation (Gey *et al.*, 2005)(Mishiro *et al.*, 2013). In this study, we show a significant variant selection in isothermal surface martensite formed on the free surface of a as-cast Fe-30%Ni sample without any applied stress. The formation of surface martensite above the bulk martensitic start temperature has been observed since the fifties in different types of steels, as for example, in high carbon steels, iron-nickel alloys and stainless steels (Klostermann & Burgers, 1964)(Klostermann, 1972). More recently, spontaneous martensitic transformation around free surface created by FIB milling in retained austenite grains of stainless duplex steel was also noticed (He *et al.*, 2014). However, to our knowledge, variant selection in surface martensite has never been reported. This study shows this phenomenon and proposes a predictive model, based on the maximization of the extension of a material fiber oriented along the normal to the sample free surface. This model is used to compare different crystallographic descriptions of the transformation. In particular, we consider the invariant plane strain and the invariant line strain based on the Phenomenological Theory of the Martensitic Crystallography (PTMC)(Bowles & Mackenzie, 1954), the Jaswon & Wheeler distortion (Jaswon & Wheeler, 1948) and the continuous distortion associated with the Kurdjumov-Sachs orientation relationship (Cayron, 2015). The study shows that all four descriptions of the transformation are able to predict correctly the trend of variant selection in surface martensite, however, the Jaswon & Wheeler distortion and the continuous distortion are more appropriate for accounting for other features of the transformation, such as the habit plane and the accommodation by twin-related variants pairing.

Material & Methods

Experimental method

A as-cast Fe-30%Ni alloy was cut and polished manually. The sample was prepared for EBSD mapping by electropolishing with the *Struers A2* electrolyte (35V, 20sec). Surface martensite appeared after the electropolishing using an electrolyte at 10°C, meaning that the transformation took place approximatively 10°C above the bulk martensitic start temperature. Maintained at the same temperature, the sample kept transforming hours later, which indicates an isothermal type of transformation. Optical images showing the evolution of the martensite transformation are available in section III of the supplementary material (Appendix A), figure S 6. EBSD characterization was performed with a *FEI-XLF 30* field emission gun SEM using the *Oxford Instruments* acquisition software.

Predictive models for variant selection

The EBSD measurements, presented in the *Results & Discussion* section, show a significant variant selection even though the material was not subjected to any stress or strain, prior or during transformation. The variant selection phenomenon is believed to result from the geometric anisotropy caused by the presence of the free surface, which allows the martensite to expand, free of constraints in the direction normal to the surface. Predictive models based on this observation and considering different modeling of the transformation are proposed.

Modeling of the transformation.

Various models are available in the literature (Bowles & Mackenzie, 1954) (Jaswon & Wheeler, 1948) (Cayron, 2015). Here, we will consider four different descriptions to compare them and analyze which is the most appropriate to predict variant selection in surface martensite. The mathematical descriptions of the transformation are defined by a transformation matrix \mathbf{F} . \mathbf{F} gives the image by the transformation of any vector \mathbf{u} : $\mathbf{u}' = \mathbf{F}\mathbf{u}$. Expressed in the austenite crystallographic basis, the four descriptions considered in this work are:

- *The Jaswon and Wheeler distortion.* The Kurdjumov-Sachs orientation relationship $(111)_\gamma \parallel (1\bar{1}0)_\alpha$; $[1\bar{1}0]_\gamma \parallel [111]_\alpha$ is often found in martensitic steels (Kurdjumov & Sachs, 1930). Based on this orientation relationship, an FCC-BCC distortion has been proposed by Jaswon and Wheeler (1948). As function of the lattice parameters, the distortion can be written:

$$\mathbf{F}^{JW} = \frac{a_\alpha}{a_\gamma} \begin{bmatrix} \frac{1}{6} + \sqrt{\frac{3}{2}} & \frac{1}{6} & -\frac{1}{2} + \sqrt{\frac{1}{6}} \\ \frac{1}{6} - \sqrt{\frac{1}{6}} & \frac{1}{6} + \sqrt{\frac{2}{3}} & -\frac{1}{2} + \sqrt{\frac{1}{6}} \\ -\frac{1}{3} + \sqrt{\frac{1}{6}} & -\frac{1}{3} + \sqrt{\frac{1}{6}} & 1 + \sqrt{\frac{1}{6}} \end{bmatrix} \quad (8.1)$$

For the Fe30%Ni, we consider the lattice parameters, $a_\alpha = 2.8635\text{\AA}$ and $a_\gamma = 3.5854\text{\AA}$, for the martensite and the austenite respectively, as measured by Goldmann and Wagner (1963).

- *The continuous distortion.* A continuous distortion for the FCC-BCC transformation has been recently proposed (Cayron, 2015). This continuous distortion, noted $\mathbf{D}^{KS}(x = \cos(\beta))$ in the aforementioned reference, leads to the Kurdjumov-Sachs orientation relationship. It can be expressed using a unique angular parameter x which evolves during the lattice transformation:

$$\mathbf{F}^{KS}(x) = \begin{bmatrix} 1 - x + \frac{1}{3}\sqrt{\frac{1-x}{1+x}}(\sqrt{6x} + \sqrt{3x}) & \frac{\sqrt{x}}{3}(-3\sqrt{x} + \sqrt{\frac{1-x}{1+x}}(\sqrt{6} + \sqrt{3x})) & \frac{1}{\sqrt{3}}(\sqrt{\frac{1-x}{1+x}}(\sqrt{2x} + x) - \sqrt{1-x^2}) \\ x - 1 + \frac{1}{3}\sqrt{\frac{1-x}{1+x}}(\sqrt{6x} + \sqrt{3x}) & \frac{\sqrt{x}}{3}(3\sqrt{x} + (\sqrt{\frac{1-x}{1+x}})(\sqrt{6} + \sqrt{3x})) & \frac{1}{\sqrt{3}}(\sqrt{\frac{1-x}{1+x}}(\sqrt{2x} + x) - \sqrt{1-x^2}) \\ \sqrt{\frac{x}{3}}\sqrt{\frac{1-x}{1+x}}(\sqrt{2} - 2\sqrt{x}) & \sqrt{\frac{x}{3}}\sqrt{\frac{1-x}{1+x}}(\sqrt{2} - 2\sqrt{x}) & \frac{1}{\sqrt{3}}(\sqrt{\frac{1-x}{1+x}}(\sqrt{2x} - 2x) + 2\sqrt{1-x^2}) \end{bmatrix} \quad (8.2)$$

The two extremal x values are $x = \frac{1}{2}$ and $x = \frac{1}{3}$, for the initial and the final distortion of the FCC lattice, respectively. It is worth recording that the complete distortion $\mathbf{F}^{KS}(x = \frac{1}{3})$ is equal to the Jaswon & Wheeler distortion with lattice parameters in hard sphere ratio, i.e. $\frac{a_\alpha}{a_\gamma} = \sqrt{\frac{2}{3}}$.

- *PTMC Invariant Plane Strain.* Variant selection caused by applied stress is classically studied using the invariant plane strain (IPS) computed from the *Phenomenological Theory of the Martensite Crystallography* (Bhadeshia *et al.*, 2008). Here, the IPS is calculated with the PTCLab software (Gu *et al.*, 2014), using the Goldmann and Wagner lattice parameters for Fe30%Ni and assuming twinning on $\{101\}_\gamma$ as lattice invariant shear (details in section V of the supplementary material in Appendix A). From the two solutions computed using PTMC, the one that best fits the experimental data is chosen.

$$\mathbf{F}^{IPS} = \begin{bmatrix} 0.99193 & 0.03516 & -0.02776 \\ -0.02808 & 1.12242 & -0.09663 \\ -0.02776 & 0.12099 & 0.90449 \end{bmatrix} \quad (8.3)$$

- *PTMC Invariant Line Strain.* Beside the IPS, the PTMC also allows computing the invariant line strain (ILS) associated with the phase transformation. For our alloy, the invariant line strain is given by:

$$\mathbf{F}^{ILS} = \begin{bmatrix} 1.11998 & 0.03516 & 0.10029 \\ -0.01947 & 1.12242 & -0.08802 \\ -0.14482 & 0.12099 & 0.78743 \end{bmatrix} \quad (8.4)$$

Variant selection criteria.

A variant selection criterion is then associated to each description of the transformation. For the invariant line strain \mathbf{F}^{ILS} , the invariant plane strain \mathbf{F}^{IPS} and the Jaswon & Wheeler \mathbf{F}^{JW}

models, the criterion is the maximization of the extension of a *material fiber* oriented along the normal to the free surface. The term *material fiber* comes from continuum mechanics and describes a set of material particles oriented along a given direction. It is not related to any texture consideration. This criterion can also be seen as the maximization of the volume change intrinsic to the transformation in a direction normal to the surface. To express it mathematically, we need to consider the gradient of displacement \mathbf{H} associated to the phase transformation $\mathbf{H} = \mathbf{F} - \mathbf{I}$. The displacement associated with the extension of a material fiber oriented along the normal to the free surface is given by the magnitude of \mathbf{H}_{zz} , when \mathbf{H} is expressed in the sample reference basis $\mathcal{B}_s = \{\mathbf{x}, \mathbf{y}, \mathbf{z}\}$. A slightly different criterion is chosen for the continuous model. Taking advantage of the continuous description, we propose to consider the maximization of the *variation* of the extension of a material fiber oriented along the normal to the free surface, at the beginning of the transformation. We thus need to compute the derivative $\dot{\mathbf{H}}^{KS}(x = \frac{1}{2}) = \frac{d\mathbf{H}^{KS}}{dx}|_{\frac{1}{2}}$ of the continuous distortion and evaluate the magnitude of $\dot{\mathbf{H}}_{zz}^{KS}$. The criterion based on the maximization of \mathbf{H}_{zz} in the case of the continuous model has also been tested in this study, but since the predictions agree with the one obtained using the Jaswon & Wheeler distortion, they are not presented here. For the variant selection, a threshold based on the absolute value of the magnitude of \mathbf{H}_{zz} or $\dot{\mathbf{H}}_{zz}$, is set to best fit the experimental data in each of these four cases. The \mathbf{H}_{zz} threshold values equal respectively 0 for the Jaswon & Wheeler model and the PTMC invariant line strain and 0.03 for the invariant plane strain. The $\dot{\mathbf{H}}_{zz}$ threshold is set to 0.2. The predictive models have been implemented using the *MTEX* toolbox (Bachmann *et al.*, 2010).

Results & Discussion

Experimental evidence of variant selection

Figure 8.1 shows two EBSD maps of surface martensite and the corresponding pole figures of the martensite. Due to the large grain size in the sample, up to millimeter scale, these maps only show a part of the parent grain. Therefore, a lower magnification EBSD measurement has been performed to verify that the measure of a single "island" of martensite is representative of the transformation produced in the whole grain. The lower magnification map is presented in the supplementary material in section I (Appendix A). From the poles figures 8.1B and 8.1D, a pronounced variant selection can be observed. In these two examples, the selection relates to variant grouping in so-called *Bain packets* (Cayron, 2013). In the martensitic transformation, there exist three Bain packets, each of them containing 8 variants which all have the same Bain strain. In $\{100\}_\alpha$ pole figures, Bain packets are easily recognizable by the circles around the $\langle 100 \rangle_\gamma$ poles. The arrows on figure 8.1B and 8.1D indicate them. It seems that the variants belonging to Bain packets having a contraction axis oriented close to the normal to the surface, *i.e.* having an expansion located in the plane parallel to the surface, appear more weakly than the others. In map 1, two Bain circles are complete whereas the third one is almost missing. In map 2, only one Bain circle is almost complete and the two others only appear partially.

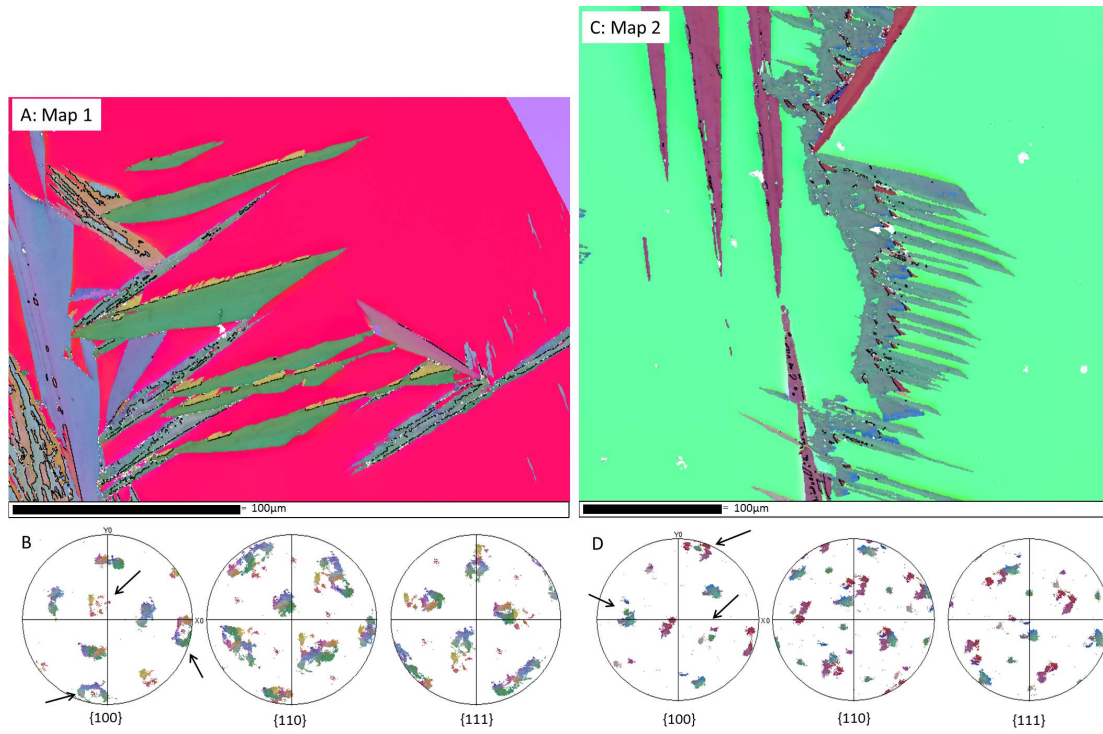


Figure 8.1: EBSD measurements of surface martensite, coloured by Euler coding. **A** and **C**: EBSD maps 1 and 2. **B** and **D**: Pole figures of the martensite in maps 1 and 2, respectively.

Variant selection predictions

Figures 8.2 and 8.3 show the predictions of the variant selection according to the four criteria applied to maps 1 and 2, respectively. When needed, detailed views have been added on the pole figures in order to better visualize the predicted variants. From figures 8.2 and 8.3 it can be seen that the trend of the variant selection by Bain packets is predicted quite correctly with all four models. Additional EBSD measurements and associated simulations, available in section II of the supplementary material (Appendix A), show the same quality of predictions.

Accommodation by twin-related variants.

The main discrepancy between the predictions -regardless of the model used- and the experiments is the light presence of the variants of the Bain packet that is associated with the compression along the surface normal. According to our computations, the variants belonging to this Bain packet are not favoured by the presence of a free surface, as for these variants the expansion mainly takes place in the xy plane. They are thus not selected in our predictive models. Nonetheless, we are able to explain their appearance by considering a "twinning" accommodation mechanism of the habit plane. By their crystallographic nature, two twin-related variants belong to two different Bain packets (Cayron, 2013). Therefore, to accommodate the nucleation of all variants belonging to two specific Bain packets that are

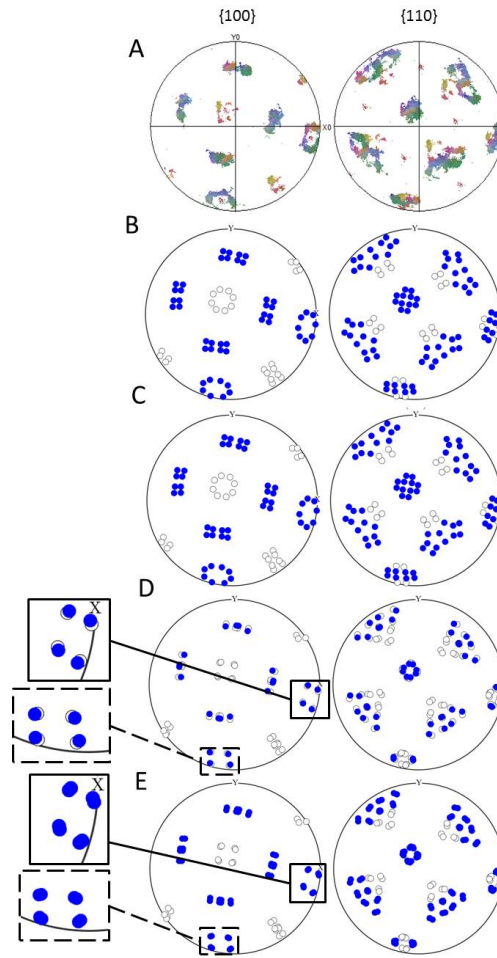


Figure 8.2: Prediction of variant selection for map 1. In blue, the selected variants. Empty circles, unselected variants. **A:** Measured pole figure. **B:** Jaswon & Wheeler distortion. **C:** Derivative of the continuous distortion. **D:** PTMC invariant plane strain. **E:** PTMC invariant line strain.

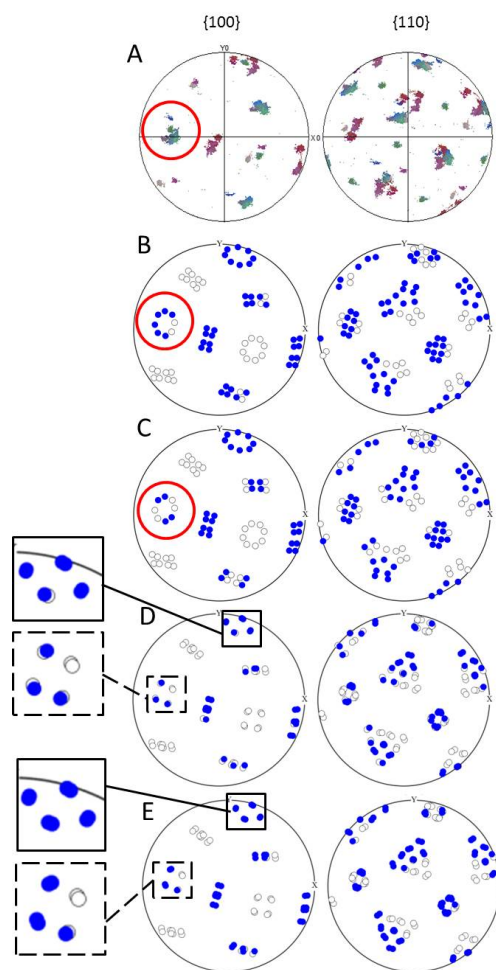


Figure 8.3: Prediction of variant selection for map 2. In blue, the selected variants. Empty circles, unselected variants. **A:** Measured pole figure. **B:** Jaswon & Wheeler distortion. **C:** Derivative of the continuous distortion. **D:** PTMC invariant plane strain. **E:** PTMC invariant line strain.

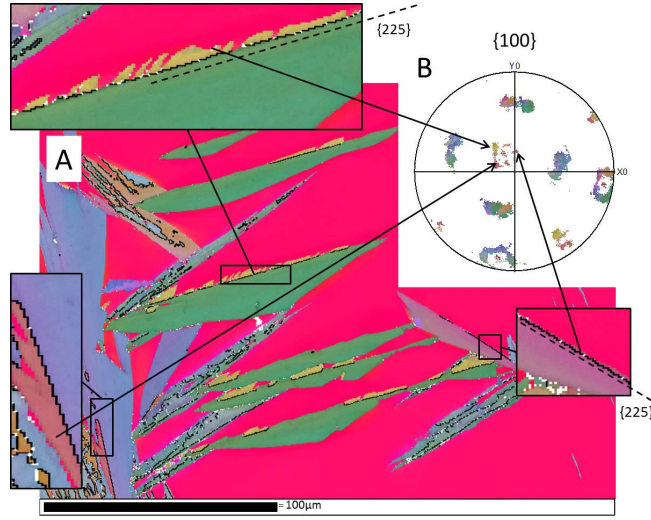


Figure 8.4: Twin-related variants combination for habit plane accommodation. **A:** EBSD map, with twin boundaries marked in black and $\{225\}_\gamma$ habit plane indicated with dashed lines. **B:** $\{100\}_\alpha$ pole figure.

favoured by the free surface, one needs variants from the third Bain packet, even if this packet is not favoured. The EBSD map in figure 8.4A with the twin boundaries marked in black shows that the variants belonging to the unpredicted Bain circle (see 8.4B) are twin-related in pair with the variant composing predominantly the martensite plates. It can be seen that the unfavoured twin-related variants are only located on the habit planes of the plates, which traces are indicated with dashed lines on figure 8.4A, confirming their role in the accommodation mechanism.

Derivative criterion vs. complete distortion criterion.

As already mentioned, for the criterion based on the maximization of the extension of a material fiber along the normal to the free surface ($\max \mathbf{H}_{zz}$), the continuous model and the Jaswon & Wheeler model give the same results. Thus, it is worth comparing figures 8.3C and 8.3B to figure 8.3A in order to analyze the effect of considering a criterion based on the *variation* of the extension ($\max \dot{\mathbf{H}}_{zz}^{KS}$), using the continuous distortion instead of the criterion based on the *total* extension ($\max \mathbf{H}_{zz}$), associated with the complete lattice distortion. By focusing on the Bain packet indicated with red circles, it seems that the criterion based on the variation improves the predictions for the variants distribution inside the indicated Bain packet, as compared to the complete distortion. This result might suggest that variant selection takes place at an early stage of the transformation, the variant being selected in the beginning of the lattice distortion. Such a vision is quite in opposition with the idea of a variant selection based on the invariant plane strain. Indeed, the IPS criterion, includes the consideration of the full distortion along with the type of accommodation as relevant for the variant selection. In other words, in the derivative criterion, the early stage of the transformation is considered

Table 8.1: Comparison of the quality for the predictions for the four different models.

| | PTMC ILS | PTMC IPS | JW distortion | Continuous distortion |
|-------|----------|----------|---------------|-----------------------|
| Map 1 | 19% | 14% | 21% | 21% |
| Map 2 | 14% | 13% | 14% | 16% |

as crucial for the selection, whereas in the IPS criterion it is the final accommodated product, which drives the selection.

Quantitative comparison of the models.

To quantify and compare more properly the quality of the predictions, we performed a computational image comparison of the predicted and the experimental datas. Binary images of the experimental and simulated pole figures are superimposed and the number of pixels that are correctly predicted, *i.e.* that are common in both the images, are counted. This number is then normalized by the union of the predicted and simulated pixels. The computational comparison is performed based on the $\{100\}_\alpha$ and $\{110\}_\alpha$ pole figures for both maps. The results are presented in table 8.1. Details of the quantitative comparison of the variant selection are available in the supplementary material in section VI (Appendix A). A second method consisting in computing the angular deviation of each experimentally measured martensite grain in respect to the closest predicted martensitic variant has also been carried out. The results were not substantially different from the one presented above and both comparisons show that the trend of variant selection is captured by all models and that we cannot completely discriminate one model from the other on the quality of variant selection prediction.

Orientation relationship and habit plane predictions.

Beside the variant selection phenomenon, it is also worth comparing the quality of the prediction for other features of the transformation, such as the orientation relationship (OR) and the habit plane. The nature of the OR can be deduced from the shape of the continuous patterns in the martensite pole figures (Suikkanen *et al.*, 2011). In particular, the curvature of the outer contour of 3-fold stars in the $\{110\}_\alpha$ pole figure tells whether the OR is closer to that of Nishiyama-Wassermann or to that of Kurdjumov-Sachs. On figures 8.5A, 8.5B and 8.5C, arrows indicate the part of the pattern to compare. If the external contour of the star is convex as it is the case in figure 8.5C, the OR is close to that of Nishiyama-Wassermann, and if it is concave as in figure 8.5B, it is close to that of Kurdjumov-Sachs. By inspection, the measured pole figures indicate that the OR is closer to that of Kurdjumov-Sachs. The measured OR is quite surprising as the NW OR has been originally observed in bulk martensite formed in Fe-30%Ni and the same OR was estimated in surface martensite by Klostermann and Burgers (Klostermann & Burgers, 1964). A closer analysis of the OR based on the misorientation across FCC-BCC boundaries has been carried out. Figure 8.5D shows the interphase boundaries associated to map 1. The boundaries are marked in green when they are close to the Kurdjumov-Sachs

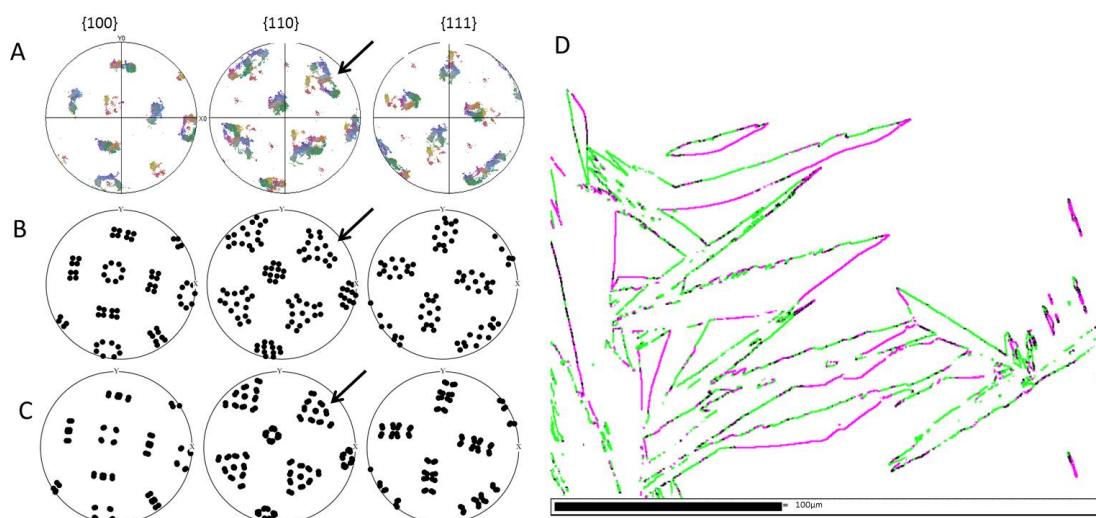


Figure 8.5: Orientation relationships. **A:** Experimental pole figures **B:** Pole figures of the Jaswon & Wheeler and continuous distortions (Kurdjumov-Sachs). **C:** Pole figures from the PTMC calculations **D:** Color map of interphase boundaries, in green, within 3° of KS, and in magenta, within 3° of NW.

OR and in magenta when they are close to the Nishiyama-Wasserman OR. It can be observed that near the habit plane the OR is closer to Kurdjumov-Sachs, but as the martensite plate grows, the OR tends to get closer to the Nishiyama-Wasserman one. The same type of gradient in the orientation relationship has already been observed by Sato & Zaefferer, in butterfly martensite (Sato & Zaefferer, 2009). They measured an OR close to Kurdjumov-Sachs near the $\{225\}_\gamma$ outer interface of the butterfly wings, while the Greninger-Troiano OR and the Nishiyama-Wassermann OR were found along the inner interface. To estimate quantitatively the occurrence of each OR in surface martensite, we measured the length of the boundaries associated with the two respective OR. In agreement with the results of analysis of the shape of the pole figure, boundaries close to KS are more often found than boundaries close to NW. Some additional details of this analysis, including the measurements of the bulk OR (figure S 17), are proposed in section VIII of the supplementary material (Appendix A). The type of habit plane is another relevant feature of the transformation that needs to be accounted in the transformation models. Based on the analysis of EBSD maps (supplementary in Appendix A, section IV), we found that the habit plane is of type $\{225\}_\gamma$. This result has been already reported in the literature (Wakasa & Wayman, 1979) (Klostermann & Burgers, 1964). The crystallography of the habit planes thus disagrees with the PTMC calculations which predict a habit plane close to $\{3\ 10\ 15\}_\gamma$. On the contrary, the Jaswon & Wheeler distortion and the continuous distortion can account for untilted $\{225\}_\gamma$ (Jaswon & Wheeler, 1948) (Cayron, 2015). In the continuous model, the $\{225\}_\gamma$ habit plane even becomes fully invariant by pairing the variants that are twin-related (Baur *et al.*, 2017). In this configuration, the shape deformation associated is exactly an IPS on $\{225\}_\gamma$. This type of accommodation agrees particularly well with Klostermann observations of isothermal martensite growth (Klostermann, 1972).

According to his study, the initial stage of the plate growth is an IPS on $\{225\}_\gamma$. The plate then grows transversally and the associated shape deformation becomes inhomogeneous. To fully appreciate the agreement between Klostermann's observations and the continuous distortion, it is worth considering again figure 8.4. It shows that an energetically unfavoured variant twin-related with a favoured one is needed to accommodate the transformation on the habit plane. The combination of these variants on the habit plane produces an IPS. This corresponds to the Klostermann's first stage. Then, once the habit plane is accommodated, the twin that is energetically most favoured grows preferentially.

Both the Jaswon & Wheeler distortion and the continuous model are able to account convincingly for the accommodation mechanism and the habit plane observed in surface martensite. Using PTMC, the surface martensite habit plane is wrongly predicted if the real lattice parameters are considered, but one can account for such a habit plane by using lattice parameters in hard sphere packing ratio as input for the computation (Baur *et al.*, 2017). In terms of orientation relationship, it appears that the Jaswon & Wheeler distortion and the continuous distortion well describe the early stage of the transformation, while PTMC prediction of the orientation relationship is valid for the fully grown plate.

Conclusion

In conclusion, we observed and analyzed variant selection in surface martensite formed in a Fe-30%Ni alloy. The variant selection was found to be related to the Bain packets. A prediction model based on the maximization of the extension of a material fiber oriented along the normal to free surface is proposed. Different descriptions of the transformation have been tested. In particular, PTMC matrices, namely the invariant plane strain and the invariant line strain, the Jaswon & Wheeler distortion and the continuous distortion have been compared. The variant selection prediction is not significantly different using these different models, such that none of the models can be discriminated from the others on this basis. However, the Jaswon & Wheeler distortion and continuous distortion allow a more complete description of the transformation as they accounts well for other features of the transformation such as the $\{225\}_\gamma$ habit plane and the accommodation mechanism by twin-related variants pairing. Finally, this study suggests that it might be worth considering of the *variation* of the extension of a material fiber oriented along the normal to the free surface at an early stage of the transformation, using the continuous description of the transformation, instead of its total extension based on the complete transformation.

Acknowledgements.

This work has been supported by the Swiss National Science Foundation (200021_159955), which is therefore gratefully acknowledged. The authors would also like to thank PX Group for its financial support to the laboratory and ArcelorMittal, in particular K. Zhu and I. Zuazo, for graciously providing the material used in this study.

Bibliography

- [1] Bachmann E, Hielscher R. & Schaeben H. (2010). *Solid State Phenom* **160**, 63-68.
- [2] Baur A.P. , Cayron C. & Logé R.E. (2017). *Sci. Rep.* **7**, doi: 10.1038/srep40938
- [3] Bhadeshia H.K.D.H, Abreu H. & Kundu S., (2008). *Int. J. Mat. Res.* **99**, 342-346.
- [4] Bowles J.S. & Mackenzie J.K.(1954). *Acta Metall.* **2**, 129-137.
- [5] Cayron C.(2013). *Acta Cryst.* **69A**, 498-509.
- [6] Cayron C.(2015). *Acta Mater.* **69**, 189-202.
- [7] Gey N., Petit B. & Humbert M. (2005). *Metall. Trans. A* **36A**, 3291-3299.
- [8] Goldmann A.J. & Wagner C.N.J. (1963). *Acta Metall.* **2**, 405-413.
- [9] Gu X.-F, Furuhashi T. & Zhang W.-Z. (2016). *J. Appl. Cryst.* **49**, 1099-1106.
- [10] He B.B., Huang M.X., Ngan A.H.W., van der Zwaag S. (2014). *Metall. Trans. A.* **A45**, 4875-4881.
- [11] Jaswon M.A. & Wheeler J.A. (1948). *Acta Cryst* **1**,216-224.
- [12] Klostermann J.A. & Burgers W.G. (1964). *Acta Metall.* **12**, 355-360.
- [13] Klostermann J.A. (1972). *J. Less Common Met.* 75-94.
- [14] Kurdjumov G.V. & Sachs G.(1930). *Z. Phys.* **74**, 325-343.
- [15] Mishiro Y., Nambu S., Inoue J. & Koseki T. (2013). *ISIJ int.* **53**, 1453-1461.
- [16] Miyamoto G., Iwata N., Takayama N. & Furuhashi T. (2012). *Acta Mater* **60**, 1139-1148.
- [17] Sato H., Zaefferer S., (2009). *Acta Mater.* **57**, 1931-1937.
- [18] Suikkanen P.P, Cayron C., DeArdo A.J. & Karjalainen L. P. (2011). *J. Mater. Sci. Technol.* **27**(10), 920-930.
- [19] Wakasa K. & Wayman C.M. (1979). *Scripta Metall.* **13**, 1163-1166.
- [20] Wittridge N.J. & Jonas J.J. (2000). *Acta Mater.* **48**, 2737-2749.

9 On the chevron morphology of surface martensite

Authors: A.P. Baur, C. Cayron and R.E. Logé, Laboratory of Thermomechanical Metallurgy-PX group Chair, Institute of materials, Ecole Polytechnique Fédérale de Lausanne, 2002 Neuchâtel, Switzerland.

Submitted to: Acta Materialia (under review)

Authors contributions: Conceptualization, A.P.B., C.C. and R.E.L.; methodology, A.P.B. and C.C.; software, A.P.B.; validation, A.P.B. and C.C.; formal analysis, A.P.B. and C.C.; investigation, A.P.B.; resources, A.P.B. and C.C.; data curation, A.P.B.; writing—original draft preparation, A.P.B., C.C. and R.E.L.; writing—review and editing, A.P.B., C.C. and R.E.L.; visualization, A.P.B.; supervision, C.C. and R.E.L.; project administration, C.C.; funding acquisition, C.C. and R.E.L.

Abstract

It is established that the annealing twin boundaries of austenite act as nucleation sites for the martensitic transformation. In the present study, we observe that in surface martensite the transformation only takes place for twin boundaries that are approximately vertical in respect with the sample free surface. This phenomenon is shown to be related to variant selection. The criterion for surface martensite formation introduced in a previous study is used here to account for the selection of the twin boundaries that promote the transformation. This criterion correctly captures the phenomenon and explains the highly symmetrical chevron morphology observed in surface martensite.

Introduction

The formation of surface martensite in steels was reported several times in the past and studied in details by Klosterman and Burgers [1]. Different alloys (stainless steels, iron-nickel and iron-nickel-manganese alloys) exhibit this particular form of martensite [2, 3, 4]. Recently, the present authors showed that a natural variant selection takes place in the martensite formed at the surface of Fe-30wt%Ni alloys [5]. The phenomenon is caused by the presence of the free surface which favours the nucleation of some particular martensite orientations. The selection was modeled by using a criterion for martensite formation based on the maximisation of the extension of a material fibre oriented along the normal to the free surface. Different transformation models were compared and we showed that the FCC-BCC distortion associated with the Kurdjumov-Sachs orientation relationship [6, 7] convincingly accounts for both the variant selection and the crystallographic features of surface martensite, such as the $\{225\}_{\gamma}$ habit plane and the Kurdjumov-Sachs orientation relationship. Like free surfaces, grain boundaries are also known to promote the nucleation of martensite [8]. Experiments on annealed samples show that twin boundaries in particular act as potent nucleation site for the martensitic transformation, in both surface and bulk martensite [2, 9, 10, 11]. In the present study, the formation of surface martensite is studied in a cold-worked and recrystallized Fe-30wt%Ni alloy, exhibiting a high number of annealing twin boundaries. We observe that not all the twin boundaries are equivalently efficient to promote the formation of surface martensite. Only the boundaries with particular spatial orientations allow the nucleation of martensite. The phenomenon is studied by considering the criterion for surface martensite formation introduced in our previous study [5]. We show that this criterion explains the austenite spatial orientations for which the transformation preferentially takes place, which rationalizes the highly symmetrical morphology observed in the surface martensite.

Experimental method

Fe-30wt%Ni samples have been cold-worked and recrystallized in quartz tubes at $1'100^{\circ}\text{C}$ for 3 hours. They were grinded down to 1 micron and electropolished with *Struers* A2 electrolyte at 35V for 20s. The temperature of the electrolyte was about 10°C . It is above the M_s temperature of Fe-30wt%Ni bulk martensite, which is reported to be lower than 0°C [12]. Surface martensite appears during electropolishing. This transformation above the M_s is believed to be caused by the removal of the stresses on the polished surface. The produced martensite is characterized by using an XLF-30 (FEI) scanning electron microscope, equipped with a Channel5/Aztec (Oxford Instruments) EBSD system.

Results and discussion

Crystallographic characterization

By analyzing the entire polished surface, we observe that almost all the martensite products have a highly symmetrical chevron morphology. This morphology is illustrated in the optical micrograph in figure 9.1 and in the EBSD measurements of figures 9.2A and 9.4A.



Figure 9.1: Optical micrograph of the chevron martensite formed on the surface of the recrystallized Fe-30wt%Ni sample.

The measurement in figure 9.2 indicates that the two austenite grains (yellow and green) are misoriented by a 60° rotation about $[111]_{\gamma}$. The trace of the grain boundary is perpendicular to the common $[111]_{\gamma}$ and indicated by the circle on figure 9.2B. The corresponding grain boundary is thus an annealing twin boundary. The nucleation of surface martensite exhibiting the chevron morphology appears to be related to the presence of such boundaries. Figure 9.3 illustrates schematically the morphology and the crystallography of chevron martensite.

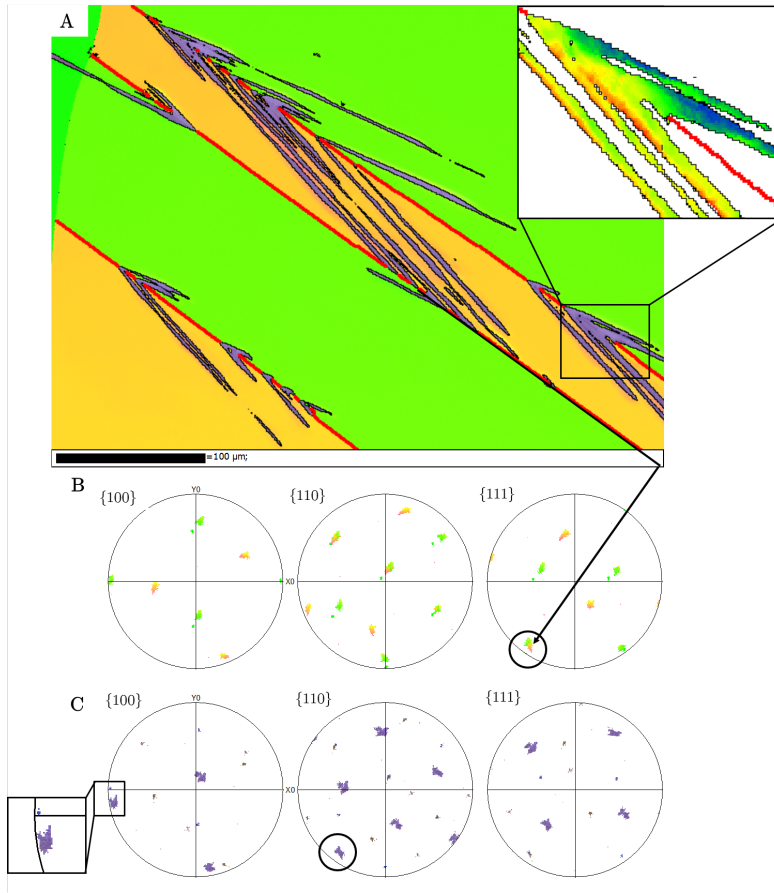


Figure 9.2: EBSD map of the chevron martensite. **A:** Austenite and martensite in Euler colour coding. Austenite twin boundaries are marked in red. Detailed window: internal misorientation of the martensite: Blue 0° to red 8°. **B:** Pole figures of the austenite. **C:** Poles figures of the martensite.

Figure 9.3A shows two twin-related austenite grains (1 and 2) separated by a twin boundary in red. On each side of the twin boundary, a lenticle of martensite appears. The chevron consists in the assembly of these two lenticles. A detailed crystallographical analysis based on the EBSD measurement suggests that the habit plane of each lenticle is of type $\{225\}_{\gamma}$, and the orientation relationship is close to Kurdjumov-Sachs, in agreement with our previous study of surface martensite (see supplement 2 (Appendix C) for the details) [5]. Figure 9.3B shows two twin-related grains (1 and 2) represented with the $\{111\}_{\gamma}$ planes. The common $(111)_{\gamma}$, which is the twin boundary, is marked in grey. The six Kurdjumov-Sachs variants having their close-packed plane parallel to the common $(111)_{\gamma}$ close-packed plane are represented with parallelograms. These six variants belong to the same close-packed plane packet (CPP packet). When the close-packed plane associated with these variants corresponds to the twin boundary, the variants have the particularity of being common to both twin-related grains. From the EBSD measurements in figure 9.2, the variants forming the chevron correspond to that case. The common $(1\bar{1}0)_{\alpha} \parallel (111)_{\gamma}$ is indicated in figure 9.2 with circles on the $\{110\}_{\alpha}$ and

$\{111\}_\gamma$ poles figures (Figure 9.2B and 9.2C). As a consequence, the chevron is in Kurdjumov-Sachs orientation relationship with both grains. The propensity of martensite to nucleate in orientation relationship with two different neighbour grains is well documented. This particularity is, for exemple, used as variant selection criterion by Tomida *et al.* [13] and its implication on the micro-mechanics of steel has been recently enlightened by Archie *et al.* [14]. The same nucleation behaviour is also observed in the heterogeneous nucleation of BCC precipitates formed on FCC annealing twin boundaries in Ni-Cr alloys and in the nucleation of FCC precipitates formed on the BCC deformation twin boundary in a duplex stainless steel [15]. The EBSD characterization of the martensite chevron (figure 9.2C) further indicates that

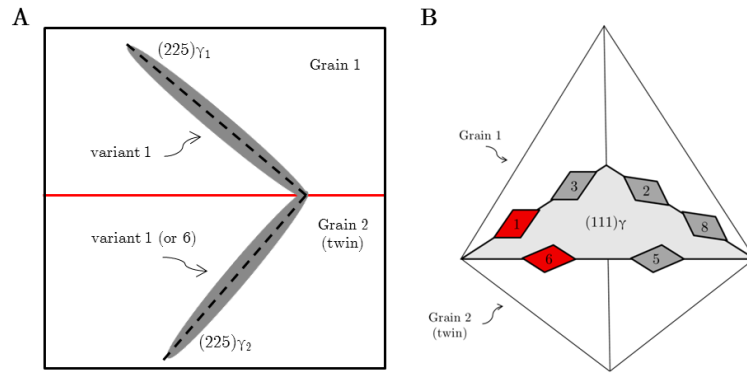


Figure 9.3: Schematic representation of the crystallography and morphology of chevron martensite. **A:** $\{225\}_\gamma$ lenticles of martensite composing the two "wings" of the chevron, each lenticle nucleating on one side of a twin boundary indicated in red. **B:** Two tetrahedras representing the $\{111\}_\gamma$ of the two twin-related austenite grains, grain 1 and grain 2 (twin). The tetrahedras are matching on the common $(111)_\gamma$ (twin boundary) coloured in grey, such that the $(111)_\gamma$ is a mirror plane between the two grains. The martensite variants belonging to the common CPP packet are represented by rectangles, which appear as parallelograms because of the 3D representation. A pair of misoriented variants are coloured in red.

the martensite orientation, in purple, spreads between the two low-misoriented Kurdjumov-Sachs variants belonging to the same CPP packet. The inserted window in figure 9.2A shows the misorientation inside the chevron. The reference orientation is taken on the top right edge of the chevron, in blue. The gradient of colour indicates the gradient of misorientation from 0° (blue) to 8° (red). We measure about 3° to 5° of misorientation between the two sides of the chevron and less than 2° of misorientation inside each wing of the chevron. Exemple of such pair of low-misoriented variants are illustrated in red in figure 9.3B. Among the six variants of the CPP that are in orientation relationship with both twin-related grains, a maximum of two low-misoriented variants appear. In fact, as schematically illustrated in figure 9.3A, the lenticles composing the chevron are either made of the same variant (1), or of the two low-misoriented variants (1 and 6). This suggests that a variant selection takes place inside the CPP packet. The phenomenon was expected as it has already been evidenced and modeled in our recent study of surface martensite [5]. As can be observed on the low magnification

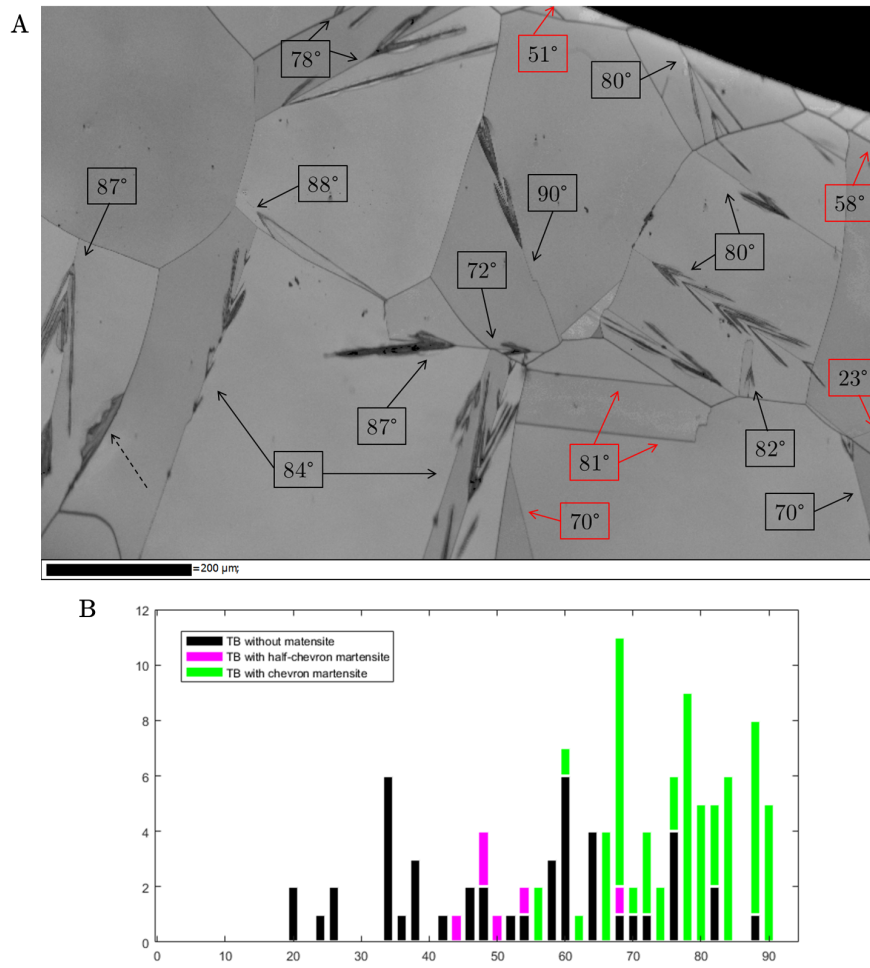


Figure 9.4: **A:** Band contrast EBSD maps of the martensite with the annotation of the angle in degrees between the normal to the $\{111\}_{\gamma}$ twinning plane and the normal to the free surface. **B:** Histogram of the angle in degrees between the normal to the $\{111\}_{\gamma}$ twinning plane and the normal to the free surface on the twin boundaries where martensite is observed. In black, the twin boundaries where no martensite is observed. In purple, the six occurrence of martensite nucleation on a single side of the boundary ("half-chevron") and in green the sixty occurrences of martensite nucleation on both sides of the grain boundary (full chevron). A total of 111 grain boundaries are analyzed. Sixty chevrons are observed and six half-chevrons.

EBSD maps in figure 9.4A, the reproducibility of the morphology produced in our sample is striking; the chevron morphology is very frequently observed (about 90% of all cases). Rarely, the martensite is seen to form on one side of the twin boundary only. We called this unfrequent morphology of martensite *half-chevron*. Maps showing half-chevrons are presented in supplement 1 (Appendix C). Another exception of the chevron morphology is illustrated in figure 9.4A and indicated by a dashed arrow on the lower left corner. Some martensite with no particular morphology appears on a grain boundary, which is not an annealing twin. The latter nucleation has been observed in other maps, but the amount of such allotriomorph

martensite is always small. It is worth mentioning that the *chevron martensite* is different from the butterfly martensite, as the chevrons are the result of the martensite nucleation in two different grains, contrarily to the butterfly martensite which forms in a single austenite grain [16, 17, 18]. The symmetry of the chevron suggests that the twin boundary where the martensite forms has a particular orientation with respect to the sample free surface. If one considers that the martensite orientation on both sides of the twin boundary is the same, the perfect symmetry is reached only for *vertical* orientation of the twinning plane, namely when the normal to the twinning plane is at 90° from the surface normal. To verify experimentally this hypothesis, the angle between the normal to the twinning plane and the surface normal is measured in different grains using EBSD measurements. As an example of this analysis, the measured angles are indicated in figure 9.4A. We annotated in black the twin boundaries where martensite is observed and in red where no martensite appears. Various EBSD maps were acquired to increase the statistics. An histogram summarizing these measurements is presented in figure 9.4B. We marked in black the twin boundaries where no martensite forms, in purple the occurrences where half-chevrons are observed, and in green the cases where full chevrons are formed. The maps associated with the measurements shown in figure 9.4B are presented in supplement 1 (Appendix C). For geometrical reasons, twin boundaries with high angles are more often seen when examining a sample surface than those with low angles. For example, a twin boundary parallel to the surface (angle of 0°) cannot be observed by surface analysis. This consideration explains why the histogram shows no twin boundaries with angles lower than 20° . The histogram indicates that there are two thresholds for the orientation of the twin boundaries to promote the nucleation of martensite. The angle between the normal to the twin boundaries where martensite nucleates and the free surface normal is greater than 44° . Half-chevrons are observed for angles between 44° and 55° , and above this value with a single exception at 68° , the morphology is always the classical chevron. The mean angle where chevron martensite is observed is 77° , while the mean angle associated with all observed twin boundaries is 65° . The measurements thus suggest that there is a selection of the twin boundaries where surface martensite forms, the relatively *vertical* twin boundaries being more efficient nucleation sites than randomly oriented ones. From our experimental measurements, we conclude that the nucleation of martensite is affected by different factors. First the nucleation takes place on the twin boundary and the martensite is in Kurdjumov-Sachs orientation relationship with both twin-related parent crystals. This implies that the variants of martensite that form belong to the CPP packet associated with the twin boundary. Second, among the six variants of the CPP, a maximum of two variants are observed per twin boundary, these variants being low-misoriented. Finally, it also appears that not all the twin boundary are equivalently efficient in promoting the phase transformation, the chevrons forming preferentially on rather *vertical* twin boundaries.

Variant selection modelling

We propose to adress the selection phenomenon occuring inside the CPP packet, by using our model for variant selection in surface martensite presented in reference [5]. We define the favoured variants as those that maximize the zz component of the gradient of displacement $\mathbf{H} = \mathbf{F}|_{x=\frac{1}{3}} - \mathbf{I}$, when expressed in the sample basis: $Max(H_{zz})$. The sample basis is such that the z -direction is normal to the free surface. This criterion is computed using the continuous FCC-BCC distortion $\mathbf{F}(x)$ where x varies from $x = \frac{1}{2}$, no transformation, to $x = \frac{1}{3}$ describing the complete transformation [Cayron, 2015]. The complete transformation corresponds to the Jaswon and Wheeler model with FCC and BCC lattice parameters in hard sphere ratio [Jaswon and Wheeler, 1948]. The complete distortion is expressed as follows:

$$\mathbf{F}\left(\frac{1}{3}\right) = \begin{bmatrix} \frac{\sqrt{6}}{18} + 1 & \frac{\sqrt{6}}{18} & -\frac{\sqrt{6}}{6} + \frac{1}{3} \\ \frac{\sqrt{6}}{18} - \frac{1}{3} & \frac{\sqrt{6}}{18} + \frac{2}{3} & -\frac{\sqrt{6}}{6} + \frac{1}{3} \\ -\frac{\sqrt{6}}{9} + \frac{1}{3} & -\frac{\sqrt{6}}{9} + \frac{1}{3} & \frac{\sqrt{6}}{3} + \frac{1}{3} \end{bmatrix} \quad (9.1)$$

The continuous model is chosen to model the transformation as it better accounts for the Kurdjumov-Sachs orientation relationship and the $\{225\}_{\gamma}$ habit plane than the PTMC (Phenomenological Theory of the Martensite Crystallography) predictions using the Fe-30wt%Ni lattice parameters [5]. As compared to our original model in reference [5], we add here an additional hypothesis on the nucleation of martensite. We consider that martensite nucleates only on the twin boundaries and that it is in Kurdjumov-Sachs orientation relationship with both grains. We thus restrict the number of variants that could form to the six variants belonging to the CPP associated with the twin boundary. From the EBSD measurements we extract the two austenite orientations and for each of them we compute the distortion associated with the six aforementioned variants. In each grain, the variant exhibiting the highest H_{zz} value is selected. The result of the simulation are presented in the pole figures in figures 9.5A and 9.5B for the green and the yellow grains, respectively. For each austenite orientation, the 24 Kurdjumov-Sachs variants are represented by empty circles. The variant selected in the green grain is marked in green on both figures 9.5A and 9.5B, similarly the variant selected in the yellow grain is marked in orange, for a better visibility. Superimposed on the simulations, we plotted the experimental martensite orientations of figure 9.2 in black. The simulation indicates that the variant that is selected in the green grain is low-misoriented with the variant selected in the yellow grain. The simulation and the experimental measurements are in good agreement. The same quality of results is obtained for two additional simulations proposed in supplement 1 (Appendix C).

Consequently, we propose to apply our criterion for variant selection to explain the selection of the twin boundary on which the martensite preferentially nucleates, and to rationalize its chevron morphology. We explore the space of all possible orientations of an austenite crystal with respect to a free surface normal to z , and evaluate H_{zz} for a given variant. The variant considered in the computation (equation 9.1) has the invariant $[1\bar{1}0]_{\gamma}$ direction and

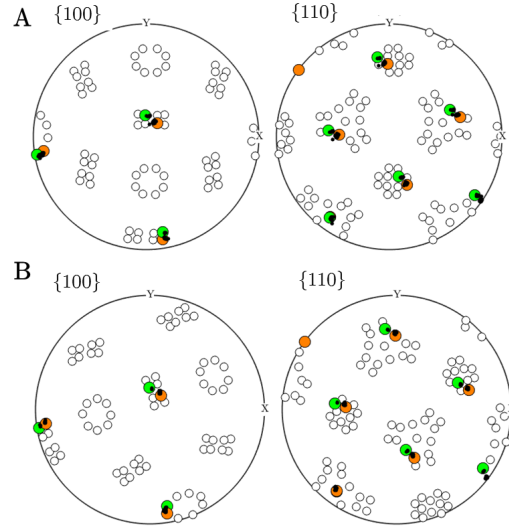


Figure 9.5: Simulated pole figure of the chevron martensite in figure 9.2. **A:** Simulation in the green grain. **B:** Simulation in the yellow grain. In green, the orientation selected by the maximum work criterion in the green grain and in orange the orientation selected by the maximum work criterion in the yellow grain. The experimental orientations are superimposed in black.

the untilted $(111)_\gamma$ plane. This variant belongs to the $(111)_\gamma$ CPP packet and accordingly is associated with a $(111)_\gamma$ twin boundary. We choose to discretize the space of the possible orientations of austenite using two rotations: the first one around $[1\bar{1}0]_\gamma$ and the second one around $[111]_\gamma$. Because the H_{zz} expresses a projection along the normal to the sample surface, only two rotations are necessary to explore the space. The angular step of each rotation is 0.01 rad. The initial orientation of the austenite crystal is such that the $[1\bar{1}0]_\gamma$ direction is along the x -axis of the sample, the $[11\bar{2}]_\gamma$ along the y -axis and the $[111]_\gamma$ along the z -axis, namely along the normal to the free surface. This initial orientation is illustrated in figure 9.6A. Figure 9.6C shows a map of the value of H_{zz} as function of the two rotation angles. The first rotation around $[1\bar{1}0]_\gamma$ is represented on the θ -axis and the second around $[111]_\gamma$ is represented on the ϕ -axis. In figure 9.6D, we plotted the maximal value of H_{zz} found as function of the θ angle between the $[111]_\gamma$ and the normal to the free surface. The dependence of the H_{zz} value to the angle between the surface normal and $[111]_\gamma$ has a symmetrical shape about 90° . The maximum value is 0.1528 and it corresponds to the angles of 73° (and 107°). This variant is thus favoured when its close-packed plane, hence the twin boundary, is rather vertical with respect to the free surface normal. An illustration of that situation is proposed in figure 9.6B. The experimental measurements reported in figure 9.4D show that there is not a unique orientation of the twinning plane that favours the martensite nucleation. The angle θ between the normal to the $\{111\}_\gamma$ twin boundary where martensite forms, with either a half or a full chevron, and the normal to the sample free surface spreads from about 44° to 90° . By using a threshold value on the H_{zz} criterion for the nucleation of martensite, we select a number

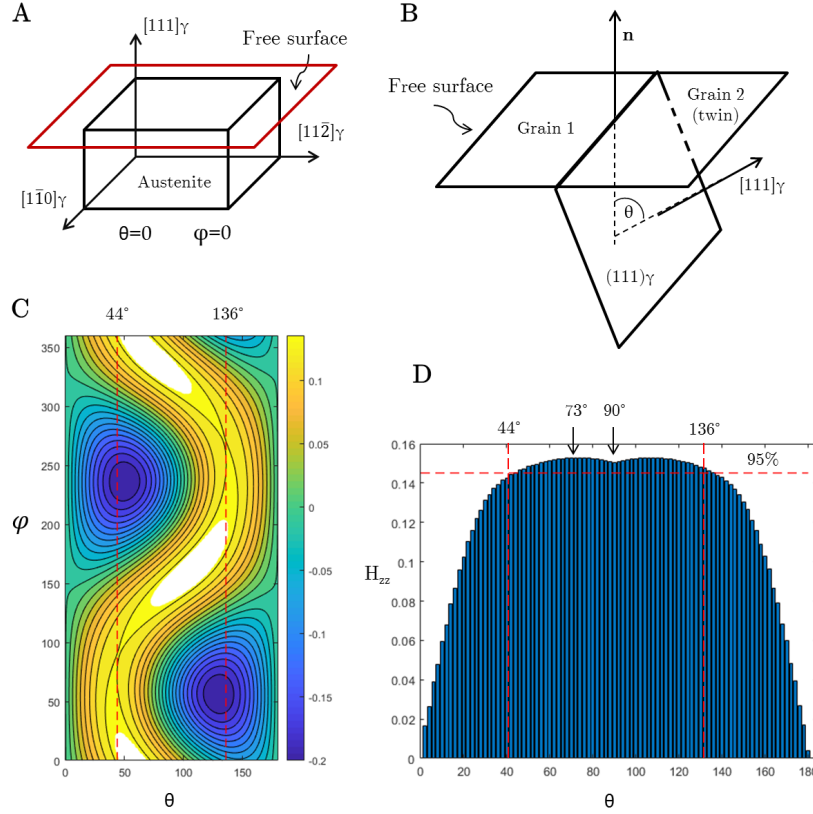


Figure 9.6: H_{zz} criterion for the martensite nucleation for a variant belonging to $(111)_\gamma \parallel (1\bar{1}0)_\alpha$ CPP packet. **A**: Initial orientation ($\phi = 0$ and $\theta = 0$) of the austenite crystal considered in the simulation. The free surface is represented by the plane drawn in red. **B**: Schematic representation of the favourable twinned austenite orientation for martensite nucleation. \mathbf{n} is the normal to the free surface. Grain 1 and grain 2 are twin-related. The θ angle between the common $(111)_\gamma$ twinning plane and the free surface normal is represented. **C**: Map of H_{zz} as function of the austenite orientation. The orientation is defined by a rotation of the austenite around $[111]_\gamma$ on the ϕ -axis and the rotation around the $[1\bar{1}0]_\gamma$ on the θ -axis. The red dashed lines represent the threshold of the H_{zz} for martensite nucleation, namely $95\% \cdot \text{Max}(H_{zz})$. **D**: H_{zz} value as function of the angle between the normal to the free surface and the $(111)_\gamma$ twinning plane. The red dashed lines indicate the values of the threshold for martensite nucleation.

of austenite orientations that are the most efficient to promote the transformation. This threshold is set to mimik the experimental range. It is found to be about 95% of the maximum value of the H_{zz} component, namely 0.1452, such as to reach a threshold angle of 44° . The threshold H_{zz} value and the corresponding angles are illustrated on figures 9.6C and 9.6D with the dashed red lines. The orientation satisfying the $95\% \cdot \text{max}(H_{zz})$ condition are marked in white in figure 9.6C.

It has been seen before that the martensite transformation tends to take place on both sides of

the twin boundary, so we also evaluate the value of H_{zz} on the other side of the twin boundary, namely in grain 2, if one refers to the sketch in figure 9.6B. This computation is performed for the six different variants that belong to the same CPP packet associated with the $(111)_\gamma$ twin boundary. Figure 9.7A-F shows the value H_{zz} of all variants as function of the θ and ϕ angles of rotation around $[1\bar{1}0]_{\gamma_1}$ and the $[111]_{\gamma_1}$. The map in figure 9.7A represents the H_{zz} of variant 1 in grain 2, and in figure 9.7B-F the maps of the H_{zz} of the other 5 variants inside the CPP packet are illustrated. The pairs of maps (A-B), (C-D) and (E-F) in figure 9.7 are very similar. This similarity was expected as these are pairs of low-misoriented variants. In each figure 9.7A-F, the orientations satisfying the $95\% \cdot H_{zz}$ criterion in grain 2 are marked in white. We also report in black the orientations that favour the nucleation of variant 1 in grain 1. They correspond to the orientations marked in white in figure 9.6C. The orientations that favour the nucleation of martensite variants on both side of the twin boundaries are the intersection of the black and the white clouds. It appears that the clouds intersect only for variant 1 (figure 9.7A) and its low-misoriented variant (figure 9.7B). These results indicate that if a twin boundary is oriented such that the nucleation of a given variant is promoted on one side of the twin boundary (grain 1), the nucleation of martensite on the other side of the boundary (grain 2) is favoured only for the variants whose orientation is either the same or low-misoriented with the variant favoured in grain 1. This result is in agreement with the experimental results in figure 9.2 showing that the martensite orientation spreads between two low-misoriented Kurdjumov-Sachs variants. The computation further indicates that the nucleation of martensite on both sides of the twin boundary is favoured when the twin boundary is exhibiting an angle above 74° with respect to the free surface. The condition that the twinned austenite should satisfy for nucleation on both side of the twin boundary, resulting in the formation of the chevron, is thus more restrictive than the condition for the nucleation on only one side of the boundary, which is associated with the formation of half chevron (44°). Taken together, the results well agree with the experimental measurements. They indicate that for angles between 44° and 74° , the martensite tends to form only in one side of the boundary, which experimentally corresponds to magenta bars in figure 9.4B, and full chevron (green bars) should be observed for angles greater than 74° . It can be noted however that some full chevrons are observed for angle between 55° and 70° , which are not accounted by our calculations. For such orientations, we predict that the transformation will take place only in one side of the twin boundary. This discrepancy could indicate that the nucleation on one side of the boundary promotes the nucleation on the other side. In other words, if the criterion for nucleation is satisfied on one side (grain 1) the computed H_{zz} value on the other side (grain 2) can be a little bit lower than the threshold value for nucleation and still the transformation occurs in both grains. It is also interesting to note that the threshold value found in this study is larger than the one we used in our previous study [5]. In the latter case, to account for all the variants formed, the most appropriate threshold was set to 0. Only the variants having negative value of H_{zz} *i.e.*, those associated with a contraction along the normal to the free surface were not formed. It seems thus that the initial state of the material affects the value of the threshold. Indeed, the sample used in reference [5] was an as-cast sample, whereas this one has been annealed after work-hardening. It should be acknowledged

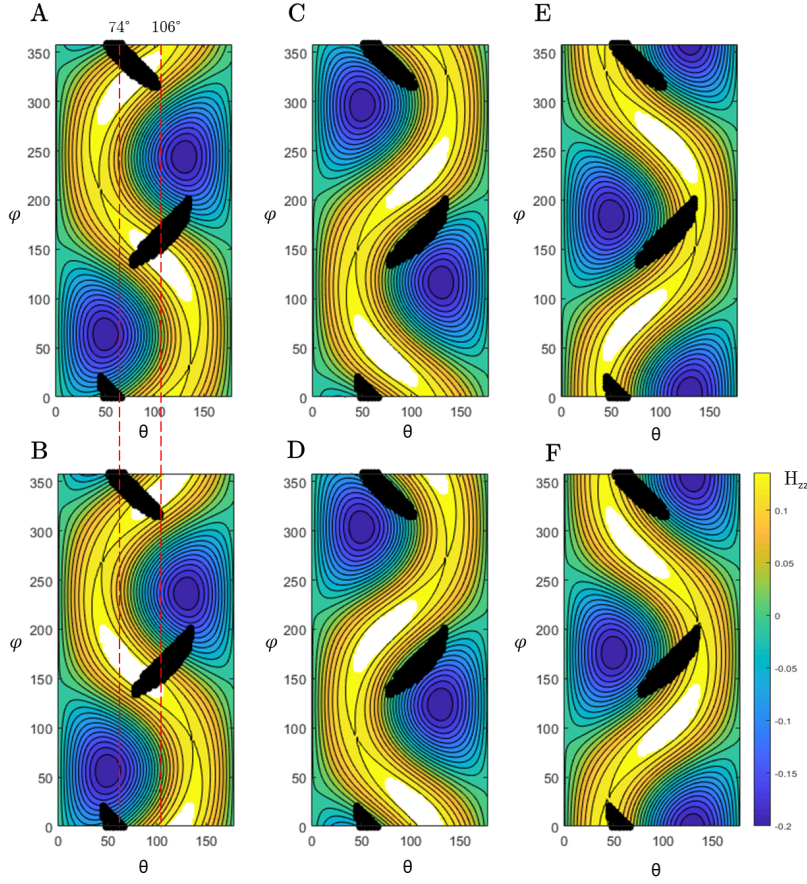


Figure 9.7: **A:** Map of H_{zz} for variant 1 in grain 2 as function of the austenite orientation. The orientation is defined by a rotation of the austenite around $[1\bar{1}0]_\gamma$ on the θ -axis and a rotation around the $[111]_\gamma$ on the ϕ -axis. The orientation satisfying the 95% $\cdot \max(H_{zz})$ criterion in grain 2 are marked in white. The orientations that are satisfying the 95% $\cdot \max(H_{zz})$ criterion in grain 1 are marked in black. **B-F:** Map of H_{zz} for the 5 other variants inside the $(111)_\gamma$ CPP packet in grain 2 as function of the austenite orientation. The orientation satisfying the 95% $\cdot \max(H_{zz})$ criterion in grain 2 are marked in white. The orientations that are satisfying the 95% $\cdot \max(H_{zz})$ criterion for variant 1 in grain 1 are marked in black. The pairs of variants represented in (A-B) (C-D) and (E-F) are low-misoriented variants. The red dashed lines indicate the θ angular range (74°-106°) where the criterion for nucleation is satisfied for at least one of the two low-misoriented variants in both grain 1 and grain 2.

also that in each case the threshold has been set to mimik the experimental data and, as such, it should be considered with care. In our previous work, we noted that using the variation \dot{H}_{zz} of the H_{zz} component at the beginning of the transformation seemed a good criterion for the variant selection. This criterion has been tested here and does not lead to more convincing results. We tested also whether the *invariant plane strain* (IPS) predicted by the PTMC was able to account for the variant selection observed in the present work. Our computations shows that given the austenite orientation the PTMC is able to predict fairly well the variants

that form preferentially. However, this model cannot account for the particular orientations of the austenite that favours the martensite nucleation. The details of the computation are available in the supplement 3 (Appendix C).

Conclusions

In conclusion, surface martensite has been formed in Fe-30wt%Ni recrystallized sample during electropolishing. The transformation occurs preferentially on twin boundaries, and the martensite formed on that boundaries exhibits a highly symmetrical chevron morphology. EBSD measurements indicate that the transformation is favoured on twin boundaries that are rather vertical with respect to the sample surface, and that the martensite is in Kurdjumov-Sachs orientation relationship with both twin-related austenite grains. The characterizations further show that the variants forming on the two sides of the twin boundary are the same or low-misoriented and that they belong to the CPP packet associated with the twin boundary. Among the six variants of the CPP packet, a maximum of two variants per twin boundary are observed indicating a variant selection phenomenon inside the CPP packet. The variant selection is addressed by using the criterion for variant selection proposed in our recent study on surface martensite based on the maximization of the extension in a direction normal to the free surface [5]. We show that starting from two experimental twin-related austenite orientations the criterion correctly predicts the martensite orientation formed on the twin boundary in three different EBSD maps. We then use the same criterion to explain why the rather vertical twin boundaries are preferred nucleation sites. Stating that the martensite nucleates on twin boundaries and that it belongs to the CPP packet associated with the twin boundary on which it nucleates, we have evaluated our criterion for surface martensite formation for all possible orientations of the austenite. The calculations were performed for each of the six variants composing the CPP packet. They indicate that only the austenite orientations associated with rather vertical twin boundaries maximize the criterion for nucleation on both side of the twin boundary, and that among the six variants, the favoured ones are either low-misoriented or the same in the two austenite grains. This study explains the selection of the twin boundaries promoting the transformation and hence rationalizes the highly symmetrical chevron morphology observed in surface martensite nucleating on twin boundaries.

Acknowledgments

We would like to thank the Swiss National Science Foundation for supporting this research (grant number 200021-159955). The authors also acknowledge ArcelorMittal, in particular Kangying Zhu for providing the material of this study. Finally, we acknowledge PX Group for its financial support to the laboratory.

Bibliography

- [1] J.Klostermann, W.Burgers, Surface martensite in iron-nickel, *Acta metallurgica*, 12(4), (1964) 355–360.
- [2] J.Breedis, Martensitic transformation in iron-chromium-nickel alloys, *Trans. AIME*, 57(230), (1964), 1583–1595.
- [3] B. He, M. Huang, A. Ngan, S. Van Der Zwaag, Effect of free surface on the stability of individual retained austenite grains in a duplex stainless steel, *Metallurgical and Materials Transactions A* 45 (11) (2014) 4875–4881.
- [4] K. Wakasa, C. Wayman, Crystallography and morphology of surface martensite in fe-20% ni-5% mn, *Scripta Metallurgica*, 13(12), (1979), 1163–1166.
- [5] A. P. Baur, C. Cayron, R. E. Logé, Variant selection in surface martensite, *Journal of applied crystallography*, 50(6), (2017), 1646–1652.
- [6] M. Jaswon, J. Wheeler, Atomic displacements in the austenite–martensite transformation, *Acta Crystallographica*, 1(4), (1948), 216–224.
- [7] C. Cayron, Continuous atomic displacements and lattice distortion during fcc–bcc martensitic transformation, *Acta Materialia* 96 (2015) 189–202.
- [8] S. Kajiwara, Roles of dislocations and grain boundaries in martensite nucleation, *Metallurgical and Materials Transactions A* 17 (10) (1986) 1693–1702.
- [9] R. Yeo, Growth of martensite in an iron-28.8% nickel alloy, *American Society for Metals, Trans. Quarterly* 57 (1964) 48–61.
- [10] C. Magee, The nucleation of martensite, In: *Phase Transformation* 3, (1970), 115–153.
- [11] Y. Sano, S. Chang, M. Meyers, S. Nemat-Nasser, Identification of stress-induced nucleation sites for martensite in fe-31.8 wt% ni-0.02 wt% c alloy, *Acta metallurgica et materialia*, 40 (2), (1992), 413–417.
- [12] Z. Nishiyama, *Martensitic transformation*, Elsevier, 2012.

Bibliography

- [13] T. Tomida, M. Wakita, M. Yasuyama, S. Sugaya, Y. Tomota, S. Vogel, Memory effects of transformation textures in steel and its prediction by the double kurdjumov-sachs relation, *Acta Materialia*, 61(8), (2013), 2828 – 2839.
- [14] F. Archie, S. Zaefferer, On variant selection at the prior austenite grain boundaries in lath martensite and relevant micro-mechanical implications, *Materials Science and Engineering: A* 731 (2018) 539–550.
- [15] T. Furuhashi, T. Maki, Variant selection in heterogeneous nucleation on defects in diffusional phase transformation and precipitation, *Materials Science and Engineering: A*, 312(1-2), (2001), 145–154.
- [16] D. Sarma, J. Whiteman, S. Keown, The structure of burst and isothermal martensites in an Fe-24 wt% Ni-0.5 wt% C alloy, *Journal of Materials Science*, 14(3), (1979), 693–698.
- [17] H. Sato, S. Zaefferer, A study on the formation mechanisms of butterfly-type martensite in Fe-30% Ni alloy using EBSD-based orientation microscopy, *Acta Materialia*, 57(6), (2009), 1931–1937.
- [18] M. Umemoto, T. Hyodo, T. Maeda, I. Tamura, Electron microscopy studies of butterfly martensite, *Acta Metallurgica*, 32(8), (1984), 1191–1203.

10 Variant Selection in Fe-20Ni-1.8C under Bending

Authors: A.P. Baur, C. Cayron and R.E. Logé, Laboratory of Thermomechanical Metallurgy-PX group Chair, Institute of materials, Ecole Polytechnique Fédérale de Lausanne, 2002 Neuchâtel, Switzerland.

Cited as: A.P. Baur et al., Variant Selection in Fe-20Ni-1.8C under Bending, *Crystals* 2018, 8(12), 474.

Authors contributions: Conceptualization, A.P.B., C.C. and R.E.L.; methodology, A.P.B. and C.C.; software, A.P.B.; validation, A.P.B. and C.C.; formal analysis, A.P.B. and C.C.; investigation, A.P.B.; resources, A.P.B. and C.C.; data curation, A.P.B.; writing—original draft preparation, A.P.B., C.C. and R.E.L.; writing—review and editing, A.P.B., C.C. and R.E.L.; visualization, A.P.B.; supervision, C.C. and R.E.L.; project administration, C.C.; funding acquisition, C.C. and R.E.L.

Abstract

Variant selection is commonly observed in martensitic steels when a stress is applied to the material during transformation. Classically, the selection phenomenon is modelled considering the work of the shape strain in the applied stress field. This shape strain is generally calculated by using the Phenomenological Theory of the Martensite Crystallography (PTMC). In the present study, we studied the martensitic transformation occurring in a Fe-20wt%Ni-1.8wt%C alloy transformed while loaded in four-point bending. A significant variant selection is observed, but surprisingly its nature cannot be explained by the classical approach. A crystallography-based empirical model which accounts for the experimental results is proposed instead.

Introduction

The effect of applied stress on the martensitic transformation has been studied for almost one century, Scheil being one of the first researchers who worked on this topic in 1932 [1]. In 1953, Patel and Cohen [2] performed a series of experiments on iron–nickel alloys and proposed a physical criterion to quantify the effect. The criterion allows to calculate the change of the martensitic start temperature as a function of the stress applied to the material. In their study, Patel and Cohen showed that if both the application of a uniaxial compressive stress and a uniaxial tensile stress increase the temperature at which martensite forms, the increase due to the latter is more significant. Accordingly, they proposed a criterion for martensite formation based on the work of the shape strain associated with the transformation in the applied stress field. This criterion is now known as the *Patel–Cohen criterion*. The shape strain considered is an invariant plane strain, where the invariant plane is the interface between martensite and austenite (habit plane). It can be calculated for any alloy by using the Phenomenological Theory of Martensite Crystallography (PTMC). The PTMC is probably the most famous crystallographic model for the martensitic phase transformation. It is the result of the work of two independent groups of researchers: Liebermann, Wechsler and Read in 1953 [3], and Bowles and Mackenzie in 1954 [4]. Both chose to model the transformation using linear algebra, but they came up with two apparently different expressions. A couple of years later, Christian showed that the two models were in fact equivalent [5]. Expressed in the Bowles and Mackenzie version, the transformation is modelled using four different matrices, each of them accounting for a part of the transformation. The structural phase change and the orientation relationship are characterized respectively, by the Bain strain \mathbf{B} [6] and a rotation \mathbf{R} , and their product \mathbf{RB} gives the *lattice strain*. The shape change is described by the matrix \mathbf{P} , which is the *shape strain*. The last matrix \mathbf{Q} renders compatible the shape strain with the lattice strain. It is named the *lattice invariant shear*. The PTMC stands then in a single equation $\mathbf{RB} = \mathbf{PQ}$. After its publication, this model quickly became very popular and remains as such today. The PTMC calculations allow in particular to study variant selection using the predicted shape strain to evaluate the Patel–Cohen criterion. Such an approach is broadly accepted and commonly used [7, 8]. However, some experiments indicate that this

criterion is not appropriate to explain the phenomenon. As an example, Mishiro et al. applied a compressive stress just above the martensitic start temperature to induce variant selection in a low-carbon steel. They noted that the lattice strain ***RB*** better accounts for the selection than the shape strain ***P*** [9]. Chiba et al. reported a significant variant selection in Fe–Ni–C lenticular martensite formed after ausforming [10]. They observed that four variants were preferentially formed in each parent grain. They applied the Patel–Cohen criterion using the residual stress to account for variant selection, but this analysis was not satisfactory. Indeed, the experimentally observed variants had their habit plane oriented rather perpendicularly to the compression direction and the resolved shear stress acting on them was very low. They concluded that variant selection was not related to the residual stress, but to the elongated morphology of the prior austenite grains. Such morphology favours the variants having a habit plane oriented parallel to the elongated direction as they induce less disturbance at the austenite grain boundary.

In the present study, we observe similar results in lenticular martensite formed in Fe-20wt%Ni-1.8wt%C under bending. A strong variant selection is measured, and the selection cannot be explained convincingly by the PTMC. The phenomenon is eventually accounted by an empirical crystallographic criterion.

Material and Methods

A Fe-20wt%Ni-1.8wt%C alloy has been homogenized at 1000 °C for 1 hour in a quartz tube. After the heat treatment, the material is directly quenched in water. A thin rectangular sample is cut out of the material. The sample is loaded in a miniaturized home-designed four-point bending device. The device is illustrated in Figure 10.1A. The loading is performed by moving the two central pins down, using a vertical screw. Such a loading system imposes a compression in the upper part of the sample and a tension in the lower part. The line in the middle of the sample thickness is called *neutral line*, as no stress acts on it. Martensitic phase transformation is induced in the sample by cooling it to –80 °C in a freezer. The specimen is maintained in the device during transformation. The imposed stress thus interacts with the transformation mechanism. The four-point bending device is designed such that the deformed sample can be directly embedded for material characterization, while keeping its exact shape. Figure 10.1B shows the embedded sample. The sample is prepared for EBSD characterization by mechanical grinding followed by a final polishing using *Vibromet* table. In order to study variant selection, some EBSD measurements have been performed in a XLF-30 (FEI) scanning electron microscope, equipped with a Channel5/Aztec (Oxford Instruments) EBSD system.

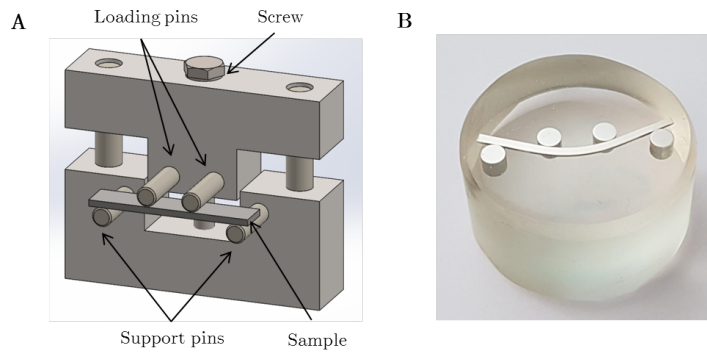


Figure 10.1: (A) Four-point bending device. (B) Bended sample embedded in epoxy for material characterization.

Results

Figure 10.2 shows an optical micrograph of the microstructure after transformation. The two pins in the upper corners of the picture are the central loading pins of the 4-point bending setup. It can be seen that the transformation only takes place in the tensile part of the sample. The propensity for the martensite to form preferentially in the tensile part of a bended sample was already observed by Kulin, Cohen and Averbach in three-point bending [11]. A few years later, this observation was rationalized by the aforementioned Patel–Cohen criterion [2]. It appears that our alloy is such that at $-80\text{ }^{\circ}\text{C}$ only the part in tension has enough driving force to induce the martensitic transformation. According to the Fe–Ni–C phase diagram, the heat treatment at $1000\text{ }^{\circ}\text{C}$ leads to the dissolution of only 0.85 wt% of the carbon, the rest is forming the carbides visible in Figure 10.2. The M_s reported for a Fe-20wt%Ni-0.8wt%C is $-74\text{ }^{\circ}\text{C}$ [12]. Considering our slightly higher carbon content, a transformation temperature close to $-80\text{ }^{\circ}\text{C}$ is reasonable. As an interesting feature, it can be noted that the transformation is localized and takes place in “columns”, the columns stopping near to the neutral line. Figure 10.3 shows the EBSD measurement of a column of martensite. This measurement indicates that only a few variants are formed in each austenitic parent grain, suggesting a probable variant selection phenomenon.



Figure 10.2: Bright-field optical micrograph of the sample in 4-point bending. The axis in red indicates the orientation of the EBSD measurement.

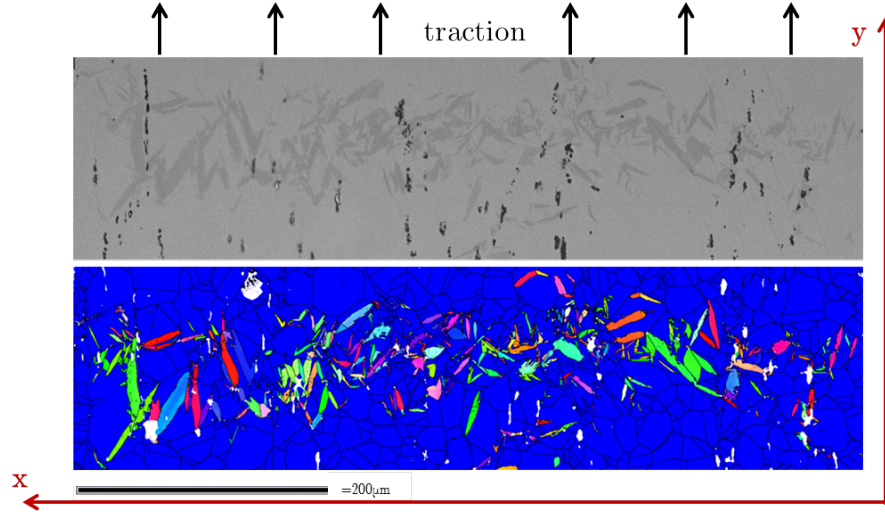


Figure 10.3: EBSD map of a column of martensite with the austenite in blue and the martensite in Euler colour coding and below, bright-field optical micrograph of the corresponding zone. The black arrows indicate the traction direction and the red axis can be related to those in Figure 10.2.

Discussion

To address variant selection, two different PTMC calculations are performed using the *PTCLab* open-source software [13]. The first calculation considers an FCC-BCC transformation and the second an FCC-BCT transformation, including the tetragonality $\gamma = \frac{c_\alpha}{a_\alpha} = 1.045$ observed in Fe–Ni–C alloys of close compositions [12, 14]. The lattice parameters $a_\alpha = 2.87 \text{ \AA}$ and $a_\gamma = 3.58 \text{ \AA}$, and $a_\alpha = 2.87 \text{ \AA}$, $c_\alpha = 3.00 \text{ \AA}$ and $a_\gamma = 3.58 \text{ \AA}$ measured in similar alloys are the inputs for the calculations of the BCC and the BCT models, respectively [15]. The simple shear version of the PTMC is used and the lattice invariant shear is chosen as suggested in the Bowles and Mackenzie original theory for the Fe–Ni–C martensite, namely a “twinning shear” of type $\langle 111 \rangle \{112\}_\alpha$ [4]. The shape strain \mathbf{P} and \mathbf{P}_T and lattice strain \mathbf{RB} and \mathbf{RB}_T matrices are given below for the FCC-BCC and the FCC-BCT transformations, respectively:

$$\mathbf{P} = \begin{bmatrix} 0.99264 & 0.03316 & -0.02733 \\ -0.02641 & 1.119 & -0.09808 \\ -0.02733 & 0.12315 & 0.8985 \end{bmatrix} \quad \mathbf{RB} = \begin{bmatrix} 1.11731 & 0.03316 & 0.09733 \\ -0.01765 & 1.119 & -0.08932 \\ -0.14049 & 0.12315 & 0.78534 \end{bmatrix}$$

$$\mathbf{P}_T = \begin{bmatrix} 0.96057 & -0.07824 & -0.02312 \\ 0.06557 & 1.13011 & 0.03844 \\ -0.02312 & -0.04587 & 0.98645 \end{bmatrix} \quad \mathbf{RB}_T = \begin{bmatrix} 1.11664 & -0.07824 & 0.13296 \\ 0.06987 & 1.13011 & 0.04274 \\ -0.18329 & -0.04587 & 0.82627 \end{bmatrix}$$

In both cases, the orientation relationship predicted by the PTMC is between the Nishiyama–Wassermann OR and the Kurdjumov–Sachs OR. The calculated habit planes are $\{0.17 \ 0.63 \ 0.76\}_\gamma$ for the BCC model and $\{0.26 \ 0.44 \ 0.86\}_\gamma$ for the BCT. These habit planes are respectively at 10°

and 5° from $\{259\}_\gamma$ and 6° and 9° from $\{3\ 10\ 15\}_\gamma$, which are the typical habit planes observed in such alloys [16]. Variant selection is studied using the Patel–Cohen criterion for martensite formation, as suggested in the literature [7]. The variants selected are the ones that maximize the work W of the shape strain \mathbf{P} , respectively \mathbf{P}_T , in the applied stress field σ ; $W = \epsilon_{ij}\sigma_{ij}$ with $\epsilon = \mathbf{P} - \mathbf{I}$ and σ is the generalized stress tensor associated with the external loading. In four-point bending, the generalized stress tensor is reduced to a single non-zero entry, as the material is either in simple compression or simple traction. Here, we choose to orientate the specimen such that the traction/compression axis is aligned with the y-axis. Accordingly, the stress tensor is $\sigma_{ij} = 0$ if $i, j \neq 2$. For each austenitic grain, the daughter variants are classified in respect with the value of their work. The variant exhibiting the maximal work is ranked first (1) and the one with the lowest work is ranked last (24). The calculations are performed using the *Mtex* toolbox [17]. Figure 10.4A,B present the histograms of the variant occurrence in the EBSD map according to the proposed ranking for the BCC and the BCT models. The occurrence of a given variant is measured by counting the number of pixels associated with the variant. With such a ranking, if the variant selection is based on the work of the shape

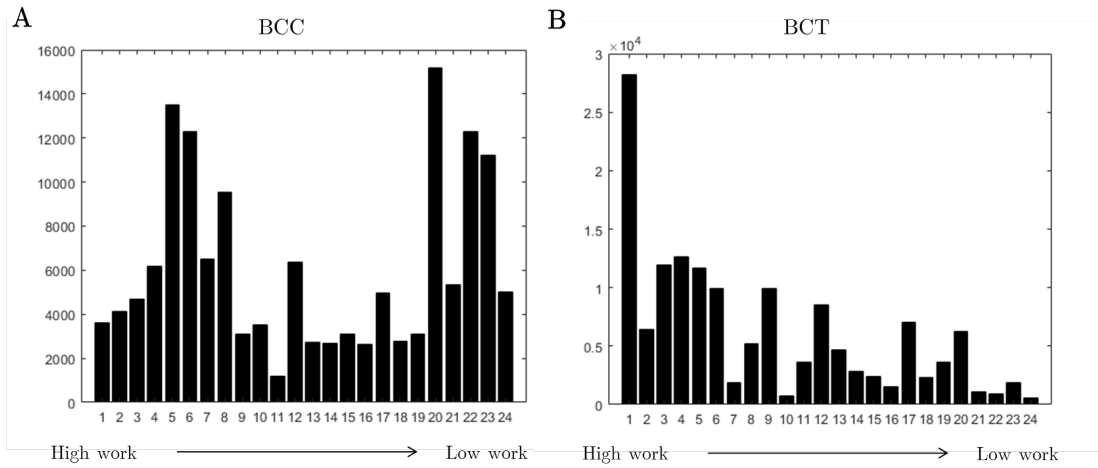


Figure 10.4: Histograms of the variants' occurrence considering the BCC model in (A) and the BCT model in (B). In the y-axis: the number of pixels associated with a given variant number. In x-axis: variants numbered with a ranking according to the value of the work.

strain, one expects that the variant with a small number, and thus exhibiting high work, would be observed more often than those associated with greater numbers. On this basis, it can be concluded that the present experiment does not exhibit a variant selection based on the work of the BCC shape strain, as there is no correlation between the ranking of the variants and their occurrence. On the contrary, the BCT model seems to correctly predict the variant selection, at least for the first variant, *i.e.*, the one with the highest work. A verification of the habit plane prediction is then performed by studying an austenite grain selected from the EBSD map presented in Figure 10.3. The grain is shown in Figure 10.5A with the austenite in blue and the martensite in Euler color coding. In Figure 10.5B,C respectively, the shape strains predicted by the PTMC calculations for the BCC and BCT models are shown for all

four variants in Figure 10.5A. The normals to the predicted habit planes are marked in green and the shear directions are marked in yellow. Numbers are given to each variant to help in associating them with their shape strain. The midrib is considered as the habit plane of the

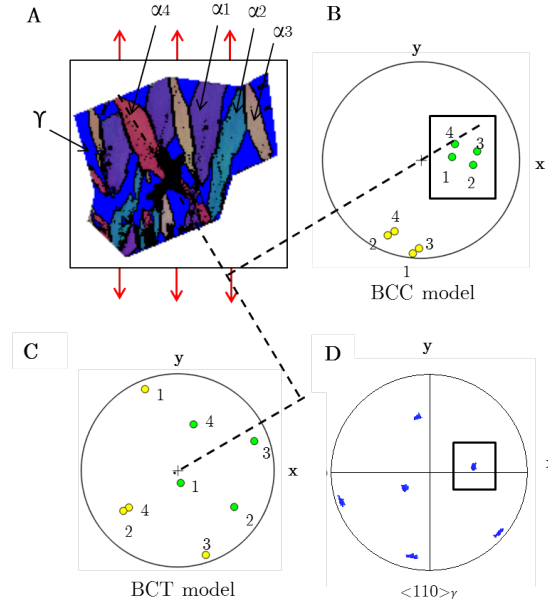


Figure 10.5: Trace analysis of the shape strain predicted by the Phenomenological Theory of Martensite Crystallography (PTMC) and variant selection prediction. (A) EBSD map of the grain with red arrows indicating the traction direction. The dashed lines indicate the normal to the habit plane of variant α_4 . (B) Pole figure of the normals to the habit planes (green) and the shear directions (yellow) predicted by the BCC model. (C) Pole figure of the normal to the habit planes (green) and the shear directions (yellow) predicted by the BCT model. (D) $\langle 110 \rangle_\gamma$ experimental pole figure.

martensite and a trace analysis is performed to verify the PTMC predictions. As an example, the normal to the habit plane of the red variant α_4 is marked with dashed lines in Figure 10.5. Our analysis clearly indicates that the BCT model does not predict the observed habit plane. This model which seemed to correctly account for variant selection is thus not satisfactory. On the contrary, the BCC model which fails to account for the variant selection seems to correctly predict the habit planes. From Figure 10.5, we can see that selected habit planes almost contain the traction direction. Hence, the shear resolved on it is almost zero, which explains why the criterion based on the work of the shape strain associated with the BCC model is not able to account for the variant selection. To be exhaustive in our variant selection analysis, we also computed the work of the elastic part of the BCC shape strain using $\epsilon = \frac{1}{2}(\mathbf{P} + \mathbf{P}^T) - \mathbf{I}$, the work of the lattice strain \mathbf{RB} and the work of the lattice invariant shear \mathbf{Q} . Additionally, we considered the couplings of variants inside the same plate group by computing the work of the average strain resulting from different shape strains, as suggested by Okamoto et al. [18]. None of these criteria accounts for the variant selection observed in the sample. These features are somewhat coherent with the results presented by Chiba et al. on variant selection

in lenticular martensite [10]. They also observed a lack of correlation between such energetic criteria and the measured variant selection. In agreement with our observations, they noted that the favoured variants have their habit planes normal to the compression axis, with low resolved shear acting on them. They concluded that the selection phenomenon was related to the elongated morphology of the prior austenite grain. In our sample, the parent austenite grains have a quite equiaxed geometry and Chiba et al.'s explanation is thus not applicable. It seems, however, that even though the thermomechanical treatments are different, the results of Chiba et al. have similarities with ours. As illustrated in Figure 10.5A, we also observe that four variants form preferentially, these variants belonging to the same *plate group*. The variant coupling in plate groups is frequently observed in lenticular martensite [19, 20, Bokros and Parker, 1963]. The plate groups were originally observed by Bokros and Parker in Fe-31%Ni [21]. They are defined in terms of habit plane orientation, as the group formed by the variants having their habit planes that cluster around a given $\langle 110 \rangle_\gamma$ direction of the parent crystal. An illustration of such a cluster is proposed in Figure 10.5D,B where squares are drawn to indicate the $\langle 110 \rangle_\gamma$ direction and the associated habit plane normals, respectively. In terms of lattice orientation, the plate group is crystallographically defined in reference [20] and illustrated with the yellow Kurdjumov–Sachs variants in Figure 10.6A. This illustration is adapted from Figure 4E of ref. [20]. The parent austenite is represented by two of the $\{111\}_\gamma$ planes, and the two others are not visible. The Kurdjumov–Sachs variants are illustrated by the green and yellow rectangles, representing the $\{110\}_\alpha \parallel \{111\}_\gamma$. The yellow rectangles represent one of the six possible plate groups. According to this definition, the plate group can be defined as the variants that have their $\langle 111 \rangle_\alpha$ that scatter about 10° from a $\langle 110 \rangle_\gamma$. It should be noted that the $\langle 110 \rangle_\gamma$ direction that defines the plate group in terms of the habit plane or in terms of lattice orientation are different. In Figure 10.6A,B, we marked in purple the considered $\langle 111 \rangle_\alpha$ and in red the associated $\langle 110 \rangle_\gamma$. In our experiment, a single

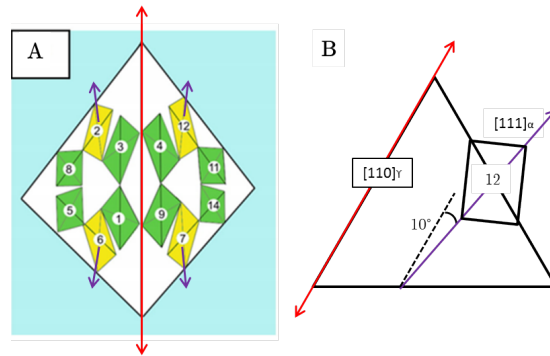


Figure 10.6: Empirical criterion for variant selection. (A) Plate group represented in 3D on two $\{111\}_\gamma$ planes. Illustration adapted from ref. [20]. (B) Triangle representing the $(1\bar{1}1)_\gamma$ plane and rectangle representing in 2D the $(1\bar{1}0)_\alpha$ of variant 12. In purple, the $[111]_\alpha$ that clusters about the $[110]_\gamma$ marked in red.

plate group is formed preferentially in each parent grain. Based on this observation, we were able to express an empirical criterion to characterize the plate group that is favoured under

traction. This criterion cannot distinguish the different variants inside the same group and thus does not treat the more severe selection that can be observed in some grains, where only one or two variants out of the four appear. Our criterion states that the selected plate group is the one formed by the four variants having their $\langle 111 \rangle_\alpha$ that cluster about the $\langle 110 \rangle_\gamma$ direction which is closest to the traction axis. In Figure 10.6A, the yellow plate group would be selected if the traction axis is close to the red arrows. Based on that empirical rule, we classify the plate groups as a function of the angle between the traction direction and the $\langle 110 \rangle_\gamma$ direction associated with each plate group. The plate group with the lowest angle is ranked first (1) and the plate group with the largest angle is ranked last (6). Figure 10.7B shows the histogram of variant occurrence according to the proposed criterion for the entire column of martensite shown in Figure 10.3. It appears that this criterion accounts very well for the

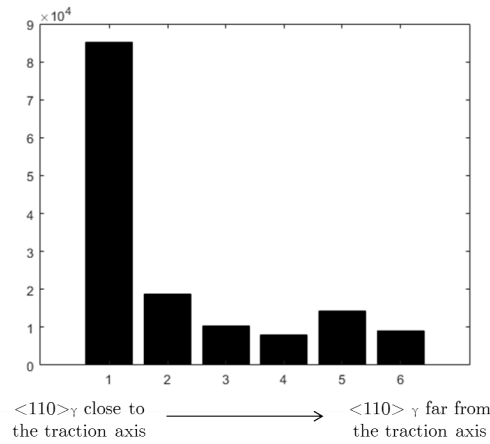


Figure 10.7: Histograms of plate group occurrence considering a ranking based on the empirical criterion. In the y-axis: the number of pixels associated with a given plate. In the x-axis: plate group numbered with a ranking according to the empirical criterion.

variant selection observed in our sample. Figure 10.8 illustrates the selection phenomenon for the grain in Figure 10.5A with the austenite in blue and the martensite in Euler color coding. Figure 10.8A presents the experimental pole figures of the grain. Figure 10.8B shows all Kurdjumov–Sachs variants with empty markers and the variants selected by our criterion with blue markers. Figure 10.8C shows the orientation of the parent grain. We marked with a circle the $\langle 110 \rangle_\gamma$ direction about which the $\langle 111 \rangle_\alpha$ of the variants of the selected plate group clusters. The circle is reported on the martensite pole figures, in Figure 10.8A,B, to indicate the $\langle 111 \rangle_\alpha$ cluster. It is quite puzzling to see that even though the BCC model prediction of the orientation relationship and the habit plane orientation are in fairly good agreement with the experimental measurements, the variant selection based on the work of the shape strain does not hold, and that on the contrary, the BCT model accounts for the variant selection but considering a shape strain which is not observed. It seems that the mechanism of the formation of lenticular martensite is not fully understood and that its current modeling is not able to depict all the physics involved in the transformation. The nature of the lattice invariant shear in particular seems to be controversial. The PTMC theory considers that a single shear

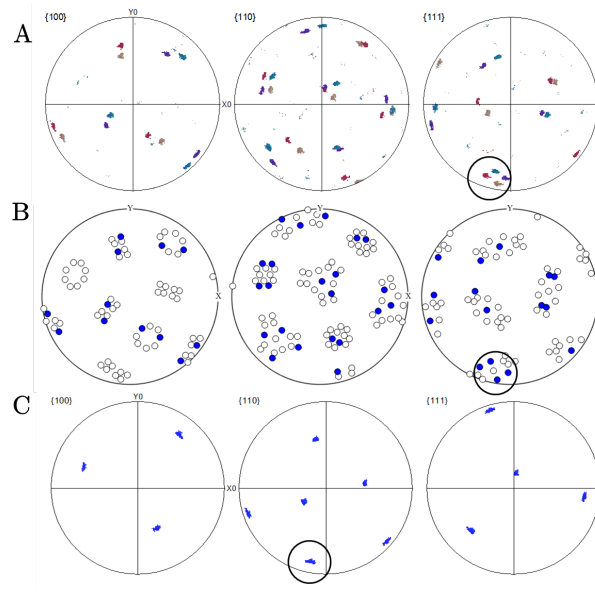


Figure 10.8: Variant selection in the single parent grain presented in Figure 10.5A. The circle indicates that the $\langle 111 \rangle_{\alpha}$ scatters about the $\langle 110 \rangle_{\gamma}$ that is closest to the traction axis which is oriented along the y-direction. (A) Experimental pole figures of the martensite. (B) Kurdjumov–Sachs pole figures with the variant selected by our criterion marked in blue. (C) Experimental pole figures of the parent austenite.

occurs to accommodate the $\{259\}_{\gamma}$ martensite. However, Thomas observed that more than one lattice-invariant shear effectively acts in the accommodation process [22].

In conclusion, variant selection has been studied in a Fe-20Ni-1.8C alloy transformed under bending. The transformation takes place only in the tensile part of the specimen and a significant variant selection is observed. It appears that a single plate group is formed preferentially in each grain. The variant selection is studied using the Patel–Cohen criterion with two different shape strains associated with the FCC-BCC and the FCC-BCT transformations. The shape strains are computed using PTMC. The BCT model is shown to correctly account for the variant selection, but the shape strain does not agree with the experimental data. In contrast, the BCC model predicts well the habit plane orientation, but is not able to explain the variant selection. These discrepancies between the experiment and PTMC predictions need to be further analyzed in order to better understand the mechanism of formation of the lenticular martensite and possibly explain what drives the observed variant selection. An empirical criterion, which captures the selection, is proposed. However, the physical explanation for such a criterion remains mysterious and more advanced characterization techniques to analyze the martensite substructure might be required to rationalize it.

Authors contributions

Conceptualization, A.P.B., C.C. and R.E.L.; methodology, A.P.B. and C.C.; software, A.P.B.; validation, A.P.B. and C.C.; formal analysis, A.P.B. and C.C.; investigation, A.P.B.; resources, A.P.B. and C.C.; data curation, A.P.B.; writing—original draft preparation, A.P.B., C.C. and R.E.L.; writing—review and editing, A.P.B., C.C. and R.E.L.; visualization, A.P.B.; supervision, C.C. and R.E.L.; project administration, C.C.; funding acquisition, C.C. and R.E.L.

Fundings

This research was funded by the Swiss National Science Foundation (grant number 200021-159955).

Acknowledgements

The authors would like to thank Mathijs van der Meer for its help in designing the four-points bending device. The authors also acknowledge ArcelorMittal, in particular Ian Zuazo and Kangying Zhu for providing the material of this study. Finally, the authors would like to thank PX Group for its financial support to the laboratory.

Additional information

The authors declare no conflict of interest.

Bibliography

- [1] Scheil, E. Über die Umwandlung des Austenits in Martensit in Eisen-Nickellegierungen unter Belastung. *Z. Anorg. Allg. Chem.* **1932**, 207, 21–40.
- [2] Patel, J.; Cohen, M. Criterion for the action of applied stress in the martensitic transformation. *Acta Metall.* **1953**, 1, 531–538.
- [3] Wechsler, M.S. Lieberman, D.; Read, T. On the theory of the formation of martensite. *Trans. AIME* **1953**, 197, 1503–1515.
- [4] Bowles, J.; Mackenzie, J. The crystallography of martensite transformations I. *Acta Metall.* **1954**, 2, 129–137.
- [5] Christian, J. Applications of the phenomenological theories of martensite I–II. *J. Inst. Met.* **1956**, 84, 386–394.
- [6] Bain, E.C.; Dunkirk, N. The nature of martensite. *Trans. AIME* **1924**, 70, 25–47.
- [7] Kundu, S.; Bhadeshia, H. Crystallographic texture and intervening transformations. *Scr. Mater.* **2007**, 57, 869–872.
- [8] Marechal, D.; Malet, L.; Godet, S.; Sinclair, C.W. Variant Selection and Texture in an AISI 301LN Stainless Steel. In *Materials Science Forum*; Trans Tech Publications: Princeton, NJ, USA, 2012; Volume 702, pp. 850–853.
- [9] Mishiro, Y.; Nambu, S.; Inoue, J.; Koseki, T. Effect of stress on variant selection in lath martensite in low-carbon steel. *ISIJ Int.* **2013**, 53, 1453–1461.
- [10] Chiba, T.; Miyamoto, G.; Furuhashi, T. Variant selection of lenticular martensite by ausforming. *Scr. Mater.* **2012**, 67, 324–327.
- [11] Kulin, S.; Cohen, M.; Averbach, B. Effect of applied stress on the martensitic transformation. *JOM* **1952**, 4, 661–668.
- [12] Kajiwar, S.; Kikuchi, T. On the abnormally large tetragonality of martensite in Fe-Ni-C alloys. *Acta Metall. Mater.* **1991**, 39, 1123–1131.
- [13] Gu, X.F.; Furuhashi, T.; Zhang, W.Z. PTCLab: free and open-source software for calculating phase transformation crystallography. *J. Appl. Crystallogr.* **2016**, 49, 1099–1106.

Bibliography

- [14] Greninger, A.B.; Troiano, A.R. The mechanism of martensite formation. *JOM* **1949**, *1*, 590–598.
- [15] Reed, R.; Schramm, R. Lattice parameters of martensite and austenite in Fe–Ni alloys. *J. Appl. Phys.* **1969**, *40*, 3453–3458.
- [16] Nishiyama, Z. *Martensitic Transformation*; Elsevier: Amsterdam, The Netherlands, 2012.
- [17] Bachmann, F.; Hielscher, R.; Schaeben, H. Texture analysis with MTEX-free and open source software toolbox. In *Solid State Phenomena*; Trans Tech Publications: Princeton, NJ, USA, 2010; Volume 160, pp. 63–68.
- [18] Okamoto, H.; Oka, M.; Tamura, I. Couplings of Thin-plate Martensites in an Fe–Ni–C Alloy. *Trans. Jpn. Inst. Met.* **1978**, *19*, 674–684.
- [19] Stormvinter, A.; Miyamoto, G.; Furuhashi, T.; Hedström, P.; Borgenstam, A. Effect of carbon content on variant pairing of martensite in Fe–C alloys. *Acta Mater.* **2012**, *60*, 7265–7274.
- [20] Cayron, C. EBSD imaging of orientation relationships and variant groupings in different martensitic alloys and Widmanstätten iron meteorites. *Mater. Charact.* **2014**, *94*, 93–110.
- [21] Bokros, J.; Parker, E. The mechanism of the martensite burst transformation in FeNi single crystals. *Acta Metall.* **1963**, *11*, 1291–1301.
- [22] Thomas, G. Electron microscopy investigations of ferrous martensites. *Metall. Trans.* **1971**, *2*, 2373.

11 Effect of tensile deformation on variant selection in $\{225\}_\gamma$ plate martensite and $\{557\}_\gamma$ lath martensite

Authors: A.P. Baur, C. Cayron and R.E. Logé, Laboratory of Thermomechanical Metallurgy-PX group Chair, Institute of materials, Ecole Polytechnique Fédérale de Lausanne, 2002 Neuchâtel, Switzerland.

Accepted in: Results in Materials

Authors contributions: Conceptualization, A.P.B., C.C. and R.E.L.; methodology, A.P.B. and C.C.; software, A.P.B.; validation, A.P.B. and C.C.; formal analysis, A.P.B. and C.C.; investigation, A.P.B.; resources, A.P.B. and C.C.; data curation, A.P.B.; writing—original draft preparation, A.P.B., C.C. and R.E.L.; writing—review and editing, A.P.B., C.C. and R.E.L.; visualization, A.P.B.; supervision, C.C. and R.E.L.; project administration, C.C.; funding acquisition, C.C. and R.E.L.

Abstract

The effect of tensile deformation on variant selection has been studied in $\{225\}_\gamma$ plate martensite and $\{557\}_\gamma$ lath martensite formed in high- and low-carbon steels, respectively. Different thermomechanical treatments are performed to analyse the effect of applied tensile stress, in the elastic and plastic range and the effect of prior plastic tensile deformation on variant selection. The variant selection is studied by computing the work of the deformation associated with the transformation in the applied stress field. Our analysis indicates that the deformation that needs to be considered to model the selection is based on lattice strains combinations. For $\{225\}_\gamma$ plate martensite, the average deformation resulting from the combination of the lattice strains of twin-related variants is the relevant deformation gradient for the work computation. On the contrary, in lath martensite, the combination of the lattice strains of low-misoriented variants appears to better model the selection phenomenon.

Introduction

Because of their implications on the industrial process of steels, the effects of applied stress and prior deformation on variant selection have been studied by various researchers, in a wide range of steels [1, 2, 3, 4, 5, 6]. It is not rare that the studies reach contradictory conclusions. A broadly accepted approach to study the effect of stress on variant selection consists in evaluating the work W of the deformation gradient \mathbf{F} associated with the phase transformation in the applied stress field $\boldsymbol{\Sigma}$:

$$W = (\mathbf{F} - \mathbf{I}) : \boldsymbol{\Sigma} \quad (11.1)$$

where \mathbf{I} is the identity matrix.

Generally, the divergence between authors lies in the choice of the deformation gradient \mathbf{F} to consider. In the classical modelling of the martensite crystallography called the *PTMC*, three different types of deformation are involved in the transformation mechanism [7]:

- The *lattice strain* \mathbf{RB} which describes the deformation of the FCC lattice to a BCC lattice. It is expressed as the product of a rotation \mathbf{R} and the Bain strain \mathbf{B} [8]. The lattice strain is defined as an *invariant line strain*, one line being left unchanged upon transformation.
- The *shape strain* \mathbf{P} , which models the change of shape associated with the transformation as an invariant plane strain. The plane which remains invariant is called the *habit plane*, and it is the interface between the martensite and the austenite. The shape strain \mathbf{P} consists in the combination of shear parallel to the habit plane and a dilatation normal to it.
- The *lattice invariant strain* \mathbf{Q}^{-1} which renders compatible the shape strain \mathbf{P} and the lattice strain \mathbf{RB} . The lattice invariant shear \mathbf{Q}^{-1} does not affect the final martensite lattice structure, but acts in order to guarantee that the macroscopic shape change is an

invariants plane strain. The mechanism associated with the lattice invariant shear is either "twinning" or slip. By "twinning", PTMC considers both mechanical twinning and twin-related variants pairing.

The PTMC stands in a single equation: $\mathbf{RB} = \mathbf{PQ}$ [7]. The comparison of the various variant selection studies found in the literature indicates that there is no common consent on which of the lattice strain or the shape strain better accounts for the phenomenon. Badheshia and co-workers used the work of the shape strain \mathbf{P} , also called the *Patel and Cohen criterion* [9] to model the selection phenomenon [5]. They claimed that it is the only proper way to model the selection [3]. However, other researchers reported that the work of the lattice distortion \mathbf{RB} better accounts for their experimental results [1]. Kato and Mori [2], Jesser and Olsen [10] and Miyaji *et al.* [11] even concluded that the Bain strain allows for the most convincing description of variant selection under stress.

A transformation model alternative to the PTMC has been recently proposed by one of the co-authors [12]. The transformation is described continuously by a unique transformation matrix, which evolves during the transformation. The complete transformation is a lattice strain of type \mathbf{RB} . The orientation relationship associated with the transformation is the one of Kurdjumov-Sachs. In this model, the lattice parameters are in hard-sphere ratio. Based on the proposed mechanism, the accommodation of the $\{225\}_\gamma$ and the $\{557\}_\gamma$ habit planes have been studied [13, 14]. In the former case, it is shown that the linear combination of twin-related variants of the transformation is an invariant plane strain on a $\{225\}_\gamma$ plane. For this particular case, the continuous model and the PTMC are shown to be equivalent [13]. Indeed, in the PTMC model for the $\{225\}_\gamma$, an additional dilatation parameter δ multiplying \mathbf{RB} is introduced to impose the lattice parameters to be in hard-sphere ratio and to force $[1\bar{1}0]_\gamma = [111]_\alpha$. The models however differ for the modeling of the $\{557\}_\gamma$ habit plane. The classical PTMC uses two lattice invariant shears to account for the $\{557\}_\gamma$ habit plane. The shear elements to consider in the model have been determined by Kelly [15]. By combining these shears to the lattice strain, a fully invariant plane close to $\{557\}_\gamma$ is obtained. Contrarily, by using the continuous model, $\{557\}_\gamma$ habit plane can be accounted by combining two low-misoriented Kurdjumov-Sachs variants [14]. However, such combination does not achieve a fully invariant plane, the plane being only *untilted* by the transformation. The average of these two low-misoriented variants is a lattice strain associated with the Nishijama-Wassermann orientation relationship.

So far, the continuous FCC-BCC distortion model has successfully modeled variant selection in surface martensite by using a criterion based on the lattice strain of each variant [16].

Like stress, prior deformation is also known to cause variant selection [4, 6]. Kundu *et al.* studied the effect of complex rolling conditions on the transformation [6]. He considered that the residual stresses due to the thermomechanical treatment caused variant selection. The selection was then modeled by using the Patel and Cohen criterion computed with the residual stress. Using a more crystallographic approach, Miyamoto *et al.* proposed a detailed study of the effect of ausforming on variant selection [4]. He indexed the variants as Kurdjumov-Sachs variants and concluded that the variant selection is based on the so-called *CPP packets*. A CPP packet consists in all the six Kurdjumov-Sachs variants having their close-packed plane

Chapter 11. Effect of tensile deformation on variant selection in $\{225\}_\gamma$ plate martensite and $\{557\}_\gamma$ lath martensite

parallel to the same close-packed plane of the austenite [17]. There are a total of four different CPP packets. Myamoto *et al.* showed that the variants preferentially formed in the ausformed material are those belonging to CPP packet associated with the primary or the secondary slip planes. This selection is explained by the formation of microbands in the austenite during the thermomechanical treatment.

In this study, we propose to analyse variant selection caused by various tensile deformations, studying both the effect of stress and the effect of prior deformation. The study is performed for two different types of martensite, $\{225\}_\gamma$ plate martensite and $\{557\}_\gamma$ lath martensite. These two types of martensite have been chosen, as they are commonly observed in carbon steels, the former being formed in high-carbon steels and the latter in low-carbon steels. The variant selection is studied by computing the work of the deformation associated with the transformation in the applied stress field according to equation (1). Besides comparing the effect of the different thermomechanical treatments on variant selection, we aim to clarify which of the shape strain or the lattice strain better models the selection phenomenon.

Materials and Method

Three different types of tensile deformation have been performed in this study. All deformations are carried in the austenitic phase, at a temperature just above the martensitic start temperature. A 3800 Gleeble machine is used to perform the different thermomechanical treatments. Figure 11.1 illustrates these treatments. The first thermomechanical treatment (TMT-1) consists in deforming plastically the material and inducing the martensitic transformation by cooling it, while maintaining the imposed deformation. The material is thus stressed when the transformation takes place. It should be noted that the applied stress is not constant during the transformation and slightly decreases due to creep. Such loading has been chosen in order to avoid any risk of failure of the sample. The second treatment (TMT-2) consists in deforming the material in the elastic regime and transforming it while keeping the external force. In both above mentioned thermomechanical treatment, the stress is maintained during the transformation, the stress applied during TMT-1 being larger than the one associated with TMT-2. The last thermomechanical treatment performed (TMT-3) consists in deforming the austenite plastically, then removing the applied stress and quenching the martensite without applied stress. To set the conditions of the thermomechanical treatments, two additional tests have been performed for each material. A first test allows to obtain the transformation temperatures by measuring the specimen dilatation using a quartz dilatometer during heating and fast cooling. Then a simple traction just above M_s has been performed in order to obtain the force-displacement curve of the different specimens until failure. In the thermomechanical treatment TMT-1, we choose to impose for each material the maximum deformation before failure. Similarly in TMT-2, we impose the force the closest to the yield of the specimen. The mechanical treatments are either performed in displacement control (TMT-1), in force control (TMT-2) or using both modes (TMT-3).

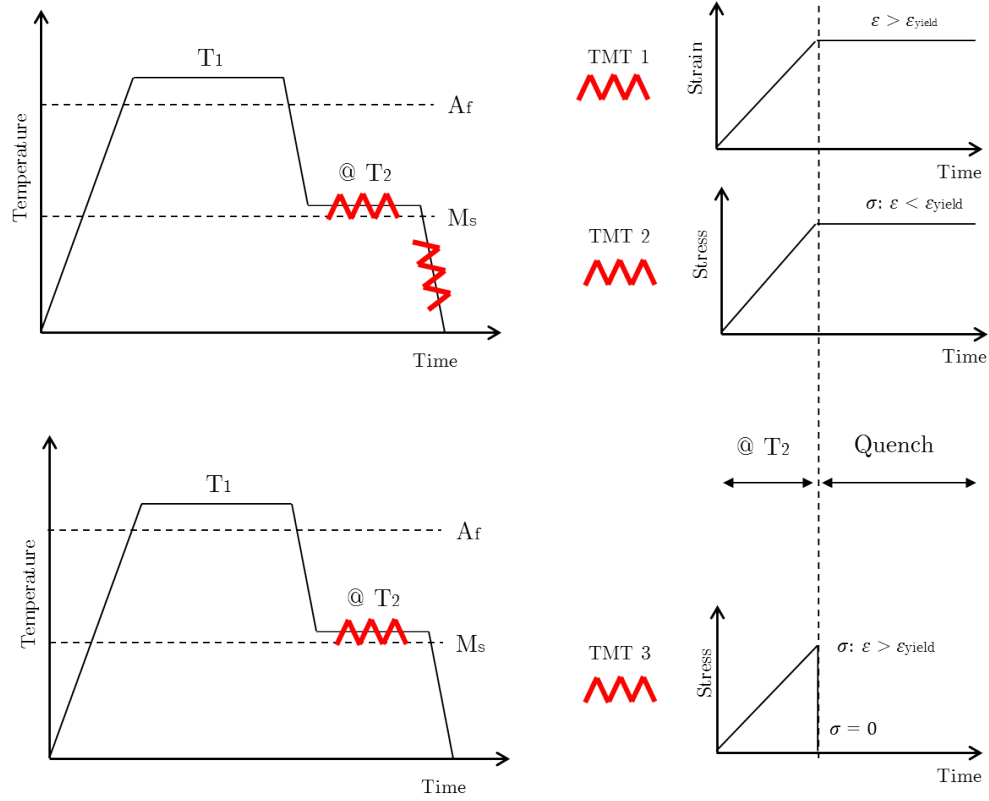


Figure 11.1: Representation of the thermomechanical treatments performed in the study. On the left, the temperature as function of time during the treatments. On the right, the different tensile deformations are performed at T_2 , just above M_s , and during the quench (for the first two thermomechanical treatments) to induce variant selection. TMT-1: Tensile deformation above the elastic limit ϵ_{yield} and transformation while keeping the deformation. TMT-2: Tensile deformation below the elastic limit and transformation while keeping the applied stress. TMT-3: Tensile deformation above the elastic limit and transformation without any applied stress, $\sigma = 0$.

These thermomechanical treatments have been performed on two different steels, a low-carbon steel (0.1C-5Mn-1.5Si) and a high-carbon steel (Fe-1.2C-0.5Cr). The low-carbon steel is a typical steel developed to be processed by *ausforming*. The temperatures of transformation of the low- and the high-carbon steels are rather different. Accordingly, the temperatures of the thermomechanical treatments also differ. Table 11.1 presents the temperature and holding time involved in the thermomechanical treatment of each material. Prior to the thermomechanical treatments, the high-carbon steel has been homogenized at 1100°C for 1 hour in a quartz tube and quenched in water. The strain ϵ and stress σ corresponding to the imposed strain and force are presented in table 11.2. It is worth mentioning here that the values of the strains are rough estimate as it is always difficult to evaluate precisely the length of the hot zone related to the Gleeble setup, where the deformation is localized.

Chapter 11. Effect of tensile deformation on variant selection in $\{225\}_\gamma$ plate martensite and $\{557\}_\gamma$ lath martensite

Table 11.1: Transformation temperatures of the high-carbon steel and the low-carbon steel and features of the heat treatments performed of both steels. Af: Austenite finish temperature. Ms: Martensite start temperature. The temperature T_1 is the austenitization temperature and T_2 is the temperature at which the tensile deformation is carried. They are also indicated in figure 11.1.

| | Af | Ms | T1 | Holding time at T1 | T2 |
|-------------------|-------|-------|--------|--------------------|-------|
| High-carbon steel | 780°C | 105°C | 1000°C | 2mn | 120°C |
| Low-carbon steel | 850°C | 380°C | 1000°C | 15mn | 400°C |

Table 11.2: Stresses and strains associated with the different thermomechanical treatments performed.

| | High-carbon steel | Low-carbon steel |
|-------|----------------------------|---------------------------|
| TMT-1 | $\epsilon = 0.02$ | $\epsilon = 0.14$ |
| TMT-2 | $\sigma = 150 \text{ MPa}$ | $\sigma = 62 \text{ MPa}$ |
| TMT-3 | $\epsilon = 0.02$ | $\epsilon = 0.14$ |

Once deformed, the tensile specimens are prepared for EBSD characterisation by mechanical grinding down to 1 micron and using a *Vibromet* table for the final polishing. The characterization is performed in an XLF-30 (FEI) scanning electron microscope equipped with a Channel5/Aztec (Oxford Instrument) EBSD system. The crystallographic computations and the variant selection analysis are performed using the Mtex software [18], and the orientations of the prior austenite grains are reconstructed with the *ARPGE* software [19].

Results and Discussion

EBSD characterisation

For a given alloy, the different thermomechanical treatments do not lead to visually different microstructure, therefore only one maps per material is shown. The maps of high-carbon steel and the low-carbon martensite are presented in figures 11.2A and 11.2B, respectively. The map in figure 11.2B is the result of the thermomechanical treatment TMT-1 and the map 11.2B the result of TMT-3. Retained austenite is observed in the high-carbon steel whereas a fully transformed microstructure is observed in the low-carbon steel. The crystallographic analysis indicates that the martensite formed in the high-carbon steel has a $\{225\}_\gamma$ habit plane whereas the martensite formed in the low-carbon steel exhibits a habit plane of type $\{557\}_\gamma$. In the following, the martensite formed in the high-carbon steel will be called *plate martensite* and the martensite formed in the low-carbon steel *lath martensite*.

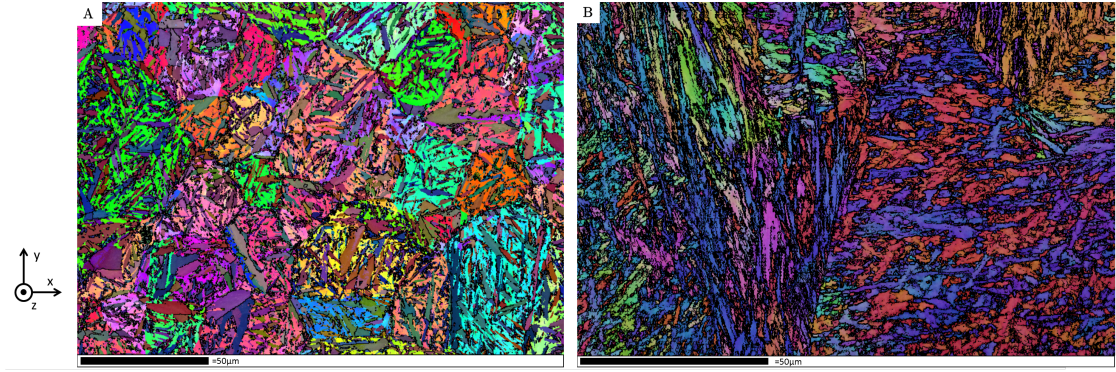


Figure 11.2: EBSD maps of the martensite in Euler colour coding. **A**: Plate martensite in the high-carbon steel submitted to TMT-2, transversal cut (i.e. traction along the z -axis). **B**: Lath martensite in the low-carbon steel, after TMT-3. Longitudinal cut (i.e. traction along the y -axis).

Variant selection

To evidence the variant selection, a quantitative approach is required. It is achieved in this study by counting the number of pixels associated to each variant. Each pixel of the EBSD map gives an information on the orientation of the crystal, then by using a crystallographic model each orientation can be indexed as an orientation variant and then related to a given distortion variant, which is defined by its proper lattice strain. The crystallography of the $\{225\}_{\gamma}$ plate martensite is modelled by using the FCC-BCC continuous model [12]. The lattice strain \mathbf{RB}_{plate} is directly given by the distortion matrix \mathbf{D}^{KS} in reference [12], and the shape strain \mathbf{P}_{plate} is obtained by the equilibrated combination of the lattice strain of twin-related variants $\mathbf{P}_{plate} = 0.5\mathbf{RB} + 0.5(\mathbf{RB})_{twin}$ [13]. The PTMC model for $\{225\}_{\gamma}$ martensite, originally proposed by Bowles and Mackenzie [7] being completely equivalent to the continuous distortion model, a modelling of $\{225\}_{\gamma}$ plate martensite using PTMC would lead to the same variant selection analysis. Regarding the crystallography of lath martensite, the continuous model considers a lattice strain and not an invariant plane strain to account for the $\{557\}_{\gamma}$ habit plane [14]. An aim of the present study is to understand which of the shape strain or the lattice strain needs to be considered in variant selection. Therefore, the crystallography of lath martensite is modeled in a first step by using the double shear solution proposed by Kelly, which considers both a lattice strain and a shape strain [15]. The *PTCLab* software is used for the PTMC calculations [20]. In Kelly's model, the $\langle 1\bar{1}0 \rangle_{\gamma} \{110\}_{\gamma}$ and $\langle 0\bar{1}1 \rangle_{\gamma} \{113\}_{\gamma}$ shear systems are considered as the first and second lattice invariant shears. The lattice parameters chosen as input for the computations are $a_{\gamma} = 3.61\text{\AA}$ and $a_{\alpha} = 2.87\text{\AA}$ for the austenite and the martensite, respectively. The lattice parameter of the martensite corresponds to a value found in the literature for similar alloys [21, 22] and the lattice parameter of the austenite is an experimental value measured in a similar alloy by the industrial partner who provided the material. The lattice strains \mathbf{RB}_{lath} and \mathbf{RB}_{plate} , and the shape strains \mathbf{P}_{lath} and \mathbf{P}_{plate} associated with the lath and plate models are expressed in the austenite crystallographic basis

Chapter 11. Effect of tensile deformation on variant selection in $\{225\}_\gamma$ plate martensite and $\{557\}_\gamma$ lath martensite

as follows:

$$\begin{aligned} \mathbf{P}_{plate} &= \begin{bmatrix} 0.9694 & -0.0306 & -0.0749 \\ -0.0306 & 0.9694 & -0.0749 \\ 0.0612 & 0.0612 & 1.1498 \end{bmatrix} & \mathbf{RB}_{plate} &= \begin{bmatrix} 1.13608 & 0.13608 & -0.07491 \\ -0.19725 & 0.80274 & -0.07491 \\ 0.06117 & 0.06117 & 1.14983 \end{bmatrix} \\ \mathbf{P}_{lath} &= \begin{bmatrix} 0.97392 & -0.02608 & -0.03234 \\ -0.1245 & 0.8755 & -0.15439 \\ 0.12544 & 0.12544 & 1.15555 \end{bmatrix} & \mathbf{RB}_{lath} &= \begin{bmatrix} 1.11423 & 0.10447 & -0.02746 \\ -0.14986 & 0.78326 & -0.12095 \\ 0.01116 & 0.08734 & 1.11746 \end{bmatrix} \end{aligned}$$

The plate martensite model is associated with the exact Kurdjumov-Sachs orientation relationship, and Kelly's model is associated with an orientation relationship between Kurdjumov-Sachs and Nishiyama-Wassermann.

A variant selection related to the applied stress is expected in the thermomechanical treatments TMT-1 and TMT-2. In the thermomechanical treatment TMT-3, no stress is acting during transformation. Additionally, as the deformation is homogenous through the whole hot zone of the sample there should be no significant residual stress. As a consequence no variant selection based on stress is expected. We start our analysis of the effect of stress on variant selection by considering the work of the shape strain \mathbf{P} in equation (1), namely the Patel and Cohen criterion [9]. The variants that maximize the work of the shape strain in the applied stress field $W = (\mathbf{P} - \mathbf{I}) : \boldsymbol{\Sigma}$ are considered to be the most favoured variants. In tensile deformation, the applied stress tensor is such that all components are zero except the diagonal component associated with the tensile axis. The variants are classified based on the value of the work. The variant that has the largest work is ranked first (1) whereas the one exhibiting the lowest work is ranked last (24). In the model for $\{225\}_\gamma$ plate martensite, there are always two variants that exhibit the same work, as the shape strain is the result of the combination of two twin-related variants in equal proportion [7]. Therefore, in that case the variants are coupled and ranked from (1) to (12). It is worth mentioning here that the resolution of the EBSD measurements performed is not sufficient to distinguish the two twin-related variants orientations. Each plate is indexed as a single orientation. However, characterisations using transmission electron microscopy indicate that at the midrib of the $\{225\}_\gamma$ plate, the two twin-related orientations are observed, in equal proportion [23].

Plate martensite: High-carbon steel

Figures 11.3A and 11.3B show the histograms of the variants occurrence as function of their ranking for the different thermomechanical treatments where plastic strain (TMT-1) and elastic strain (TMT-2) are applied during transformation. The height of the bar corresponds to the number of pixels associated with the variant and the colour of the bar indicates the average work value of the observed variant. The work is computed using a normalized value of stress. This analysis indicates that the variant selection can be modelled reasonably well by considering the work of the shape strain (Patel and Cohen criterion). The variants for which shape strains exhibit a low work are present in smaller amount than those with higher work. Or,

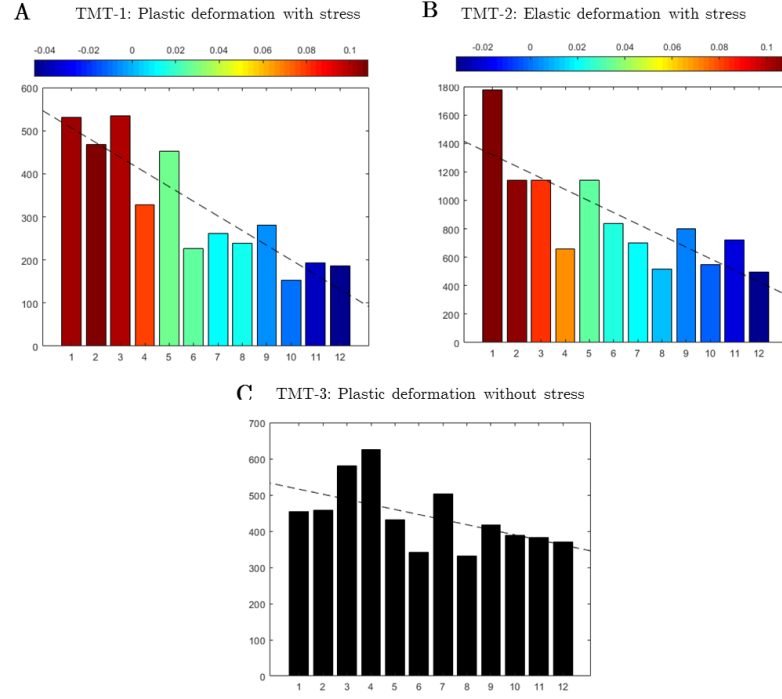


Figure 11.3: Histogramm of the variant occurrence with a ranking based on work of the shape strain (Patel and Cohen criterion). **A:** Results for TMT-1. **B:** Results for TMT-2. **C:** Results for TMT-3. The colour of the bars indicates the average work associated with the variants. The dashed lines indicate the linear fitting of the variant occurrence as a function of their ranking.

in other words, the variants with high work values have the tendency to grow bigger than those with lower work values. To help in visualizing this tendency, a linear fitting drawn with a black dashed line is superimposed on the graphs. Figure 11.3C shows the results of the same analysis performed on the plastically deformed sample without stress (TMT-3). In that case, the "stress" considered in the evaluation of the work is chosen to be parallel to the direction of the prior plastic deformation. The linear fitting indicates a slight decrease of the variant occurrence as the variant number increases, but this tendency is very light and we concluded that no significant variant selection is taking place in the plastically deformed sample (TMT-3). We also checked whether or not considering the work of the lattice distortion \mathbf{RB} associated with each variant instead of considering the average distortion \mathbf{P} resulting from the combination of the twin-related lattice distortions is appropriate to model the selection. Our analysis indicates no good correlation between the variant occurrence and the magnitude of the lattice strain \mathbf{RB} , and confirms that the deformation gradient to consider in the computation of the work in equation (1) is $\mathbf{F} = \mathbf{P}$, as suggested by Patel and Cohen [9].

Chapter 11. Effect of tensile deformation on variant selection in $\{225\}_\gamma$ plate martensite and $\{557\}_\gamma$ lath martensite

Lath martensite: Low-carbon steel

The same variant selection analysis has been performed for the lath martensite. The results in figure 11.4A indicate that the work of the shape strain is not able to account convincingly for the variant selection. Indeed, there is no correlation between the variant ranking and their occurrence. Such lack of correlation exists for all tested thermomechanical treatments. The computation of the work has also been performed using the lattice strain **RB**. The results are presented in figure 11.4B. The analysis is not more satisfactory. The lack of correlation can

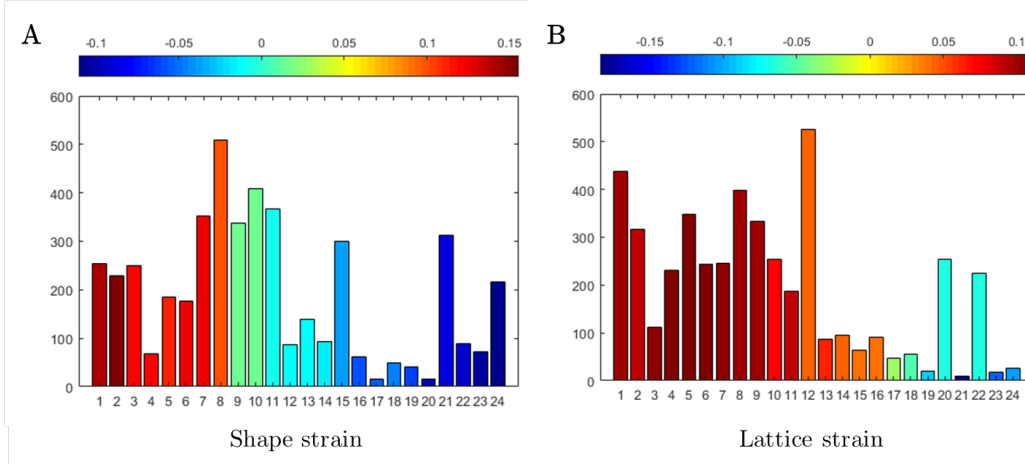


Figure 11.4: Histogramm of the variant occurrence in the lath martensite submitted to the TMT-1 with a ranking based on the work criterion. **A**: Computation of the work based on the shape strain **P**. **B**: Computation of the work based on the lattice strain **RB**.

suggest that another type of selection is taking place in the sample. When studying the effect of ausforming on lath martensite, Miyamoto *et al.* evidenced a variant selection based on CPP packets [4]. Accordingly, we treated our results under such light. Figure 11.5B presents a reconstructed austenite map acquired in the sample deformed plastically and transformed, while keeping the stress in the sample (TMT-1). The pie graphs added on several grains indicate the repartition of the variants in the four different CPP packets. The colour of each part of the pies is chosen arbitrarily, only to indicate the uneven repartition between the different CPP packets. It appears that for each prior austenite grain there is a CPP packet which is favoured among the four ones. In figure 11.5C, we represent the orientation of the normal to the favoured CPP in red. The remaining of the $\langle 111 \rangle_\gamma$ directions are indicated in black. We observed that none of the $\{111\}_\gamma$ normals close to the traction axis are selected, even though a $\langle 111 \rangle_\gamma$ fibre texture along this direction has developed as a consequence of the tensile deformation. Two green circles have been added on the $\langle 111 \rangle_\gamma$ pole figure to highlight the fibre. This analysis indicates that the dominant CPP packet is never the one perpendicular to the traction axis, and suggests that the variants belonging to that CPP packet are less favoured than those belonging to other CPP packets. This phenomenon can be understood if considering the lattice distortions associated with the variants belonging to the CPP normal to the traction axis. To simplify the explanation, let us consider the variants of the

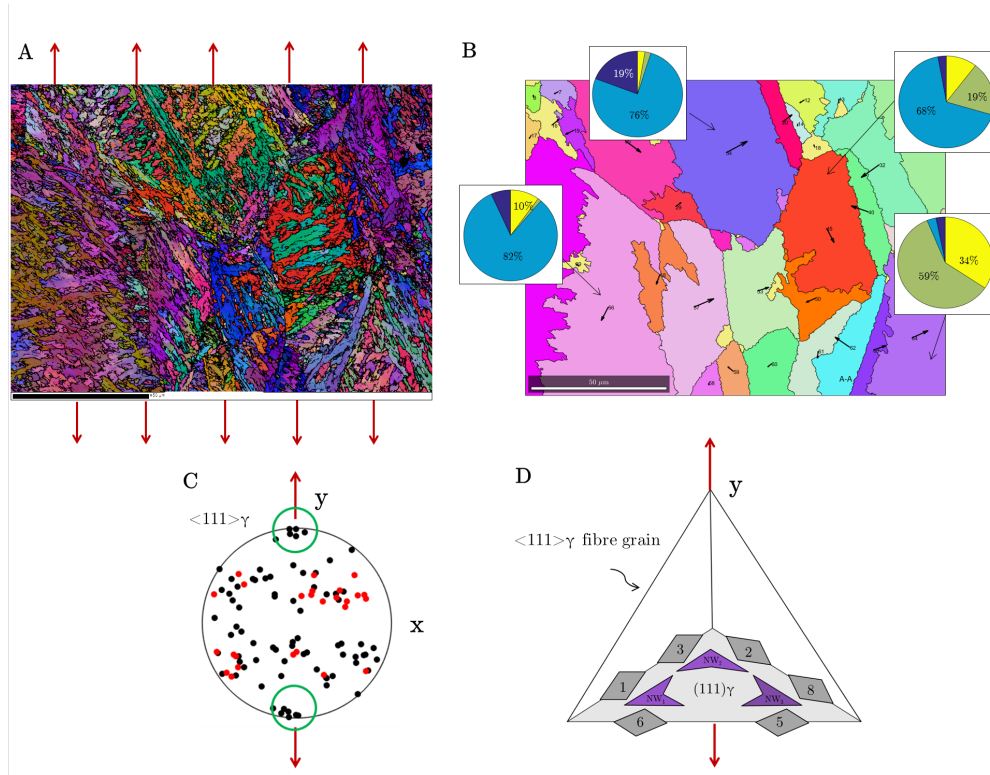


Figure 11.5: **A:** EBSD map in Euler colour coding of the lath martensite formed in the low-carbon sample submitted to TMT-1. The red arrows indicate the traction direction along the sample y -axis. **B:** Reconstructed austenite map. The black arrows indicate the normal to the close-packed plane associated with the selected CPP packet. The pie graphs illustrate the uneven repartition of the CPP packet formed in the grains. **C:** Pole figure representing the directions normal to the $\{111\}_{\gamma}$ planes. The directions normal to the close-packed planes associated with the selected CPP packets are indicated in red. The traction direction along the y -axis is indicated by the red arrows. The green circles indicate the $\langle 111 \rangle_{\gamma}$ fibre texture. **D:** Tetrahedron representing a $\langle 111 \rangle_{\gamma}$ fibre grain with its four $\{111\}_{\gamma}$ planes. The traction direction is indicated with the red arrows. The six Kurdjumov-Sachs variants belonging to the $(111)_{\gamma}$ CPP packet are represented with grey rectangles that appear as parallelograms because of the 3D perspective. The Nishijama-Wassermann variants resulting from the combination of low-misoriented Kurdjumov-Sachs variants are marked in purple.

exact Kurdjumov-Sachs orientation relationship and not those of the orientation relationship proposed by Kelly, in order to have a perfect parallelism between the close-packed planes of the FCC and the BCC phase. We note however that because the two aforementioned orientation relationships only differ from a few degrees, the following explanation holds also for the lattice strains of the Kelly's solution. We will consider an austenite grain belonging to the $\langle 111 \rangle_{\gamma}$ fibre, as represented in figure 11.5D. On this figure, the austenite grain is represented by its four $\{111\}_{\gamma}$ planes forming a tetrahedron. The orientation of the grain is such that it has the $[111]_{\gamma}$ direction along the y -traction axis, and consequently the $(111)_{\gamma}$ perpendicular

Chapter 11. Effect of tensile deformation on variant selection in $\{225\}_\gamma$ plate martensite and $\{557\}_\gamma$ lath martensite

to it. The variants 1, 2, 3, 5, 6 and 8 are the six Kurdjumov-Sachs variants belonging to the $(111)_\gamma$ CPP perpendicular to the traction axis. The variants are chosen in agreement with the numbering in reference [14]. The distortion matrices of each of these variants can be expressed in a basis formed by the $[1\bar{1}0]_\gamma$, $[111]_\gamma$ and $[1\bar{1}0]_\gamma \times [111]_\gamma = [11\bar{2}]_\gamma$. The work of the lattice strain in the applied stress field (traction along the y -axis) is equal to the diagonal value H_{yy} of the displacement gradient $\mathbf{H} = \mathbf{RB} - \mathbf{I}$. The calculations indicate that for all the variants belonging to the $(111)_\gamma$ normal to the traction axis, H_{yy} is equal to zero. This implies that *none* of the variants in the CPP packet is favoured by the application of the stress. The latter explanation rationalizes why the CPP normal to the traction axis is never the one of the dominant CPP packet. It is however not sufficient to explain why one of the CPP packets out of the three remaining ones is favoured. Indeed considering a $\langle 111 \rangle_\gamma$ fibre grain, all three remaining CPP packets are symmetrically oriented about the traction direction, and as such are equivalently favoured. Further investigations of the substructure of the deformed austenite might be needed to explain the CPP packet selection. The same type of uneven repartition of CPP packet have been observed in the samples submitted to TMT-2 and TMT-3. Unfortunately, because of the few grains present in the maps associated with these samples, we do not observe the $[111]_\gamma$ fibre texture and thus cannot reasonably conclude whether the same CPP packet selection takes place as a consequence of the external loading, or if the uneven repartition is only due to a self-accommodation process, the variants belonging to the same CPP being formed together to minimize the internal stress associated with the transformation. Indeed, the temperature of transformation of lath martensite is relatively high, such that the external applied stress is low and it is possible that the applied stress enters in competition with the minimization of the internal stresses by self-accommodation. If the self-accommodating process is predominant, the choice of the formed CPP would not be related to the external loading, but rather to randomness.

Once identified the selection based on the CPP packets, we propose to analyse the repartition of the different variants belonging to the favoured CPP packet. Investigations of variant grouping in low-carbon steel suggest that the low-misoriented Kurdjumov-Sachs variants (10.5° around $\langle 110 \rangle_\alpha$) come by pairs and form blocks [17, 14]. The pairs of variants 1-6, 2-3 and 5-8 in figure 11.5D are pairs of such variants. The geometrical average of the lattice strains of the two low-misoriented variants leads to a lattice distortion associated with Nishiyama-Wassermann orientation relationship [14]. This lattice distortion will be called Nishijama-Wassermann distortion, but it is worth mentioning that it is different from the model originally proposed by Nishiyama [24]. There are three different Nishiyama-Wassermann variants in a CPP. They are illustrated in purple in figure 11.5D and noted NW_1 , NW_2 and NW_3 . We note here that as for the Kurdjumov-Sachs variants discussed above, none of the three Nishijama-Wassermann variants belonging to the CPP normal to the traction axis is working in the applied stress field. Therefore the previous explanation for the lack of selection of the variant belonging to that CPP also holds by considering the work of the Nishijama-Wasserman variants. To analyse the variant selection inside the favoured CPP, we computed the work of the resulting average distortion for all variants belonging to the favoured CPP packet and ranked the variants accordingly. Figure 11.6 illustrates the occurrence of the

three Nishiyama-Wassermann variants in the selected packet of the map presented in figure 11.5A. This analysis suggests that an additional selection takes place in the sample. Among

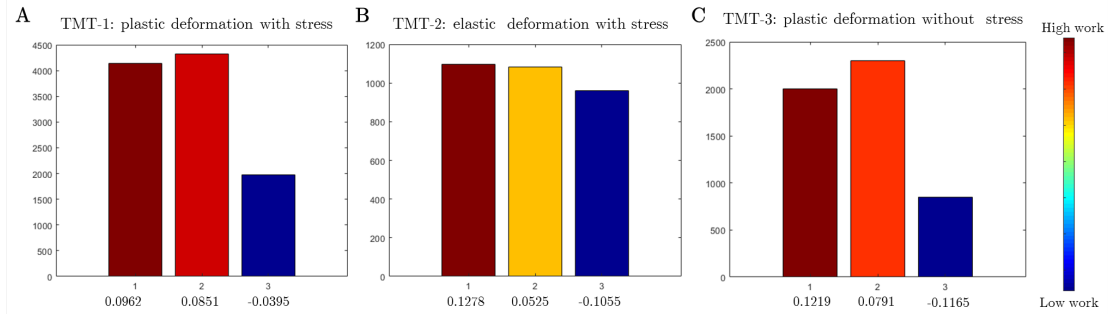


Figure 11.6: Repartition of the Nishiyama-Wassermann variants inside the selected CPP. The variants are ranked according to the work of the Nishiyama-Wassermann average distortion: $W = (\mathbf{F}^{NW} - \mathbf{I}) : \boldsymbol{\Sigma}$. **A:** Results for the TMT-1, sample deformed plastically and transformed with applied stress. **B:** Results for TMT-2, sample deformed elastically and transformed with applied stress. **C:** Results for TMT-3, sample deformed plastically and transformed without stress. The average work associated with the variants is indicated below each bar.

the three different Nishiyama-Wassermann variants, the variant exhibiting a negative work appears less often than those exhibiting a positive work. The selection inside the CPP is also observed in the sample submitted to pure plastic deformation (TMT-3) represented in figure 11.6C, but is almost not observed in the sample elastically stressed before transformation (TMT-2) represented in figure 11.6B. We believe that the lack of variant selection in the elastic loading case is related to the low magnitude of the stress imposed during the transformation. For the lath martensite, the temperature at which the tensile deformation is performed is elevated (400°C). As a consequence, the elastic limit is low, and the stress applied in the elastic thermomechanical treatment is only 62MPa. As a comparison, in the same thermomechanical treatment applied to the plate martensite, where variant selection has been observed (figure 11.3B), the applied stress in the elastic regime reaches 150MPa. The selection observed in the sample submitted to plastic deformation only prior to transformation (TMT-3, figure 11.6C) was unexpected as no stress is applied during transformation. Some residual stresses caused by the prior deformation might be present in the material during transformation, which might explain the variant selection observed.

Taken together the results of variant selection in plate and lath martensite indicate that the phenomenon is related to the nature of the strain accommodation process. In $\{225\}_{\gamma}$ plate martensite, the accommodation of the habit plane is based on the coupling of Kurdjumov-Sachs twin-related variants. The deformation that matters in the computation of the work in equation (1) is therefore the combination of the lattice strains of both variants, namely the shape strain. On the contrary, in lath martensite, a self-accommodation is achieved by the concomitant formation of all variants belonging to the same CPP packet. In addition, low-misoriented variants of the same packet appears together, forming a bifoliated block [14]. For that type of martensite, we observe a two-steps variant selection, first there is a selection of

Chapter 11. Effect of tensile deformation on variant selection in $\{225\}_\gamma$ plate martensite and $\{557\}_\gamma$ lath martensite

a particular CPP packet and then a selection inside the packet. A CPP packet is systematically not selected, and it is the one for which the work of all the variant's lattice strain is zero. Inside the selected CPP packet, the variant selection can be explained by considering the work of the combination of the lattice strains of low-misoriented variants in the stress field.

Conclusions

The effect of tensile deformation in both elastic and plastic ranges on variant selection has been studied in lath and plate martensites. The effect of a prior tensile plastic deformation with no applied stress is also investigated. The selection is primarily studied by considering the work of the deformation gradient \mathbf{F} associated with the transformation in the applied stress field Σ : $W = (\mathbf{F} - \mathbf{I}) : \Sigma$. In plate martensite, the variant selection is successfully modelled by considering the average of the two lattice distortions of the twin-related variants composing the plate, $\mathbf{F} = 0.5\mathbf{RB} + 0.5(\mathbf{RB})_{\text{twin}} = \mathbf{P}$, namely the Patel and Cohen criterion. A selection is observed when stress is applied during transformation, but no significant selection is observed as a consequence of a prior plastic deformation. In lath martensite, the selection is observed in both thermomechanical treatments involving plastic deformation (TMT-1 and TMT-3), and not when the applied stress remains below the elastic limit (TMT-2). The selection phenomenon is somewhat more complex than in the plate martensite and we could not explain the selection by using a simple analysis based on the work of the lattice distortion or of the shape strain. We observed that some CPP packets are favoured. The CPP packet selected are those that are not oriented along the tensile direction. This can be explained by considering the lattice distortion associated with the variants in the CPP packet, as this CPP orientation is such that none of the variants belonging to that CPP packet works in the stress field. A second selection is observed inside the selected CPP packet. This latter could be modelled by considering the work of the lattice distortion associated with the Nishijama-Wassermann orientation relationship, which results from the combination of lattice strains of the two low-misoriented Kurdjumov-Sachs variants forming a block. We concluded that in both cases, *i.e.* plate and lath martensite, it is the combination of lattice distortions that matters in the computation of the work, and that the nature of the combination is related to the strain accommodation in the martensite product.

Acknowledgments

We would like to thanks the Swiss National Science Foundation for supporting this research (grant number 200021-159955). We also thanks Mathijs van der Meer for its help in conducting the experiments. The authors also acknowledge ArcelorMittal, in particular Kangying Zhu for providing the material of this study. Finally, we acknowledge PX Group for its financial support to the laboratory.

Bibliography

- [1] Y. Mishiro, S. Nambu, J. Inoue, T. Koseki, Effect of stress on variant selection in lath martensite in low-carbon steel, *ISIJ international* 53 (8) (2013) 1453–1461.
- [2] M. Kato, T. Mori, Orientation of martensite formed in Fe-23Ni-5Cr crystals under uniaxial stress along [001], *Acta Metallurgica* 25 (8) (1977) 951–956.
- [3] H. Bhadeshia, H. Abreu, S. Kundu, Calculation of crystallographic texture due to displacive transformations, *International Journal of Materials Research* 99 (4) (2008) 342–346.
- [4] G. Miyamoto, N. Iwata, N. Takayama, T. Furuhashi, Quantitative analysis of variant selection in ausformed lath martensite, *Acta Materialia* 60 (3) (2012) 1139–1148.
- [5] S. Kundu, H. Bhadeshia, Crystallographic texture and intervening transformations, *Scripta Materialia* 57 (9) (2007) 869–872.
- [6] S. Kundu, Prediction of transformation texture under complex rolling condition, *Materials Science and Engineering: A* 516 (1-2) (2009) 290–296.
- [7] J. Bowles, J. K. Mackenzie, The crystallography of martensite transformations iii. face-centred cubic to body-centred tetragonal transformations, *Acta Metallurgica* 2 (2) (1954) 224–234.
- [8] E. C. Bain, N. Dunkirk, The nature of martensite, *trans. AIME* 70 (1) (1924) 25–47.
- [9] J. Patel, M. Cohen, Criterion for the action of applied stress in the martensitic transformation, *Acta metallurgica* 1 (5) (1953) 531–538.
- [10] G. Olsen, W. Jesser, The effect of applied stress on the fcc-bcc transformation in thin iron films, *Acta Metallurgica* 19 (12) (1971) 1299–1302.
- [11] H. Miyaji, M. Nobuki, N. Sakuma, T. Mitsui, H. Nakajima, E. Furubayashi, In i. tamura, editor, in: *Proceedings of International Conference on Physical metallurgy of thermomechanical processing of steels and other metals*, Vol. 200, 1988, pp. 815–822.
- [12] C. Cayron, Continuous atomic displacements and lattice distortion during fcc–bcc martensitic transformation, *Acta Materialia* 96 (2015) 189–202.

Bibliography

- [13] A. P. Baur, C. Cayron, R. E. Logé, {225} γ habit planes in martensitic steels: from the ptmc to a continuous model, *Scientific Reports* 7 (2017) 40938.
- [14] C. Cayron, A. Baur, R. Logé, Intricate morphologies of laths and blocks in low-carbon martensitic steels, *Materials & Design* 154 (2018) 81–95.
- [15] P. M. Kelly, Crystallography of lath martensite in steels, *Materials Transactions, JIM* 33 (3) (1992) 235–242.
- [16] A. P. Baur, C. Cayron, R. E. Logé, Variant selection in surface martensite, *Journal of applied crystallography* 50 (6) (2017) 1646–1652.
- [17] S. Morito, H. Tanaka, R. Konishi, T. Furuhashi, T. Maki, The morphology and crystallography of lath martensite in Fe-C alloys, *Acta Materialia* 51 (6) (2003) 1789–1799.
- [18] F. Bachmann, R. Hielscher, H. Schaeben, Texture analysis with mtex—free and open source software toolbox, in: *Solid State Phenomena*, Vol. 160, Trans Tech Publ, 2010, pp. 63–68.
- [19] C. Cayron, ARPGE: a computer program to automatically reconstruct the parent grains from electron backscatter diffraction data, *Journal of applied crystallography* 40 (6) (2007) 1183–1188.
- [20] X.-F. Gu, T. Furuhashi, W.-Z. Zhang, Ptclab: free and open-source software for calculating phase transformation crystallography, *Journal of applied crystallography* 49 (3) (2016) 1099–1106.
- [21] J. Bolton, E. Petty, G. Allen, The mechanical properties of α -phase low-carbon Fe-Mn alloys, *Metallurgical Transactions* 2 (10) (1971) 2915–2923.
- [22] E. Jimenez-Melero, N. Van Dijk, L. Zhao, J. Sietsma, S. Offerman, J. Wright, S. Van der Zwaag, Characterization of individual retained austenite grains and their stability in low-alloyed TRIP steels, *Acta Materialia* 55 (20) (2007) 6713–6723.
- [23] Kelly, P.M. and Nutting, J., The martensite transformation in carbon steels, *Proc. R. Soc. Lond. A* 259 (1961) 45–58.
- [24] Z. Nishiyama, X-ray investigation of the mechanism of the transformation from face centered cubic lattice to body centered cubic, *Sci. Rep. Tohoku Univ.* 23 (1934) 637.

12 General discussion

Comparison of the continuous FCC-BCC distortion model with the PTMC

The $\{225\}_\gamma$ habit plane case

An important result obtained during this thesis is the demonstration of the equivalence between the continuous distortion model and the PTMC model in the prediction of the $\{225\}_\gamma$ habit plane (chapter 5). We showed that under the same assumptions, namely considering the same orientation relationship and the same ratio of lattice parameters, the two models are equivalent. As a consequence, we offered a mechanistic dimension to the famous phenomenological theory.

We propose here to briefly compare the two models in this particular $\{225\}_\gamma$ case. The comparison of the inputs and outputs associated with each model is summarized in table 12.1. The major input associated with the PTMC is the assumption that the macroscopic shape change is an invariant plane strain. As additional inputs, the ratio of lattice parameters, the Bain correspondence and type of accommodation, namely the nature of the lattice invariant shear are needed. Through the PTMC calculations, the orientation relationship and the type of habit plane are predicted. On the contrary, in the continuous model, the Kurdjumov-Sachs orientation relationship is a starting hypothesis. Besides, the ratio of lattice parameters is implicitly imposed as the atoms are considered to behave like hard spheres. As in the PTMC, the Bain correspondence is assumed. The habit plane and the accommodation by twin-related variants pairing are emerging from the distortion.

Table 12.1: Comparison between the PTMC and the continuous model in the $\{225\}_\gamma$ case

| Model | Inputs | Outputs |
|------------|--|--|
| PTMC | <ul style="list-style-type: none"> • Nature of the shape strain • Accommodation mechanism • Lattice parameters • Bain correspondence | <ul style="list-style-type: none"> • Orientation relationship • Shape strain |
| Continuous | <ul style="list-style-type: none"> • Orientation relationship • Lattice parameter • Bain correspondence | <ul style="list-style-type: none"> • Shape strain • Accommodation mechanism |

Concept of habit plane

The habit plane is an experimentally observable feature of the transformation. However, its nature is envisioned in a different way by the two approaches. The assumption of the existence of a completely invariant habit plane is central in the PTMC calculations, whereas in the continuous model it is only a consequence of the combination of two particular variants. In general, like Jaswon and Wheeler [Jaswon and Wheeler, 1948], the approach based on the continuous model considers as a sufficient condition for the existence of a habit plane that the plane remains untilted by the transformation. As a matter of fact, in the $\{557\}_\gamma$ model presented in chapter 7, there is no invariant plane. The habit plane of each lath is tilted by 0.5° and globally untilted by the neighbouring bloc. The remaining of the martensite accommodation is ensured by plasticity both in the austenite and the martensite. In the $\{557\}_\gamma$ habit plane case, contrarily to the $\{225\}_\gamma$, the continuous model is not yet able to predict the exact type of accommodation mechanism needed to guarantee an invariant plane. Disclinations and dislocations are considered to be good candidates.

Importance of the lattice parameters

If both models need some lattice parameters as inputs, the attention paid to them is radically different. In the PTMC, the variation of the ratio of lattice parameters leads to change in the predictions. As an example, with using the same lattice invariant shear, the PTMC predicts a Kurdjumov-Sachs orientation relationship with a $\{225\}_\gamma$ habit plane, for lattice parameter in hard-sphere ratio $\frac{a_\gamma}{a_\alpha} = \sqrt{\frac{3}{2}}$, but it predicts a orientation relationship between Kurdjumov-Sachs and Nishiyama-Wassermann and a $\{259\}_\gamma$ habit plane for a larger ratio. In the continuous model, a hard sphere ratio is assumed to simplify the computation of the atoms trajectories. In this model, a change of lattice parameter could potentially be accounted for by varying the size of the atoms during the transformation. The mechanism of transformation will however remain the same. In our opinion, for steels, considering the exact lattice parameter ratio is not so important to model the transformation. Actually, the relationship between the ratio of lattice parameters and crystallographic features such as the orientation relationship and

the habit plane as it is intrinsically assumed in the PTMC is questionable. In the supplements of the first study on surface martensite (Appendix A), we compare the crystallography of the surface martensite and the bulk martensite produced in Fe-30%Ni. In the same material, the orientation relationship changes from Kurdjumov-Sachs on the surface to Nishiyama-Wasserman in the bulk. Similarly, the habit plane moves from $\{225\}_\gamma$ on the surface to $\{259\}_\gamma$ in the bulk. On a PTMC stand point, a rather natural explanation for such changes in the crystallography could be the change of the lattice parameters ratio due to thermal contraction, as the bulk and surface martensite formation takes place at two different temperatures. To test the validity of this hypothesis, we computed the change of the ratio of lattice parameter due to the difference in temperature between room temperature, when the surface martensite appears, and the liquid nitrogen temperature in which we formed the martensite in the bulk. For such temperature difference, the ratio $\frac{a_\gamma}{a_\alpha}$ decreased by 0.06%. It is extremely low in comparison with the 2% difference of ratio that needs to be considered in the PTMC to move from a $\{225\}_\gamma$ hard sphere solution to a $\{259\}_\gamma$ solution. Therefore, we believe that the change of accommodation mechanisms, related to the decrease in Ms, is a more meaningful explanation for the change in the crystallography rather than a change in lattice parameters.

Contributions of the continuous description

Contrarily to the PTMC model where only the final distortion is considered, the continuous model describes the complete atomic path. It has thus the strong advantage of giving a realistic idea of how the martensitic transformation "looks like". It is typically what is aimed when we present the film of the formation of $\{225\}_\gamma$ thin plate (chapter 5). We believe such illustration of the martensitic transformation more pedagogical than PTMC computations. Even, we think that such animation could help in understanding what is behind the phenomenological description of the PTMC, as it is somehow closer to reality.

Regarding the prediction of variant selection, our studies indicate, using a selection criterion based on the work of the distortion, that the continuous description does not improve the prediction with respect to the final transformation. Although we first suggested that the consideration of the *variation* of the extension in a direction normal to the surface at the beginning of the transformation could better model the variant selection phenomenon in surface martensite (chapter 8), our second study on the same type of martensite (chapter 9), which more clearly allows to discriminate the different models, let us conclude that the complete distortion is more appropriate to study variant selection.

Still, we are convinced that the continuous description of the transformation could help in refining the variant selection prediction, for example by offering insights on the accommodation mechanism in the austenite. Additionally, the continuous model could potentially allow for the explanation of interesting crystallographic features, such as the spread of orientation relationship visible by the continuous patterns in the martensite pole figures.

Variant selection modelling

In our mathematical introduction in chapter 4 (equation 4.32), we explained that the effect of stress on variant selection can be studied by considering the work of the deformation \mathbf{F} associated with the transformation in the applied stress field $\mathbf{\Sigma}$, similarly to the Patel and Cohen criterion [Patel and Cohen, 1953]:

$$W_\sigma = (\mathbf{F} - \mathbf{I}) : \mathbf{\Sigma} = \mathbf{H} : \mathbf{\Sigma} = tr(\mathbf{H}\mathbf{\Sigma}^T) \quad (12.1)$$

The experimental studies of variant selection carried out on the different martensite types suggest that such a criterion is appropriate to model variant selection. In this section, we will discuss in more details the different elements involved in the computation of the work W_σ .

Applied stress in the variant selection model

In equation 12.1, the stress tensor $\mathbf{\Sigma}$ considered is the *macroscopic* applied stress, but it is well-known that in polycrystalline materials the local stress, acting in each individual grain, is not equal to the macroscopic one. Such simplification in the evaluation of the quantity W_σ could have been detrimental for the prediction of variant selection. However, our results suggest that the consideration of the macroscopic stress allows for a reasonably good prediction of the variant selection. Nonetheless, it would be interesting to study variant selection considering the local stress by using polycrystalline models, in order to quantify the loss of quality in the prediction using the Reuss (iso-stress) assumption. It is worth mentioning that by studying surface martensite, we manage to somehow circumvent the difficulties associated with the change of local stress state between different grains. Indeed, in that particular case, the effect of the free surface is identical for all grains.

Effect of free surfaces on variant selection

On the free surface contrarily to the bulk, there is no austenite to impede the deformation of the martensite in the direction normal to the free surface. As a consequence, W_{def} (in equation 4.31 in chapter 4) is different for each variant, even if no stress is applied to the material ($W_\sigma = 0$). This particularity gives rise to a natural variant selection in surface martensite, as it has been reported in chapters 8 and 9. In these studies, we modelled the variant selection phenomenon by using the H_{zz} component of the displacement gradient, when it is expressed in the sample reference frame, z defining the normal to the free surface. The variant that exhibits the largest H_{zz} value is more prone to form as it maximizes the deformation in the direction normal to the free surface. In the context of variant selection caused by applied stress, this criterion can be seen as the general criterion presented in equation 12.1, where the stress tensor $\mathbf{\Sigma}$ is associated with a *fictitious* force normal to the free surface. Figure 12.1 illustrates this equivalence, by using the principle of superposition. In figure 12.1A, we modelled the effect of the free surface by considering that it is equivalent to considering the nucleation of

martensite in the bulk and removing the "hat" of austenite above the nucleus of martensite. When a martensite nucleus is formed in the bulk, it is constrained by the surrounding austenite which impedes its transformation. However in the case of a transformation on a free surface, these constraints are partially removed. Such a situation is equivalent to a nucleation in the bulk plus a contribution of a tensile force normal to the free surface (figure 12.1B). As the effect of the bulk on the nucleation of the martensite is assumed to be the same for all variants, only the effect of the *fictitious* tensile force matters for variant selection. We can then consider the effect of the free surface as the interaction of the *fictitious* force with the transformation mechanism, which gives a fictitious $W_\sigma = \Sigma_{fict} : \mathbf{H}$, where Σ_{fict} has all the components equal to zero, except the Σ_{zz} diagonal component, z being oriented normal to the sample free surface. To compare the free surface effect and the effect of an applied stress on the

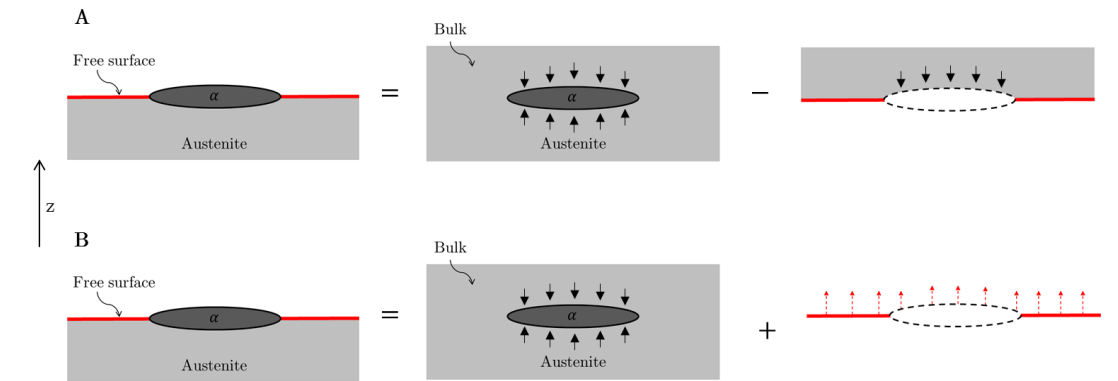


Figure 12.1: Illustration of the anisotropy associated with the nucleation of surface martensite. The free surface is marked in red. The black arrows represent the constraints caused by the austenite and the red dashed arrows represent the fictitious force associated with the free surface.

surface martensite formation, we performed a simple experiment using the 4-point bending device presented in chapter 10. As-cast Fe-30%Ni samples have been polished down to 1 micron. The samples have then been loaded in 4-point bending and electropolished directly on the machine, such that the imposed stress interacts with the transformation mechanism. The produced martensite has been characterized with EBSD measurements and the variant selection studied. The pole figures presented in figure 12.2 show the martensite formed in an austenite grain with a cube orientation, in tension along the x -axis. This measurement indicates that the trend of variant selection is essentially the same as for surface martensite without applied stress. Namely, the Bain group close to the z -axis almost disappears. The expected effect of the applied stress would have been that the Bain group close to the x -axis would disappear as well. It is not the case, and this little experiment leads us to conclude that the effect of an applied stress is of second order with respect to the effect of the free surface.

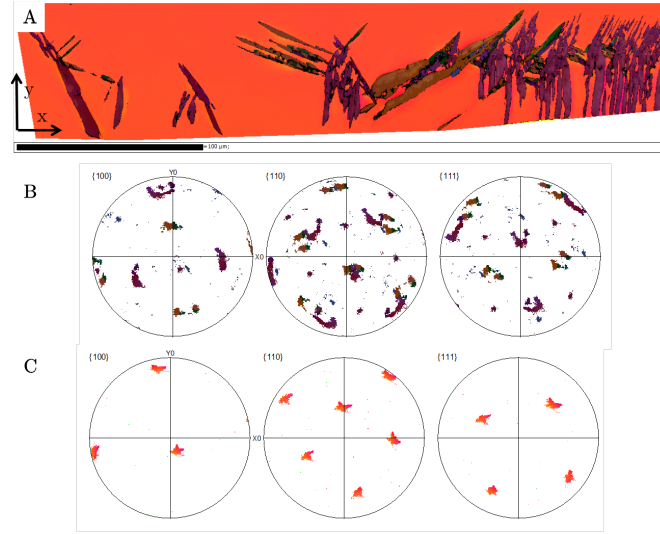


Figure 12.2: EBSD map (A) and associated pole figures of the surface martensite (B) produced on a sample electropolished while loaded in 4-point bending. The tensile axis is along the x -direction. In C: Pole figure of the austenite parent grain.

We try to quantify the effect of the free surface by using a rather rough approach which consists in evaluating the maximum elongation authorized in elasticity $\epsilon_{\max} = \frac{\sigma_y}{E}$ and compare it to the elongation associated with the transformation mechanism ϵ_{trans} . The max elongation associated with the transformation mechanism is computed by using the Green deformation tensor $\mathbf{E} = \frac{1}{2}(\mathbf{F}^T \mathbf{F} - \mathbf{I})$. For standard mechanical values of the austenite, we have $\epsilon_{\max} \cong 1 \cdot 10^{-3}$. By computing \mathbf{E} using the continuous model, we find $\epsilon_{\text{trans}} \cong 1.7 \cdot 10^{-1}$. Based on this calculation, it appears that the maximal deformation authorized in elasticity is significantly lower than the elongation associated with the transformation, which illustrates also that plasticity is needed to accommodate the transformation. In agreement with the experiment, it indicates that it is more favourable for a variant to maximize its deformation in a direction normal to the free surface, where there is no limit in the allowed elongation, rather than maximizing it in the tensile direction.

Deformation associated with the martensite transformation

Our studies indicate that the deformation gradient \mathbf{F} that needs to be considered in the computation of W_σ (equation 12.1) is not always the shape deformation as originally proposed by Patel and Cohen, and commonly accepted as being *the* appropriate criterion, but it depends on the martensite type, in particular on the accommodation mechanism in the martensite. We concluded that the deformation \mathbf{F} to consider is always based on the lattice strain \mathbf{RB} . Depending on whether the martensite product is accommodated independently, by means of dislocations, or by variant couplings, it is either directly the lattice strain, or the result of the combination of different lattice strains, that needs to be considered in the prediction.

For example, in the $\{225\}_\gamma$ plates formed in the bulk of high-carbon steel (chapter 11), a coupling of twin-related variants is required to accommodate the martensite formation. In that case, the variants are formed simultaneously. The deformation to consider is thus the resulting deformation caused by both variants, namely the shape strain $\mathbf{P} = 0.5\mathbf{RB} + 0.5\mathbf{RB}_{twin}$. When $\{225\}_\gamma$ martensite is formed on the surface of the sample, the accommodation of the habit plane is only partially made by the twin-related variants. In our first study on surface martensite (chapter 8), we noted that the variant which is twin-related with a favoured variant slightly appears, participating in the accommodation. However, the amount of that variant is very low, such that the situation appears to be far from the 50%-50% fully accommodating ratio. Even in our second study (chapter 9), we observed no trace of the unfavoured twin-related variant. Actually because it forms on the surface, the motion of dislocation is facilitated and it is very likely that the accommodation of surface martensite is achieved by dislocations, similarly to what is proposed in our Frank-Bilby analysis (chapter 6). Therefore, in that case, a variant can "live by itself" and only the lattice deformation associated with individual variants needs to be considered in the computation of the work. In that case, the consideration of the individual lattice strain better accounts for variant selection. In $\{557\}_\gamma$ lath martensite, the selection phenomenon appears to be more complex. We could not convincingly relate the selection to the work of a particular distortion. Actually, we noted two types of selections. A first selection based on the CPP packet and a second selection occurring inside the formerly favoured CPP packet. The first selection mechanism would require a more detailed study. We rationalized the second one by using the work of the combination of the two low-misoriented martensite variants forming a bloc, namely the distortion associated with the Nishijama-Wassermann orientation relationship. In the $\{259\}_\gamma$ lenticular martensite, we were not able to find the deformation that could model variant selection. All the classical models have been tested, but none of them accounts for the selection. By analyzing the internal structure of the lenticular martensite, we observed a complex crystallographic architecture, as illustrated in the TEM micrograph in figure 12.3.

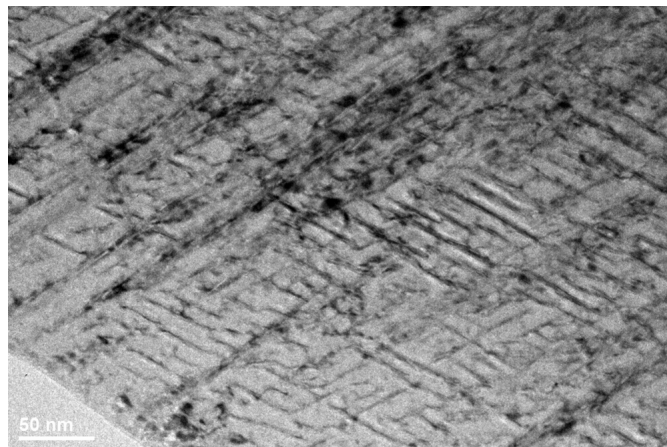


Figure 12.3: TEM brightfield micrograph of the internal substructure of $\{259\}_\gamma$ lenticular martensite

In the light of such a microstructure, the inability of our different models to capture the variant selection is understandable. Indeed, it is very likely that the deformation associated with the nucleation of lenticular martensite involves more complexity than a coupling of two variants, as proposed in the PTMC for the $\{259\}_\gamma$ or in our model for $\{225\}_\gamma$. A detailed TEM analysis of the internal microstructure of lenticular martensite combined with a measure of the macroscopic shape change would help in modelling the variant selection in this material.

To summarize our modelling of variant selection in the different investigated steels, a schematic map is proposed in figure 12.4. The different martensites are classified as a function of the complexity of the martensite strain accommodation and the temperature at which there are formed. By *simple* accommodation we consider a mechanism essentially based on dislocations. An increased complexity is considered if variant grouping are needed for the accommodation of the martensite product.

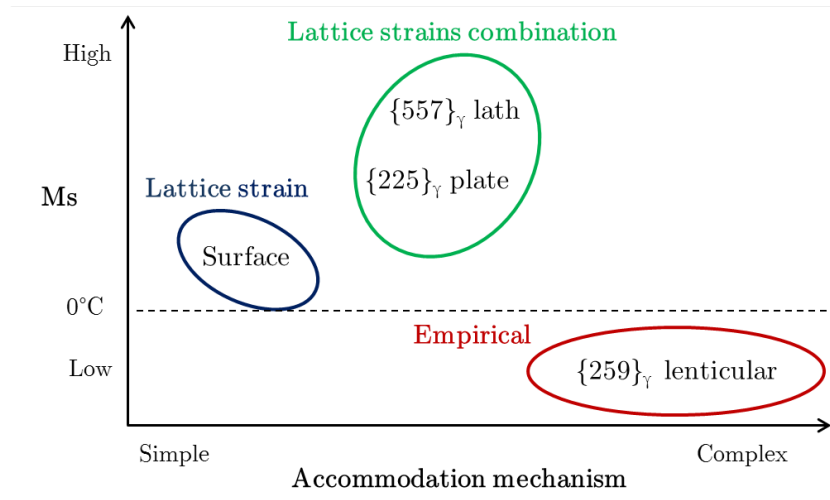


Figure 12.4: Map of the variant selection modelling for different types of martensite. In the x -axis, the increasing complexity of the martensite accommodation mechanism. In the y -axis, the martensitic start temperature.

Relation between variant selection and martensite morphology

The results obtained in this thesis suggest that the martensite morphology is related to the variant selection phenomenon. The effect is clearly evidenced in our study of the chevron morphology (chapter 9). We showed a selection of the twin boundaries that favour the transformation. The selection is such that it induces a symmetry in the martensite morphology (illustrated in figure 12.5A). Besides, the strain accommodation by local variant selection as proposed in our models for the $\{225\}_\gamma$ and $\{557\}_\gamma$ habit planes are also related to proper morphologies. In the $\{225\}_\gamma$, we showed that the only way to accommodate the habit plane by variants pairing of the continuous distortion is an equilibrated combination of twin-related variants. This implies an alternated martensite microstructure, as presented in figure 12.5B. In

the study of $\{557\}_\gamma$ laths, we concluded that blocks have a bifoliate morphology (figure 12.5C), allowing for good angular compatibility between the laths and the surrounding blocs.

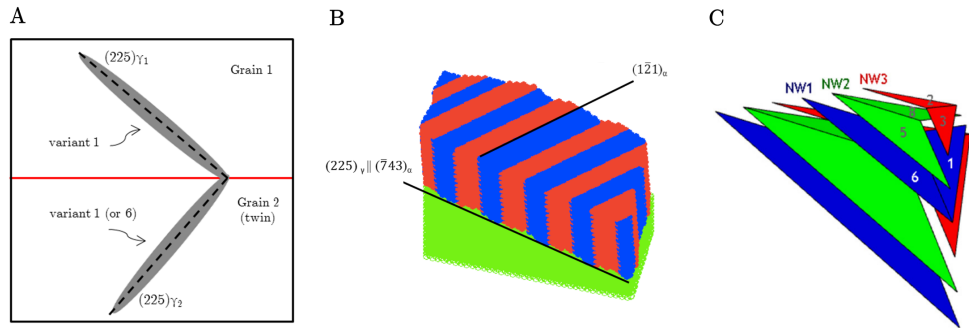


Figure 12.5: Morphologies related to the variant selection phenomenon. **A:** Chevron morphology caused by the selection of the twin boundary. **B:** Alternate structure of $\{225\}_\gamma$ martensite. **C:** Bifoliate morphology of $\{557\}_\gamma$ martensite blocks composing a packet.

Texture inheritance

The texture inheritance has been only briefly addressed in this thesis. Only the last experiments presented in chapter 11 consider the effect of plastic deformation without stress on variant selection. Our results suggest that the variant selection on the plastically deformed sample without stress is very similar to the variant selection when the stress is maintained during transformation. This is quite surprising, but might potentially be explained by residual stress arising from the hot deformation. Further work is required to confirm this hypothesis. This result even though not explained is still of interest as it indicates that texture inheritance takes place when the material is strained before transformation. As a starting point for the texture inheritance study, we think valuable to investigate in more details the selection of the CPP packet observed in lath martensite.

13 Conclusions and perspectives

The variant selection phenomenon at both local and global scales has been studied in different martensitic steels. It has been characterized by EBSD measurements. Two different transformation models are considered in this thesis, the *Phenomenological Theory of the Martensite Crystallography* and the continuous distortion model.

Global variant selection has been studied in Fe-Ni surface martensite, and in bulk transformations of $\{557\}_\gamma$ lath martensite formed in a low-carbon steel, $\{259\}_\gamma$ lenticular martensite formed in a Fe-Ni-C alloy and in $\{225\}_\gamma$ plate martensite formed in a high-carbon steel. It has been shown that a criterion based on the work of the deformation associated with the transformation and the applied stress allows a good prediction of variant selection. Our work further suggests that the deformation to consider in the computation of the work depends on the type of martensite, more precisely on the accommodation mechanism in the martensite. When the martensite is essentially accommodated with dislocations, the work of lattice distortion well accounts for the selection phenomenon. This is typically what is observed in surface martensite. On the contrary, when the accommodation is performed by variant pairing, as for the $\{225\}_\gamma$ plate martensite, the variant selection is better modelled by using the average of the lattice distortions of each variant, which is in that case the shape strain. The analysis of variant selection in $\{557\}_\gamma$ appears more complex, but we could also relate the selection by the combination of lattice strains of different variants. In that case, the low-misoriented Kurdjumov-Sachs variants of the same CPP packet have been used to model the selection. The study of the $\{259\}_\gamma$ lenticular martensite is somewhat less conclusive as we could not relate the observed variant selection to any defined accommodation process.

Local variant selection to accommodate the transformation has also been studied. By using the continuous distortion model, we could explain the $\{225\}_\gamma$ and the $\{557\}_\gamma$ habit planes by variants combinations. In the $\{225\}_\gamma$ case, the habit plane is kept completely invariant, whereas in the $\{557\}_\gamma$ case, the variants combination only allows to obtain an untilted, or low tilted (0.5°) plane.

Besides the variant selection study, this thesis also enlightens the similarities and dissimilarities between the continuous model and the classical PTMC. It appears that the models are much closer than could be initially believed. In particular, under the same assumptions,

the models are shown to be equivalent. Our work thus offered a mechanistic dimension to a theory which was up to now phenomenological.

In summary, the following general results are achieved in this thesis:

- We evidenced that contrarily to the widespread expectation it is not *always* the shape strain that needs to be considered to model variant selection, but rather the lattice strain or appropriate combination of lattice strains, depending on the accommodation mechanism.
- We proposed a mechanistic vision of the PTMC by showing its equivalence with the continuous model.
- We explained two different habit planes, by using the continuous model and without any additional parameter; in each case, a local variant selection of different nature allows for the existence of the habit plane.

Perspectives

In our opinion, the $\{259\}_\gamma$ lenticular martensite case should be more carefully studied. In particular, investigating in details the substructure of such martensite is of interest to achieve a better understanding of the variant selection phenomenon observed in our bending experiments. In addition to the microscopic characterization, we also believe that a measure of the shape deformation associated with the $\{259\}_\gamma$ martensite would advantageously complete the study. Digital image correlation methods combined with interferometry or confocal microscopy could be useful tools to achieve such measurements.

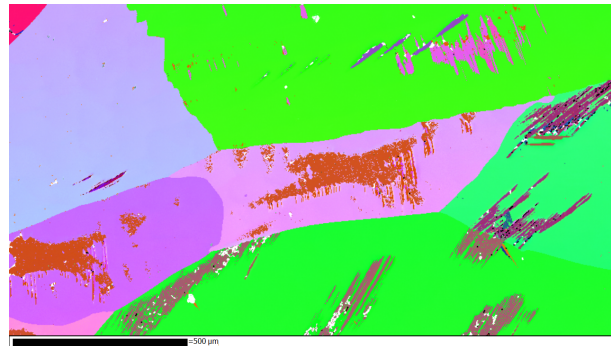
Another point that needs to be investigated in more details is the effect of prior deformation on the transformation. This point has been only briefly addressed in $\{225\}_\gamma$ plate and in $\{557\}_\gamma$ lath martensite. Our conclusions on the effect of prior deformation are not completely satisfactory. In plate martensite, no clear effect is observed, and on the contrary, an effect similar to the effect of applied stress is observed in lath martensite. We could not explain this phenomenon. Since the texture inheritance caused by deformation prior to transformation has crucial implications in the industrial processing of steel, this point needs to be further studied. In particular the selection of the CPP packet observed in the deformed lath martensite seems of interest and would require a dedicated study. In this respect, it could be of interest to perform thermomechanical treatments where a constant strain rate is imposed during the transformation. Besides, the recent developments of EBSD allowing for a better statistical analysis seems a good approach to study the variant selection phenomenon. Although the mechanisms of variant selection due to prior deformation appear to be more complex than those due to applied stress, we believe that our work will help in the further understanding of texture inheritance, by bringing a sound basis on the effect of stress on variant selection. Finally, we believe it is worth continuing exploring the predictive capabilities offered by the

continuous transformation model. The accommodation mechanisms related to the transformation appear to be of great importance in the variant selection phenomenon, and considering the full atomic path during transformation could offer significant insights on these mechanisms. In particular, using the continuous transformation model in computational methods, instead of only taking into account the final distortion, might offer new perspectives on the transformation.

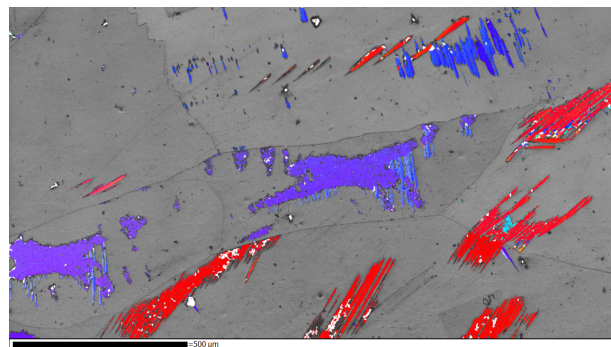
A Supplements to *Variant selection in surface martensite*

A.1 Characterization at lower magnification

The EBSD measurements presented in the main text are showing "islands" of martensite formed in only a part of the parent grain. In order to verify that the variant selection occurring in a single island of martensite is representative of the transformation behaviour of the entire grain, a lower magnification EBSD characterization is proposed here. The grain size in the



(a) Euler colour coding



(b) Band contrast and Euler colour coding

Figure A.1: EBSD map of surface martensite at lower magnification (x65).

sample is large, and grains can reach the millimetric size. From this measurement, it can be seen that all the islands of martensite formed in a given grain are very similar, which allows us to consider only one of them as representative of the whole. The analysis of the variant selection phenomenon proposed in the main manuscript is thus based on the measure at higher magnification (x500) of few of these islands.

A.2 Additional simulations

EBSD measurements

Additional simulations have been performed based on different EBSD maps acquired from the same as-cast Fe30%Ni sample. Figures A.2 and A.3 show the two additional maps and their respective pole figures of the BCC phase.

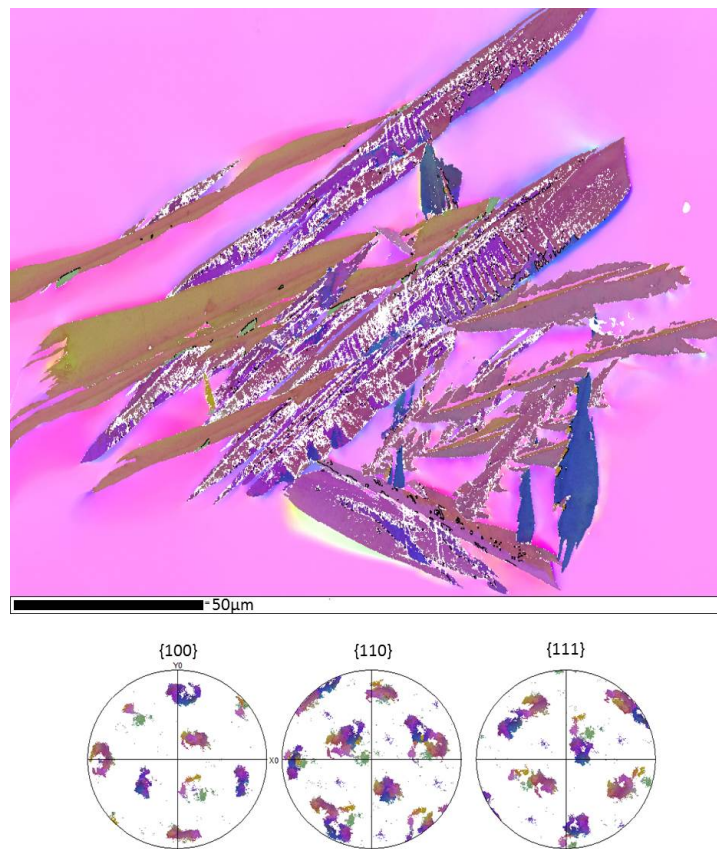


Figure A.2: EBSD measurements of surface martensite and pole figures of the martensite.

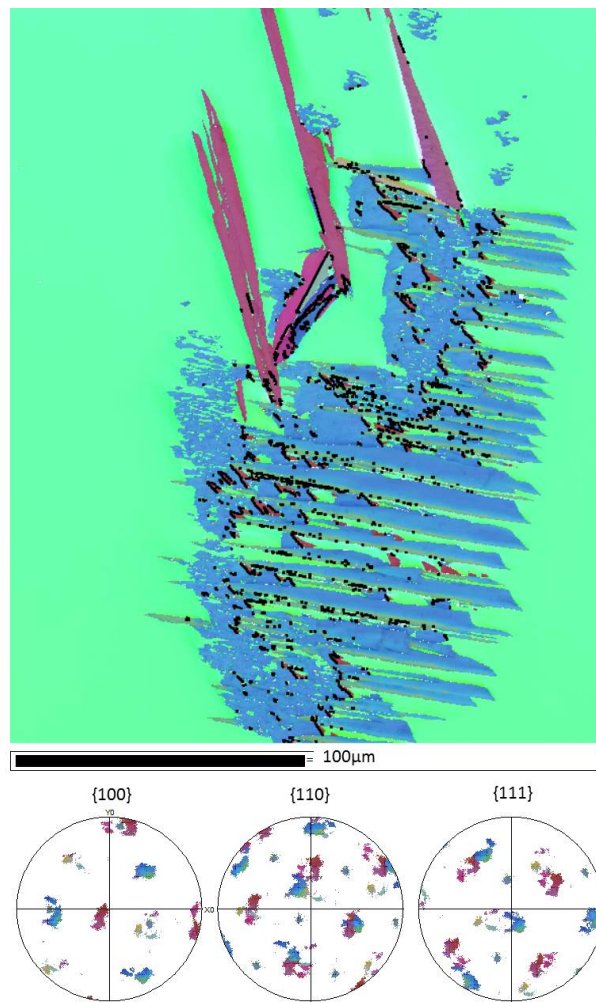


Figure A.3: EBSD measurements of surface martensite and pole figures of the martensite.

Variant selection predictions

Using the same criterion as in the article, the prediction of the variant selection is presented in figures A.4 and A.5 for the first and the second additional maps, respectively.

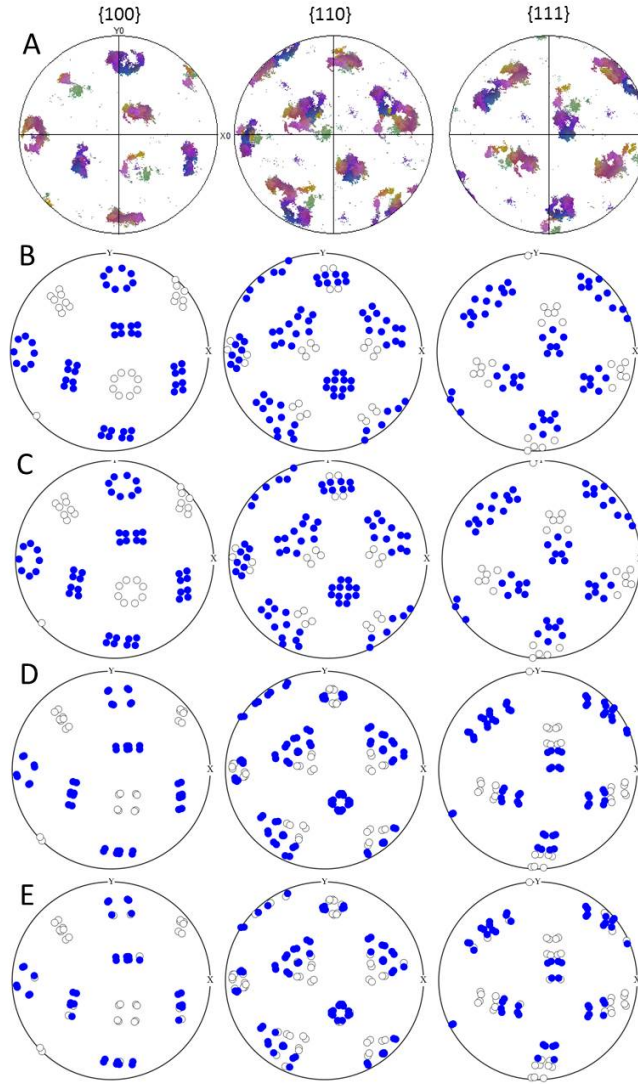


Figure A.4: Prediction of variant selection for the map 1. In blue, the selected variants. Empty circles, unselected variants. **A:** Measured pole figure. **B:** Kurdjumov-Sachs distortion. **C:** Derivative of the Kurdjumov-Sachs distortion. **D:** PTMC invariant plane strain. **E:** PTMC invariant line strain.

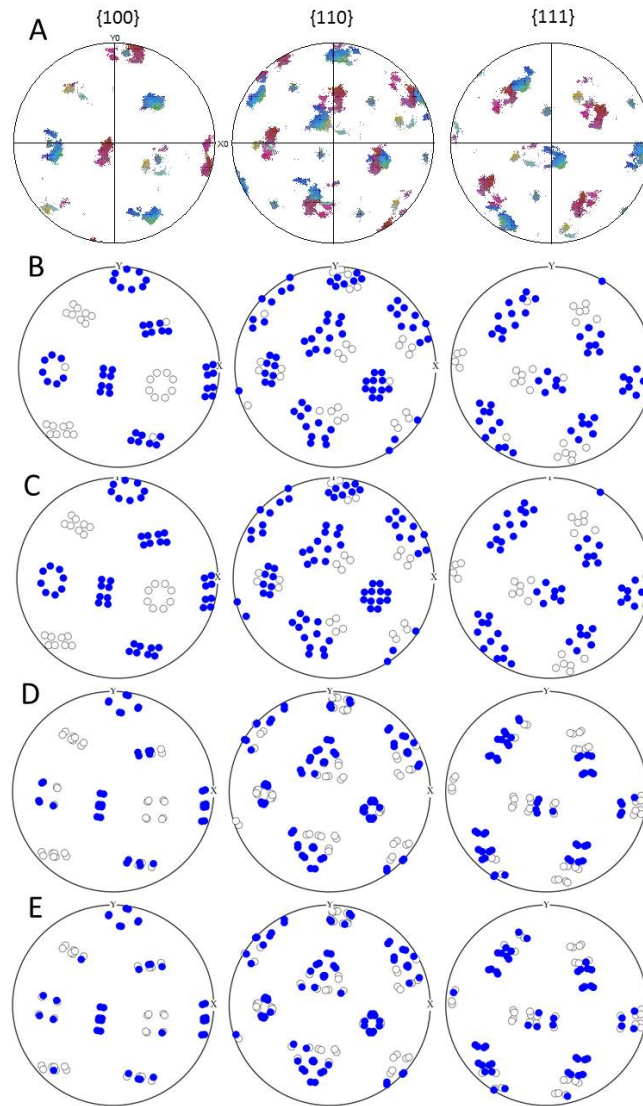
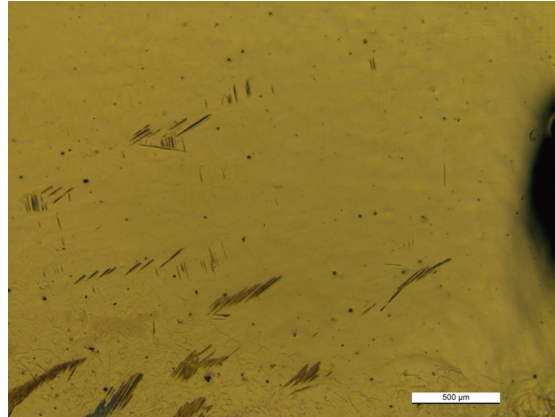


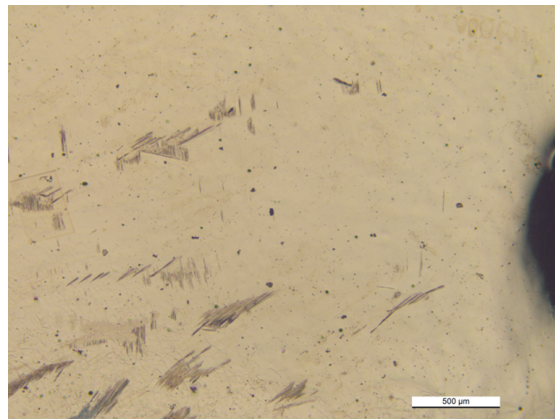
Figure A.5: Prediction of variant selection for the map 2. In blue, the selected variants. Empty circles, unselected variants. **A:** Measured pole figure. **B:** Kurdjumov-Sachs distortion. **C:** Derivative of the Kurdjumov-Sachs distortion. **D:** PTMC invariant plane strain. **E:** PTMC invariant line strain.

A.3 Isothermal surface martensite

Directly after electro-polishing and some days later, micrograph pictures have been taken showing the presence of surface martensite. These respective pictures are presented in figure A.6a and A.6b. By comparing the two micrographs, it can be observe that new martensite



(a) After polishing



(b) A few days after polishing

Figure A.6: Bright field micrographs of surface martensite

plates continue to appear even though the temperature is constant (the sample stayed in the fridge at the same temperature as the electrolyte). The surface martensite observed is thus *isothermal* martensite.

A.4 Crystallography of the habit plane

Comparison between typical habit planes

Using PTMC, the habit plane of Fe30%Ni is predicted to be close to $\{3\ 10\ 15\}_\gamma$ and this prediction is generally experimentally verified, *in the bulk*. However, in the surface martensite observed by Klostermann (1972) and later by Wakasa and Wayman (1979) the habit plane is of type $\{225\}_\gamma$. In our sample, we studied the crystallography of habit plane by verifying whether the traces of the habit planes visible on the EBSD maps correspond to $\{3\ 10\ 15\}_\gamma$ or to $\{225\}_\gamma$. Figures A.7a and A.7b present the results of this study for the $\{3\ 10\ 15\}_\gamma$ and $\{225\}_\gamma$ habit planes, respectively. By comparing figures A.7a and A.7b, it appears that the habit plane

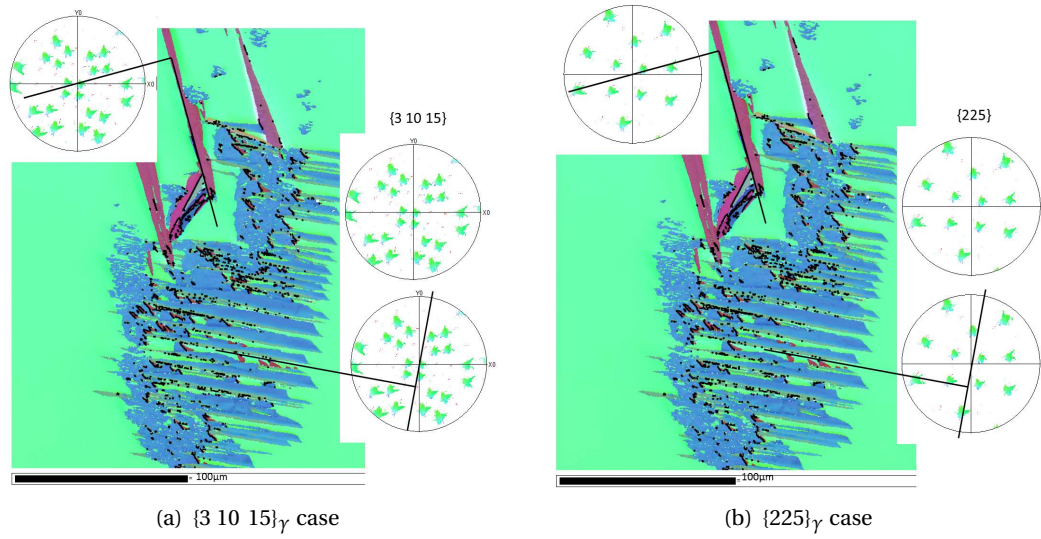


Figure A.7: Study of the habit plane of surface martensite

is not of type $\{3\ 10\ 15\}_\gamma$ but is likely to be of type $\{225\}_\gamma$. Indeed, figure A.7a shows that for several plates of martensite, the normal to the trace of the habit plane does not intersect any $\{3\ 10\ 15\}_\gamma$ poles, except the pole oriented along the z-direction. However, these plates have different habit planes one to another, and by inspection none has a habit plane normal to z. This means that the habit plane cannot be of type $\{3\ 10\ 15\}_\gamma$. Figure A.7b, on the contrary, shows the study of the $\{225\}_\gamma$ habit plane case. Here, it can be observed that each plate can be associated to a $\{225\}_\gamma$ pole. Surface martensite in Fe30%Ni seems therefore to have $\{225\}_\gamma$ habit planes.

Verification of the choice of the habit plane trace

Figure A.8 shows the misorientation in the austenite around the martensite plates in respect with the austenite orientation far from the plates. The red colour means that the misorientation is about 7° and the blue colour indicate that there is no misorientation. This allows to get

convinced that the traces of the habit plane have been chosen in an appropriate way, as the distortion of the austenite near this region is weaker than anywhere else on the border of the plate.

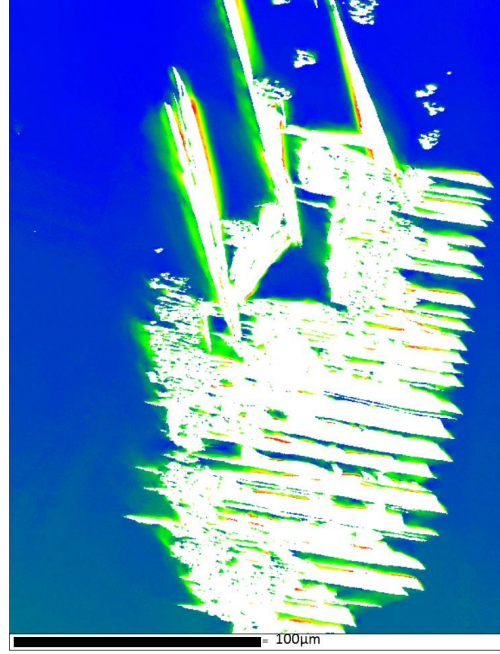


Figure A.8: EBSD measurements of surface martensite: Internal misorientation of the austenite. Blue colour, no misorientation. Red colour, misorientation of 7° .

A.5 The PTMC solutions

The PTMC solutions for the Fe30%Ni have been computed thanks to the open source software *PTCLab*. The inputs for the computations are the lattice parameters of the FCC and the BCC phases, the correspondence matrix and the lattice invariant shear system. In our study, the Bain correspondence has been chosen and the lattice invariant shear is assumed to occur by twinning on $\{101\}_\gamma$. No dilatation parameter is considered, such that we pose $\delta = 1$. The lattice parameter of the alloy in the two different phases are respectively: 3.5854\AA for the austenite and 2.8635\AA for the martensite. These lattice parameters are taken from Goldmann and Wagner (1963). Figure A.9 shows the output of the *PTCLab* software, where four solutions are proposed. It can be seen that the shapes of the patterns in the pole figures are relatively different in the two solutions. In the main article, solution 2 is chosen as it better fits the experimental data in terms of orientation relationship and variant selection prediction. In order to offer a comprehensive study, in this section, we present the results of the simulations using solution 1.

A.5. The PTMC solutions

| Phase | a | b | c | alpha | beta | gamma | SG | | | Lattice C. | 1.0 | -1.0 | 0.0 | Delta | 1.0 |
|------------|----------|-----------|----------|------------|----------|-----------|----------|------------|----------|------------|----------|------------|----------|-----------|----------|
| Phase 1 | 3.5854 | 3.5854 | 3.5854 | 90 | 90 | 90 | Fm-3m | | | | 1.0 | 1.0 | 0.0 | | |
| Phase 2 | 2.8635 | 2.8635 | 2.8635 | 90 | 90 | 90 | Im-3m | | | | 0.0 | 0.0 | 1.0 | | |
| Condition: | SP: | 1.0 | 0.0 | 1.0 | | SD: | -1.0 | 0.0 | 1.0 | | | | | | |
| | | | | | | | | | | | | | | | |
| Solution 1 | | | | Solution 2 | | | | Solution 3 | | | | Solution 4 | | | |
| IL(in 1) | -0.65745 | IL(in 2) | -0.23105 | IL(in 1) | -0.65745 | IL(in 2) | -0.81909 | IL(in 1) | -0.65745 | IL(in 2) | -0.23105 | IL(in 1) | -0.65745 | IL(in 2) | -0.81909 |
| | -0.36814 | | -0.81909 | | 0.36814 | | -0.23105 | | -0.36814 | | -0.81909 | | 0.36814 | | -0.23105 |
| | 0.65745 | | 0.52507 | | 0.65745 | | 0.52507 | | 0.65745 | | 0.52507 | | 0.65745 | | 0.52507 |
| IL*(in 1) | 0.52507 | IL*(in 2) | 0.74804 | IL*(in 1) | 0.52507 | IL*(in 2) | 0.74804 | IL*(in 1) | 0.52507 | IL*(in 2) | -0.09059 | IL*(in 1) | 0.52507 | IL*(in 2) | -0.09059 |
| | -0.66977 | | -0.09059 | | -0.66977 | | -0.09059 | | -0.66977 | | 0.74804 | | -0.66977 | | 0.74804 |
| | 0.52507 | | 0.65745 | | 0.52507 | | 0.65745 | | 0.52507 | | 0.65745 | | 0.52507 | | 0.65745 |
| RB | 1.09818 | 0.12099 | 0.16593 | RB | 1.11998 | 0.03516 | 0.10029 | RB | 1.11998 | -0.03516 | 0.10029 | RB | 1.09818 | -0.12099 | 0.16593 |
| | -0.11087 | 1.12242 | -0.04232 | | -0.01947 | 1.12242 | -0.08802 | | 0.01947 | 1.12242 | 0.08802 | | 0.11087 | 1.12242 | 0.04232 |
| | -0.23961 | 0.03516 | 0.78008 | | -0.14482 | 0.12099 | 0.78743 | | -0.14482 | -0.12099 | 0.78743 | | -0.23961 | -0.03516 | 0.78008 |
| OR Mat. | 0.61177 | -0.77211 | -0.17202 | OR Mat. | 0.67915 | -0.71489 | -0.16641 | OR Mat. | 0.72318 | -0.6905 | -0.01492 | OR Mat. | 0.76327 | -0.63328 | -0.12799 |
| | 0.76327 | 0.63328 | -0.12799 | | 0.72318 | 0.6905 | -0.01492 | | 0.67915 | 0.71489 | -0.16641 | | 0.61177 | 0.77211 | -0.17202 |
| | 0.20776 | -0.05299 | 0.97674 | | 0.12557 | -0.11022 | 0.98594 | | 0.12557 | 0.11022 | 0.98594 | | 0.20776 | 0.05299 | 0.97674 |
| HP(in 1) | -0.60978 | HP(in 2) | -0.93902 | HP(in 1) | -0.17721 | HP(in 2) | -0.57113 | HP(in 1) | -0.17721 | HP(in 2) | 0.41436 | HP(in 1) | -0.60978 | HP(in 2) | 0.04647 |
| | 0.77251 | | 0.04647 | | 0.77251 | | 0.41436 | | -0.77251 | | -0.57113 | | -0.77251 | | -0.93902 |
| | -0.17721 | | -0.34072 | | -0.60978 | | -0.7086 | | -0.60978 | | -0.7086 | | -0.17721 | | -0.34072 |
| Macro s | 0.68873 | m2 | 0.22741 | Macro s | -0.20015 | m2 | -0.22741 | Macro s | -0.20015 | m2 | -0.22741 | Macro s | 0.68873 | m2 | 0.22741 |
| | 0.69684 | | | | -0.69684 | | | | 0.69684 | | | | -0.69684 | | |
| | 0.20015 | | | | -0.68873 | | | | -0.68873 | | | | 0.20015 | | |
| F | 0.90449 | 0.12099 | -0.02776 | F | 0.99193 | 0.03516 | -0.02776 | F | 0.99193 | -0.03516 | -0.02776 | F | 0.90449 | -0.12099 | -0.02776 |
| | -0.09663 | 1.12242 | -0.02808 | | -0.02808 | 1.12242 | -0.09663 | | 0.02808 | 1.12242 | 0.09663 | | -0.09663 | 1.12242 | 0.02808 |
| | -0.02776 | 0.03516 | 0.99193 | | -0.02776 | 0.12099 | 0.90449 | | -0.02776 | -0.12099 | 0.90449 | | -0.02776 | -0.03516 | 0.99193 |
| m1 | 0.41552 | | | m1 | 0.25114 | | | m1 | 0.25114 | | | m1 | 0.41552 | | |
| OR | in 1 | in 2 | Angle | OR | in 1 | in 2 | Angle | OR | in 1 | in 2 | Angle | OR | in 1 | in 2 | Angle |
| Plane | 1 -1 1 | 1. 0. 1. | 0.60093 | Plane | 1 -1 1 | 1. 0. 1. | 0.60093 | Plane | 1 1 1 | 0. 1. 1. | 0.60093 | Plane | 1 1 1 | 0. 1. 1. | 0.60093 |
| Direction | 1 0 -1 | 1. 1. -1. | 3.82625 | Direction | 1 1 0 | 0. 2. 0. | 1.57542 | Direction | 1 -1 0 | 2. 0. 0. | 1.57542 | Direction | 1 0 -1 | 1. 1. -1. | 3.82625 |

Figure A.9: Chart of the PTMC solutions computed from *PTCLab*

We can see that there exist only two crystallographically different solutions, as solutions 1 is equivalent to solution 4, and solution 2 equivalent to solution 3. Figure A.10 shows the pole figures of the martensite associated to the two different solutions.

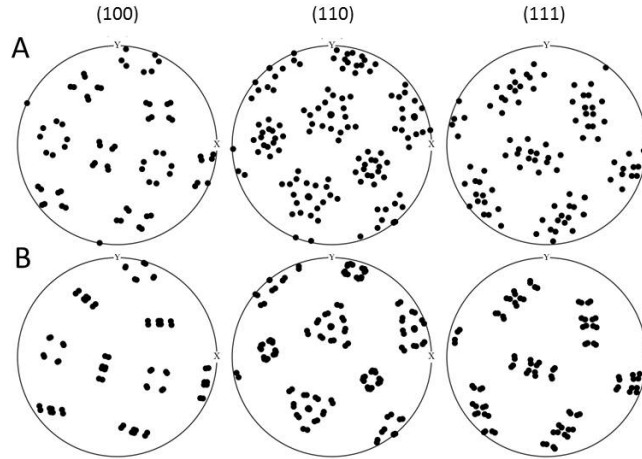


Figure A.10: Martensite pole figure of the two PTMC solutions. **A:** Solution 1. **B:** Solution 2.

Simulations for the other solution

For the simulation, the same criterion as the ones imposed in the main article have been chosen. The results for map 1 and map 2 of the article are illustrated in figures A.11 and A.12, respectively. By inspection, it can be noted that according to this solution, the invariant strain line allows a slightly better prediction for the variant selection than the invariant plane strain.

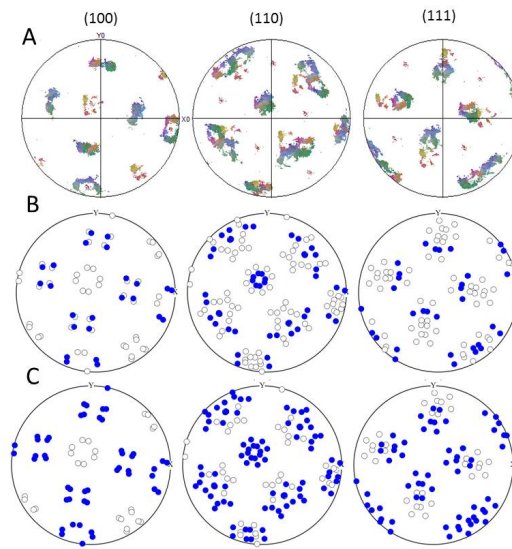


Figure A.11: Prediction of variant selection for the map 1. In blue, the selected variants. Empty circles, unselected variants. **A:** Measured pole figure. **B:** PTMC invariant plane strain. **C:** PTMC invariant line strain.

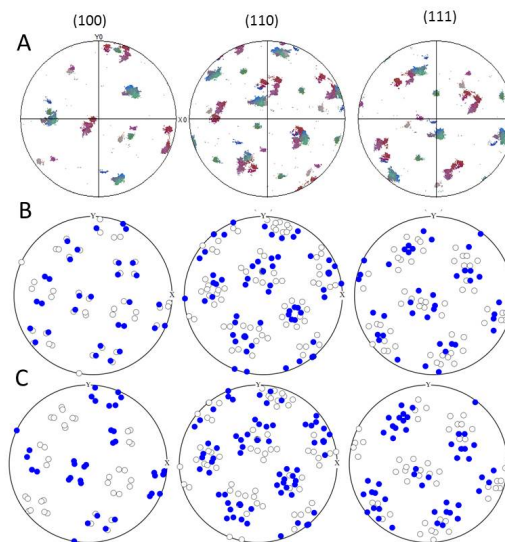


Figure A.12: Prediction of variant selection for the map 2. In blue, the selected variants. Empty circles, unselected variants. **A:** Measured pole figure. **B:** PTMC invariant plane strain. **C:** PTMC invariant line strain.

A.6 Quantitative analysis of the variant selection prediction

The quality of the predictive models for variant selection is generally performed qualitatively, by comparing visually the experimental and the simulated pole figures. We propose a method based on image processing to quantify more properly the quality of the predictions. This method is briefly explained in this supplementary material.

Method

The quantitative measure of the quality of the prediction is based on pole figures analysis. The concept is to superimpose binary image of the predicted and the experimental pole figure. The measure of the quality is then performed by counting the number of pixels that are correctly predicted. In other words, we count the number of black pixels that are present in both the experimental and the predicted pole figures. This value is then normalized by the union of the predicted pixels and the experimentally measured pixels.

Comparison of the prediction for the various models

Figures A.13 and A.14 show the superimposition of the experimental and measured $\{100\}_\alpha$ and $\{110\}_\alpha$ pole figure for the PTMC invariant line strain, the PTMC invariant plane strain, the Jaswon & Wheeler distortion and the continuous distortion for map 2.

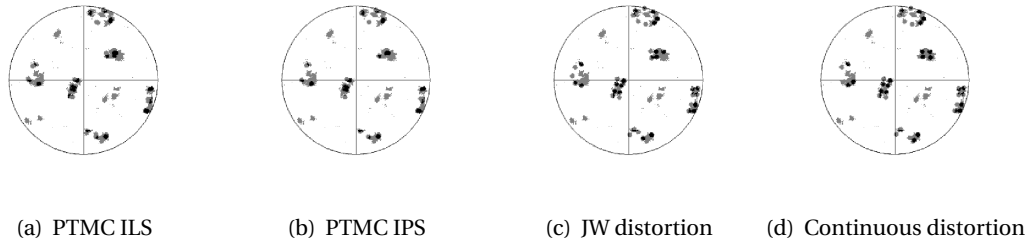


Figure A.13: Superimposition of the experimental and predicted $\{100\}_\alpha$ pole figures of map 2: In black, common pixels; in grey, pixels written in one of the two pole figures.

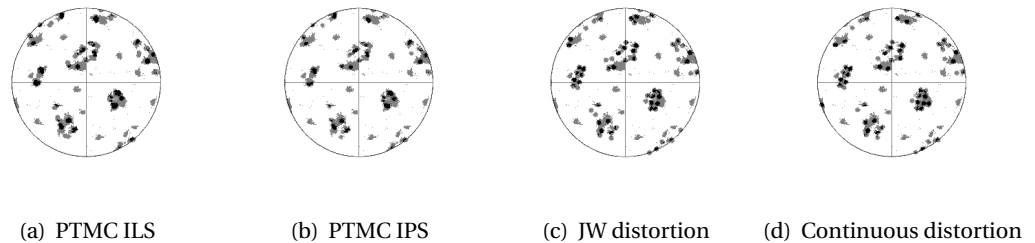


Figure A.14: Superimposition of the experimental and predicted $\{110\}_\alpha$ pole figures of map 2: In black, common pixels; in grey, pixels written in one of the two pole figures.

A.7 The PTMC solution with hard sphere ratio

We recently show (Baur *et al.*, 2017) that if one imposes the lattice parameters in a hard-sphere ratio, i.e. $\frac{a_\gamma}{a_\alpha} = \sqrt{3/2}$, the continuous distortion associated with the Kurdjumov-Sachs OR and the PTMC calculations lead to the same results. More precisely, the continuous distortion is equal to the invariant line strain of the PTMC and the equibalanced combination of twin-related variant of the continuous distortion is equal to the invariant plane strain.

Our study shows that in the case of surface martensite, the PTMC with the *real* lattice parameters of the Fe-30%Ni does not predict neither the correct orientation relationship nor the correct habit plane. Indeed, the habit plane measured is of type $\{225\}_\gamma$ and the OR is Kurdjumov-Sachs, whereas the PTMC predicts habit plane close to $\{259\}_\gamma$ and a Nishiyama OR. Imposing a hard sphere ratio as input to the PTMC, the calculations offers a correct prediction of these features. If we do so, the invariant line strain leads to a good variant selection prediction, exactly as the continuous distortion does. One could however wonder what would be the prediction of variant selection if one consider the shape deformation (IPS) instead. The results of such a prediction are presented in this supplementary.

Simulations based on the invariant plane strain

The shape deformation associated with a hard sphere lattice parameters ratio takes the following form in the crystallographic γ -basis.

$$\mathbf{F}^{IPS} = \begin{bmatrix} 0.9694 & -0.0306 & -0.0749 \\ -0.0306 & 0.9694 & -0.0749 \\ 0.0612 & 0.0612 & 1.1498 \end{bmatrix} \quad (\text{A.1})$$

The calculation for the variant selection is conducted exactly in the same way as what is done in the main paper. The simulated pole figures as well as the experimental EBSD measurements are shown in figure A.15.

Qualitatively, it can be noted that the prediction are not really convincing and that the prediction based on the invariant line strain (ILS) are better. For map 1 only, we analysed the quality of the predictions as described in the supplementary 5 and compare the result with the one obtained using the ILS. The results are presented in table A.1. The associated superimposed $\{110\}_\gamma$ pole figures are shown in figure A.16.

Table A.1: Quality of the predictions with hard sphere lattice parameters

| | PTMC IPS | PTMC ILS |
|---------|----------|----------|
| Quality | 12% | 21% |

A.7. The PTMC solution with hard sphere ratio

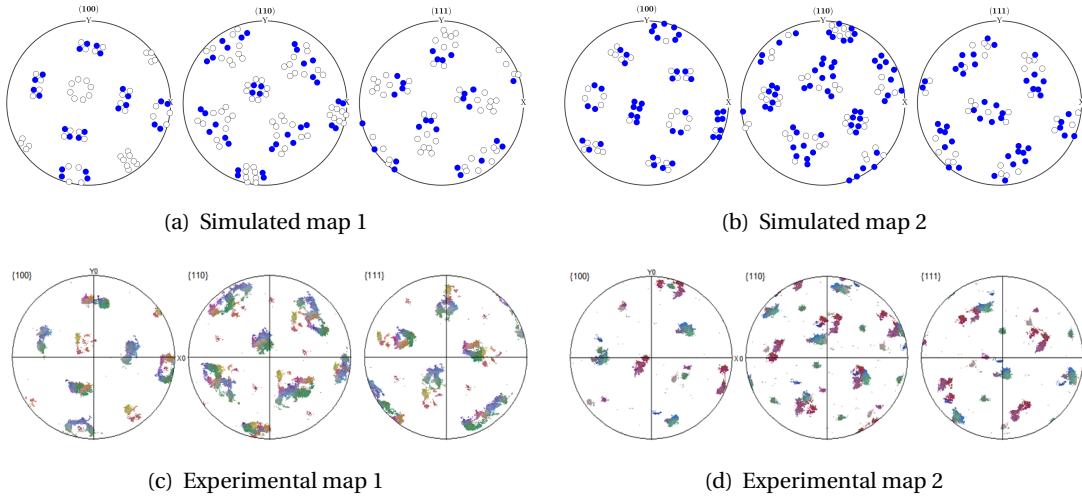


Figure A.15: Simulations based on the IPS associated with hard-sphere ratio

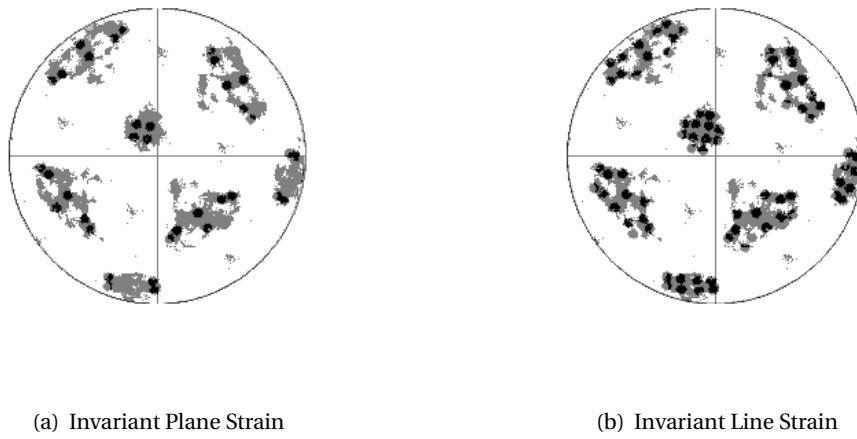


Figure A.16: Superimposition of the predicted and the measured $\{110\}_\alpha$ pole figure: In black, pixels that are written in the predicted pole figure *and* in the experimental measurement; in grey, pixels that are either predicted *or* measured

A.8 Orientation relationships

The analysis of the orientation relationship in the surface martensite found in our Fe-30%Ni, based on the pole figures shape, indicates that it is closer to the Kurdjumov-Sachs OR than to the Nishiyama-Wassermann OR. As mentioned in the main text, this is quite surprising as it is with such an alloy that Nishiyama and Wassermann derived their famous OR (Nishiyama, 1934) (Wassermann, 1933), but both worked on bulk martensite and not on surface martensite. It seems therefore that the OR changes from a KS type to a NW type depending on whether the martensite is formed on the surface or in the bulk.

The same alloy as the one that presented surface martensite as been quenched in liquid nitrogen to form bulk martensite and the sample has then be prepared for EBSD mapping. The bulk martensite pole figure of a single grain of austenite is presented in figure A.17. It can be compared to figure A.18, the pole figure associated to the map 1 in the main manuscript. The

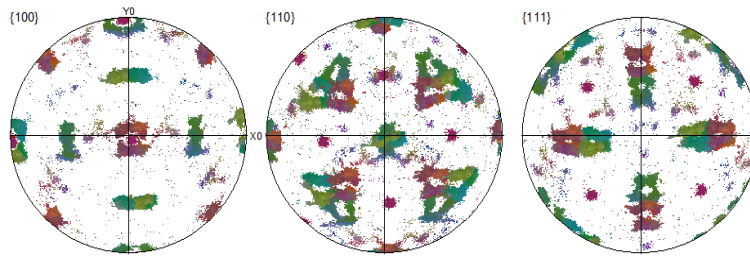


Figure A.17: Pole figures of the bulk martensite

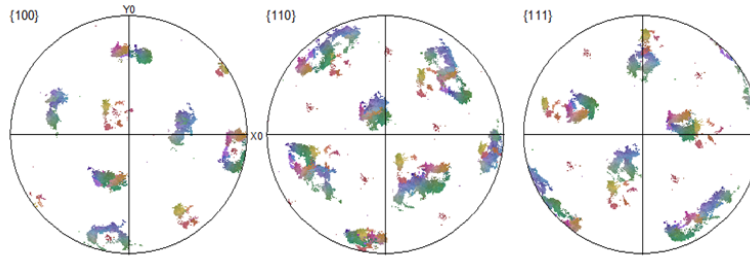


Figure A.18: Pole figures of the surface martensite

incurvation of the outer three-fold star in the $\{110\}$ pole figure reveals that surface martensite is closer to KS than bulk martensite, as in the former the shape tends to be more concave than in the latter where it is more convexe.

In order to assess more quantitatively the difference of OR, we used the HKL EBSD software to compute the misorientation on the interphase boundaries. On figure A.19 the interphase boundaries which show an misorientation within less than 3 degrees from the Kurdjumov-Sachs OR and the Nishiyama-Wasserman OR are indicated in green and magenta respectively. In black, are marked the boundaries that are at three degrees from both ORs. Figure A.19 seems to indicate that close to the habit plane the orientation relationship is of type Kurdjumov-

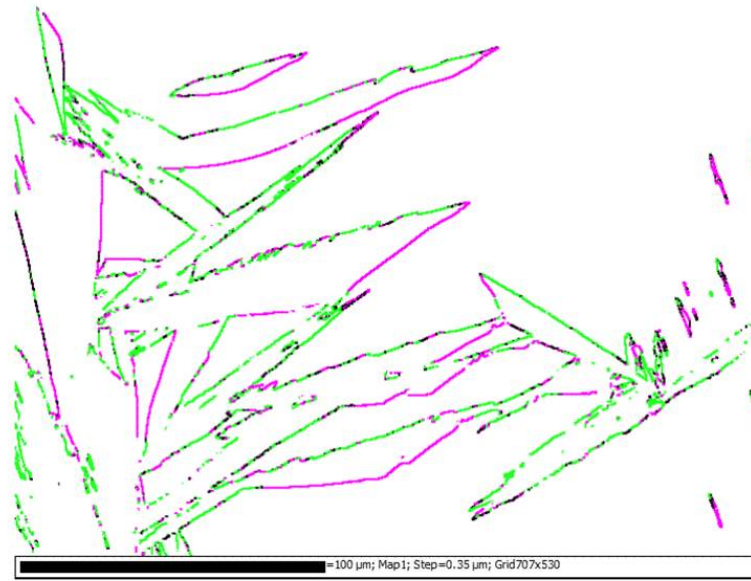


Figure A.19: Orientation relationship at the grain boundaries. Green indicates the boundaries within 3° from KS and magenta indicates the one within 3° from NW.

Table A.2: Comparison of the quality for the predictions for the four different models.

| | KS OR | NW OR |
|-------|-------|-------|
| Map 1 | 64% | 44% |
| Map 2 | 65% | 47% |

Sachs, and that it moves towards a Nishyama-Wasserman type of OR when the martensite plate grows. By counting the pixels associated to each type of boundary in both map 1 and 2, it is possible to assess to which OR the martensite formed is closer to. The number of pixels belonging in a interphase boundary that is associated to the KS OR (within 3°) and the number of pixels belonging in a interphase boundary that is associated to the NW OR (within 3°) are counted and normalized by the total number of pixels defining the interphase boundary. The results are presented in table A.2. It can be noted that the sum of the percentage is greater than 100%, this is due to the fact that some boundaries are in the same time within 3° of NW and KS.

Figure A.20 shows the map of orientation relationship of the martensite plate based on the reconstruction of the parent austenite, using the method presented in the following reference: Cayron, C. *EBSD imaging of orientation relationships and variant groupings in different martensitic alloys and Widmanstätten iron meteorites*, Material Characterization, **94**, 93-110, (2014)). This second analysis confirms that the plate start to transform with a KS OR and far from the habit plane the OR changes towards NW OR and even locally towards Pitsch OR.

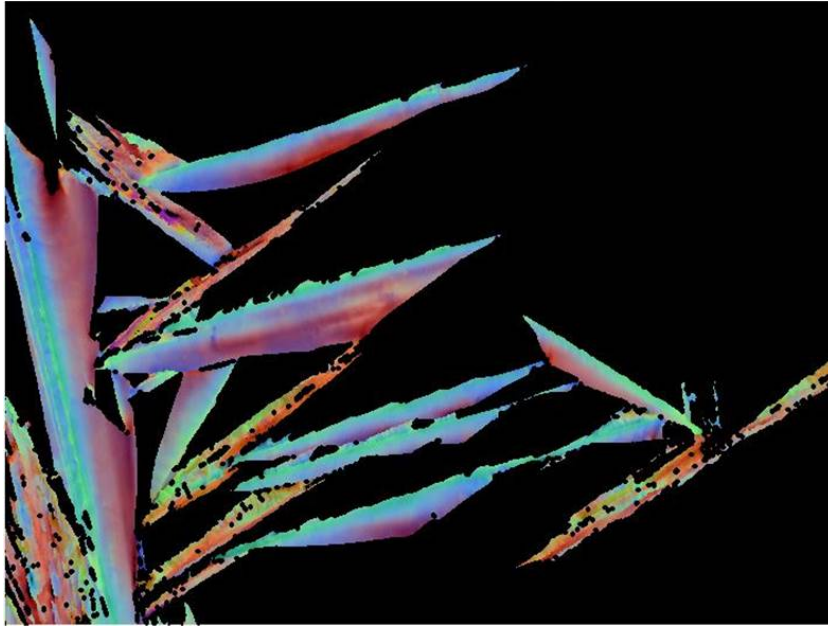


Figure A.20: Orientation relationship in the plate. Color coding: KS in green, NW in blue and Pitsch in red.

B Supplements to *Intricate morphologies of laths and blocks in low-carbon martensitic steels*

Supplementary Materials

S1: Plotting the traces of planes with GenOVa

GenOVa (Generation of Orientational Variants) is a computer program that calculates the orientational variants and their groupoid composition table. It can simulate the pole figures and SAEDs of the variants and their parent crystal. A new functionality has been developed to plot the traces of the habit planes. A snapshot is shown in Fig. A1. For this simulation the zone axis of the parent austenite is $[112]_{\gamma}$ and the calculated zone axis of the variant α_{12}^{KS} is close to $[1-13]_{\alpha}$ within a tolerance angle of 2° . The simulated SAED of the fcc parent and bcc variant α_{12}^{KS} are shown in (a) by using small red spots (1 pixel) and larger blue spots (5 pixels) for the fcc and bcc phases respectively. The small diameter of the fcc spots was chosen because there is no retained austenite in the low-carbon steels studied in this paper. The overlap of the simulation with the experimental SAED is shown in (b). One can check that the positions of the simulated spots are exactly those of the experiments, except far from transmitted beam because of the Ewald sphere curvature. The traces of the twelve $\{557\}_{\gamma}$ planes of the parent crystal are shown by the red lines in (c). The traces of the $\{557\}_{\gamma}$ planes that are parallel to a $\{156\}_{\alpha}$ within a tolerance angle of 2° are marked by the yellow bold lines. Here, two planes obey this condition. One of these two lines fits very correctly with the morphology of the lath on which the diffraction pattern was acquired. The overlap of the simulated trace on the experimental TEM image is shown in (d).

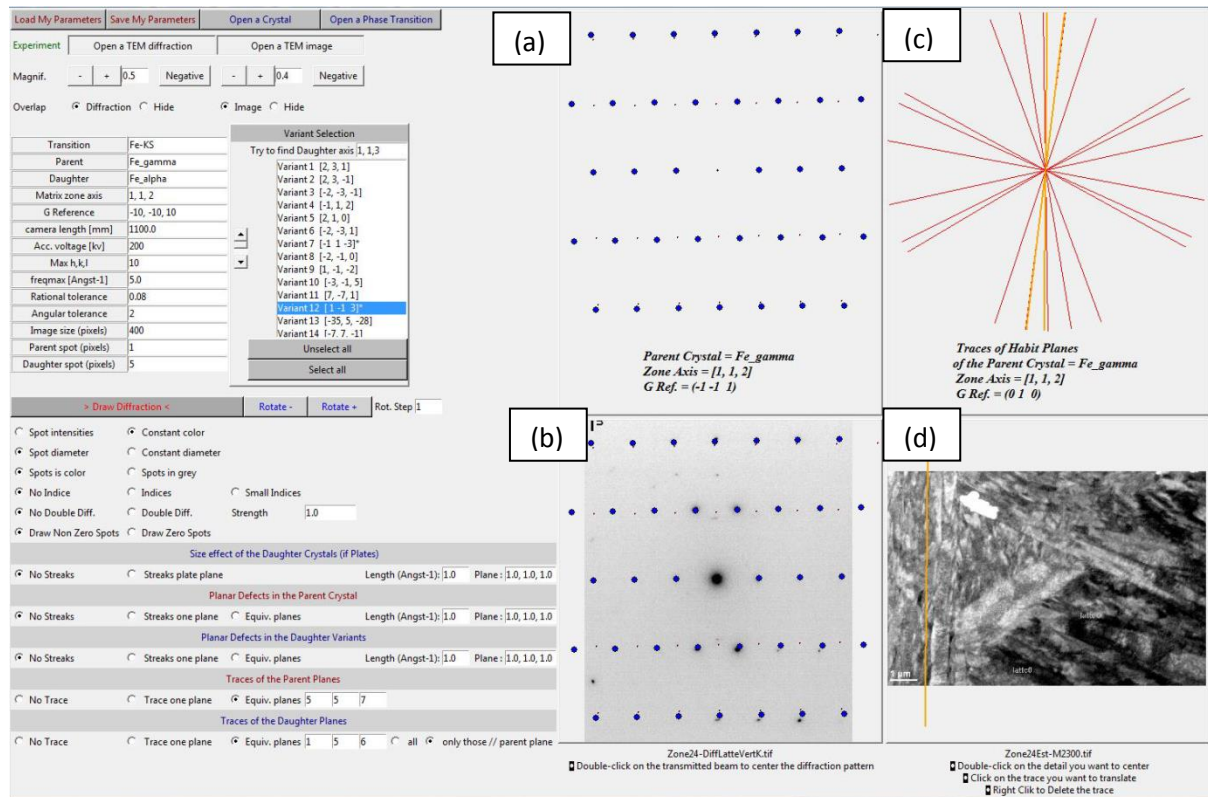


Fig. A1. Snapshot of the module developed into GenOVa to simulate the diffraction patterns of variants and plot the traces of the habit planes.

S2: Habit planes in iron nickel meteorites

A piece of the octahedrite iron nickel meteorite “Muionalusta” was bought on eBay by the author. The sample was polished and the 4x8 maps have been acquired at low magnification with stage displacements between the maps. A large map (0.4 x 1.5 mm) was then reconstituted by stitching. The parent austenitic (taenite) γ grain is reconstructed with ARPGE and the trace of $\{111\}_{\gamma}$ planes are automatically plotted and manually positioned along the martensitic/bainitic (kamacite) laths where good fit is found (Fig. A2). It is then checked by a fully automatic procedure that those planes are obey the condition $\{111\}_{\gamma} // \{110\}_{\alpha}$ (Fig. A3).

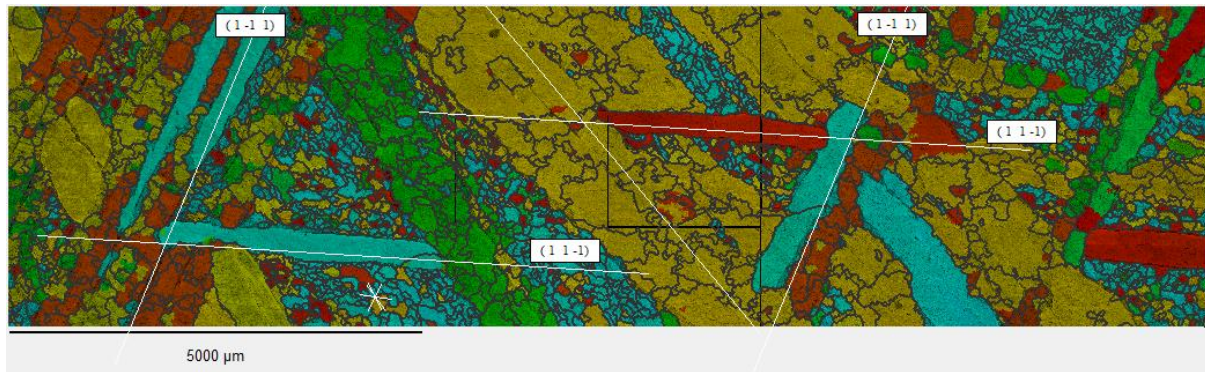


Fig. A2. EBSD map of the “Muionalusta” meteorite with the trace of the $\{111\}_{\gamma}$ planes, automatically calculated and manually positioned.

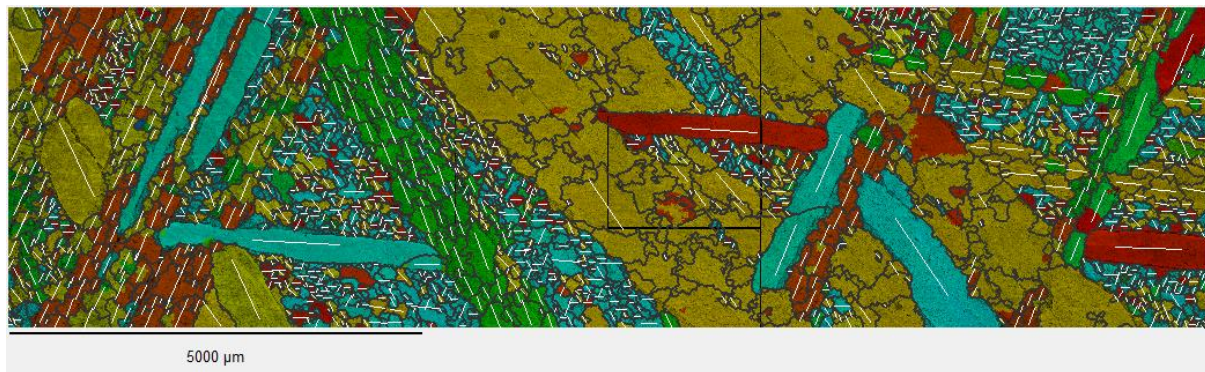
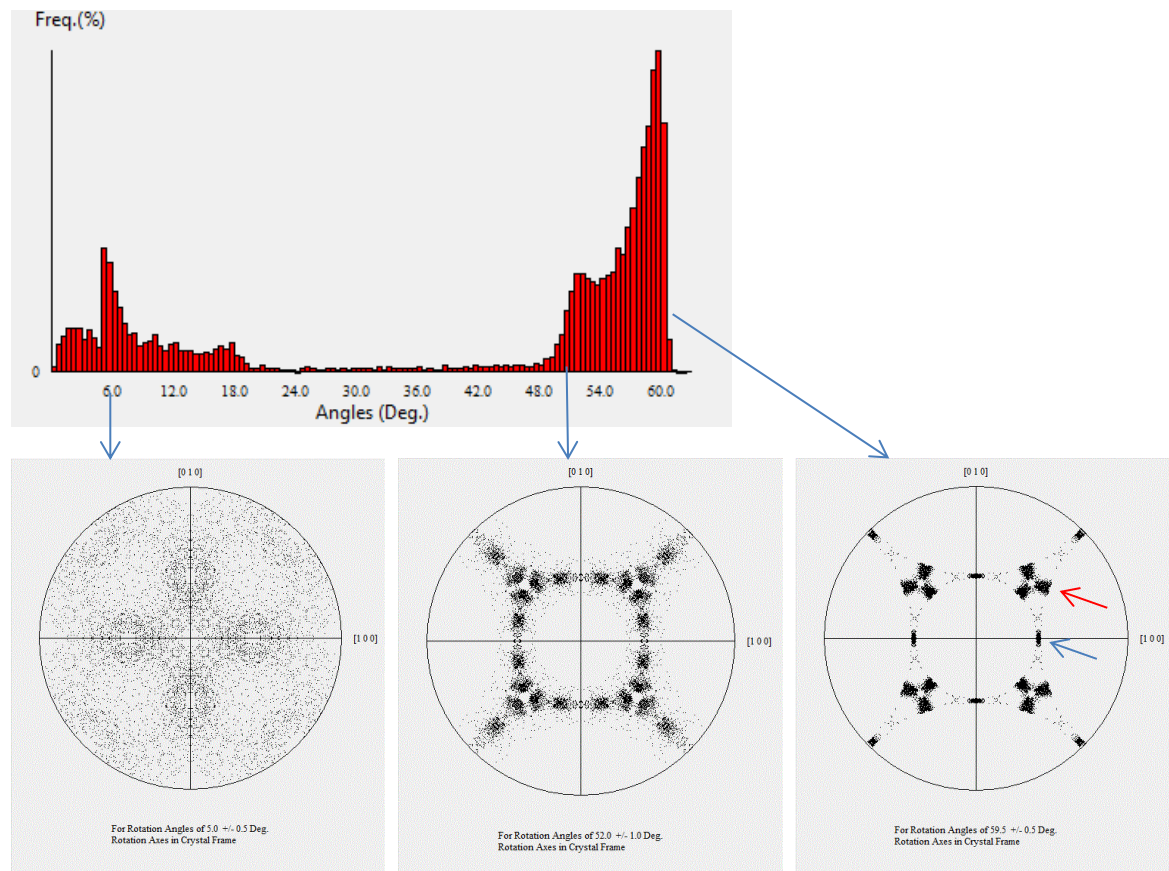


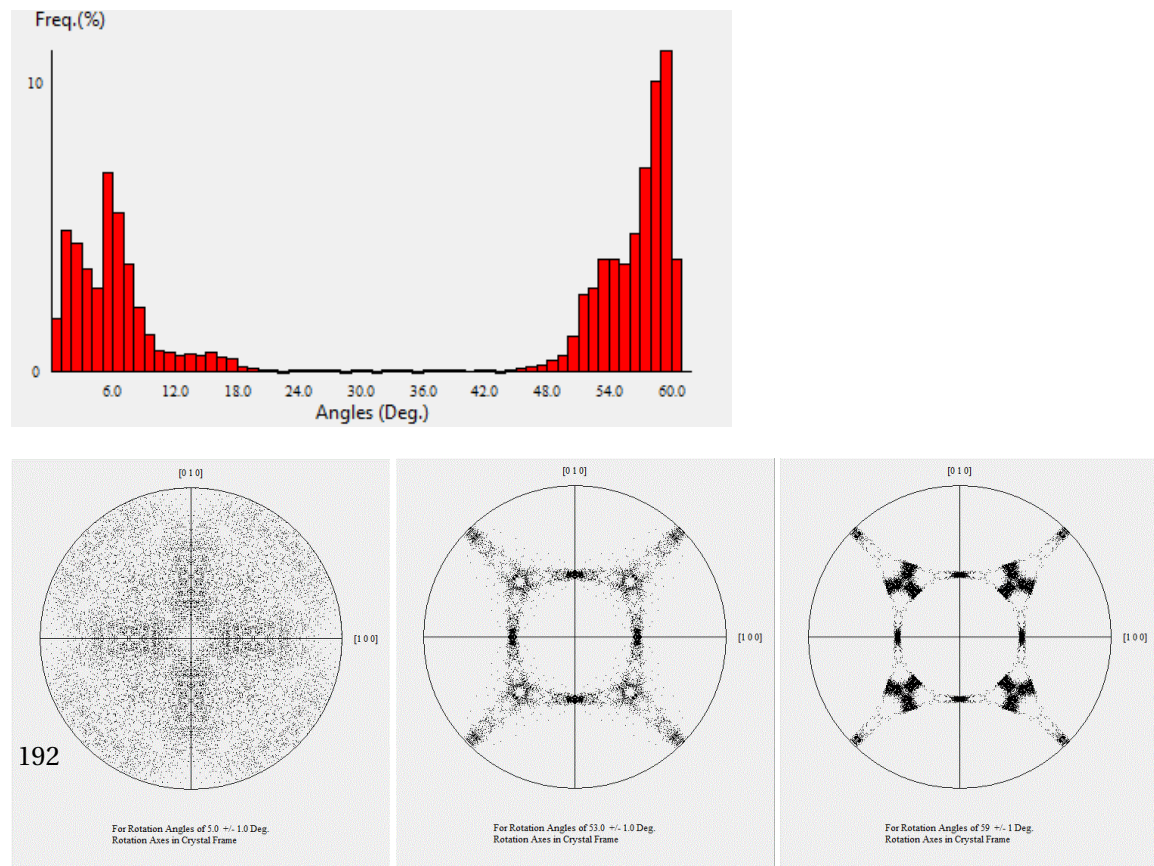
Fig. A3. Trace of the $\{110\}_{\alpha} // \{111\}_{\gamma}$ planes, automatically calculated and automatically positioned in all the daughter bcc grains. (a) By manually choosing and positioning the traces of the $\{111\}$ planes that fit with the morphology of the kamacite grains, and (b) by a fully automatic process plotting the traces of the planes $\{111\}_{\gamma} // \{110\}_{\alpha}$.

S3: Histograms of misorientations between the variants.

1018 steel



Eurofer steel



EM10 steel

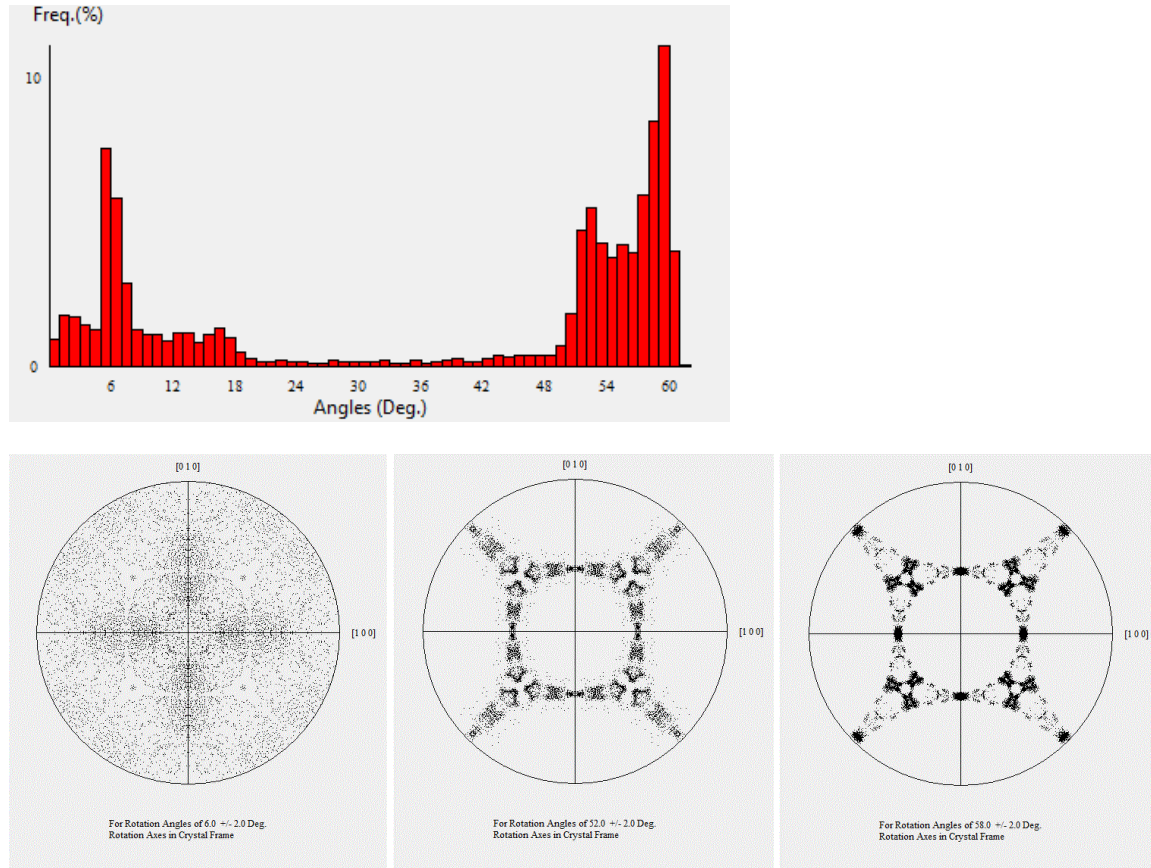


Fig. A4. Histograms of misorientations (rotation angle) between the martensitic grains in the EBSD maps of different low-carbon steels in their as-quenched states. The rotation axes corresponding to the rotation angles 6° , 52° and $60^\circ \pm 1^\circ$ are plotted in stereographic projections. The rotations axes related to the 60° misorientations are $\langle 110 \rangle_{\text{bcc}}$ (blue arrow) and close (but not equal) to a $\langle 111 \rangle_{\text{bcc}}$ direction (red arrow). This proves that the mean OR that can be measured in EBSD is close to (but not equal to) a KS OR. A good agreement is found with the GT OR (calculations not detailed here).

S4: Habit planes in a as-quenched 1018 steel

The paper shows two EBSD maps acquired on an as-quenched 1018 steels. More maps were acquired and treated. We give here the results obtained on two other maps, one acquired again on an as-quenched 1018 steel (Fig. A5 and Fig. A6), and another one in an as-quenched Eurofer steel (Fig. A7 and Fig. A8).

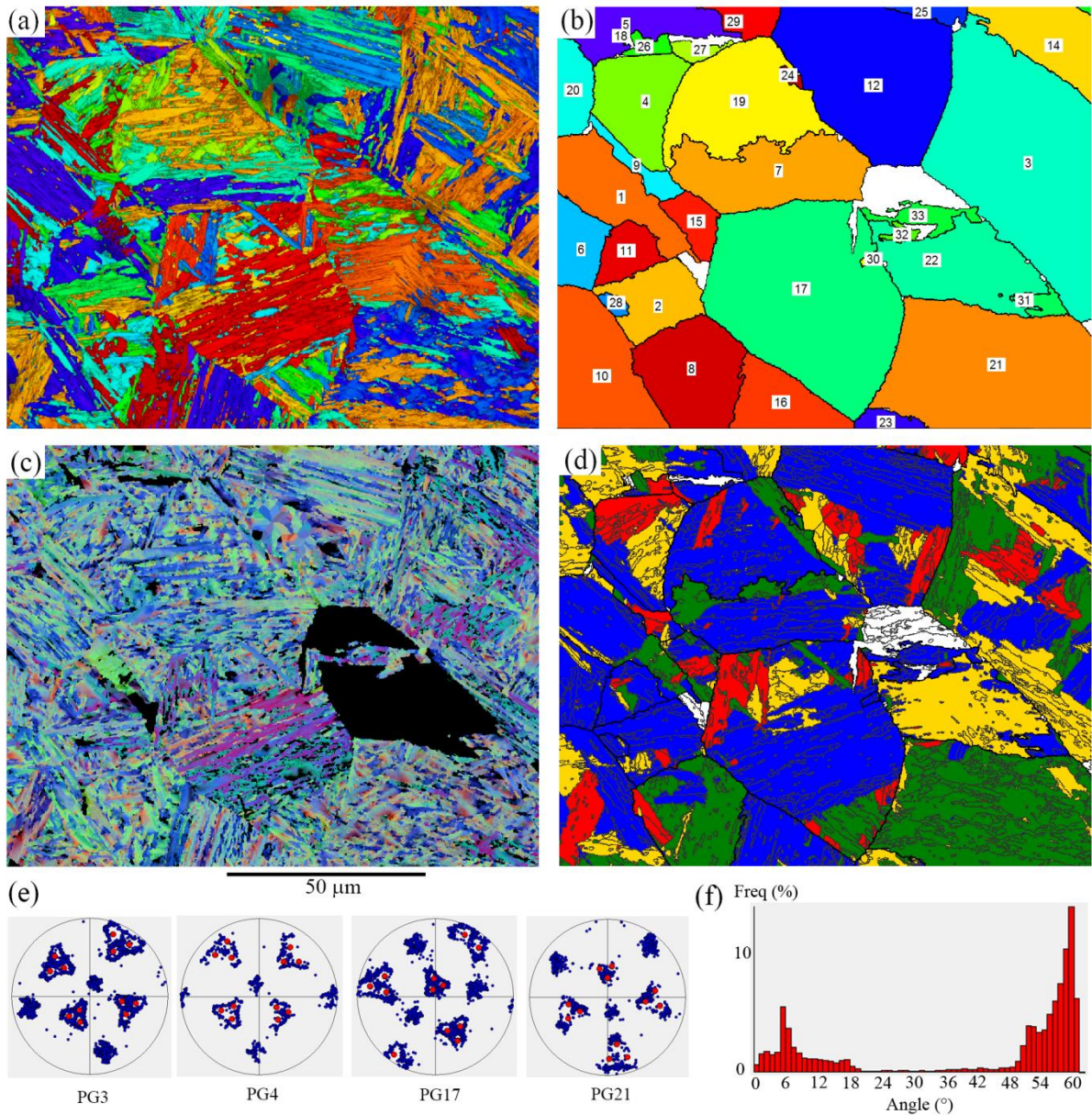


Fig. A5. EBSD map of a 1018 steel in as-quenched state. (a) Daughter bcc grains, (b) reconstructed austenitic grains, (c) orientation gradients in the bcc grains in RGB coloring (Red = Pitsch, Green = KS, Blue = NW), (d) Close-packed plane packets in each prior austenitic grains represented with four colors, (e) pole figures on some parent grains with the $\langle 110 \rangle_{\alpha}$ direction in blue, and the calculated $\langle 557 \rangle_{\gamma}$ directions in red. (f) Histogram of disorientations between the daughter bcc grains in the whole map.

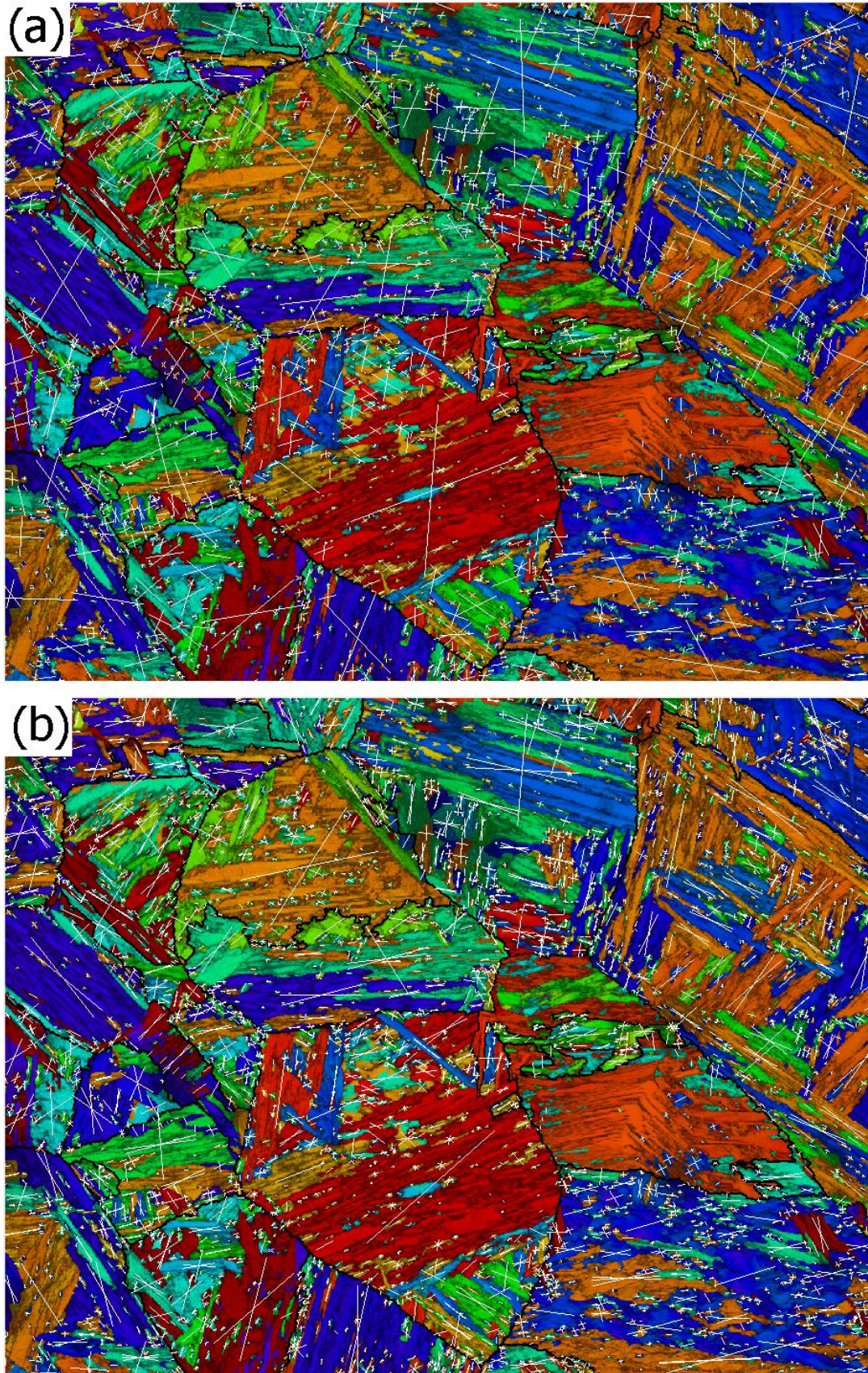


Fig. A6. Determination of the habit planes in the EBSD map of Fig. A5 by (a) automatically plotting for all the bcc grains the traces of the planes $\{057\}_\alpha // \{557\}_\gamma$, (b) automatically plotting for all the bcc grains the traces of the planes $\{156\}_\alpha // \{557\}_\gamma$.

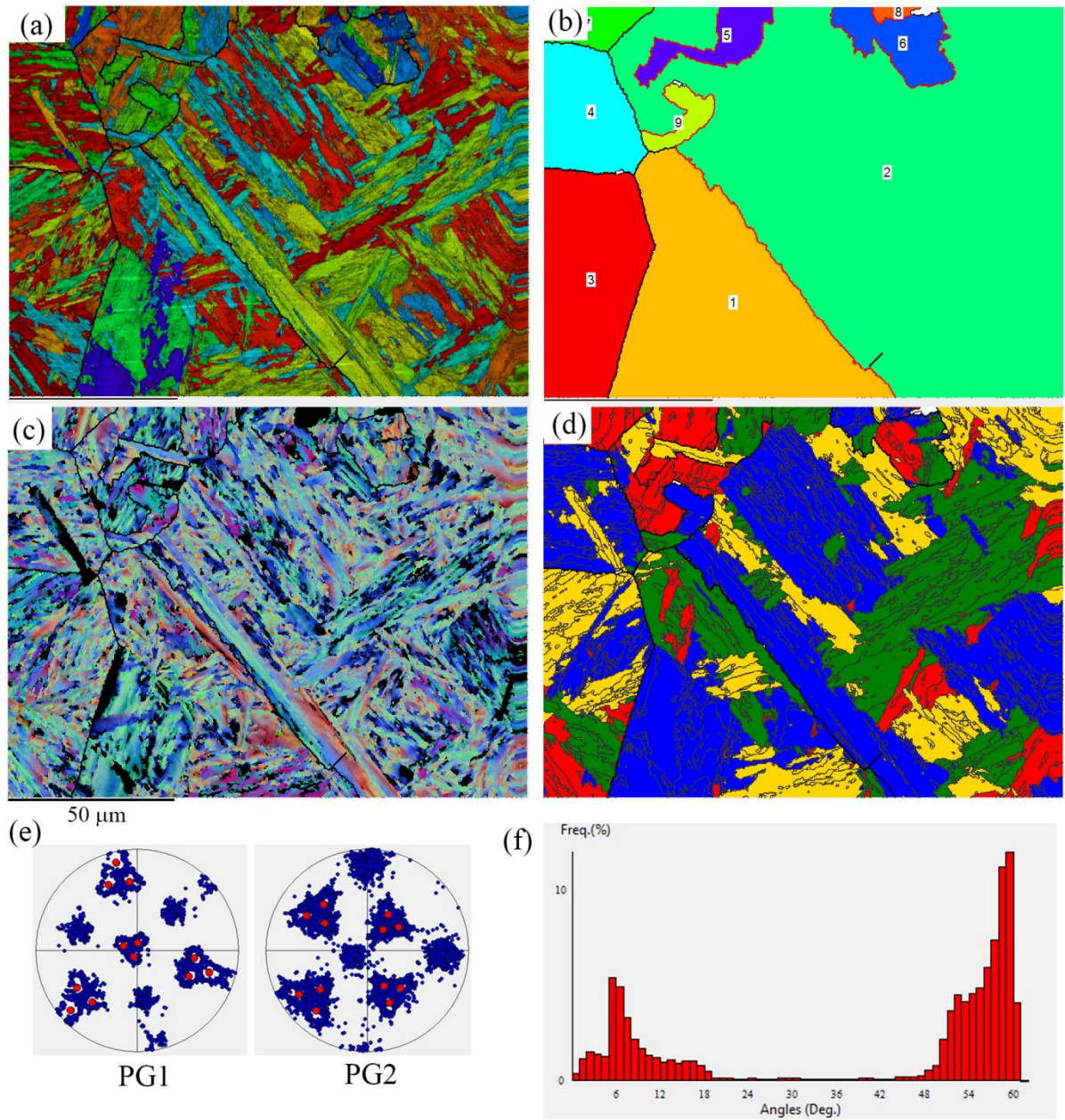


Fig. A7. EBSD map of a Eurofer steel in as-quenched state. (a) Daughter bcc grains, (b) reconstructed austenitic grains, (c) orientation gradients in the bcc grains in RGB coloring (Red = Pitsch, Green = KS, Blue = NW), (d) Close-packed plane packets in each prior austenitic grains represented with four colors, (e) pole figures on some parent grains with the $\langle 110 \rangle_\alpha$ direction in blue, and the calculated $\langle 557 \rangle_\gamma$ directions in red. (f) Histogram of disorientations between the daughter bcc grains in the whole map.

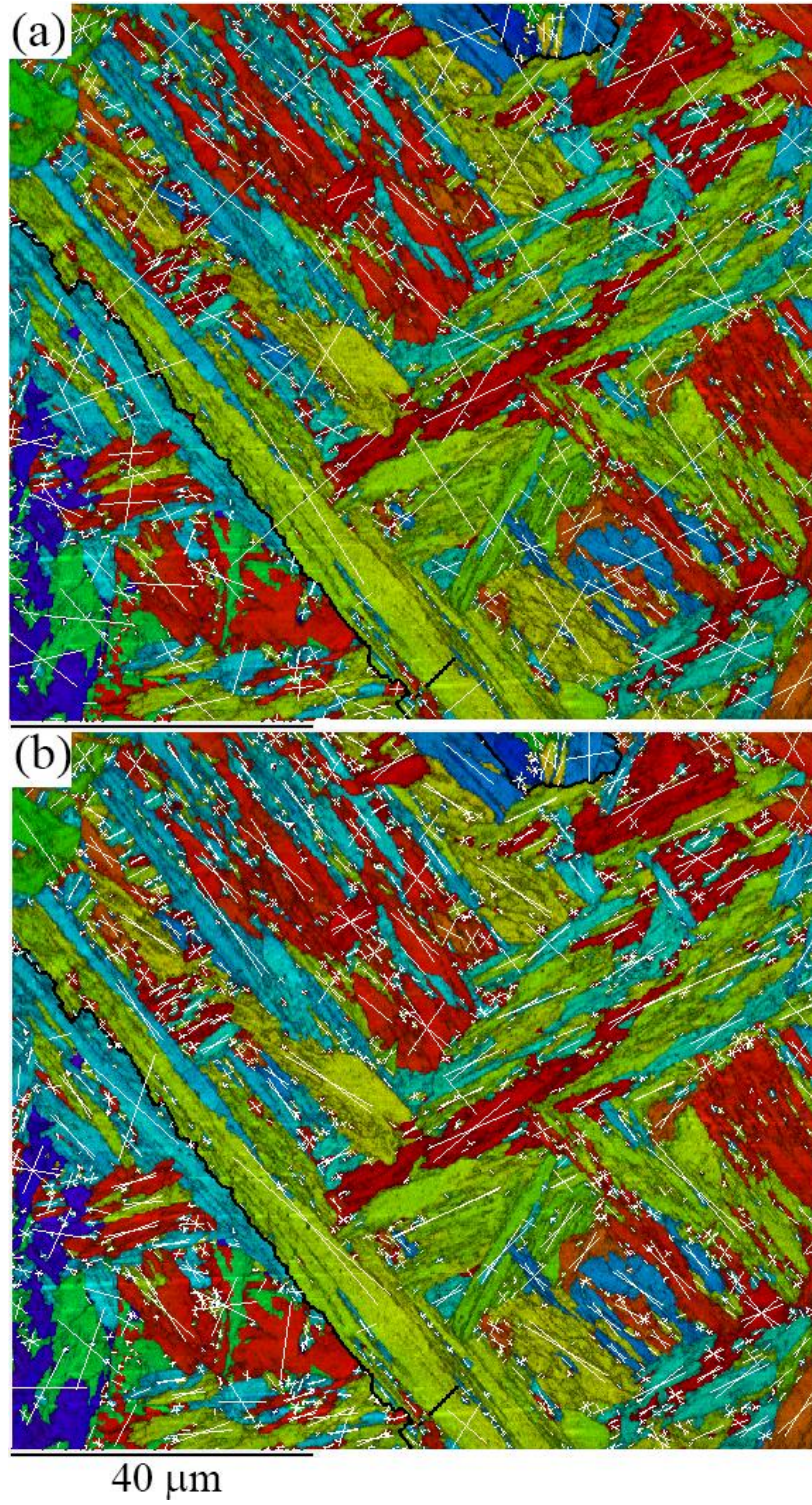


Fig. A8. Determination of the habit planes in the EBSD map of Fig. A7 by (a) automatically plotting for all the bcc grains the traces of the planes $\{057\}_\alpha // \{557\}_\gamma$, (b) automatically plotting for all the bcc grains the traces of the planes $\{156\}_\alpha // \{557\}_\gamma$.

C Supplements to *On the chevron morphology of surface martensite*

C.1 Additional maps

Figures C.1 show additional band contrast maps of the surface martensite formed on annealed samples. The orientation of the twin boundary where martensite is observed are marked in black and the ones where no martensite is observed are marked in red. When only one side of the chevron is formed, the angle is marked in black with a dashed line box. It is for example the case on the right down corner of the map in figure C.1C.

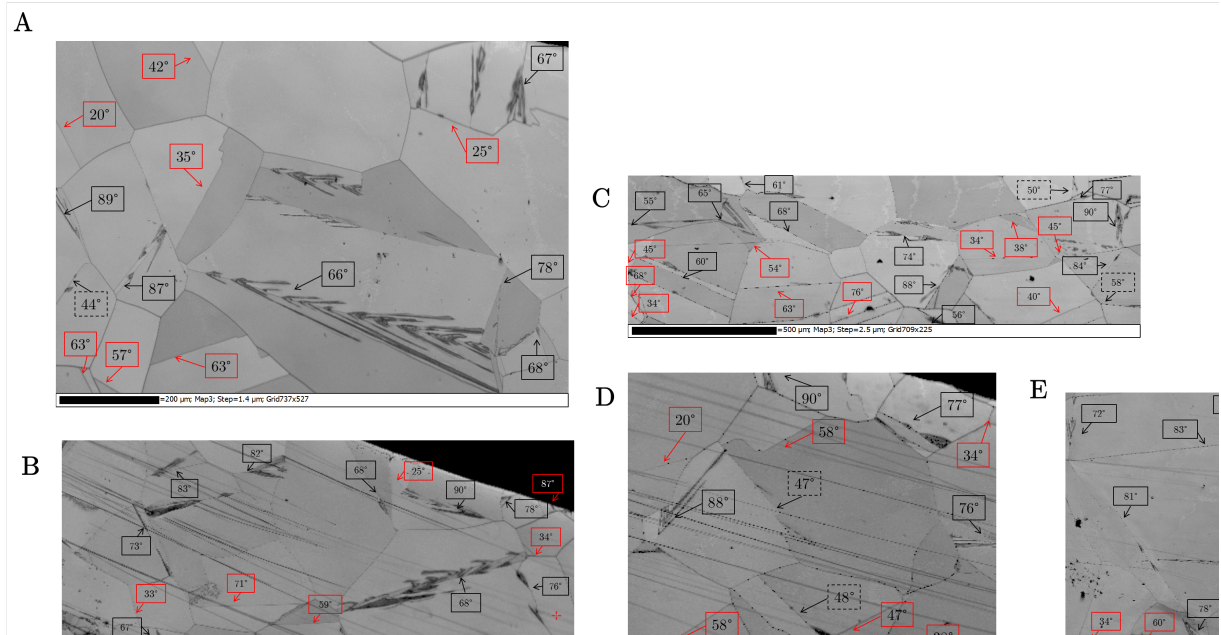


Figure C.1: Band contrast EBSD map with annotation of the θ -angle between the normal to the annealing twin grain boundary and the normal to the free surface.

Figure C.2 shows a high magnification map of chevron martensite and its associated BCC pole figures both experimental (figure C.2B) and simulated (figure C.2C and figure C.2D). Figure

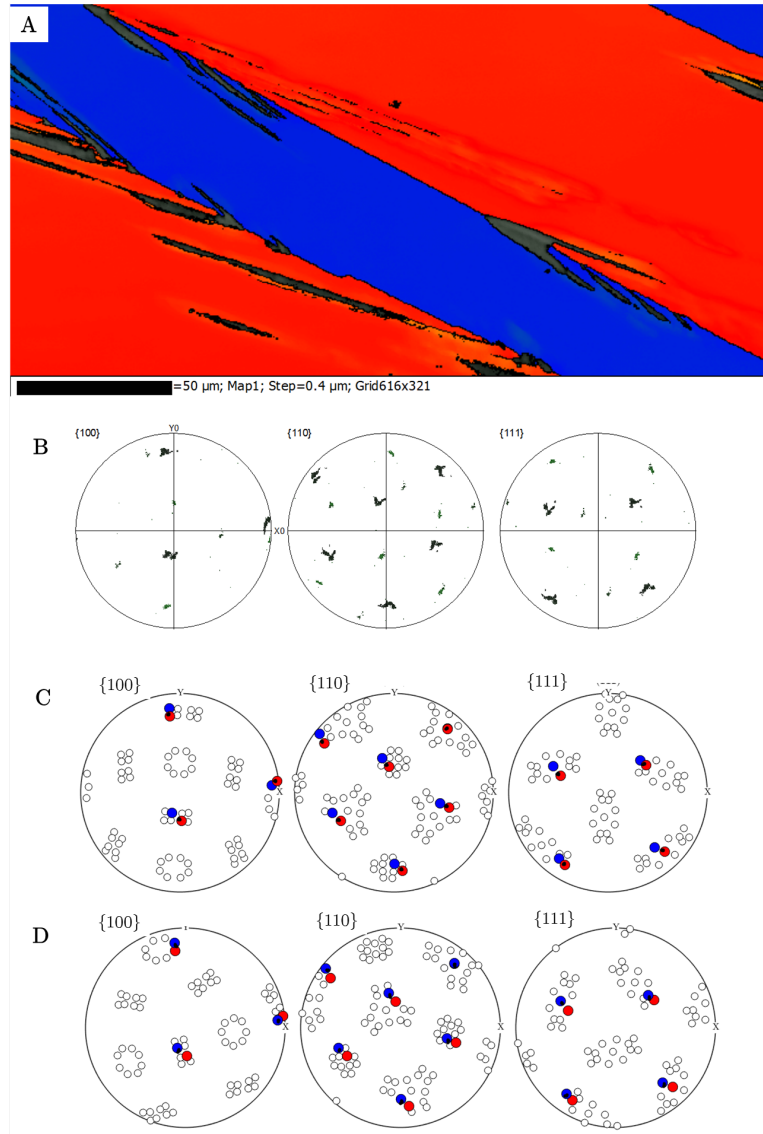


Figure C.2: EBSD map of chevron martensite and associated pole figures of the martensite. **B**: Experimental pole figure. **C**: Simulation of the variant selected considering the orientation of the red grain. **D**: Simulation of the variant selected considering the orientation of the blue grain.

C.3 shows another high magnification map of chevron martensite and its associated BCC pole figures both experimental (figure C.3B) and simulated (figure C.3C and figure C.3D). In that case, the orientation of each wing of the chevron is the same. As compared with the two previous simulated maps (figure 2A of the main study and figure C.1A), in this one the twin-related variant slightly appears. This variant is not predicted by our model as it not favoured by the free surface and nucleates only for the accommodation of the $\{225\}_{\gamma}$ habit

plane.

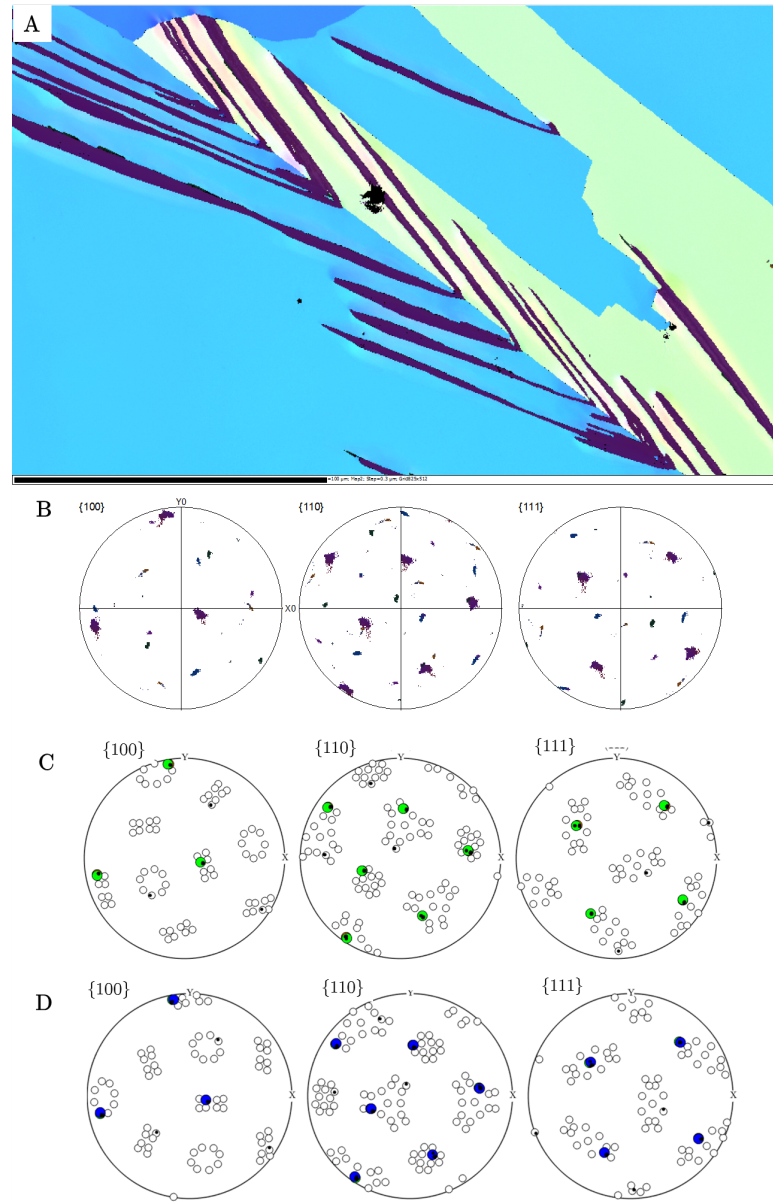


Figure C.3: EBSD map of chevron martensite and associated pole figures of the martensite. **B**: Experimental pole figure. **C**: Simulation of the selected variant considering the orientation of the light green austenite grain. **D**: Simulation of the selected varariant considering the orientation of the blue austenite grain.

C.2 Crystallographic features

$\{225\}_\gamma$ Habit plane

Figure C.4 shows the trace analysis of the habit plane of the surface martensite. The habit plane is of type $\{225\}_\gamma$ in agreement with the measurements performed previously (Ref: A.P. Baur, C. Cayron, R.E. Logé, Variant selection in surface martensite, *J. Appl. Cryst.*, **50**, 1646-1652, (2018)). This type of habit plane is accounted by the continuous model, whereas for the Fe-30wt%Ni lattice parameters, the PTMC calculations predict a habit plane close to $\{259\}_\gamma$.

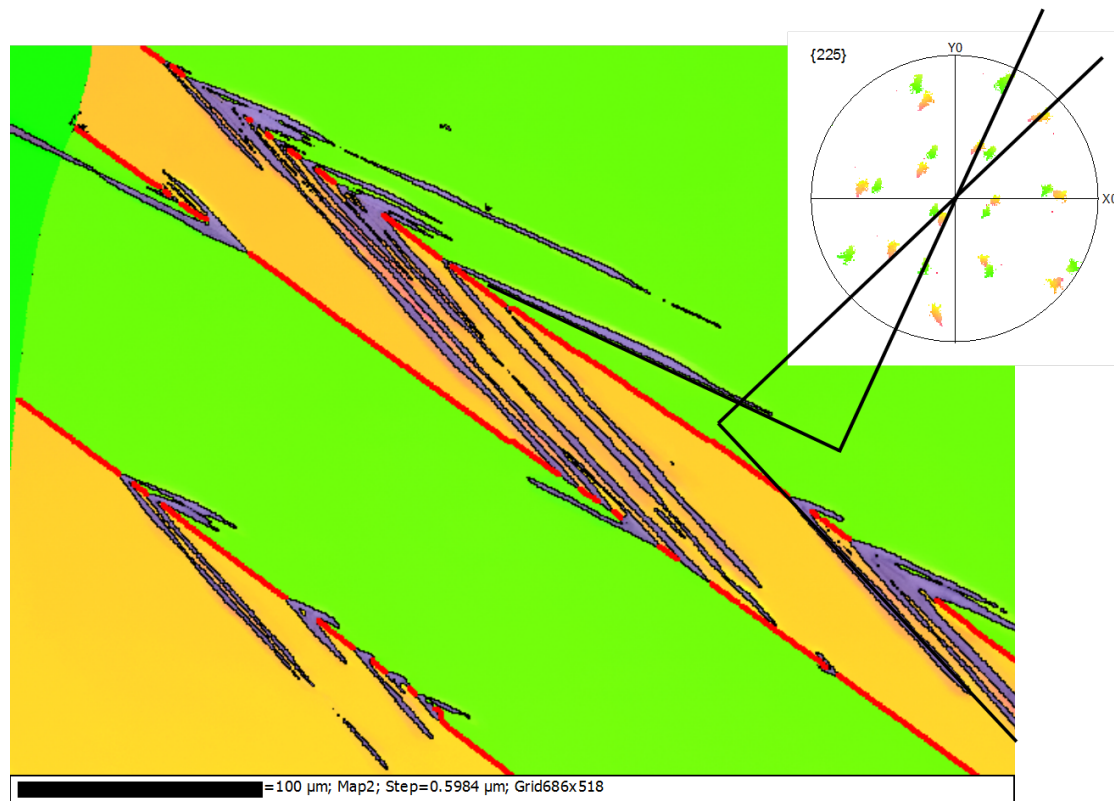
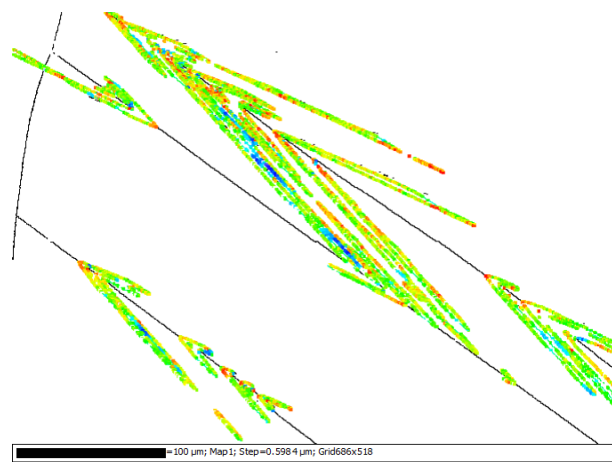


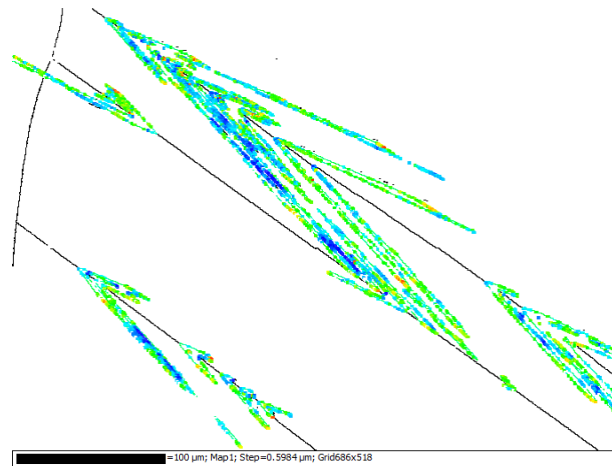
Figure C.4: Trace analysis of the $\{225\}_\gamma$ habit plane of chevron martensite

Orientation relationship

The nature of the orientation relationship at the interphase boundary is represented in figure B.8.5. The colour of the contour indicates in (a) how far from the Kurdjumov-Sachs OR the interphase boundary is and in (b) how far from the Nishijama-Wassermann OR it is. The red colour indicates that the deviation from the reference OR is less than 2° , in yellow between 2° and 3° , green between 3° and 4° , in cyan between 4° and 6° and blue navy above 6° . The warmer the colour on the interphase boundary, the closer is the experimental orientation relationship to the reference one. This analysis confirms that the orientation relationship is closer to Kurdjumov-Sachs (figure C.5(a)) than Nishijama-Wasserman (C.5(b)). The analysis has been performed using the HKL Channel5 software from Oxford Instruments.



(a) Kurdjumov-Sachs



(b) Nishijama-Wasserman

Figure C.5: Analysis of the orientation relationship. On the top figure, the reference OR is Kurdjumov-Sachs and on the bottom figure, the reference OR is Nishijama-Wassermann. In red: $<2^\circ$; In yellow: 2° - 3° ; In green: 3° - 4° ; In cyan: 4° - 6° ; In blue navy: $>6^\circ$. The closer the measured OR is from the reference one, the warmer are the colours on the figures.

C.3 Variant selection predictions and predictions of the favoured austenite orientations based on the PTMC

In our paper entitled *Variant selection in surface martensite* (Ref: A.P. Baur *et al.*, *J. Appl. Cryst.*, **50**, 1646-1652, (2018)), we compare the transformation models based on the PTMC using both the *Invariant Line Strain* **RB** and the *Invariant Plane Strain* **P**; and the continuous FCC-BCC distortion model. All models were able to capture the selection trend rather correctly, and it was difficult to discriminate a model on this basis. We showed however that the continuous FCC-BCC distortion better accounts for the Kurdjumov-Sachs orientation relationship and the $\{225\}_\gamma$ habit plane. In the present study as well, these crystallographic features are better modelled with the continuous distortion than with the PTMC predictions (see supplement A for details).

In this supplementary section, we will analyse whether the PTMC models could or not explain the chevron morphology and the variant selection observed. The PTMC computations are performed identically to the calculations made in our previous paper, without dilatation parameter and assuming twinning on $\{101\}_\gamma$ as lattice invariant shear. Under these assumptions, the PTMC model predicts an habit plane close to $\{259\}_\gamma$. To account for the $\{225\}_\gamma$ habit plane experimentally observed the dilatation parameter has to be considered in order to ensure a matching of the close-packed atomic rows of both phases. Under that condition, the PTMC and the continuous distortion models give the same results (Baur *et al.*, *Sci. Rep.* **7**, 2017). Here below, we give the two shape strains associated with $\{259\}_\gamma$ and $\{225\}_\gamma$, **P** and **P_δ** respectively. We also write the invariant line strain **RB** predicted by the PTMC without dilatation parameter. The invariant line strain predicted by the PTMC with dilatation parameter δ is the distortion studied in the main study (equation 1, section 3.2).

$$\mathbf{P} = \begin{bmatrix} 0.99193 & 0.03516 & -0.02776 \\ -0.02808 & 1.12242 & -0.09663 \\ -0.02776 & 0.12099 & 0.90449 \end{bmatrix} \quad \mathbf{P}_\delta = \begin{bmatrix} 0.9694 & 0.0749 & -0.0306 \\ -0.0612 & 1.1498 & -0.0612 \\ -0.0306 & 0.0749 & 0.9694 \end{bmatrix}$$

$$\mathbf{RB} = \begin{bmatrix} 1.11998 & 0.03516 & 0.10029 \\ -0.01947 & 1.12242 & -0.08802 \\ -0.14482 & 0.12099 & 0.78743 \end{bmatrix} \quad (\text{C.1})$$

We first verify the variant selection using the two invariant plane strains **P** and **P_δ** and the invariant line strain **RB**. The criterion is therefore respectively $\max[\mathbf{H}_{zz}] = \max[(\mathbf{RB} - \mathbf{I})_{zz}]$, $\max[\mathbf{H}_{zz}] = \max[(\mathbf{P} - \mathbf{I})_{zz}]$ and $\max[\mathbf{H}_{zz}] = \max[(\mathbf{P}_\delta - \mathbf{I})_{zz}]$. The simulations are performed for the EBSD map presented in figure 1. The results for the invariant plane strain **P** and the invariant line strain without dilatation parameters **RB** give exactly the same results, presented in figure C.6. The results for the invariant plane strain **P_δ** with the dilatation parameter are presented in figure C.7. The simulations can be compared with the simulations using the

C.3. Variant selection predictions and predictions of the favoured austenite orientations based on the PTMC

FCC-BCC distortion model in figure 2.

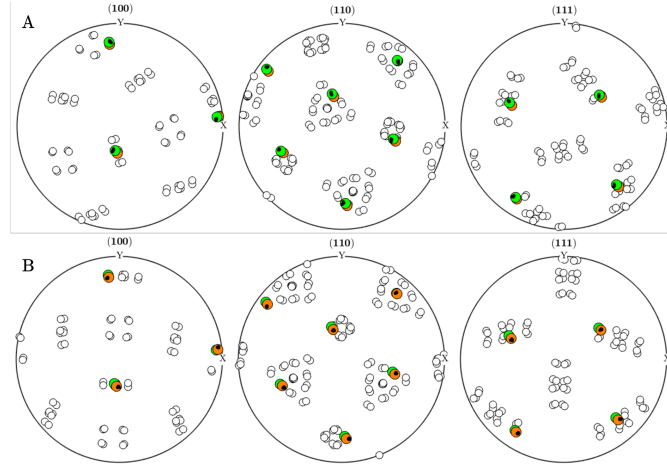


Figure C.6: Simulated pole figures of the chevron martensite in figure 2, using the invariant plane strain model **P** and the invariant line strain **RB**. **A**: Simulation in the green crystal. **B**: Simulation in the yellow twin. In green, the orientation selected by the $\text{Max}(\mathbf{H}_{zz})$ criterion in the crystal and in yellow the orientation selected by the criterion in the twin. The experimental orientations are superimposed in black.

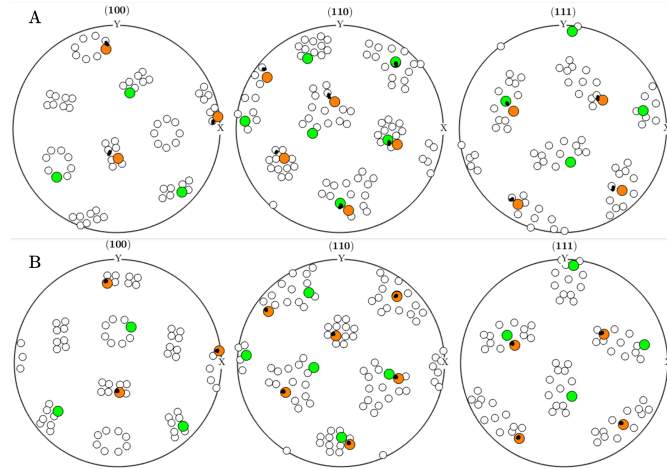


Figure C.7: Simulated pole figures of the chevron martensite in figure 1, using the invariant plane strain model with the dilatation parameter \mathbf{P}_δ . **A**: Simulation in the green crystal. **B**: Simulation in the yellow twin. In green, the orientation selected by the $\text{Max}(\mathbf{H}_{zz})$ criterion in the crystal and in yellow the orientation selected by the criterion in the twin. The experimental orientations are superimposed in black.

From the simulations it can be seen that the variant selection prediction is accurate for both the invariant plane strain and the invariant line strain of the PTMC without dilatation parameter. The invariant plane strain with dilatation parameter appears to be a less convincing model. Actually, one variant is well predicted, but the model also predicts its twin-related variant which is almost not observed. It is only observed sometimes near the habit plane (see the additional map in figure C.3 in the appendix C, section A). As both PTMC models without dilatation parameter seem to well account for the variant selection, we propose to do the same simulations as those presented with the FCC-BCC continuous model, namely to explore all the austenite orientation to see if the PTMC can also explain the selection of the austenite orientations where the martensite preferentially nucleates. Figure C.8 presents the values of H_{zz} , as function of the angle between the twin boundary normal and the surface normal.

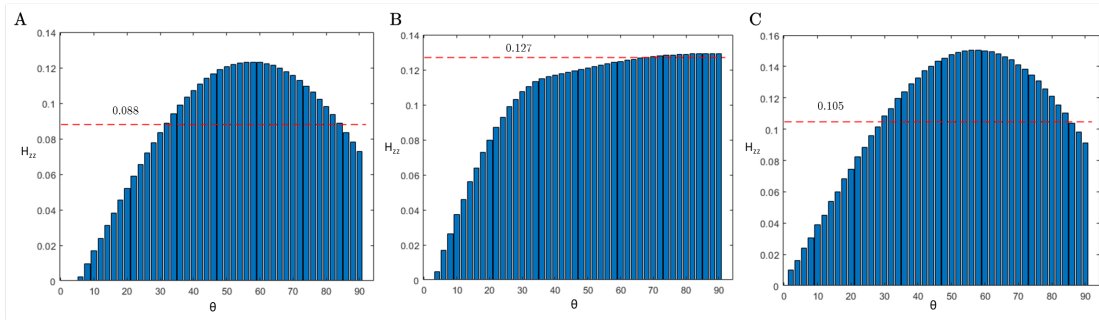


Figure C.8: Magnitude of H_{zz} as function of the θ angle in degrees between the normal to the twinning plane normal and the sample surface. The red line indicates the value of H_{zz} associated with the selected variant in the EBSD map of figure 2. **A**: with the invariant plane strain without dilatation **P**. **B**: with the invariant line strain without dilatation **RB**. **C**: with the invariant plane strain with dilatation **P_δ**

This simulation clearly indicates that the criterion based on the invariant plane strain is not able to account for the particular orientations on which the martensite nucleates. Indeed, the favoured orientations are such that the angle between the surface normal and the twin boundary normal are about 60° (figures C.8A and C.8C). This result would imply that martensite should form preferentially on twin boundary orientated about 60° and not for larger angles, as reported experimentally. The line in red indicates the value of H_{zz} reached by the most favoured variant in the experiment. This line is clearly below the maximum value of H_{zz} , which is 0.1231. On the contrary, the PTMC model based on the invariant line strain **RB** well captures the selection of the favoured orientation of the austenite. By comparing figure C.8B to figure 9.6D and showing the results for the continuous distortion model, it appears that the shape of the variation of the magnitude of H_{zz} as function of the θ angle is similar. Only the magnitude varies a little due to the bigger dilatation associated with the hard sphere model in figure 9.6D. This result is not surprising as these two models only differ from a small rotation. Analogously, figure C.8A and figure C.8C have a similar shape.

In conclusion, the variant selection prediction and the prediction of the favoured orientation of the austenite are well modelled by both the invariant line **RB** of the PTMC without dilatation

C.3. Variant selection predictions and predictions of the favoured austenite orientations based on the PTMC

and the continuous model (which is equivalent to invariant line strain of the PTMC with dilatation parameter). On the contrary, the invariant plane strain \mathbf{P}_δ with dilatation and \mathbf{P} without dilatation parameter cannot explain the favoured orientations of the austenite. Beside, the invariant line \mathbf{RB} predicted without dilatation and the continuous distortion model differ in the prediction of the habit plane and the orientation relationship. The analysis presented in the supplementary section B indicates that surface martensite has a $\{225\}_\gamma$ habit plane and exhibits a Kurdjumov-Sachs orientation relationship. These crystallographic features are accounted only if adding the dilatation parameter, or in other words by using the continuous model.

D Variants table

In this appendix, we detail the different Kurdjumov-Sachs variants and the particular grouping of variants that are mentioned in this thesis. A misorientations table for all the Kurdjumov-Sachs variants as defined in this thesis is presented in table D.1. This table is taken directly from the supplementary 3 of reference [Cayron, 2014]. In that latter work, the misorientations between the variants are defined as *operators*, noted Op. The first column of table D.1 gives the number of each operator. The second column defines the misorientation, as an angle in degree and an axis in the α phase. The last column gives all the pairs of variants that are linked by the operator.

There are two pairs of variants of particular interest in this thesis. The pair called *twin-related variants*, which is associated with the operator Op.3, and the pair called *low-misoriented variants*, which is associated with the operator Op.5. The former pair is of importance for the accommodation of the $\{225\}_{\gamma}$ habit plane, and the latter pairing is observed in the $\{557\}_{\gamma}$ lath martensite.

Appendix D. Variants table

| | | |
|--------|-----------------------|--|
| Op. 0 | Id. | [1, 1], [2, 2], [3, 3], [4, 4], [5, 5], [6, 6], [7, 7], [8, 8], [9, 9], [10, 10], [11, 11], [12, 12], [13, 13], [14, 14], [15, 15], [16, 16], [17, 17], [18, 18], [19, 19], [20, 20], [21, 21], [22, 22], [23, 23], [24, 24] |
| Op. 1 | 60.0° / [1 0 1] | [1, 5], [2, 1], [3, 8], [4, 11], [5, 2], [6, 3], [7, 4], [8, 6], [9, 14], [10, 19], [11, 7], [12, 9], [13, 10], [14, 12], [15, 23], [16, 18], [17, 24], [18, 21], [19, 13], [20, 15], [21, 16], [22, 17], [23, 20], [24, 22] |
| Op. 2 | 60.0° / [1 1 1] | [1, 3], [2, 8], [3, 1], [4, 9], [5, 6], [6, 5], [7, 14], [8, 2], [9, 4], [10, 15], [11, 12], [12, 11], [13, 23], [14, 7], [15, 10], [16, 17], [17, 16], [18, 22], [19, 20], [20, 19], [21, 24], [22, 18], [23, 13], [24, 21] |
| Op. 3 | 10.5° / [1 1 1] | [1, 4], [2, 10], [3, 9], [4, 1], [5, 16], [6, 17], [7, 18], [8, 15], [9, 3], [10, 2], [11, 13], [12, 23], [13, 11], [14, 22], [15, 8], [16, 5], [17, 6], [18, 7], [19, 21], [20, 24], [21, 19], [22, 14], [23, 12], [24, 20] |
| Op. 4 | 60.0° / [1 1 0] | [1, 2], [2, 5], [3, 6], [4, 7], [5, 1], [6, 8], [7, 11], [8, 3], [9, 12], [10, 13], [11, 4], [12, 14], [13, 19], [14, 9], [15, 20], [16, 21], [17, 22], [18, 16], [19, 10], [20, 23], [21, 18], [22, 24], [23, 15], [24, 17] |
| Op. 5 | 10.5° / [1 1 0] | [1, 6], [2, 3], [3, 2], [4, 12], [5, 8], [6, 1], [7, 9], [8, 5], [9, 7], [10, 20], [11, 14], [12, 4], [13, 15], [14, 11], [15, 13], [16, 22], [17, 21], [18, 24], [19, 23], [20, 10], [21, 17], [22, 16], [23, 19], [24, 18] |
| Op. 6 | 50.5° / [16 24 15] | [1, 16], [2, 4], [3, 15], [4, 13], [5, 10], [6, 9], [7, 1], [8, 17], [9, 22], [10, 21], [11, 18], [12, 3], [13, 2], [14, 23], [15, 12], [16, 7], [17, 20], [18, 19], [19, 11], [20, 8], [21, 5], [22, 6], [23, 24], [24, 14] |
| Op. 7 | 49.4° / [1 0 1] | [1, 8], [2, 6], [3, 5], [4, 14], [5, 3], [6, 2], [7, 12], [8, 1], [9, 11], [10, 23], [11, 9], [12, 7], [13, 20], [14, 4], [15, 19], [16, 24], [17, 18], [18, 17], [19, 15], [20, 13], [21, 22], [22, 21], [23, 10], [24, 16] |
| Op. 8 | 49.4° / [1 1 1] | [1, 9], [2, 15], [3, 4], [4, 3], [5, 17], [6, 16], [7, 22], [8, 10], [9, 1], [10, 8], [11, 23], [12, 13], [13, 12], [14, 18], [15, 2], [16, 6], [17, 5], [18, 14], [19, 24], [20, 21], [21, 20], [22, 7], [23, 11], [24, 19] |
| Op. 9 | 57.2° / [22 13 26] | [1, 11], [2, 19], [3, 14], [4, 5], [5, 18], [6, 24], [7, 21], [8, 23], [9, 8], [10, 1], [11, 10], [12, 20], [13, 7], [14, 17], [15, 6], [16, 2], [17, 3], [18, 4], [19, 16], [20, 22], [21, 13], [22, 12], [23, 9], [24, 15] |
| Op. 10 | 57.2° / [13 22 26] | [1, 10], [2, 16], [3, 17], [4, 18], [5, 4], [6, 15], [7, 13], [8, 9], [9, 23], [10, 11], [11, 1], [12, 22], [13, 21], [14, 3], [15, 24], [16, 19], [17, 14], [18, 5], [19, 2], [20, 12], [21, 7], [22, 20], [23, 8], [24, 6] |
| Op. 11 | 14.8° / [4 56 21] | [1, 17], [2, 9], [3, 10], [4, 23], [5, 15], [6, 4], [7, 3], [8, 16], [9, 18], [10, 24], [11, 22], [12, 1], [13, 8], [14, 13], [15, 11], [16, 14], [17, 19], [18, 20], [19, 12], [20, 2], [21, 6], [22, 5], [23, 21], [24, 7] |
| Op. 12 | 47.1° / [56 24 49] | [1, 18], [2, 11], [3, 23], [4, 10], [5, 19], [6, 14], [7, 5], [8, 24], [9, 17], [10, 16], [11, 21], [12, 8], [13, 1], [14, 20], [15, 9], [16, 4], [17, 15], [18, 13], [19, 7], [20, 6], [21, 2], [22, 3], [23, 22], [24, 12] |
| Op. 13 | 50.5° / [20 5 16] | [1, 15], [2, 17], [3, 16], [4, 22], [5, 9], [6, 10], [7, 23], [8, 4], [9, 13], [10, 12], [11, 3], [12, 18], [13, 24], [14, 1], [15, 21], [16, 20], [17, 7], [18, 6], [19, 8], [20, 11], [21, 14], [22, 19], [23, 2], [24, 5] |
| Op. 14 | 50.5° / [16 20 5] | [1, 14], [2, 23], [3, 11], [4, 8], [5, 24], [6, 18], [7, 17], [8, 19], [9, 5], [10, 6], [11, 20], [12, 10], [13, 9], [14, 21], [15, 1], [16, 3], [17, 2], [18, 12], [19, 22], [20, 16], [21, 15], [22, 4], [23, 7], [24, 13] |
| Op. 15 | 50.5° / [24 15 16] | [1, 7], [2, 13], [3, 12], [4, 2], [5, 21], [6, 22], [7, 16], [8, 20], [9, 6], [10, 5], [11, 19], [12, 15], [13, 4], [14, 24], [15, 3], [16, 1], [17, 8], [18, 11], [19, 18], [20, 17], [21, 10], [22, 9], [23, 14], [24, 23] |
| Op. 16 | 14.8° / [21 56 4] | [1, 12], [2, 20], [3, 7], [4, 6], [5, 22], [6, 21], [7, 24], [8, 13], [9, 2], [10, 3], [11, 15], [12, 19], [13, 14], [14, 16], [15, 5], [16, 8], [17, 1], [18, 9], [19, 17], [20, 18], [21, 23], [22, 11], [23, 4], [24, 10] |
| Op. 17 | 47.1° / [49 24 56] | [1, 13], [2, 21], [3, 22], [4, 16], [5, 7], [6, 20], [7, 19], [8, 12], [9, 15], [10, 4], [11, 2], [12, 24], [13, 18], [14, 6], [15, 17], [16, 10], [17, 9], [18, 1], [19, 5], [20, 14], [21, 11], [22, 23], [23, 3], [24, 8] |
| Op. 18 | 21.0° / [0 4 9] | [1, 19], [2, 18], [3, 24], [4, 21], [5, 11], [6, 23], [7, 10], [8, 14], [9, 20], [10, 7], [11, 5], [12, 17], [13, 16], [14, 8], [15, 22], [16, 13], [17, 12], [18, 2], [19, 1], [20, 9], [21, 4], [22, 15], [23, 6], [24, 3] |
| Op. 19 | 57.2° / [21 7 18] | [1, 24], [2, 14], [3, 19], [4, 20], [5, 23], [6, 11], [7, 8], [8, 18], [9, 21], [10, 22], [11, 17], [12, 5], [13, 6], [14, 10], [15, 7], [16, 12], [17, 13], [18, 15], [19, 9], [20, 1], [21, 3], [22, 2], [23, 16], [24, 4] |
| Op. 20 | 20.6° / [5 9 9] | [1, 21], [2, 7], [3, 20], [4, 19], [5, 13], [6, 12], [7, 2], [8, 22], [9, 24], [10, 18], [11, 16], [12, 6], [13, 5], [14, 15], [15, 14], [16, 11], [17, 23], [18, 10], [19, 4], [20, 3], [21, 1], [22, 8], [23, 17], [24, 9] |
| Op. 21 | 51.7° / [9 9 5] | [1, 22], [2, 12], [3, 13], [4, 15], [5, 20], [6, 7], [7, 6], [8, 21], [9, 16], [10, 17], [11, 24], [12, 2], [13, 3], [14, 19], [15, 4], [16, 9], [17, 10], [18, 23], [19, 14], [20, 5], [21, 8], [22, 1], [23, 18], [24, 11] |
| Op. 22 | 20.6° / [4 0 13] | [1, 23], [2, 24], [3, 18], [4, 17], [5, 14], [6, 19], [7, 20], [8, 11], [9, 10], [10, 9], [11, 8], [12, 21], [13, 22], [14, 5], [15, 16], [16, 15], [17, 4], [18, 3], [19, 6], [20, 7], [21, 12], [22, 13], [23, 1], [24, 2] |
| Op. 23 | 57.2° / [21 18 7] | [1, 20], [2, 22], [3, 21], [4, 24], [5, 12], [6, 13], [7, 15], [8, 7], [9, 19], [10, 14], [11, 6], [12, 16], [13, 17], [14, 2], [15, 18], [16, 23], [17, 11], [18, 8], [19, 3], [20, 4], [21, 9], [22, 10], [23, 5], [24, 1] |

Figure D.1: The first column defines the number of the operator as defined in the GenOVa program developed by Cayron [Cayron, 2007]. The second column gives the misorientation in terms of a rotation angle in degrees and an axis angle in the α phase associated with each operator. The third column lists all the pairs of variants sharing the given misorientation. Table taken from Ref.[Cayron, 2014].

D.1 Grouping of variants

In this thesis, we evidenced that the grouping of variants, also referred as local variant selection is of importance in the study of the martensitic transformation and the associated global variant selection phenomenon. In the present section, we propose to illustrate the different groups of variants encountered in our study, namely the Close-Packed Plane packet (CPP packet), the Bain group and the Plate group. Table D.1 presents the list of the variants classified in the different groups.

Table D.1: Kurdjumov-Sachs variant classed in the different groups mentioned in this thesis: CPP Packet, Bain group and the Plate group

| Groups | Variants inside the groups | Operators inside the groups |
|--------------|--|-----------------------------|
| CPP Packets | $(\alpha_1, \alpha_2, \alpha_3, \alpha_5, \alpha_6, \alpha_8)$ | Op.0, Op.1, Op.2, |
| | $(\alpha_4, \alpha_7, \alpha_9, \alpha_{11}, \alpha_{12}, \alpha_{14})$ | Op.4, Op.5, Op.7 |
| | $(\alpha_{10}, \alpha_{13}, \alpha_{15}, \alpha_{19}, \alpha_{20}, \alpha_{23})$ | |
| | $(\alpha_{16}, \alpha_{17}, \alpha_{18}, \alpha_{21}, \alpha_{22}, \alpha_{24})$ | |
| Bain Groups | $(\alpha_1, \alpha_4, \alpha_6, \alpha_{12}, \alpha_{17}, \alpha_{19}, \alpha_{21}, \alpha_{23})$ | Op.0, Op.3, Op.5, Op.11, |
| | $(\alpha_5, \alpha_8, \alpha_{11}, \alpha_{13}, \alpha_{14}, \alpha_{15}, \alpha_{16}, \alpha_{22})$ | Op.16, Op.18, Op.20, Op.22 |
| | $(\alpha_2, \alpha_3, \alpha_7, \alpha_9, \alpha_{10}, \alpha_{18}, \alpha_{20}, \alpha_{24})$ | |
| Plate Groups | $(\alpha_2, \alpha_6, \alpha_7, \alpha_{12})$ | Op.0, Op.7, Op.20, Op.21 |
| | $(\alpha_3, \alpha_5, \alpha_{13}, \alpha_{20})$ | |
| | $(\alpha_1, \alpha_8, \alpha_{21}, \alpha_{22})$ | |
| | $(\alpha_4, \alpha_{14}, \alpha_{19}, \alpha_{15})$ | |
| | $(\alpha_9, \alpha_{11}, \alpha_{16}, \alpha_{24})$ | |
| | $(\alpha_{10}, \alpha_{17}, \alpha_{18}, \alpha_{23})$ | |

D.1.1 The Close-Packed Plane packet (CPP packet)

The Close-Packed Plane packet (CPP packet) is formed by the variants having their close-packed plane involved in the orientation relationship parallel to the same closed-packed plane of the austenite. There are four different close-packed planes in an austenite crystal, such that there are four different CPP packets. Each group contains six Kurdjumov-Sachs variants. One of the four CPP packet is illustrated in figure D.2A, in red. In figure D.2B, the six variants of the same CPP packet are represented on a pole figure. The blue dots are the $\langle 110 \rangle_\alpha$ directions and the red dots are the $\langle 111 \rangle_\gamma$ directions of the parent grain. The arrow on the pole figure indicates the normal to the common $(111)_\gamma$ plane. It can be seen that that normal is parallel to the normal to the $(1\bar{1}0)_\alpha$ of all variants of the CPP packet. Note that here the orientation relationship is chosen such that: $(111)_\gamma \parallel (1\bar{1}0)_\alpha$; $[1\bar{1}0]_\gamma \parallel [111]_\alpha$.

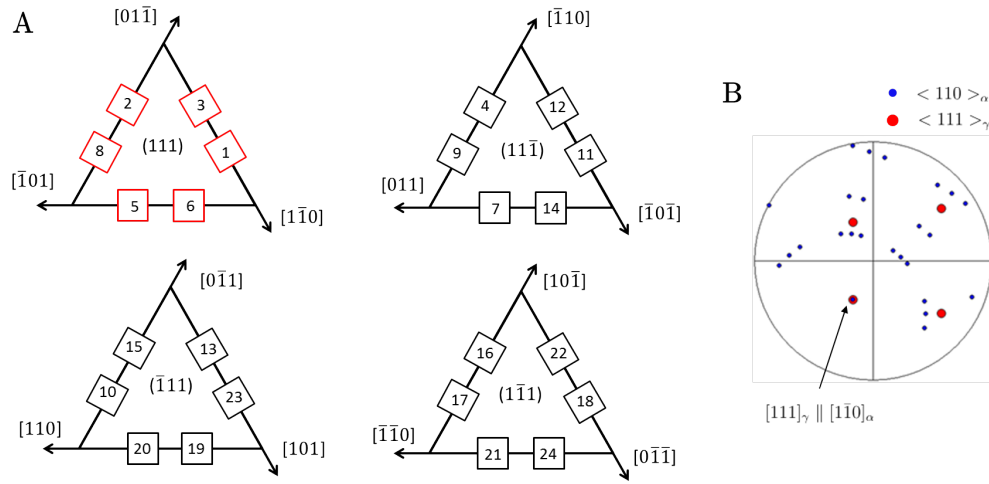


Figure D.2: **A:** The triangles represent the four $\{111\}_\gamma$ planes of an austenite crystal. On each of these face, the Kurdjumov-Sachs variant are represented by rectangles on the $\{111\}_\gamma$ plane parallel to the $\{110\}_\alpha$ involved in the orientation relationship. The direction forming the border of the triangles are the dense $\{110\}_\gamma$ directions of the austenite. The variants are positioned on the top of the $\{110\}_\gamma$ which is invariant during the variants formation. Six Kurdjumov-Sachs belonging to the same CPP packet are marked in red. **B:** The variants belonging to the same CPP packet are represented on a pole figure, with in blue the $\langle 110 \rangle_\alpha$ directions and in red the $\langle 111 \rangle_\gamma$ directions of the parent grain.

D.1.2 The Bain group

The Bain group is defined by all the Kurdjumov-Sachs variants having the same Bain strain, when decomposing the lattice distortion \mathbf{F} in the product of a rotation and the Bain strain, $\mathbf{F} = \mathbf{R}\mathbf{B}$. There are three different Bain groups, each group being composed of eight variants. One of the three of Bain group is illustrated in figure D.3A, in blue.

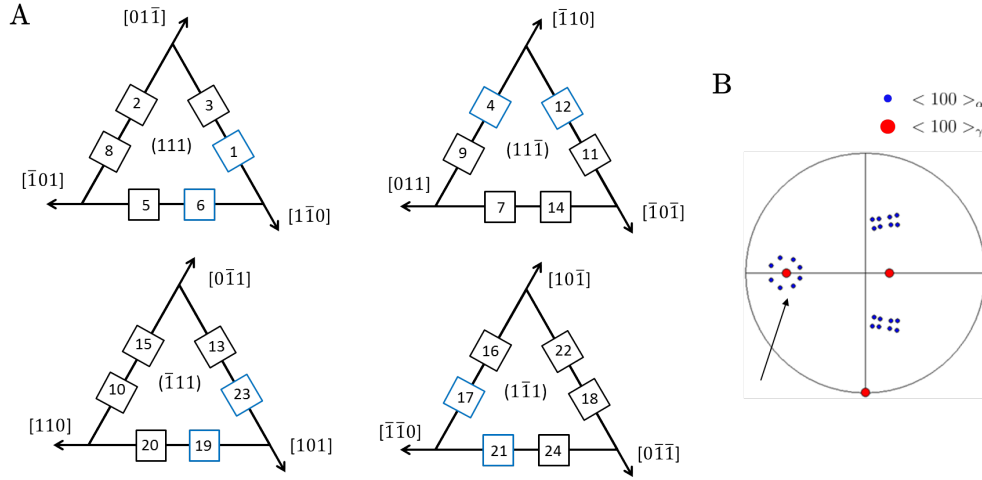


Figure D.3: The triangles represent the four $\{111\}_\gamma$ plane of an austenite crystal. On each of these faces, the Kurdjumov-Sachs variant are represented by rectangles on the $\{111\}_\gamma$ planes parallel to the $\{110\}_\alpha$ involved in the orientation relationship. The direction forming the border of the triangles are the dense $\{110\}_\gamma$ directions of the austenite. The variants are positioned on the top of the $\{110\}_\gamma$ which is invariant during the variants formation. Eight Kurdjumov-Sachs belonging to the same Bain group are marked in blue. **B**: The variants belonging to the same Bain group are represented on a pole figure, with in blue the $\langle 100 \rangle_\alpha$ directions and in red the $\langle 100 \rangle_\gamma$ directions of the parent grain.

D.1.3 The Plate group

The plate group is crystallographically complicated to define. Actually, we do not have any crystallographic explanation for the presence of such a group of variants. Plate groups are found in high carbon martensite or iron-nickel alloys, it is named after the type of martensite where such group are observed, the *Plate* martensite. This type of martensite and the formation of Plate groups are typically associated with the *burst* phenomenon, when the nucleation of a given variant catalyses the creation of another. Such type of martensite is also called zig-zag martensite, due to the zig-zags that the plates of martensite form by the auto-catalytic process. Plate martensite exhibits habit plane of type $\{259\}_\gamma$. Bokros and Parker are the pioneer of the study of this type of martensite and they propose a definition in term of habit plane orientation to define the plate group [Bokros and Parker, 1963]. In their work, the plate group is defined by the variants having their habit plane low-misoriented with respect to the other variants belonging to the same group. The continuous distortion associated with the Kurdjumov-Sachs orientation relationship cannot account for the $\{259\}_\gamma$ habit plane. As a consequence, we use a definition of the plate group based on the crystallographic orientation of the martensite lattice, using the operators of misorientation as proposed by Cayron [Cayron, 2014]. An example of plate group is illustrated in green in figure D.4A. On figure D.4B, we illustrate the plate group on a pole figure. A plate group is characterized by the fact that the $\langle 111 \rangle_\alpha$ cluster about a common $\langle 110 \rangle_\gamma$ direction, as indicated by the arrow.

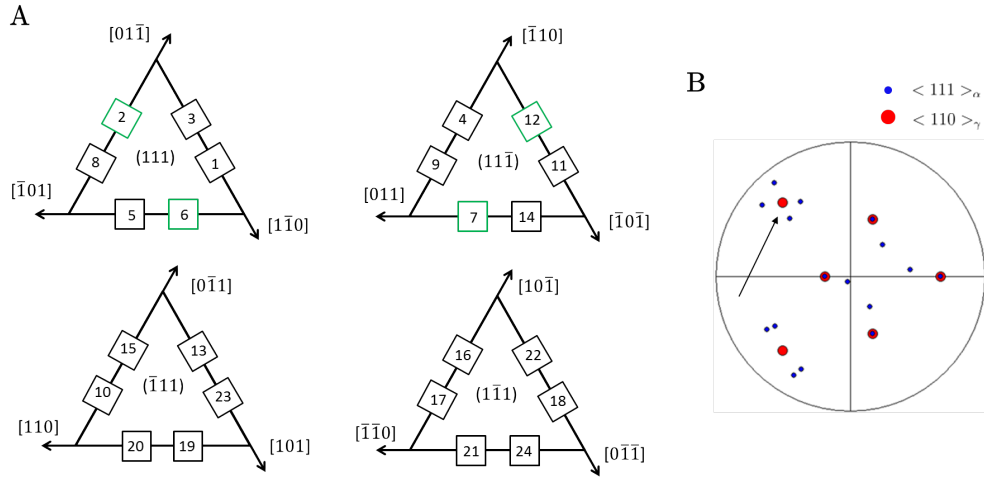


Figure D.4: The triangles represent the four $\{111\}_\gamma$ planes of an austenite crystal. On each of these faces, the Kurdjumov-Sachs variant are represented by rectangles on the $\{111\}_\gamma$ plane parallel to the $\{110\}_\alpha$ involved in the orientation relationship. The direction forming the border of the triangles are the dense $\{110\}_\gamma$ directions of the austenite. The variants are positioned on the top of the $\{110\}_\gamma$ which is invariant during the variants formation. Four Kurdjumov-Sachs belonging to the same plate group are marked in green. **B:** The variants belonging to the same plate group are illustrated on a pole figure. In blue, the $\langle 111 \rangle_\alpha$ directions and in red the $\langle 110 \rangle_\gamma$ directions. The arrow indicates the cluster of the $\langle 111 \rangle_\alpha$ about a common $\langle 110 \rangle_\gamma$.

Bibliography

- [Abreu et al., 2009] Abreu, H. F. G. d., Silva, M. J. G. d., Herculano, L. F. G., and Bhadeshia, H. (2009). Texture analysis of deformation induced martensite in an aisi 301l stainless steel: microtexture and macrotexture aspects. *Materials Research*, 12(3):291–297.
- [Acton and Bevis, 1969] Acton, A. and Bevis, M. (1969). A generalised martensite crystallography theory. *Materials Science and Engineering*, 5(1):19–29.
- [Bain and Dunkirk, 1924] Bain, E. C. and Dunkirk, N. (1924). The nature of martensite. *trans. AIME*, 70(1):25–47.
- [Ball and James, 1987] Ball, J. and James, R. (1987). Fine phase mixtures as minimizers of energy. *Arch. Rat. Mech. Analysis* 100: 13, 52.
- [Bhadeshia et al., 2008] Bhadeshia, H., Abreu, H., and Kundu, S. (2008). Calculation of crystallographic texture due to displacive transformations. *International Journal of Materials Research*, 99(4):342–346.
- [Bhattacharya, 2003] Bhattacharya, K. (2003). *Microstructure of martensite: why it forms and how it gives rise to the shape-memory effect*, volume 2. Oxford University Press.
- [Bogers and Burgers, 1964] Bogers, A. and Burgers, W. (1964). Partial dislocations on the {110} planes in the bcc lattice and the transition of the fcc into the bcc lattice. *Acta Metallurgica*, 12(2):255–261.
- [Bokros and Parker, 1963] Bokros, J. and Parker, E. (1963). The mechanism of the martensite burst transformation in fe–ni single crystals. *Acta Metallurgica*, 11(12):1291–1301.
- [Bowles and Barrett, 1952] Bowles, J. and Barrett, C. (1952). Crystallography of transformations. *Progress in Metal Physics*, 3:1–41.
- [Bowles and Mackenzie, 1954a] Bowles, J. and Mackenzie, J. (1954a). The crystallography of martensite transformations i. *Acta metallurgica*, 2(1):129–137.
- [Bowles and Mackenzie, 1954b] Bowles, J. and Mackenzie, J. K. (1954b). The crystallography of martensite transformations iii. face-centred cubic to body-centred tetragonal transformations. *Acta Metallurgica*, 2(2):224–234.

Bibliography

- [Bowles and Wayman, 1972] Bowles, J. and Wayman, C. (1972). The bain strain, lattice correspondences, and deformations related to martensitic transformations. *Metallurgical Transactions*, 3(5):1113–1121.
- [Britannica, 2011] Britannica, E. (2011). Hexagonal close-packed structure, crystallography.
- [Butrón-Guillén et al., 1997] Butrón-Guillén, M., Viana, C. D. C., and Jonas, J. (1997). A variant selection model for predicting the transformation texture of deformed austenite. *Metallurgical and Materials Transactions A*, 28(9):1755–1768.
- [Cayron, 2006] Cayron, C. (2006). Groupoid of orientational variants. *Acta Crystallographica Section A: Foundations of Crystallography*, 62(1):21–40.
- [Cayron, 2007] Cayron, C. (2007). Genova: a computer program to generate orientational variants. *Journal of applied crystallography*, 40(6):1179–1182.
- [Cayron, 2013] Cayron, C. (2013). One-step model of the face-centred-cubic to body-centred-cubic martensitic transformation. *Acta Crystallographica Section A: Foundations of Crystallography*, 69(5):498–509.
- [Cayron, 2014] Cayron, C. (2014). Ebsd imaging of orientation relationships and variant groupings in different martensitic alloys and widmanstätten iron meteorites. *Materials Characterization*, 94:93–110.
- [Cayron, 2015] Cayron, C. (2015). Continuous atomic displacements and lattice distortion during fcc–bcc martensitic transformation. *Acta Materialia*, 96:189–202.
- [Cayron, 2016] Cayron, C. (2016). Angular distortive matrices of phase transitions in the fcc–bcc–hcp system. *Acta Materialia*, 111:417–441.
- [Cayron, 2018] Cayron, C. (2018). The transformation matrices (distortion, orientation, correspondence), their continuous forms, and their variants.
- [Cayron et al., 2010] Cayron, C., Barcelo, F., and de Carlan, Y. (2010). The mechanisms of the fcc–bcc martensitic transformation revealed by pole figures. *Acta materialia*, 58(4):1395–1402.
- [Chen et al., 2013] Chen, X., Srivastava, V., Dabade, V., and James, R. D. (2013). Study of the cofactor conditions: conditions of supercompatibility between phases. *Journal of the Mechanics and Physics of Solids*, 61(12):2566–2587.
- [Chiba et al., 2012] Chiba, T., Miyamoto, G., and Furuhashi, T. (2012). Variant selection of lenticular martensite by ausforming. *Scripta Materialia*, 67(4):324–327.
- [Chluba et al., 2015] Chluba, C., Ge, W., de Miranda, R. L., Strobel, J., Kienle, L., Quandt, E., and Wuttig, M. (2015). Ultralow-fatigue shape memory alloy films. *Science*, 348(6238):1004–1007.

- [Christian, 1956] Christian, J. (1956). Applications of the phenomenological theories of martensite i–ii. *J. Inst. Met.*, 84:386–394.
- [Curnier, 2005] Curnier, A. (2005). *Mécanique des solides déformables: Cinématique, dynamique, énergétique*, volume 1. PPUR presses polytechniques.
- [Della Porta, 2019] Della Porta, F. (2019). On the cofactor conditions and further conditions of supercompatibility between phases. *Journal of the Mechanics and Physics of Solids*, 122:27–53.
- [Dunne and Wayman, 1971] Dunne, D. and Wayman, G. (1971). An assessment of the double shear theory as applied to ferrous martensitic transformations. *Acta Metallurgica*, 19(5):425–438.
- [Gautier et al., 1989] Gautier, E., Simon, A., and Zhang, X. (1989). Transformation plasticity and resulting microstructures for strain-induced martensitic transformation in fe-ni-c alloys. In *European Symposium on Martensitic Transformations*, pages 451–458. EDP Sciences.
- [Greninger and Troiano, 1949] Greninger, A. B. and Troiano, A. R. (1949). The mechanism of martensite formation. *JOM*, 1(9):590–598.
- [Gu et al., 2016] Gu, X.-F., Furuhashi, T., and Zhang, W.-Z. (2016). Ptclab: free and open-source software for calculating phase transformation crystallography. *Journal of applied crystallography*, 49(3):1099–1106.
- [Higo et al., 1974] Higo, Y., Lacroix, F., and Mori, T. (1974). Relation between applied stress and orientation relationship of α' martensite in stainless steel single crystals. *Acta Metallurgica*, 22(3):313–323.
- [Jana and Wayman, 1970] Jana, S. and Wayman, C. (1970). The morphology and substructure of {225} f martensite in an fe- mn- cr- c alloy. *Metallurgical Transactions*, 1(10):2825–2832.
- [Jaswon and Wheeler, 1948] Jaswon, M. and Wheeler, J. (1948). Atomic displacements in the austenite–martensite transformation. *Acta Crystallographica*, 1(4):216–224.
- [Kato and Mori, 1976] Kato, M. and Mori, T. (1976). Stress-induced martensite in single crystals of an fe-23ni-5cr alloy. *Acta Metallurgica*, 24(9):853–860.
- [Kaufman and Cohen, 1958] Kaufman, L. and Cohen, M. (1958). Thermodynamics and kinetics of martensitic transformations. *Progress in Metal Physics*, 7:165–246.
- [Kelly and Nutting, 1961] Kelly, P. and Nutting, J. (1961). The martensite transformation in carbon steels. *Proc. R. Soc. Lond. A*, 259(1296):45–58.
- [Kelly, 1992] Kelly, P. M. (1992). Crystallography of lath martensite in steels. *Materials Transactions, JIM*, 33(3):235–242.

Bibliography

- [Koumatos and Muehlemann, 2016] Koumatos, K. and Muehlemann, A. (2016). Optimality of general lattice transformations with applications to the bain strain in steel. *Proc. R. Soc. A*, 472(2188):20150865.
- [Kundu, 2009] Kundu, S. (2009). Prediction of transformation texture under complex rolling condition. *Materials Science and Engineering: A*, 516(1-2):290–296.
- [Kundu and Bhadeshia, 2007] Kundu, S. and Bhadeshia, H. (2007). Crystallographic texture and intervening transformations. *Scripta Materialia*, 57(9):869–872.
- [Kurdjumov and Sachs, 1930] Kurdjumov, G. and Sachs, G. (1930). Über den mechanismus der stahlhärtung. *Zeitschrift für Physik*, 64(5-6):325–343.
- [Machlin and Cohen, 1951] Machlin, E. and Cohen, M. (1951). Habit phenomenon in the martensitic transformation. *JOM*, 3(11):1019–1029.
- [Maki, 2012] Maki, T. (2012). Morphology and substructure of martensite in steels. In *Phase Transformations in Steels: Diffusionless Transformations High Strength Steels Modelling and Advanced Analytical Techniques*, pages 34–58. Elsevier.
- [Maki et al., 1973] Maki, T., Shimooka, S., Arimoto, T., and Tamura, I. (1973). The morphology of thin plate-like martensite in fe-ni-c alloys. *Transactions of the Japan Institute of Metals*, 14(1):62–67.
- [Mishiro et al., 2013] Mishiro, Y., Nambu, S., Inoue, J., and Koseki, T. (2013). Effect of stress on variant selection in lath martensite in low-carbon steel. *ISIJ international*, 53(8):1453–1461.
- [Miyamoto et al., 2012] Miyamoto, G., Iwata, N., Takayama, N., and Furuhashi, T. (2012). Quantitative analysis of variant selection in ausformed lath martensite. *Acta Materialia*, 60(3):1139–1148.
- [Morito et al., 2003] Morito, S., Tanaka, H., Konishi, R., Furuhashi, T., and Maki, T. (2003). The morphology and crystallography of lath martensite in fe-c alloys. *Acta materialia*, 51(6):1789–1799.
- [Muehlemann and Koumatos, 2015] Muehlemann, A. and Koumatos, K. (2015). The morphology of lath martensite: a new perspective. *arXiv preprint arXiv:1507.02127*.
- [Nishiyama, 1934] Nishiyama, Z. (1934). X-ray investigation of the mechanism of the transformation from face centered cubic lattice to body centered cubic. *Sci. Rep. Tohoku Univ.*, 23:637.
- [Nishiyama, 2012] Nishiyama, Z. (2012). *Martensitic transformation*. Elsevier.
- [Olsen and Jesser, 1971] Olsen, G. and Jesser, W. (1971). The effect of applied stress on the fcc-bcc transformation in thin iron films. *Acta Metallurgica*, 19(12):1299–1302.

- [Otsuka and Wayman, 1999] Otsuka, K. and Wayman, C. M. (1999). *Shape memory materials*. Cambridge university press.
- [Patel and Cohen, 1953] Patel, J. and Cohen, M. (1953). Criterion for the action of applied stress in the martensitic transformation. *Acta metallurgica*, 1(5):531–538.
- [Pitsch, 1959] Pitsch, W. (1959). The martensite transformation in thin foils of iron-nitrogen alloys. *Philosophical Magazine*, 4(41):577–584.
- [Ross and Crocker, 1970] Ross, N. and Crocker, A. (1970). A generalized theory of martensite crystallography and its application to transformations in steels. *Acta metallurgica*, 18(4):405–418.
- [Sato and Zaefferer, 2009] Sato, H. and Zaefferer, S. (2009). A study on the formation mechanisms of butterfly-type martensite in fe–30% ni alloy using ebsd-based orientation microscopy. *Acta Materialia*, 57(6):1931–1937.
- [Scheil, 1932] Scheil, E. (1932). Über die umwandlung des austenits in martensit in eisen-nickellegierungen unter belastung. *Zeitschrift für anorganische und allgemeine Chemie*, 207(1):21–40.
- [Stormvinter et al., 2012] Stormvinter, A., Miyamoto, G., Furuhashi, T., Hedström, P., and Bor-genstam, A. (2012). Effect of carbon content on variant pairing of martensite in fe–c alloys. *Acta Materialia*, 60(20):7265–7274.
- [Sum and Jonas, 1999] Sum, M. and Jonas, J. (1999). A dislocation reaction model for variant selection during the austenite-to-martensite transformation. *Texture, Stress, and Microstructure*, 31(4):187–215.
- [Tadaki and Shimizu, 1970] Tadaki, T. and Shimizu, K. (1970). Electron microscope study of the martensite transformation in an ordered fe₃pt alloy. *Transactions of the Japan Institute of Metals*, 11(1):44–50.
- [Thomas, 1971] Thomas, G. (1971). Electron microscopy investigations of ferrous martensites. *Metallurgical Transactions*, 2(9):2373.
- [Tomida, 2018] Tomida, T. (2018). Variant selection mechanism by elastic anisotropy and double ks relation for transformation texture in steel; difference between martensite and ferrite. *Acta Materialia*, 146:25–41.
- [Tomida et al., 2013] Tomida, T., Wakita, M., Yasuyama, M., Sugaya, S., Tomota, Y., and Vogel, S. (2013). Memory effects of transformation textures in steel and its prediction by the double kurdjumov–sachs relation. *Acta Materialia*, 61(8):2828–2839.
- [Umemoto et al., 1983] Umemoto, M., Yoshitake, E., and Tamura, I. (1983). The morphology of martensite in fe–c, fe–ni–c and fe–cr–c alloys. *Journal of materials science*, 18(10):2893–2904.

Bibliography

- [Wassermann, 1933] Wassermann, G. (1933). Influence of the α - γ transformation of an irreversible ni steel onto crystal orientation and tensile strength. *Arch. Eisenhüttenwes*, 126:647.
- [Wechsler and Read, 1953] Wechsler, M.S. Lieberman, D. and Read, T. (1953). On the theory of the formation of martensite. *Trans. AIME*, 197:1503–1515.
- [Young, 1926] Young, J. Z. (1926). The crystal structure of meteoric iron as determined by x-ray analysis. *Proc. R. Soc. Lond. A*, 112(762):630–641.



Annick Baur

EPF Mechanical Engineer



27 February 1990



Nationality: Swiss



Chemin de Bellevue 3
CH-1272 Genolier



+41 76 548 44 14



baur.annick@gmail.com

About me

I have a strong interest in research applied to products development. Naturally attracted by the experimental approach, I also appreciate numerical methods for the liberty they offer in the testing of new solutions.

Languages

German

Italian

English

French

Computer Skills

- Conception: Catia
- Finite Element: Abaqus
- CFD: Fluent, Palabos
- Programming: C++, Matlab

Professional Experience

- 2015-2018 Teaching assistant EPFL, Lausanne
Preparation of the exercises
— Simulation of materials (2017-2018)
— Deformation of materials (2015-2017)
— Materials for engineers in microtechnology (2016)
- 2014-2015 Patent Engineer Casalonga & Associés, Paris
French and European process
— Search reports analysis
— Patents writing
- 2014 Internship as patent engineer Moinas & Savoye, Geneva
Introduction to the intellectual property
- 2013 Master internship AO Research Institute, Davos
Cement flow analysis during vertebroplasty
— Mechanical testing
— Medical imaging
— Finite Element simulation

Education

- Since 2015 Phd Student EPFL, Neuchâtel
Variant selection in martensitic steels
— Steel metallurgy
— Crystallography
— Materials characterization
— Solid phase transformations
- 2011-2013 Master in Mechanical Engineering EPFL, Lausanne
Master thesis (AO Research Institute, Davos and Flowkit) :
Cement distribution in vertebroplasty
— Computational Flow Dynamics
- 2008-2011 Bachelor in Mechanical Engineering EPFL, Lausanne
Bachelor thesis :
Determination of the mechanical properties of a thin-ply composite
— Mechanical testing
— Rheology of composites

Publications

- 2018 Baur et al., *Variant selection in Fe-20Ni-1.8C in bending*, Crystals, 8, 474.
- 2018 Baur et al., *Variant selection in surface martensite*, J. Appl. Cryst., 50, 1646-1652.
- 2018 Cayron et al., *Intricate morphologies of laths and blocks in low-carbon martensitic steels*, Materials and design, 154, 81-95.
- 2017 Baur et al., $\{225\}_{\gamma}$ habit plane in martensitic steels : from the PTMC to a continuous model, Scientific Reports, 7 : 40938.
- 2016 Stadelmann et al., *Composite time-lapse computed tomography and micro finite element simulations : A new imaging approach for characterizing cement flows and mechanical benefits of vertebroplasty*, Medical engineering and physics, 38, 97-107.

Conferences

- 2017 ICOMAT-17, 9-14 July, Chicago
- 2016 Junior EUROMAT, 10-14 July Lausanne

Hobbies

Outdoor sports (trail running, climbing, skiing, sailing) and volleyball.

